UNIVERSITY OF SOUTHAMPTON

FACULTY OF NATURAL AND ENVIRONMENTAL SCIENCES

Ocean and Earth Sciences

Multi-decadal Variability of Sea Surface Temperature and Phytoplankton in the Subpolar North Atlantic: Insights from Observation and Model

by

Chongyuan Mao

Thesis for the degree of Doctor of Philosophy

November 2013

UNIVERSITY OF SOUTHAMPTON

<u>ABSTRACT</u>

FACULTY OF NATURAL AND ENVIRONMENTAL SCIENCES

Ocean and Earth Sciences

<u>Doctor of Philosophy</u>

MULTI-DECADAL VARIABILITY OF SEA SURFACE TEMPERATURE AND PHYTOPLANKTON IN THE SUBPOLAR NORTH ATLANTIC: INSIGHTS FROM OBSERVATION AND MODEL

Chongyuan Mao

This thesis investigates the physical controls of variability in phytoplankton abundance in the subpolar North Atlantic. A multi-decadal set of monthly SST data (HadISST1) is used to identify the dominant variability in the SST annual cycle during the period 1870-2009. Long-term variability in phytoplankton abundance is examined using data from the *in situ* Continuous Plankton Recorder (CPR) observations for 1946-2007. Physical factors that determine the strength of the annual phytoplankton bloom are identified using a state-of-the-art coupled physical and biogeochemical model. Mixed layer depth (MLD) in particular is examined because of its importance in controlling the growth of phytoplankton through determining the distribution of light and nutrients in the water column. .

Multi-decadal variability is observed in the amplitude of the SST annual cycle, though the variability is inconsistent across the subpolar basin. The leading EOF modes of seasonal SSTs reveal that about 70% of the observed variability is explained by the seasonal variation of the strength and action centers of the dominant climatic indices (e.g. NAO). Phytoplankton abundance in the eastern shelf region shows variability similar to SST on decadal scales. However, phytoplankton abundance in the subpolar basin is less influenced by SST and is more sensitive to changes in stratification and MLD.

The northeastern subpolar basin is examined in more detail because it is a region where the model simulates observations reasonably well. The hypothesis tested is that the timing and characteristics of the MLD shoaling determines the timing, duration and strength of the following spring phytoplankton bloom. The results show that there are two contrasting scenarios in MLD development and bloom strength. Years with early and lengthy MLD shoaling are characterised by repeated short episodes of vertical mixing when stratification is disturbed, and have a weak and continuous spring bloom as a result. Years with late and rapid MLD shoaling have intense but short spring phytoplankton blooms. MLD influences the growth of zooplankton indirectly, which also modulates the spring phytoplankton bloom. The occurrence of early MLD shoaling in the late winter coincides with a prevalence of atmospheric blocking events (high pressure features) in the northeastern subpolar.

Table of Contents

List of Tables

List of Figures

DECLARATION OF AUTHORSHIP

I, <u>Chongyuan Mao</u> declare that this thesis and the work presented in it are my own and has been generated by me as the result of my own original research.

Multi-decadal Variability of Sea Surface Temperature and Phytoplankton in the

Subpolar North Atlantic: Insights from Observation and Model

I confirm that:

1. This work was done wholly or mainly while in candidature for a research degree at this University;
2. Where any part of this thesis has previously been submitted for a degree or any other qualification at this University or any other institution, this has been clearly stated;
3. Where I have consulted the published work of others, this is always clearly attributed;
4. Where I have quoted from the work of others, the source is always given. With the exception of such quotations, this thesis is entirely my own work;
5. I have acknowledged all main sources of help;
6. Where the thesis is based on work done by myself jointly with others, I have made clear exactly what was done by others and what I have contributed myself;
7. None of this work has been published before submission.

Signed: ....

Date: ....

Graduate School of the

National Oceanography Centre, Southampton

This PhD dissertation by

Chongyuan Mao

has been produced under the supervision of the following persons

Supervisor/s:

N. Penny Holliday, Sheldon Bacon, Ekaterina Popova and P. Chris Reid

Chair of Advisory Panel

Meric Srokroz

Member/s of Advisory Panel

N. Penny Holliday, Sheldon Bacon and Ekaterina Popova

Acknowledgements

Firstly I would like to thank my primary supervisor Penny Holliday. It has been an honour to be her first Ph.D. student. I have enjoyed all of our meetings and discussions during which she provided inspiring ideas and careful guidance, but at the same time gave me enough freedom to develop my own understanding and thinking. I particularly appreciated the time and effort she contributed to our two trips to Plymouth, it was great fun and very useful. She also sets an excellent example, both consciously and unconsciously, on how professional and personal life should be balanced as a female researcher in natural science. I would also like to thank my other supervisors: Sheldon Bacon, Ekaterina (Katya) Popova and P. Chris Reid for their time and ideas, especially at critical transitional turns of my Ph. D. I also appreciated the suggestions my panel chair Professor Meric Srokroz made during panel meetings on topics from general management of my Ph. D. to specific scientific questions.

I would like to thank many of the colleagues working at the Sir Alister Hardy Foundation of Ocean Sciences. In particular, I appreciate the insightful discussion with Pierre Helaouet, Martin Edwards and Abigail McQuatters-Gollop, which provides me with a basic understanding of the biological data. I am also thankful to David Jones who provided me data with specific requirements. Many thanks to Darren Stevens, Anthony Walne, Claudia Castellani, Priscilla Licandro and various enthusiastic lab technicians who explained the sampling and processing processes of the Continuous Plankton Recorder observation thoroughly to me.

I want to thank Robert Pickart, the advisor during my stay at Woods Hole Oceanographic Institution under the NOC-WHOI Exchange Programme, for accepting me as an exchange student and allowing me to participate in an amazing cruise to the Beaufort Sea on the US Coast Guard Healy. Bob is enthusiastic, energetic and full of ideas, not only a good supervisor in science but also a good friend in life. I would like to thank my cruise roommate Motoyo Ithon, who was patient and thorough when teaching me new software and impressively hardworking and serious in science. I appreciate all the help from Frank Barh, Donglai Gong, Wilken-Jon von Appen, Terry Mckee, Kate Lewis and all the fun I had with friends Cherel Balkma, Rebecca Certner and Lola Perez. Especially I would also like to thank Professor Harry Bryden for selecting me

under the programme and being encouraging in many other events during my Ph.D. years.

My friends, officemates and housemates have been a great resource for support through my Ph. D., without whom the four-year experience would be a lot tougher. I remember all the exciting and lovely moments with my first-year housemates in the happy Woolston house: Alex Meier saved me from various kitchen disasters and I appreciated all the gorgeous cakes/cookies Elise Van Meerssche made. Our trips in and around Southampton were fantastic, though our Friday film evenings were also awesome. The dinner parties Tingting Shi and Zongpei (Fox) Jiang organised on many weekends were of great comfort after a busy week. Thank you all for helping me successfully adapt to a new life using a different language, in a different culture and away from family. Thanks to my first landlord Phil Weaver, who had comforted me even before my arrival in the UK by assuring me that 'we will take care of you.'

I would like to thank my officemates, Freja Hunt and Mark Pickering, for introducing Boris, the cutest crab in the Universe, to our office tank. I especially want to thank Gavin Evans, who has been extremely patient and supportive through my Ph. D. years as my primary free proofreader, providing both grammar-related and scientific suggestions. Even the professional proofreaders confirmed that the Gavin-edited documents were very well written.

Lastly, I would like to thank my parents, Feng Mao and Hongmei Huang, for their love and support both emotionally and financially. My mother has always been encouraging, especially during the toughest times in my Ph. D. years, without her love and encouragement I would have never gone this far. Thanks to my uncles, aunts and cousins for simply being proud of me. Thank you all.

Definitions and Abbreviations

Symbol	Definitions
Q_{net}	Net Heat Flux
Q_{sw}	Shortwave Heat Flux
Q_{lw}	Long Wave (Infrared) Heat Flux
Q_{sh}	Sensible Heat Flux
Q_{lh}	Latent Heat Flux
T_{MLD}	Length of the MLD-shoaling period
ρ	Sampling Error
λ	Eigenvalue
θ	Potential Temperature
σ	Potential Density
$s.t.d.$	Standard Deviation

Abbreviations	Full Names
ACA	Annual Cycle Amplitude
AMO	Atlantic Multi-decadal Oscillation
AMOC	Atlantic Meridional Overturning Circulation
AO	Arctic Oscillation
AVHRR	Advanced Very High-Resolution Radiometer
CCM	Coupled Ocean-Atmosphere Climate Model
Chl-a	Chlorophyll-a
COADS	Comprehensive Ocean-Atmosphere Data Set
CPR	Continuous Plankton Recorder
DIN	Dissolved Inorganic Nitrogen
EAP	Eastern Atlantic Pattern
EGC	East Greenland Current
EOF	Empirical Orthogonal Functions
ESC	European Shelf Current
ESRL	Earth System Research Laboratory
GMEPD	Meso-zooplankton grazing on diatom
GMEPN	Meso-zooplankton grazing on non-diatom
GMIPN	Micro-zooplankton grazing on non-diatom
GS	Gulf Stream
GTS	Global Telecommunication System
HadISST1	Hadley Centre Sea Ice and Sea Surface Temperature
ICOADS	International Comprehensive Ocean-Atmosphere Data Set
INT_PP	Depth-integrated Primary Production

Abbreviations	Full Names
LC	Labrador Current
LIM	Louvain-la-Neuve Ice Model
MDB	Marine Data Bank
MEDUSA	The Model Of Ecosystem Dynamics, Nutrient Utilisation, Sequestration and Acidification
MLD	Mixed Layer Depth
MOHSST	Met Office Historical Sea Surface Temperature
NAC	North Atlantic Current
NAF	North Atlantic Front
NAO	North Atlantic Oscillation
NCAR	National Centre For Atmospheric Research
NCEP	National Centres For Environmental Prediction
NEMO	The Nucleus For European Modelling Of The Ocean
NH	North Hemisphere
NOAA	National Oceanic and Atmospheric Administration
NOCS	National Oceanography Centre, Southampton
NS	North Sea
OISST	Optimum Interpolation Sea Surface Temperature
P-E	Precipitation minus Evaporation
PC	Principal Component
PCA	Principal Component Analysis
PCI	Phytoplankton Colour Index
PSD	Physical Sciences Division

Abbreviations	Full Names
RSOI	Reduced Space Optimal Interpolation
SA	Standard Area
SEC	Shelf Edge Current
SEM	Standard Error of the Mean
SH	South Hemisphere
SLP	Sea Level Pressure
SPF	Subpolar Front
SSS	Sea Surface Salinity
SeaWiFS	Sea-Viewing Wide Field-of-View Sensor
UML	Upper Mixed Layer
WGC	West Greenland Current

Chapter 1
Introduction

1.1   Annual Cycle

The Earth System consists of several interacting sub-systems, namely the atmosphere, the hydrosphere, the biota, the cryosphere, and the solid earth [Kump *et al.*, 2011]. Periodical variations of parameters within the Earth System can result in complex yet distinguishable features during this period. One of the most significant naturally occurring periods is the solar year, within which the Earth completes a full revolution around the Sun. The main result of the annual cycle is the variation of solar radiation received on the surface due to the Earth's rotation with an angle to its tilt (Figure 1.1, [McKnight and Hess, 2005]). Twice a year, at the vernal and autumnal equinox respectively (usually around 21 March and 23 September), sunshine reaches the equator perpendicular to the Earth surface. Around these dates, the distribution of heat from the Sun is generally equal between the Northern and Southern Hemispheres. Day length is longest around 21 June in the NH (the summer solstice), when the Earth tilts towards the Sun. As a result of the tilt, the Sun reaches its highest (lowest) elevation in the NH (SH), and hence more heat is distributed towards the north. Conversely, the shortest day length in the NH is seen around 23 December (the winter solstice) when the Earth tilts away from the Sun, and the Sun reaches its lowest (highest) elevation in the NH (SH).

In the ocean, annual cycles corresponding to the variation of solar radiation are observed in almost all parameters ranging from the sea surface temperature to the life cycle of deep-sea organisms. These annual cycles are vital to the local climate and ecosystems as the annual cycles affect the distribution and storage of heat and freshwater, and also alter the timing of many biological processes, such as phytoplankton spring bloom, animal migration and reproduction [Wallace, 2003]. However, the long-term variation of the annual cycles is unclear as they are typically assumed unchanged and hence removed from climatic datasets [Wallace, 2003; Cannaby and Husrevoglu, 2009]. Under a changing climate, the adjustment of environmental processes on the annual and regional scales is crucial for determining the effect of greenhouse warming on ecosystems and society [Hegerl *et al.*, 2011]. A better knowledge of the physical annual cycles is required to provide a thorough understanding of the global climate. With long-term observations of sea surface temperature (SST), phytoplankton abundance, and model outputs, this thesis aims to

shed some light on the decadal to multi-decadal variability of annual cycles and its impact on the local ecosystem is analysed in the subpolar North Atlantic.

In this chapter, the existing knowledge on the topics of SST annual cycle and potential controlling mechanisms is reviewed. The main questions on long-term variability of physical annual cycles and their impact on ecosystems in subpolar North Atlantic that will be examined in the thesis are proposed.

1.1.1   Definition of Seasons

There are several ways to define seasons. The most straightforward definition is astronomical, which defines seasons according to the orientation of the Earth relative to the Sun during one solar year [Wallace, 2003]. The two solstices (usually 21 June and 22 December, see Figure 1.1) and two equinoxes (usually 21 March and 23 September) should be in the middle of each corresponding season. In regions of continental climate, these dates are considered as the start of the seasons. The lengths of the seasons are not uniform across the latitudes due to the elliptical orbit of the Earth and the different speeds along the orbit [Trenberth, 1983].

Meteorological seasons are also widely used in practice. These seasons are defined mainly by temperatures: summer is the quarter of the year with highest temperature, winter is the quarter of the year with lowest temperature, and spring and autumn are the two quarters of the year in between. Each season lasts three months, and the start dates of the four seasons from spring to winter are the first day of March, June, September, and December, respectively. In the ocean, similar definitions of seasons exist and the meteorological seasons are used most widely, though the seasons are defined using sea temperature.

For living organisms, one annual cycle is usually divided into six ecological seasons instead of four: prevernal (1 March-1 May), vernal (1 May-15 June), estival (15 June-15 August), serotinal (15 August-15 September), autumnal (15 September-1 November), and hibernal (1 November-1 March). In marine biology, the period from April to August is usually referred to as the "growing season", when light and nutrient conditions are favourable for growth [Edwards *et al.*, 2001].

1.1.2   Global Distribution of Seasons

The definitions of seasons are based on the climate in temperate regions, which represents the global averaged status with four distinct seasons. In other parts of the globe, the number of seasons and the length of seasons do not necessarily follow the definitions. In the tropics and subtropics, a year is divided into rainy and dry seasons based on precipitation, since no distinguishable change in temperature is observed throughout a year. In other tropical regions, three seasons are observed: hot, rainy, and cool [de-Blij and Miller, 1996]. In the regions of seasonal ice coverage, seasons are distinguished based on ice: ice formation, sea ice, ice melt, and ice-free seasons [Parkinson, 1992; Gloersen et al., 1999; Belchansky et al., 2004]. In some parts of the globe, specific seasons are defined by particular events, such as monsoon seasons in the Indian Ocean and hurricane seasons along the American southeastern coast (Figure 1.2). Seasons in the ocean usually have a 2-month lag to the seasons on land due to the larger heat capacity of the sea water, as well as the vertical mixing that distributes the heat over depth and delays the change of seasons.

Annual variations are observed in the oceans (e.g. North Atlantic and North Pacific), especially in mid-latitudes [Pickard and Emery, 1990]. Previous literature on the long-term variation of SST annual cycle has mainly focused on the Pacific and tropical regions [Chen et al., 1994; Yu et al., 2006; Ding et al., 2009]. The annual cycles in the continental regions and the open ocean are both mainly modulated by the annual variation of solar radiation, though in the open ocean the annual cycle is also modulated by oceanic factors. The SST annual cycle in the tropical Pacific, for example, shows two annual peaks in the eastern boundary but one annual peak in the western boundary, resulting from the differences in vertical mixing at the two boundaries [Chen et al., 1994]. The subpolar North Atlantic is a region of complex physical and biological processes (see detailed discussion below) from intra-annual to multi-decadal scales; however, the long-term variability of annual cycles and its controlling mechanisms are less understood.

1.2   Subpolar North Atlantic

1.2.1   Mean Circulation

The subpolar North Atlantic (Figure 1.3) is characterised by a cyclonic subpolar gyre, which is a key factor for ocean and climate both locally and globally. The southern boundary of the subpolar gyre is the North Atlantic Front, where the warm and salty North Atlantic Current (NAC) encounters the cold Labrador Current (LC). NAC flows northeastward across the Iceland Basin and turns northward after it reaches the eastern continental area [Holliday, 2002]. NAC splits into two branches southeast of Iceland, one branch flows into the Nordic Sea through the Faroe-Shetland channel as the Norwegian Atlantic Current, and the other branch flows westward across the Iceland Basin before it bifurcates again. A small portion of the western branch of NAC keeps flowing northward west of Iceland, whilst the rest of this branch flows into the Irminger Basin, which eventually reaches the Labrador Sea basin and transforms to deep water in the central Labrador Sea due to large amount of surface heat loss [Curry and Mauritzen, 2005].

The NAC flowing in the eastern subpolar basin brings warm and salty water into the eastern subpolar basin [Hansen and Østerhus, 2000; Yaremchuk *et al.*, 2001] together with the southern origin Shelf Edge Current (SEC, [White and Bowyer, 1997], also known as the European Shelf Current, ESC, [De-Jong, 2010]). The advective heat compensates the heat loss due to air-sea interaction and heat exchange with northern water masses [Bonjean, 2001]. The warm eastern subpolar water, combined with deep winter convection, acts as a heat source and releases heat to the atmosphere, allowing milder winters in northern Europe than that at equivalent latitudes [Ellett, 1993]. On the eastern Greenland shelf, cold and fresh Arctic origin water, the East Greenland Current (EGC), enters the subpolar North Atlantic through the Denmark Strait and flows southwestward alongside the western branch of NAC. EGC turns northward after flowing around the southern end of Greenland, resulting in the West Greenland Current (WGC), which is joined by Arctic origin water flowing through the Davis Strait. The cold and fresh water re-circulate within the Labrador Sea and Irminger Sea, and are transported eastward into the interior subpolar basin along the cyclonic gyres. A small branch of the cold water flows southward along the narrow Labrador Shelf,

encountering the northern wall of the Gulf Stream at ~40° N [Taylor and Stephens, 1998]. In general, advective warming occurs to the south and east of NAC, roughly along the NAC pathway whilst advective cooling occurs in the central subpolar basin due to the eastward transport of cold Arctic origin water across the subpolar basin.

1.2.2   Average Annual Cycle of SST and MLD

The oceans play an important role in the global climate system, mainly owing to their large thermal inertia [Hanawa and Sugimoto, 2004]. The oceans are coupled with the atmosphere, which is also crucial to climate system, through energy exchange at the sea surface [Deser *et al.*, 2009]. The sea surface temperature (SST) impacts these exchanges significantly and is determined by both atmospheric and oceanic processes. The variation of mixed layer depth (MLD) links atmospheric and oceanic activities, which also affect the spatial and temporal distribution of SST. Thus, SST and MLD are the key parameters analysed and discussed in this thesis.

In this section, the average annual cycles of SST and MLD in the subpolar North Atlantic are introduced. The average SST in February, May, August, and November are presented in Figure 1.4, representing winter, spring, summer, and autumn SSTs, respectively. Seasonal SST used here is from HadISST1, which is produced by the Met Office Hadley Centre. The representative annual cycle of MLD (Figure 1.5) is adapted from Kara *et al.* (2003), which is produced using Levitus data at 45° N, 30° W with a 0.8 °C temperature difference and includes the effect of salinity. The subpolar North Atlantic is located between subtropical and Arctic regions, and solar insolation varies significantly on annual scale; hence, this region shows four distinct seasons.

The seasonal distribution of SST isotherms is spatially inconsistent in the subpolar basin, and presents clear regional characteristics. In winter, SST falls below 0 °C along the shelf in the western subpolar basin and the thermohaline gradient that defines the North Atlantic Front is at its sharpest (Figure 1.4). In the Irminger Sea, the isotherms are distributed roughly northeast-southwest. Isotherms in the eastern and southern open ocean are distributed along the latitudes, and SST decreases from 15 °C in the south to 8 °C in the north. SST in the shelf seas (e.g. the North Sea) is ~3 °C colder than in the open ocean of equivalent latitudes. In spring, SST starts to increase though it is still lower than 5 °C in the western subpolar basin. In the eastern subpolar basin, isotherms

are distributed along the latitudes, including the shelf seas. Summer SST is above 10 °C in the majority of the subpolar North Atlantic, and the only exception is seen in regions influenced by Arctic origin currents along the Greenland and northern Labrador Sea. The isotherms are distributed along the latitudes, except in the Labrador Sea where a "warm tongue" enters the Labrador Sea from the subpolar North Atlantic. The distribution of autumn SST closely resembles that in spring, except that the southwest-northeastward SST gradient is weaker in autumn. Within a typical annual cycle, coldest SST is observed in February or March, and warmest SST is observed in August.

MLD refers to the layer above which the water column is quasi-homogeneous, vertically uniform, and well mixed by varied surface processes such as wind driven mixing and surface buoyancy loss [Pickard and Emery, 1990; Kara *et al.*, 2000; Thomson and Fine, 2003; Montegut *et al.*, 2004]. It can be defined using various criteria and methods, which may lead to different results. Criteria are predominately temperature-based and density-based, with the former criterion easier in practice and the latter criterion typically providing a more accurate estimation [Kara *et al.*, 2003]. Before the deployment of Argo floats, the estimates of MLD were sparse in most ocean basins. In regions with sparse density data (e.g. subpolar North Atlantic), temperature can be a good alternative parameter [Montegut *et al.*, 2004]. The choice of temperature difference from surface can vary from 0.2 °C to 0.8 °C, based on the spatial scale of the study focus and the resolution of the chosen dataset.

The winter subpolar North Atlantic is generally well mixed, especially in the Labrador Sea and Irminger Basin, where winter mixing could exceed 2000m in severe winters [Våge *et al.*, 2009]. This deep convection is mainly related to the large buoyancy loss in winter, together with strong westerly winds and the coexistence of several layers of water masses under the surface [Killworth, 1983]. In the northeastern subpolar basin, maximum winter mixing is ~500m, which results from large buoyancy loss and weak vertical density gradient as the density difference between the 50 and 500m levels is ~0.2 kgm^{-3} in the late summer [Ellett, 1993]. In spring, the MLD shoals following the increase of isolation and weakening of the westerly winds. Shallow stratification is reached in spring, and the MLD remains shallower than 50m through the summer months. The shoaling of MLD and establishment of shallow stratification are critical processes determining the development of phytoplankton bloom, which will be

discussed in more detail in later chapters. MLD starts to deepen again in late summer or early autumn, coinciding with the increasing heat loss associated with decreasing isolation and stronger wind mixing. The deepest MLD is usually reached in February or March, and shallowest stratification is observed in August.

1.3   Mechanisms Controlling the SST and MLD Annual Cycles

The variation of physical and biological parameters on the annual scale is one of the most noticeable phenomena in the Earth System. In the subpolar North Atlantic, large annual cycles are observed in SST and MLD, where the amplitudes are >5 °C and >400m, respectively. The large annual cycles are important in local and global heat and water transport, which are modulated by annual cycles of other related parameters, such as the processes that determine the atmosphere-ocean interaction. In this section, the parameters that are responsible for the observed annual cycles of SST and MLD in the subpolar North Atlantic are summarised.

1.3.1   Heat Flux

One of the determining parameters for both SST and MLD is surface heat flux. The net heat flux, Q_{net}, is defined as

$$Q_{net} = Q_{sw} + Q_{lw} + Q_{sh} + Q_{lh},$$
<div align="right">Eq. 1.1</div>

where Q_{sw} is net shortwave insolation, Q_{lw} is the net long wave (infrared) radiation, Q_{sh} is sensible heat flux, and Q_{lh} is latent heat flux [Deser *et al.*, 2009]. Solar radiation is always positive, and is the major heat source to the surface layer. Net infrared radiation is always negative and is the heat escaped from the Earth into space. Sensible heat flux is usually negative and is controlled by wind speed and air-sea temperature difference. Latent heat flux can be either positive or negative and is controlled by wind speed and relative humidity [Stewart, 1997]. The combination of sensible and latent heat fluxes ($Q_{sh} + Q_{lh}$) is usually referred as the turbulent heat flux, which is proportional to the wind speed and air-sea temperature and humidity difference [Deser *et al.*, 2009].

The solar radiation in the subpolar North Atlantic is high in summer and low in winter (using meteorological definition), and is also latitude dependent as it decreases towards the north. The insolation peaks in June when the Sun's apparent position in the sky reaches the Tropic of Cancer. The subpolar ocean stores heat in summer and releases heat in winter, and the annual mean is a net heat loss from the ocean to the atmosphere [Kallberg *et al.*, 2005]. SST in the subpolar North Atlantic peaks in August instead of June due to vertical mixing and the bigger heat capacity of seawater compared to the atmosphere [Yashayaev and Zveryaev, 2001]. In addition to the direct heating, stronger solar radiation also enhances the stratification in the upper ocean, which prohibits vertical mixing and results in a shallow MLD [Chen *et al.*, 1994; Yu *et al.*, 2006]. However, winter isotherms are distributed perpendicular to latitude in some parts of the subpolar basin, suggesting that other factors also play important roles in determining the SST annual cycle.

In the subpolar North Atlantic, the annual range of Q_{lw} is from -60 W m^2 to -30 W m^2, and Q_{lw} is larger in winter than in summer (more heat loss in winter) [Kallberg *et al.*, 2005]. Q_{lw} mainly depends on cloud thickness and atmospheric water vapour content [Stewart, 1997], though cloud height, water temperature, and ice or snow cover also contribute to its variation. In summer, higher SST leads to larger upward infrared radiation (heat leaving the ocean) while at the same time the amount of water vapour and vapour-carrying capacity of the atmosphere also increases, which leads to larger downward infrared radiation (heat entering the ocean) [Lagerloef *et al.*, 2010]. The resulting thicker clouds and more water vapour, and hence larger downward infrared radiation, leads to less net heat loss in summer than in winter [Gupta *et al.*, 1992].

Sensible heat flux (Q_{sh}) is related to the wind speed and the temperature difference between ocean and atmosphere [Stewart, 1997]. In the subpolar North Atlantic, Q_{sh} is generally balanced in summer, and only out of balance in regions near the Newfoundland shelf where a net gain of ~15 W m^{-2} is observed due to a large temperature difference between the air and ocean surface. The ocean loses heat to the atmosphere from autumn to the following spring [Kallberg *et al.*, 2005]. In winter, Q_{sh} is related to cold air from the North American continent, which remains generally unmodified as it flows over the partially ice-covered Labrador Sea and Irminger Sea.

Latent heat flux (Q_{lh}) is mainly influenced by wind speed and relative humidity; strong winds and dry air lead to more latent heat loss [Stewart, 1997]. In the subpolar North Atlantic, Q_{lh} heat loss is seen in all seasons in the majority of the subpolar region, except in regions near the Newfoundland and the Labrador Sea where the ocean gains Q_{lh} in summer. Summer heat loss through Q_{lh} is weaker than in winter due to weaker winds and higher water vapour content in the atmosphere in summer [Gupta *et al.*, 1992].

To summarise, the long-term average seasonal net surface heat flux, produced using the NOCS1.1 heat flux climatology (Figure 1.6), suggests that the ocean stores heat in summer and loses heat to the atmosphere in winter in the subpolar North Atlantic. Heat loss is significant mainly in the Labrador Sea, the Gulf Stream, and southwest of Iceland in winter and autumn. From spring to summer, the most significant heat gain is observed on the western shelf and southeastern subpolar basin including the North Sea. Considering all of the heat flux components, the turbulent heat fluxes influence the subpolar circulation and water mass transformation, which can potentially impact SST and MLD [Moore *et al.*, 2012]. As both solar radiation and infrared heat fluxes remain relatively stable on inter-annual, the variation of the turbulent heat fluxes may play a more important role in determining the variability of SST and MLD annual cycles. On longer time scales, the strength solar radiation generally follows an 11-year cycle and may vary corresponding to certain event, such as the global dimming period observed between the 1950s and 1980s [Wild, 2009], these all potentially affect the long-term variability of the SST annual cycle.

1.3.2   Wind Stress

Wind stress is the primary drive force of ocean currents in the world ocean and plays an important role in determining the seasonal variation in the subpolar North Atlantic. In parts of the subpolar basin, wind driven mixing contributes to the initialisation of winter deep convection [Killworth, 1983]. The variability of wind stress is also associated with the development and strength of the subpolar gyre [Flatau *et al.*, 2003; Hátún *et al.*, 2005]. In the North Atlantic, wind stress, especially the westerlies, is strongly modulated by the North Atlantic Oscillation (NAO) [Hurrell, 1995]. Wind stress responds to the variation of NAO on multiple scales ranging from seasonal to decadal.

Wind stress in the subpolar North Atlantic shows clear seasonality, also responding to the seasonal variation of SLP between Azores and Iceland. The long-term average seasonal near surface wind stress is produced using the climatology from the National Centres for Environmental Prediction/National Centre for Atmospheric Research (NCEP/NCAP) 20th century reanalysis (Figure 1.7). The dominant winds in the interior subpolar basin are westerlies in the four seasons, though the wind presents a southwesterern wind component. Wind is strongest in winter, with its speed exceeding 5 m s^{-1} in the majority of the subpolar basin except in boundary areas (between 2 m s^{-1} and 4 m s^{-1}). Maximum westerly wind stress is observed in December in the North Atlantic north of 45° N and in January further south [Trenberth *et al.*, 1990]. The strengthened cyclonic gyre centring on the Icelandic Low is clear in winter (Figure 1.7a), whilst in summer the influence of the Subtropical High expands northward (Figure 1.7c).

The annual variation of wind stress directly influences the strength and distribution of the turbulent heat flux, which in turn impacts the development of deep convection. Wind stress also affects the strength of the subpolar gyre and wind-driven horizontal advection that redistributes heat in the upper ocean [Trenberth *et al.*, 1990; Chen *et al.*, 1994]. Wind-driven Ekman transport in the central subpolar basin spreads cold water formed in the Labrador Sea to the southern and eastern basin. Under positive NAO and stronger subpolar gyre, cold and fresh water is observed in the central and eastern subpolar basin whilst under negative NAO and weaker subpolar gyre, cold and fresh Arctic-origin water is trapped mainly in the western subpolar basin [Flatau *et al.*, 2003]. Stronger subpolar gyre leads to larger Ekman transport of cold water to the southern and eastern basin, which cools the sea surface in the central subpolar. Wind stress in the North Atlantic can also lead to a barotropic response of Atlantic inflow into the Arctic with a 15-month lag. This process adjusts the physical annual cycle in the subpolar North Atlantic in addition to the variation of Ekman transport [Orvik and Skagseth, 2003].

1.3.3   Vertical Mixing

The annual variation of MLD is mainly due to the competing influences of solar radiation and wind stress [Chen *et al.*, 1994]. Solar radiation increases the stability of

the water column by enhancing the stratification between surface and deep water, which prevents vertical mixing. Wind stress, on the other hand, weakens the stratification by mechanically stirring the water column, which increases vertical mixing and potentially leads to deeper MLD. Five processes potentially lead to deep convection in the Northern Hemisphere: 1) a cyclonic background circulation that leads to diversion in the centre, which allows the upwelling of deeper water and a "doming" of the isopycnal; 2) preconditioned water columns with weak density stratification; 3) several layers of water masses; 4) sufficient surface forcing; and 5) the sinking and spreading of the cooling and convective signal [Killworth, 1983]. One good example of deep convection resulting from combinations of these elements is observed in the Labrador Sea. The northward flowing West Greenland Current and the southward flowing Labrador Current form a cyclonic background circulation and increasing westerlies during late autumn to early winter help the preconditioning process. The water column in the Labrador Sea consists of several layers, so the subsurface water functions as a heat source. When MLD sinks to a lower layer, it deepens dramatically to the bottom of the well-mixed lower layer. A large amount of turbulent heat loss and strong westerly winds provide sufficient surface forcing. The baroclinic instability is involved in the final sinking and spreading phase, and the ice cover in the Labrador and Irminger Sea also influences the deep convection [Våge *et al.*, 2009].

Variation of vertical mixing can influence the depth to which heat is distributed. In summer, solar radiation is at its peak and wind is relatively weak, thus the solar energy is distributed within the stratified surface layer and contributes to the peak of summer SST. On the other hand, in winter, solar radiation is at its minimum and heat loss increases substantially, coinciding with strengthened westerly winds, with the combination leading to deep vertical mixing. The cold and fresh surface water in the western subpolar basin, flowing into the subpolar basin from the Arctic along the West Greenland Current in summer, facilitates ice formation and the accompanying brine increases surface salinity and density, which is favourable for deep convection. The low solar energy is thus distributed over a deep layer and hence contributes to the low winter SST.

In the southern subpolar North Atlantic near 40 ° N where maximum mixing is less than 150m, the annual cycle of vertical mixing also presents deeper mixing in winter and

shallower mixing in summer. The vertical mixing is governed by the variation of heat loss, but is also modulated by the strength of the NAC that transport heat and salt pole ward. Warm advection tends to stabilise the water column and reduces the vertical mixing while salt affects the density of surface water, which might lead to vertical mixing [Tomczak and Godfrey, 1994].

1.3.4 "Re-emergence" of SST Anomalies

The term "re-emergence" referrs to the re-appearance of SST anomalies that formed in the previous winter and are preserved below the mixed layer during summer [Alexander and Deser, 1995]. Seven re-emergence areas in the global ocean have been determined using various SST, surface heat flux, and upper ocean thermal datasets in the literature [Hanawa and Sugimoto, 2004]. One of the northern areas is located in the subpolar North Atlantic (19°-35° W, 41°-53° N). According to this study, the common features of these regions are large MLD annual cycle and deep winter MLD. The average annual MLD range in the re-emergence area in the subpolar basin is over 300m, and the re-appearance of SST anomalies occurs 7 to 13 months after its original formation.

The re-emergence area in the subpolar basin also corresponds to the North Atlantic subpolar mode water formation area, and the thickness of mode water nearly equals the annual range of MLD. The water properties of the winter mode water are hence well preserved during summer months [Sugimoto and Hanawa, 2005]. With adequate surface buoyancy loss in the following autumn, MLD deepens and water masses preserving SST anomalies in the previous winter entrain into the mixed layer, which later re-appear at the surface as vertical mixing occurs. This indicates that in this region, the SST annual cycle may be influenced by the surface conditions in the previous winter in addition to the surface processes during the same year. Even though deep winter MLD and large annual MLD range are necessary for re-emergence, winter SST anomalies do not re-appear in all regions with deep convection. For instance, there is evidence that the re-emergence of winter SST anomalies do not occur in the mode water areas in the eastern subtropical Atlantic and Pacific, because the SST anomalies lose its properties through vigorous mixing from both upper and lower parts of the mode water and insufficient buoyance loss that is close to zero whilst negative net buoyance loss is required to trigger the re-emergence [Sugimoto and Hanawa, 2005].

1.3.5   Precipitation & Evaporation

The annual variation of the difference between precipitation and evaporation (P-E), also known as the net surface freshwater flux, is one of the direct mechanisms that affect the annual cycles of SST and sea surface salinity (SSS) [Walsh and Portis, 1999]. In the subpolar North Atlantic, precipitation and evaporation both peak in late autumn and early winter, and reach a minimum in summer (Figure 1.8). Positive P-E or net surface freshwater flux gain reduces surface salinity, whilst negative P-E increases surface salinity. In the subpolar basin, the total precipitation exceeds total evaporation, which results in a net freshwater gain for the ocean [Walsh and Portis, 1999; Häkkinen, 2002].

Within one annual cycle of P-E and SSS, decreasing SSS from spring to summer coincides with increasing P-E. The minimum SSS occurs in August (Figure 1.8a, Levitus SSS and two model outputs), however P-E in August is at its annual median level (Figure 1.8a, thin solid line, [Rasmusson and Mo, 1996]). In January, both SSS and P-E remain at their high levels. This suggests that local variation of P-E might not be the most important factor influencing the surface salinity. Other processes, such as vertical mixing, may also impact surface salinity. Large inter-annual variability of P-E is reported, and the model outputs suggest that the standard deviation of P-E is equivalent to 10-20% of its annual mean (Figure 1.8b) [Walsh and Portis, 1999; Häkkinen, 2002]. The annual cycles of P-E using different datasets provide different results: the annual cycle based on operational analyses and forecast products from August 1991 to July 1993 suggests P-E is relatively high during summer months (Figure 1.8b, thick dashed line, [Rasmusson and Mo, 1996]); the annual cycle calculated as averaged monthly P-E from 52 years of NCEP Reanalysis (1949-2000) suggests that P-E is lower than average from July to November (Figure 1.8b, thick solid line, [Häkkinen, 2002]). Due to the difficulties of estimating precipitation, evaporation, and surface salinity, the influence of P-E on surface temperature and MLD is difficult to evaluate in more detail.

1.3.6   Sea Ice

Another possible variable that may affect the annual cycle of physical parameters in the subpolar North Atlantic is sea ice. The estimated Greenland ice sheet ablation is 500 km^3 annually and the annual sea ice export from the Arctic is 2000-2800 km^3

[Häkkinen, 2002]. The sea ice melt and net precipitation in the subpolar North Atlantic are the major contributors of the surface freshwater flux [Mauritzen and Häkkinen, 1997]. About 40% of the total ice export from the Arctic enters the subpolar basin through the Denmark Strait, driven by wind and ocean currents. The maximum ice mass is reached in May, and maximum ice extent is reached in March. The minimum ice mass and ice extent are both reached in September [Mauritzen and Häkkinen, 1997]. The freshwater flux stabilizes the upper layers in the water column, which is favourable for early stratification and transport of cold Arctic-origin water in the northern and western subpolar basin.

1.3.7   Summary

In summary, the annual cycles of SST and MLD are associated with multiple physical processes in the ocean. Heat fluxes impact the variation of SST directly, and heat absorption and losses are the main drive of thermal stratification and deep convection in the subpolar North Atlantic. Major currents that adjust surface water properties include the NAC, EGC, and WGC. NAC brings southern-origin salty and warm water into the subpolar basin, while EGC and WGC bring fresh and cold water from the Arctic. Wind stress is another factor that influences the development and extent of the subpolar gyre, which is related to the distribution of Arctic-origin cold and fresh water. Wind driven mixing is one of the surface forcings that initialises the deep convection in the northern subpolar basin. The subpolar North Atlantic is one of the major regions presenting deep convection, which modulates surface temperature through exchanging and mixing water masses between surface and at depth. In the southwestern subpolar basin, winter SST anomalies might re-emerge at the surface in the following winter, which adjusts the SST annual cycle through influencing winter SST. Other parameters that can modulate the annual cycles of SST and MLD include precipitation, evaporation, and sea ice.

1.4   Phytoplankton

Phytoplankton plays an essential role in the marine ecosystem by providing food for organisms of higher trophic levels, supplying about half of the total primary production on Earth [Richardson and Schoeman, 2004; Stramska, 2005; Hoegh-Guldberg and Bruno, 2010]. Phytoplankton is the origin of most of the organic matter in the sea and influences seawater composition through the uptake of inorganic carbon and nutrients

for photosynthesis and producing cellular organic materials [Eppley and Peterson, 1979; Biddanda and Benner, 1997]. The seasonal development and decay of phytoplankton blooms also cause physicochemical changes in the seawater through redistribution of inorganic macronutrients [McAllister *et al.*, 1961]. Phytoplankton also release organic material to the ocean, about 5 − 30% of marine primary production is directly released as dissolved organic material (DOM) [Baines and Pace, 1991], though the concentration of dissolved organic carbon (DOC), the major currency of global carbon cycle, varies in different studies [Hansell and Carlson, 2001]. It is agreed that the DOC derived from phytoplankton accumulate at ocean surface during blooms and are exported to deeper ocean, with about 80% of this DOC flux is used and remineralised by other organisms [Hopkinson and Vallino, 2005]. Phytoplankton plays a role at various stages of the carbon cycle and it is therefore important to understand the phytoplankton bloom dynamics, especially under a changing climate, to better understand the impact on the local ecosystems and carbon export. The variation of phytoplankton in the ocean is regulated by the seasonal changes of its surrounding physical environment. For instance, the seasonal and longer-term variation of light intensity, water temperature, nutrients availability, and mixing can all influence the growth and decay of phytoplankton. In recent years, the importance of SST in determining biological variation has been emphasised in multiple studies [e.g. Reid *et al.*, 1998; Henson *et al.*, 2009a; Martinez *et al.*, 2009]. In later chapters, the impact of SST on phytoplankton dynamics is examined, and other physical parameters that contribute to phytoplankton growth are discussed. This subsection introduces phytoplankton, which is modulated by the physical processes presented above.

The term "phytoplankton" comes from two Greek words "phuto-" meaning "plant", and reemer"planktos" meaning "drifter" [Lalli and Parsons, 1997]. Phytoplankton can be divided into several groups based on their sizes, cell structures, and ways of utilizing resources. The two major groups are diatoms and dinoflagellates. Diatoms are unicellular organisms ranging from about 2 μm to over 1000 μm. One specific feature of diatoms is their external silicate skeleton, thus silica is an additional limiting resource for diatoms compared to other phytoplankton groups. Diatoms are autotrophic, and they build organic materials and obtain all their energy from photosynthesis. Hence, it is essential for diatoms to remain in lit surface waters, and they are very sensitive to stratification [Lalli and Parsons, 1997]. These organisms are observed in a wide range

of regions, especially in temperate latitudes where light and nutrients are both adequate. In the subpolar North Atlantic, diatoms are the dominant phytoplankton group because the water column is turbulent (the coefficient of eddy diffusion is in the range from 3 to 100 cm^2/s) with rich nutrients and stratification shallower than 50 m in summer, which is favoured by diatoms (Figure 1.9) [Margalef, 1978], and the average annual cycle in this area presents a typical diatom biannual peaks feature.

Another important phytoplankton group is dinoflagellates, which are also unicellular. In contrast to diatoms, dinoflagellates have two flagella, which allow the organisms to move along the water column to some extent. Dinoflagellates thrive in stratified, nutrients poor water coloum, where the coefficient of eddy diffusion is between 0.02 and 1 cm^2/s [Margalef, 1978]. Not all dinoflagellates absorb energy only from sunlight. In fact, about 50% of dinoflagellates are strict heterotrophic producers that lack chloroplasts and are incapable of carrying out photosynthesis. These heterotrophic dinoflagellates feed on other phytoplankton and even small zooplankton. Some dinoflagellates are mixotrophic and carry out photosynthesis when the environment is favourable, and produce heterotrophic production when light or nutrients are not adequate. For those motile dinoflagellates, it is even possible for them to sink into a deeper nutrient-rich layer and swim back to the surface to continue photosynthesis. As a result of these features, dinoflagellates usually dominate the stratified, nutrient-poor subtropical regions [Lalli and Parsons, 1997].

Other groups of phytoplankton are less populated as the diatoms and dinoflagellates in the subpolar region. Coccolithophorids are small unicellular organisms of sizes around 20 μm, they also possess two flagella like the dinoflagellates. This group of phytoplankton contains plates of calcium carbonate that may lead to increased sinking speed in the water column [Margalef, 1978]. Production by coccolithophorids typically increases in warm areas, and its dependence on light intensity is low. In parts of clear oceanic tropical waters, some species reach maximum production at depths of ~100 m. In the North Atlantic, the most abundant Coccolithophorids is Emiliania huxleyi, which can form blooms covering approximately 1000 km by 500 km of sea surface [Lalli and Parsons, 1997]. The algal group Prymnesiophyceae typically live in low salinity water and is claimed to be a major cause of mortality in farmed salmon along the Norwegian coast. Silicoflagellates, the best know forms of the Chrysophyceae, is most abundant in

cold waters and is not well know because the difficulties of sampling them. The taxonomic division of phytoplankton is formed by species of small, naked and flagellated cells. Some of these species are very small (0.2 – 2 μm) and are difficult to collect and preserve. One single genus, Oscillatoria, in the phytoplankton group Cyanophyseae or Cyanobacteria has cause a lot interests due to their ability to utilise and fix dissolved gaseous nitrogen while other phytoplankton can only use combined forms of nitrogen such as nitrate and nitrite [Lalli and Parsons, 1997].

In the subpolar North Atlantic, diatoms dominate the functional group structure, and the average annual cycle presents two phytoplankton peaks in spring and autumn. It has been proposed that under global warming, dinoflagellates may take over the dominance of the functional structure [Edwards *et al.*, 2001]. Increases in SST could lead to stronger and potentially longer shallow stratification, dinoflagellates survive better under stratified conditions than diatoms both because diatoms prefer turbulent environment and the ability of some dinoflagellates to consume other phytoplankton cells. In addition, the optimum temperature for growth is higher for dinoflagellates than diatoms. All these contribute to the potential changes to the phytoplankton community structure in the warming ocean. Zooplankton is sensitive to the timing of food availability [Colebrook, 1979]. Changes to the phytoplankton phenology and community structure influence the development of zooplankton population or even organisms of higher trophic levels through the match-mismatch scheme [Cushing, 1990]. Better understanding of the phytoplankton bloom dynamics hence contributes to more thorough knowledge of the local ecosystem in the subpolar North Atlantic and its potential responses to a warming climate.

1.5   Natural Variability vs. Observations

Natural variability of physical and biological parameters is presented in the ocean on various scales, from daily to centennial. Observation of these processes, however, has not been easy. The observation of SST used in this study is a monthly global complete data, including data resources from shipboard measurements of surface properties and satellite data. The resulting spatial resolution is 1° × 1°. The observation of phytoplankton used in this study mainly depends on shipboard measurements from ships of opportunity, with data averaged over standard areas defined by average

distribution of phytoplankton and certain physical processes. The surveys are carried out monthly, and heavily controlled by the routes of these commercial ships. The detailed description of the datasets is discussed in later chapters regarding observed physical and biological variability.

There are two issues to consider when analysing time series data. The first is the aliasing of signals on different time scales, which is influenced by the length of consistent data coverage. One arbitrary ocean signal is shown in Figure 1.10, composed of inter-annual variability, annual cycle, and random noise. Two consistent annual observations of this 10-year signal are constructed; one observation lasts 10 years, and the other observation lasts 4 years. The two resulting annual series show different trends, which could lead to very different hypotheses explaining the observed trends. Without information regarding earlier variations, one might conclude a consistent decreasing trend from the second signal whilst the first signal suggests that the decreasing trend towards the end of the time series is indeed a part of the inter-annual variability. This suggests that long-term consistent observations are important in revealing the real variability and predicting future changes. Thus in this study, the length of time series is an extra factor considered in addition to spatial and temporal resolutions.

The second issue concerns the spatial coverage of parameters, especially for the observations from ships of opportunity. Phytoplankton develops patchily in ocean, affected by advection and mixing [Martin, 2003]. In regions where commercial ships are less frequent, shipboard observation may miss the developing phytoplankton bloom, or miss the real annual peak. Direct measures of phytoplankton abundance are available in a limited area around the ship whilst the average abundance over a standard area remains an estimate. Changes of ship routes could also lead to gaps or discontinuities in the resulting observation time series. In regions with frequent commercial cruises that nearly cover the entire region, e.g. the North Sea and eastern subpolar basin, the shipboard observation of phytoplankton is more reliable. The representativeness of the time series in each standard is thus evaluated before detailed analysis.

1.6   Observations vs. Models

Early ocean models assumed the globe was uniformly covered by a shallow layer of water, with an infinite heat capacity which kept the surface temperature constant at all times [Manabe *et al.*, 1965]. One of the first coupled ocean-atmosphere models assumed five ocean levels, and there was one continent and one ocean covering the globe [Manabe and Bryan, 1969]. Since the 1960s, ocean model simulations have improved significantly, with realistic topography and high spatial resolution of 1/12° [Treguier *et al.*, 2005]. Observed variability, such as El Niño and Atlantic Multi-decadal Oscillation (AMO), can be simulated. However, small-scale processes such as turbulence and coastal processes still need further studies. The simulation of biological processes present larger discrepancies compared to physical models as the governing mechanisms are more complex and simulating activities of living organisms and interactions is naturally more difficult.

Some ocean reanalyses use ocean model outputs to fill in the temporal and spatial gaps in available observation, combining the advantages of the coverage of ocean models with the accuracy of observations [Carton and Giese, 2005]. In regions with adequate observations, the reanalysis datasets remain close to observation whilst in regions lacking observations the resulting datasets would depend heavily on the simulation. Even though models may have discrepancy with observation, especially for ecological models, they still remain useful tools in predicting changes in the future and understanding underlying mechanisms through experimentation. Before detailed prediction and experiments, the accuracy of model outputs should be validated. Any improvement of model simulations that results in more realistic results could lead to better understanding of ocean processes.

1.7   Research Questions

The long-term variability of physical and biological annual cycles of the subpolar North Atlantic may provide new knowledge regarding the interaction of the physical environment and ecosystems, which has been previously overlooked. With long-term physical and biological observation time series and outputs from coupled physical and ecological models, there is a great opportunity to address the long-term variability of the

physical annual cycle and the physical mechanisms influencing local ecosystems. In recent decades, significant increases in SST have been observed under a changing climate, which may leave a fingerprint on the variability of the SST annual cycle and phytoplankton bloom dynamics. The impact of SST and MLD on phytoplankton growth through modulating nutrients, light, and grazing will be the focus in later chapters (e.g. chapter 5). This main hypothesis will be tested by addressing the following questions.

- Does the SST annual cycle change on decadal or longer time scales?
- What climatic processes contribute to the observed variability?
- Does phytoplankton abundance present a clear variability pattern on decadal or longer time scales?
- How well does the current generation of coupled physical and biogeochemical models simulate the variability of physical and biological parameters regarding phytoplankton growth and its surrounding environment?
- What are the most important physical mechanisms determining the observed phytoplankton variability?

1.8   This Thesis

These topics are covered in this thesis in the following structure.

- Chapter 2 focuses on the decadal to multi-decadal variability of sea surface temperature annual cycle in the subpolar North Atlantic and the impact of climatic indices on the annual cycle. The discussed variability after 1995 is emphasised to examine the influence of climate change.
- Chapter 3 describes the decadal and inter-annual variability of phytoplankton abundance using the Continuous Plankton Recorder observation. Statistical analysis introduced in Colebrook (1979) is adapted to supplement simple analysis and potential changes in phytoplankton abundance since the 1970s is discussed.
- The performance of a coupled physical and biogeochemical model with respect to the available observations is investigated in Chapter 4.
- Chapter 5 investigates the physical mechanisms that control the phytoplankton bloom dynamics through modulating the mixed layer depth using model outputs. The necessity and results of dividing the subpolar basin into ecological provinces

are discussed.

- Chapter 6, the last chapter, discusses to what extent the questions in Section 1. 7 can be answered based on the results presented in previous chapters. The remaining questions for future study are also discussed.

Copyright © 2005 Pearson Prentice Hall, Inc.
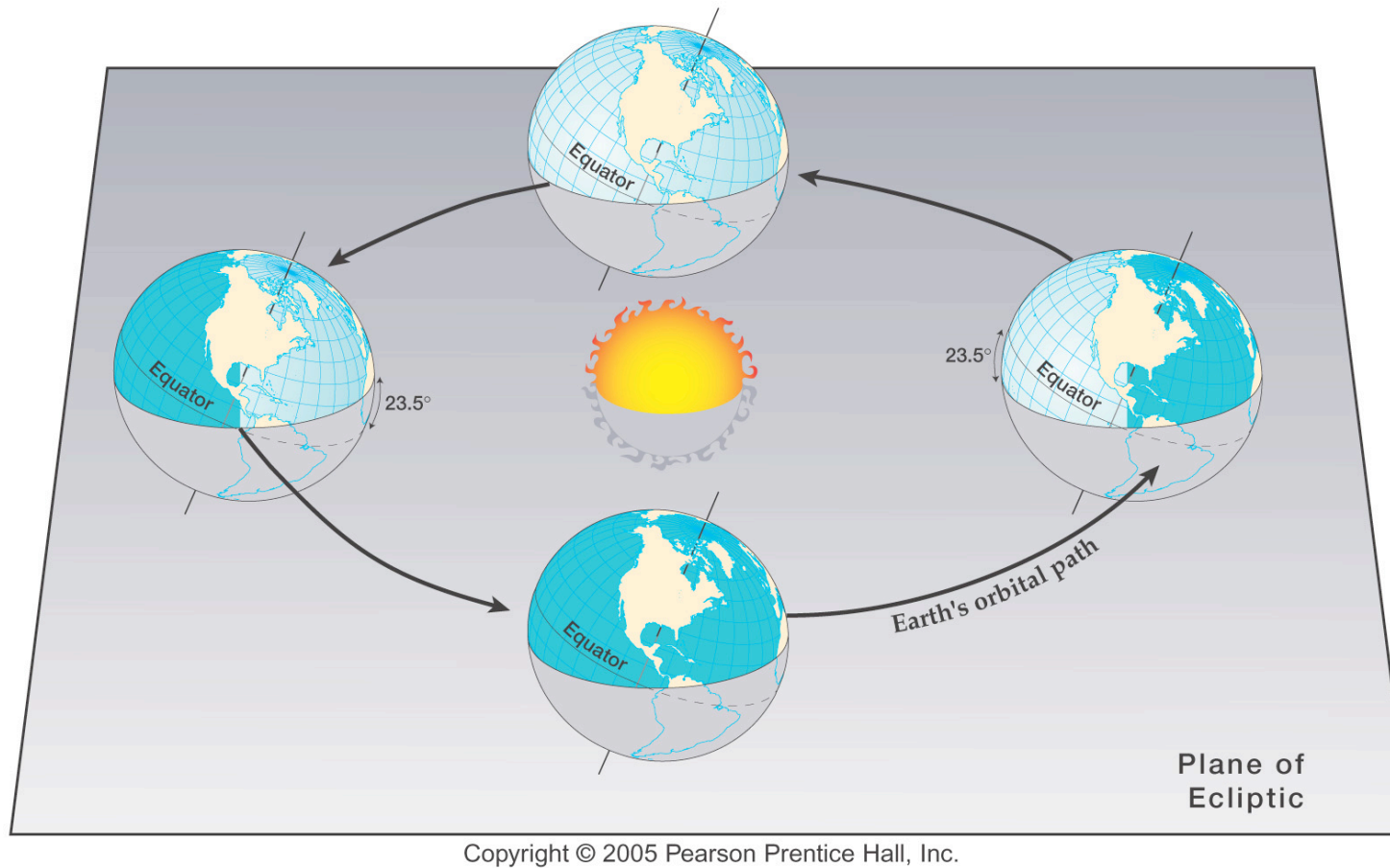
Figure 1.1 A schematic of the full revolution of the Earth around the Sun within one solar year [McKnight and Hess, 2005].
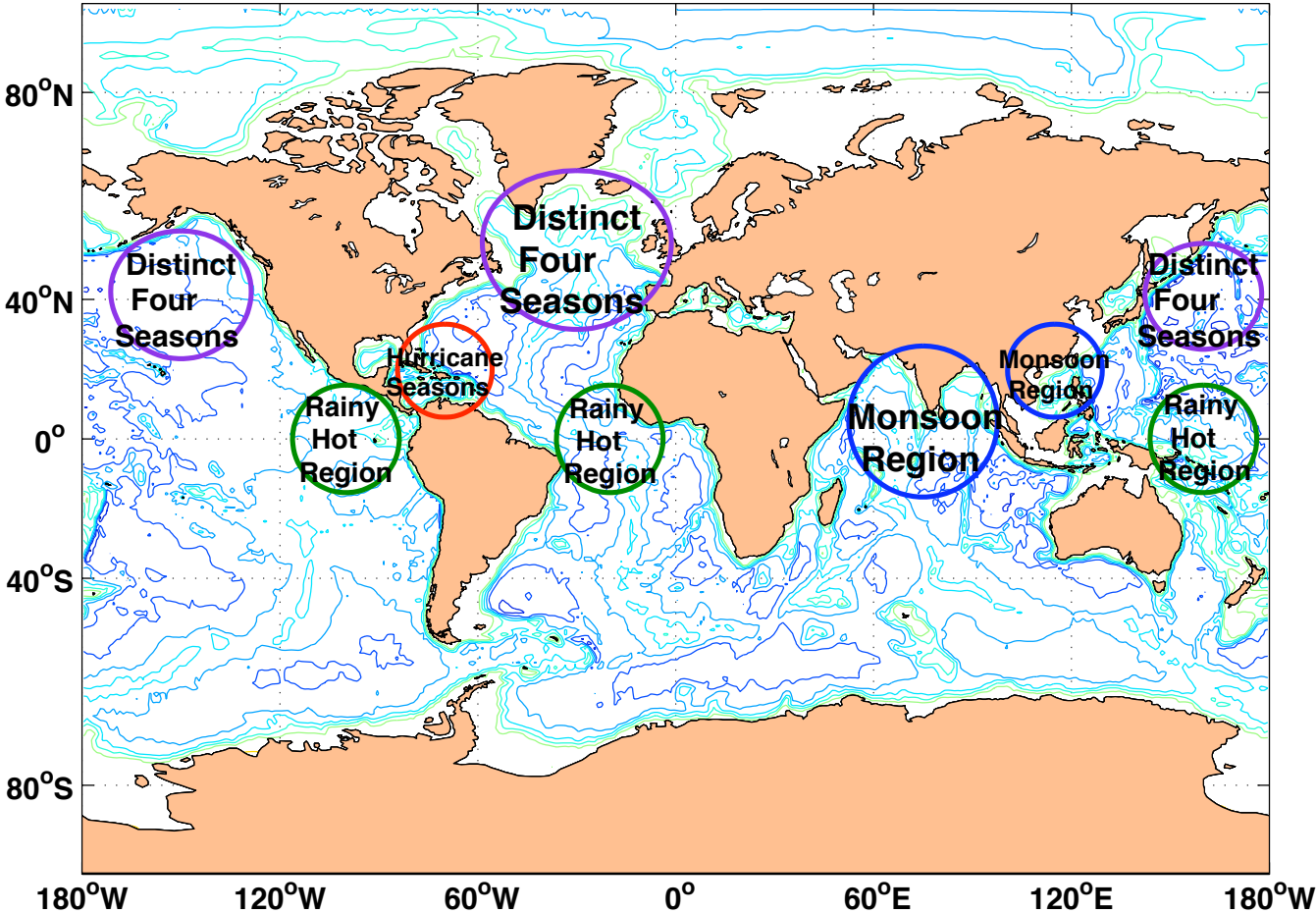
Figure 1.2 Distribution of the number of seasons in the Northern Hemisphere.
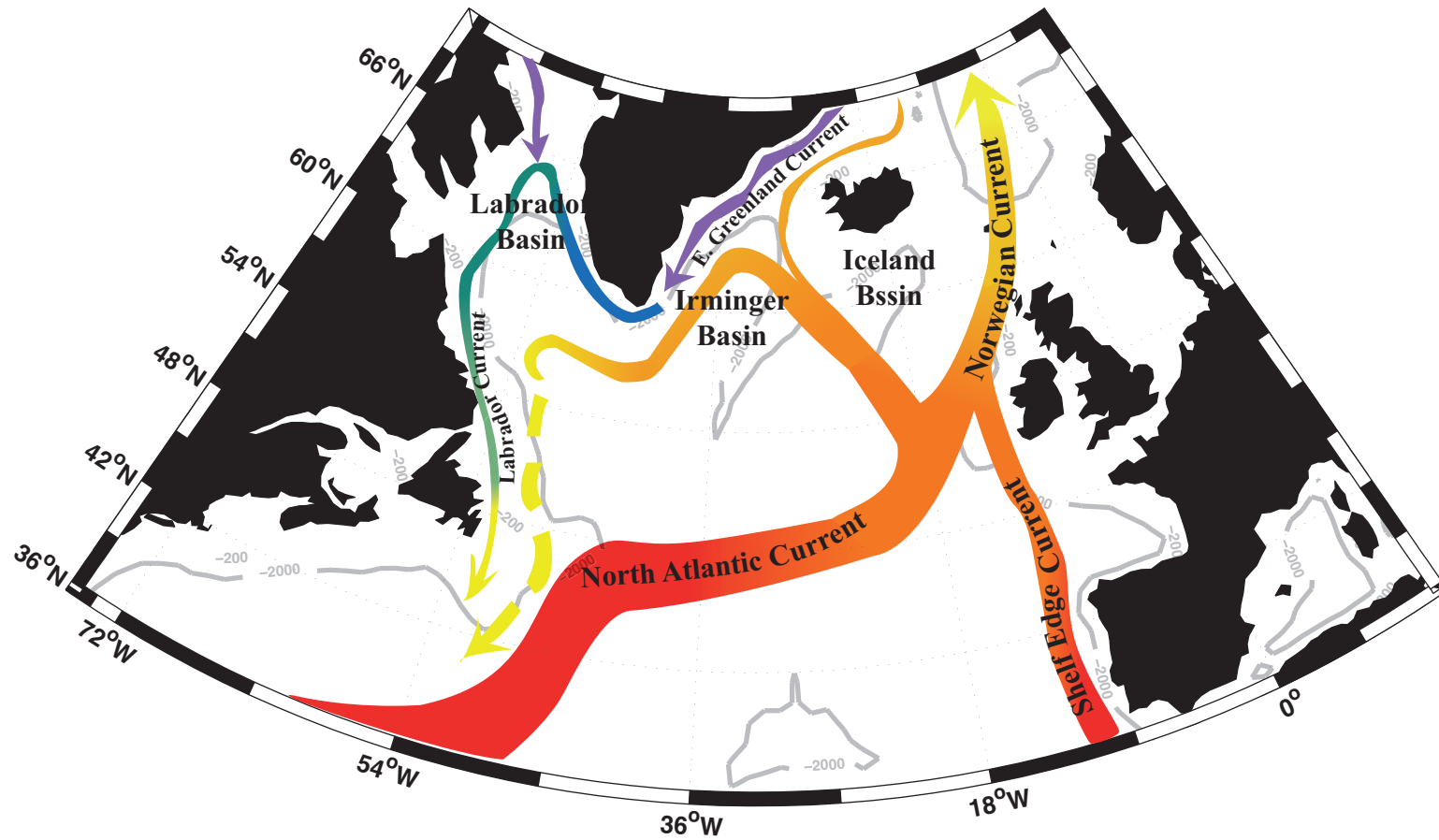
Figure 1.3 Map of the subpolar North Atlantic. The grey lines denote 2000m contours, the colours indicate the temperature of the currents, with red to yellow marking warm currents and purple to green marking cold currents.
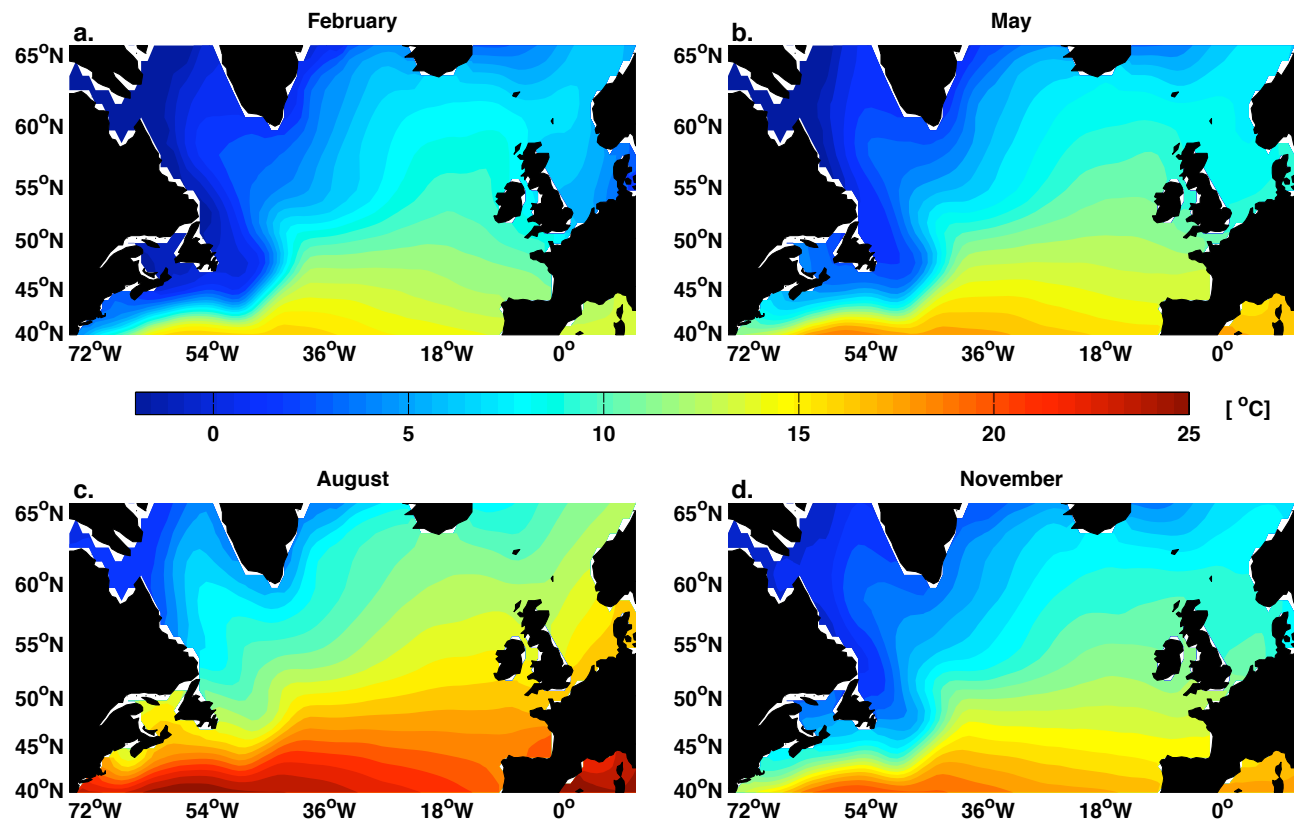
Figure 1.4 Sea surface temperature distribution in (a) February, (b) May, (c) August and (d) November in an average annual cycle in the subpolar North Atlantic. Figures are produced using the HadISST1 from the Met Office Hadley Centre.
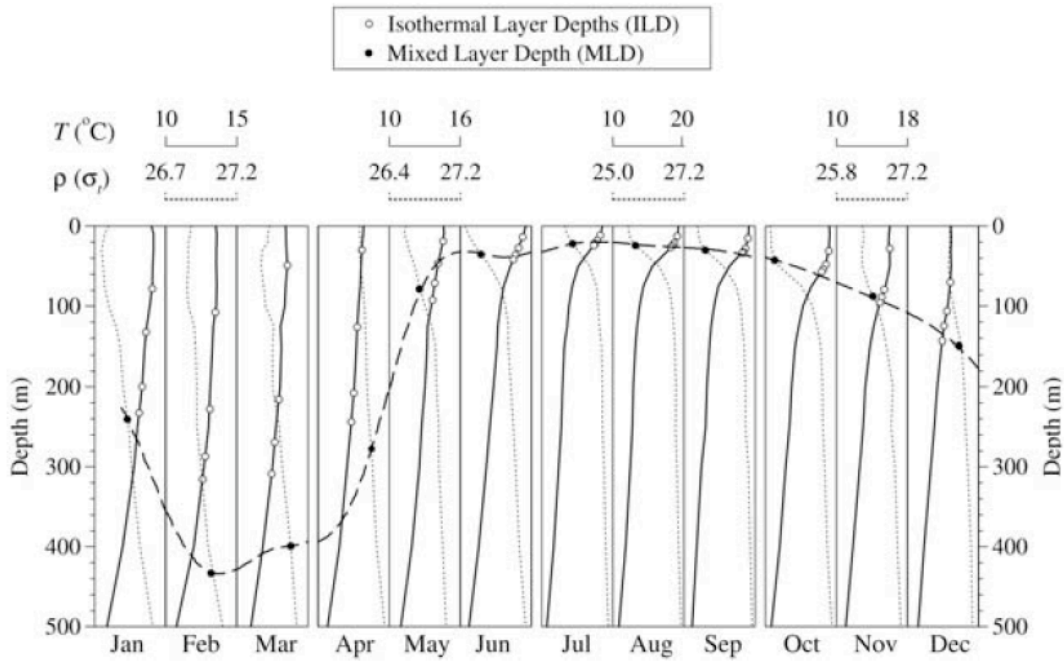
Figure 1.5 Monthly averaged mixed layer depth (MLD, dash line with filed circle) at 45 °N, 30 °W in the North Atlantic. The mixed layer depth is obtained using variable density criteria with a 0.8 °C difference from SST and variable salinity. The isothermal layer depth (ILD, open circles) is obtained solely on temperature difference from the surface with ΔT = 0.1 °C, 0.5 °C, 0.8 °C and 1.0 °C. Monthly temperature (light grey lines) and density (dark grey lines with open circles) profiles are also shown [Kara *et al.*, 2003].
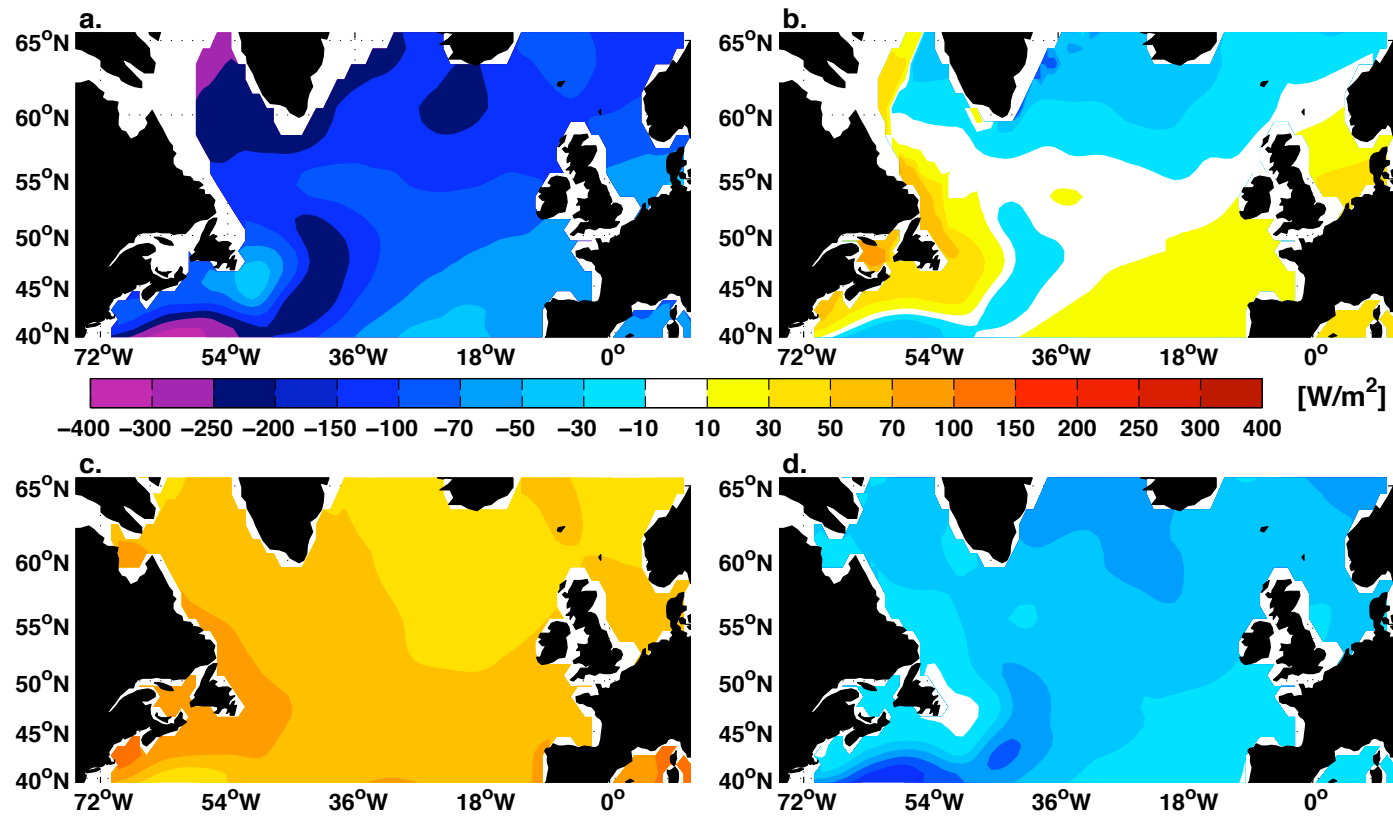
Figure 1.6 The net heat flux in the subpolar North Atlantic in (a) winter, (b) spring, (c) summer and (d) autumn, produced using the NOC 1.1 Net Heat Flux climatology. Winter is December-February, spring is March-May, summer is June-August and autumn is September-November. Positive net heat flux indicates ocean gains heat from the atmosphere.
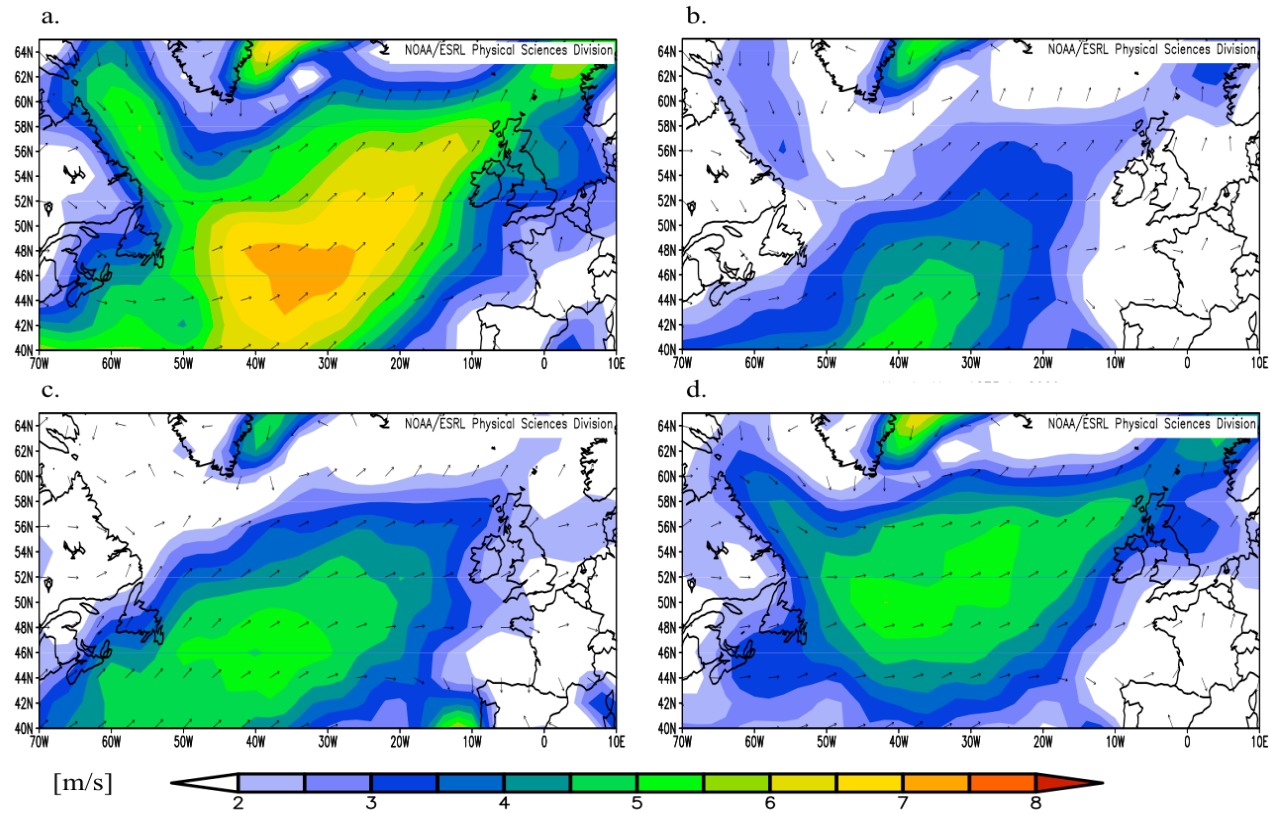
Figure 1.7 The near surface wind speed and wind direction in the subpolar North Atlantic in (a) December – February, (b) March – May, (c) June – August and (d) September – October. Figures are produced using the NCEP/NCAR 20th Century Reanalysis climatology.
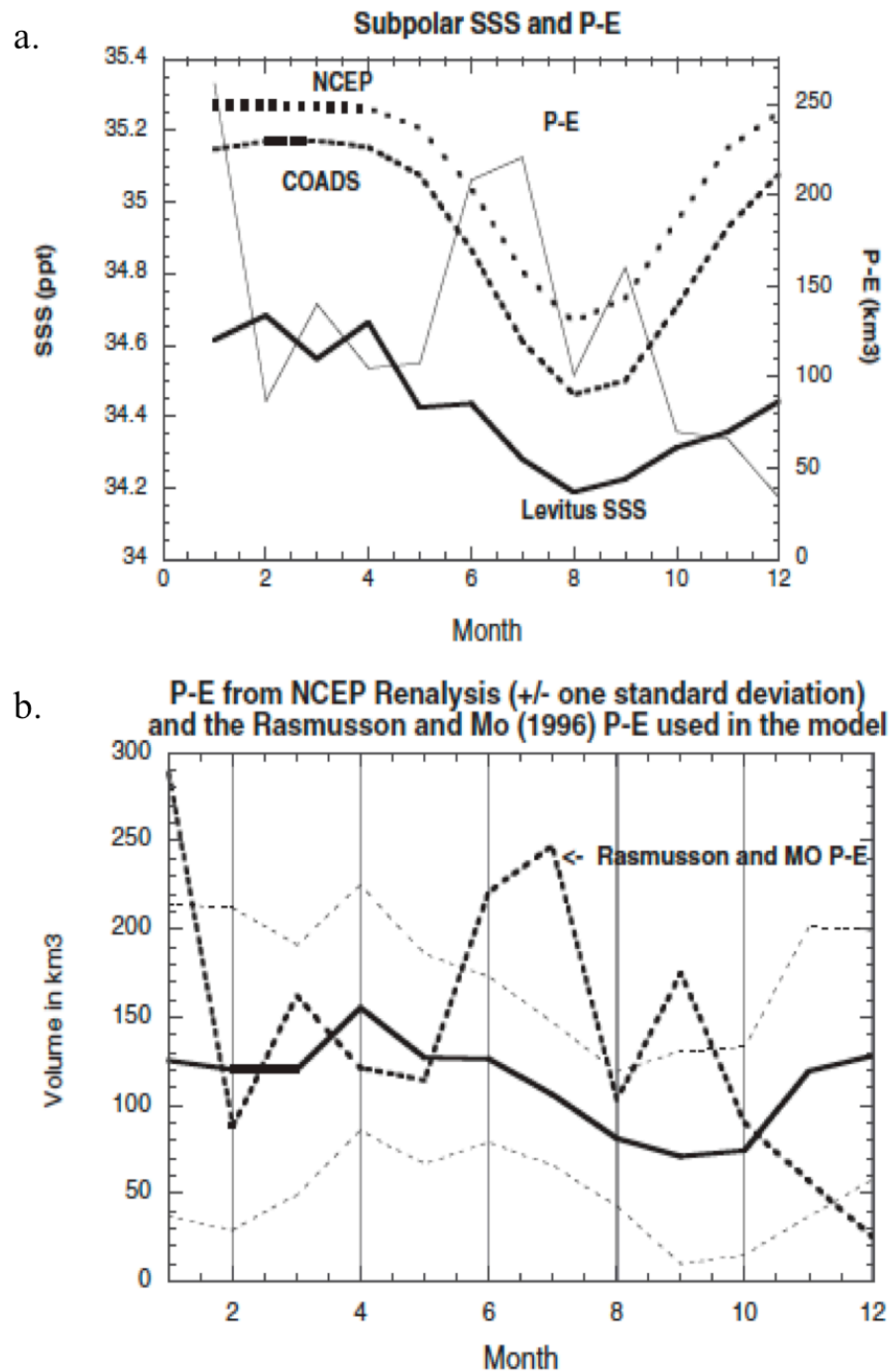
Figure 1.8. The annual cycle of the average sea surface salinity (SSS) over the area 45°-60° N, 30°-60° W and its relation with P-E. In (a), the SSS is calculated from Levitus climatology (thick solid line) and two model simulations (dashed lines), the P-E (thin solid line) is from Rasmusson and Mo (1996); in (b), monthly P-E is calculated from the 52-year NCEP reanalysis (thick solid line) with ±1 standard deviation (thin dashed line) and from Rasmusson and Mo (1996) in thick dashed line [Häkkinen, 2002].
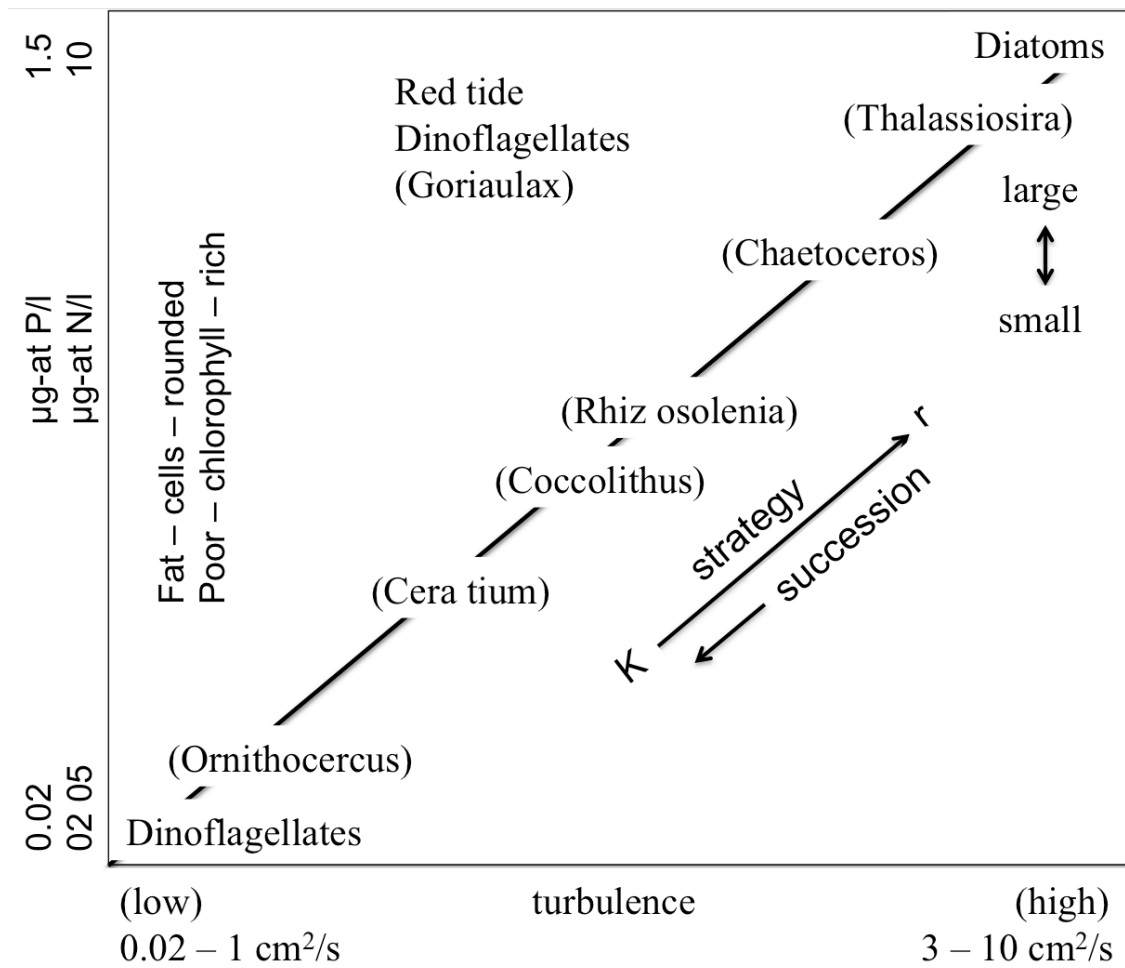
Figure 1.9. The main strategies in the principal phytoplankton community. The groups of phytoplankton are placed in an ecological space defined by the concentration of nutrients and the coefficient of vertical eddy diffusivity. K is the coefficient of eddy diffusion and r is the rate of increase [Margalef, 1978].
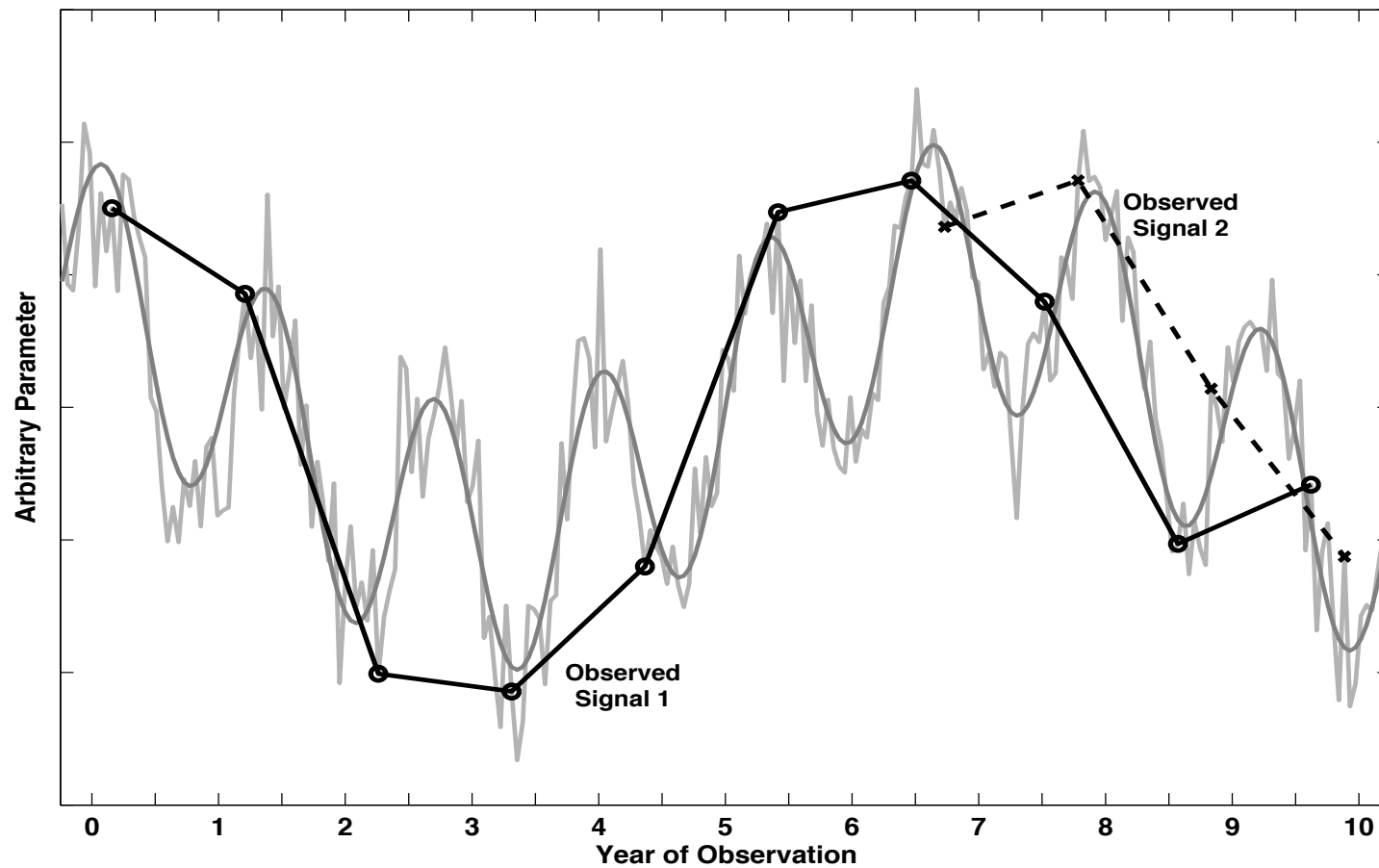
Figure 1.10 Aliasing of a signal composed of inter-annual variability, annual cycle and random noise (light grey lines). Two sampling processes with different coverage periods are shown with solid line with circles and dashed line with crosses.

Chapter 2

Decadal Variability of Sea Surface Temperature Annual Cycle in the Subpolar North Atlantic

2.1   Introduction

In order to study the link between physical and biological processes, an understanding of the main physical variability should first be established. As stated in many existing works by various authors, sea surface temperature (SST) is one of the most critical factors in controlling the environment in which organisms grow and reproduce [Reid *et al.*, 1998; Edwards *et al.*, 2001; Edwards and Richardson, 2004; Beaugrand, 2009; Henson *et al.*, 2009a; Martinez *et al.*, 2009]. In the previous chapter, the importance of the usually overlooked annual cycle to the climate has been illustrated. In this chapter, a thorough description of the variability in the SST annual cycle over the last century and its interaction with other parameters are presented.

Only sea surface data were analysed, but it is recognised that depth of water column, surface circulation and wind forcing can all leave a fingerprint on the surface data. For example, the shelf seas in the subpolar North Atlantic are well mixed down to the bottom in winter and respond to external forcing in a more barotropic way whereas in the open ocean the average mixing is down to 500 m, and in the Labrador Sea mixing can be as deep as 2000 m [Våge *et al.*, 2009], and responds to external forcing in a more baroclinic way. In addition, SST anomalies from the previous winter can be preserved underneath the stratified layer through summer and entrained back into the mixed-layer, re-emerging at the surface during the mixed layer deepening process in the following autumn/winter [Hanawa and Sugimoto, 2004]. Thus, the ocean responds differently to the same external forcing in different regions, not to say to different external forcing.

The eastern side of the basin is mainly fed by the warm North Atlantic Current (NAC) and southern origin Shelf Edge Current (SEC, [White and Bowyer, 1997]; also known as European Shelf Current, ESC, [De-Jong, 2010]); the resultant North Atlantic Water here is warm and saline, its variation reflecting changes in the two currents and their interaction with atmosphere, as well as responding to the strength of subpolar gyre [Holliday, 2002; Hátún *et al.*, 2005]. On the other hand, on the western side of the subpolar basin, e.g. the Labrador Sea, cold and fresh Arctic-origin water dominates the surface to near-surface layers, resulting in much colder and fresher water compared to eastern water. Variation here is likely to reflect influence from higher latitude [Frajka-Williams and Rhines, 2010].

Considering all these processes, differences in long-term variation in different parts of the subpolar North Atlantic are expected. Averaging over the whole subpolar basin might overlook the factors that influence SST annual cycle on smaller spatial scales and differences in various parts of the basin would be eliminated. Therefore, to provide a more thorough description of the SST annual cycle in the subpolar North Atlantic, it would be helpful to select representative locations to examine the long-term time series and identify the variability pattern. Here, 24 locations, covering both sides of the basin and in both shelf seas and open ocean (Figure 2.1 and Table 2.1), were chosen. In the western subpolar basin, the shape of the chosen open ocean locations were the same as the corresponding Standard Area (SA) defined in Continuous Plankton Recorder (CPR) observation, while in the western shelf seas the locations sit within the corresponding SAs but with rectangle shapes. In the eastern open ocean, some SAs sit on the edge of the shelves, so the chosen eastern-open-ocean locations in this study keep only the open ocean parts of the corresponding SAs. The chosen eastern shelf locations all lay within the corresponding SAs if not exactly the same area. The choice was made primarily on bathymetry, though for a few shelf regions the choice was based on known geographic regions (e.g. Irish Sea). The Rossby radius of deformation is bigger in the open ocean than in the shelf seas, so, on average, the size of open ocean regions is larger than shelf seas regions.

In the following sections, decadal to multi-decadal variability in SST annual cycle amplitude (hereafter ACA, whose definition will be given in more detail in section 2.3) is described. The difference between the variability in different parts of the subpolar basin is also presented and discussed. A period towards the end of the time series was picked as a case study to compare with earlier decades. Then main basin-scale signals of variation were detected by an Empirical Orthogonal Function (EOF) analysis. In section 2.2, the dataset used in this chapter is introduced. The climatology of seasonal SST in subpolar North Atlantic is described in section 2.3. Observed ACA variability is presented and described in section 2.4. The last section, section 2.5, concludes the description of observed decadal to multi-decadal variability with an overall summarizing discussion.

2.2   Data and Data Processing

2.2.1   Criteria of Datasets

The aim of this study is to examine decadal to multi-decadal evolution of the SST annual cycle in the subpolar North Atlantic. So the optimum dataset would have the following features: (1) a time-series at least several decades long to capture decadal and longer-term variability, (2) combination of various data sources to reduce bias, (3) high quality interpolation methods so there are no significant differences between pre-satellite and satellite periods, (4) good temporal and spatial resolutions, with reasonable uncertainty in shelf regions. With these criteria, the dataset that fits the criteria best could be selected. Following the revision and selection by Hughes *et al.* (2009), the Hadley Centre Sea Ice and Sea Surface Temperature data set (HadISST1) and Optimum Interpolation Sea Surface Temperature Analysis (OISST. v2) were compared by examining the average winter and summer SSTs over the overlapping years and comparing the results to *in situ* time series shown in Hughes *et al.* (2009).

HadISST1, developed at the Met Office Hadley Centre, is derived from both *in situ* and satellite-based input data. The *in situ* input data includes ship observations from the Met Office Marine Data Bank (MDB), Global Telecommunication System (GTS) data from 1982 onward and Comprehensive Ocean-Atmosphere Data Set (COADS, now ICOADS) from 1871 to 1995. The satellite-based input data was obtained from the advanced very high-resolution radiometer (AVHRR) from January 1982 onward [Rayner *et al.*, 2003]. The quality-controlled, bias-adjusted data of various sources were then combined and reconstructed using Reduced Space Optimal Interpolation (RSOI) techniques. RSOI is a statistical technique used to reconstruct a dataset from sparse observation. This method consists three main steps: 1) obtain a reduced space from a Principal Component Analysis (PCA) with limited number of leading eigenvectors, the choice number is usually experience-based and considered to suit the dataset best; 2) computation of the errors between the values calculated from selected principal component (PC) and measurement at locations with available observations; 3) the final estimate is then made by linearly combining the PC-loading determine in step 1 and the errors estimated in step 2 for the whole grid field over the reconstructed period [Schiemann *et al.*, 2010]. This method has been successfully applied to datasets with

sparse observation or historical records [e.g. Kaplan *et al.*, 1997; Kaplan *et al.*, 2000] HadISST1 was downloaded from <http://hadobs.metoffice.com/hadisst/>. In this study, we used monthly mean SST from January 1870 to December 2009 for the subpolar North Atlantic and adjacent seas (40° N – 65° N, 75° W – 10° E).

OISST. v2 is a SST product developed at the National Centers for Environmental Prediction (NCEP), which is a global complete dataset on 1 ° grid and both weekly and monthly temporal scales. This product uses both satellite derived (from AVHRR) and in-situ SSTs. Ship and buoy data was used together with satellite SST data and the in situ data was also obtained from the ICOADS for the 1980s. Satellite data were bias adjusted following the method described in Reynolds (1988) and Reynolds and Marsico (1993). Optimal Interpolation (OI) analysis was used to combine and reconstruct data from all sources and is introduced in Reynolds and Smith (1994). OISST. v2 is available from 1982 onwards and monthly data over the subpolar basin was extracted to compare with HadISST1 in this study.

HadISST1 is available from 1870 to present day on monthly intervals, with 1° spatial resolution. OISST. v2 is available on weekly and monthly intervals, also with 1° spatial resolution, covering the time period from December 1981 to present day. The size of the eastern shelf of the subpolar basin is roughly 20×10 degrees, so the 1° spatial resolution is able to capture some characteristics whilst on the western shelf where the width of the shelf is about 3°, this spatial resolution might not be enough to capture finer scale variability on the shelf. Both datasets include *in situ* and satellite resources, though the *in situ* inputs are not identical. Satellite data is available from the beginning of OISST time series and *in situ* data was mainly used to calibrate and validate satellite data, as well as reducing the bias due to influence from clouds [Reynolds *et al.*, 2002], while HadISST1 relies heavily on *in situ* data before satellite era. Several calculations were done to compare the uncertainty and homogeneity of the two datasets over the overlapping period, 1982 – 2009.

Firstly, raw monthly SST climatology for 1982 – 2009 derived from HadISST1 and OISST. v2 was compared. Climatology of SST differences (OISST. v2 minus HadISST1) for the first month of the four seasons (January, April, July and October) is shown in Figure 2.2. Generally, the differences between the two datasets were within ±

0.5 °C intervals for the majority area of subpolar basin except in the Irminger basin and along the Gulf Stream where the differences are ~1 °C. OISST. v2 is warmer than HadISST1 in three months but in July, HadISST1 gave warmer SST results in the southern subpolar basin, especially in the Newfoundland Shelf and the Gulf of Maine where the difference could be -1.5 °C. In the north, OISST v.2 was still warmer than HadISST1 in July, with maximum difference in the Irminger Sea of about 1 °C. The differences between the two SST datasets were large in regions of high turbulence, such as the Gulf Stream, and in the Irminger Sea off the region influenced by sea ice. Rayner *et al.* (2003) suggested that the differences between the two datasets around the region with seasonal sea ice coverage were due to an inadequate adjustment used to produce OISST v.2.

The period of 1982 – 2009 showed an overall warming trend [Rayner *et al.*, 2003]. Thus, this linear trend was derived from SST annual mean and removed from both datasets before monthly standard deviation was calculated to examine the homogeneity of the two datasets through time (Figure 2.3, a-b for OISST v.2, and c-d for HadISST1). The standard deviation for January (Figure 2.3a and 2.3c) and July (Figure 2.3b and 2.3d) of the two datasets, representing two extreme seasons in a year, is shown. Differences between the standard deviation of OISST v.2 and HadISST1 were small in both seasons, though generally variability was smaller in HadISST1 than in OISST v.2, as the area with low variability was larger in HadISST1 than in OISST v.2. A few similarities between the distribution of standard deviation of the two datasets were summarised as following: 1) in the subpolar North Atlantic, variability was smaller in January than in July; 2) largest variability was observed in the Gulf Stream area, where maximum standard deviation was around 1.2 °C in January and around 1.5 °C in July; 3) in the eastern subpolar basin, standard deviation was about 0.2 °C in January and about 0.4 °C in July, except in the North Sea where variability was about 1 °C in both seasons.

Following Rayner *et al.* (2003), the autocorrelation of detrended SST anomalies in 1982 – 2009 with one-month lag was shown for OISST v.2 (Figure 2.4a) and HadISST1 (Figure 2.4b) to examine temporal homogeneity. The greatest temporal coherence in both datasets was found in the interior subpolar basin and the Iceland basin. In OISST v.2, autocorrelation higher than 0.6 was also found in the Labrador Sea, though in

HadISST1, autocorrelation was lower than 0.5 or not available in this region. The maximum autocorrelation was slightly higher in OISST v.2 than in HadISST1, but the overall field was in the same intervals for both datasets.

After the description of the comparison between HadISST1 and OISST v.2 in average seasonal difference, long-term monthly variability and temporal coherence, HadISST1 was chosen to carry out more detailed analysis in this study. HadISST1 was generally colder than OISST v.2, except in the northern subpolar North Atlantic where HadISST1 was warmer. The differences between HadISST1 and OISST v.2 were likely caused by the differences in data sources and interpolation methods, though the overall differences were relatively small and distributed mainly in regions with high turbulence. HadISST1 was more homogenous compared to OISST v.2 in the period of 1982 – 2009. The temporal coherence of the two datasets was similar, with OISST v.2 slightly more coherent than HadISST1. Overall, HadISST1 was favoured because its overall more coherent and its length made this dataset unique and more suitable for this study.

2.2.2   Uncertainty

HadISST1 is a globally complete dataset, which takes into account the influence from sea ice and atmosphere in both hemispheres. Generally, the uncertainty in HadISST1 is high mainly in coastal and seasonally ice-covered regions, e.g. coast along Greenland and the Labrador Sea coast. For the subpolar North Atlantic interior, which is the main focus of this study, HadISST1 gives reasonably reliable results. The major processes that may introduce SST uncertainty are discussed below.

Sea ice is observed at high latitudes in both hemispheres and affects seawater temperature through various processes [Mauritzen and Häkkinen, 1997; Rayner *et al.*, 2003]. Sea ice data used to produce HadISST1 came from multiple data sources, including historical records and satellite observation. Historical records using different observing methods may result in inconsistency in the resultant data. In addition, when combining historical records and satellite data, biases need to be adjusted. However, when producing sea ice data various statistical methods were used to reduce the bias and uncertainty as much as possible. Therefore, although the sea ice records used in HadISST1 were imperfect they improved the data by combining all available sea ice data resources and homogenizing them. After the 1970s, HadISST1 gave more detailed

sea ice data whereas it had previously only provided a general indication of sea ice extent on decadal scale [Rayner *et al.*, 2003]. In the region discussed in this study, sea ice was only observed in the Labrador Sea, and perhaps the southeastern North Sea during severe winters. Thus at times when sea ice was recorded in data, these data were then removed.

Similar to sea ice data, HadISST1 combined various sources to produce the SST part of the data. Before 1982, HadISST1 was based on *in situ* data and from 1982 onwards it included both *in situ* and satellite data. All *in situ* data was bias-adjusted, according to the methods and instruments used to carry out the observations. AVHRR night-time data was used because of its good coverage and lengthy record. This record was bias-adjusted to reduce the influence of clouds and sea ice. When combining *in situ* and satellite data, statistical methods were used to reduce the inconsistency between the two data sources.

Satellite data (if available) were first used to fill in the area where bias-adjusted *in situ* data was not available. RSOI was used to fill in the gaps where neither observation was available [Rayner *et al.*, 2003]. In the subpolar North Atlantic, where *in situ* and satellite observations were relatively abundant, gaps still exist, especially in the shelf areas, so interpolating might cause small scale noise and thus temporal inconsistency. Due to the limits of historical records and statistical methods, the accuracy of SST observations before the 1920s will be poorer than that in the present day. In this section the uncertainties are only discussed qualitatively and future work is needed to provide quantitative estimate of the uncertainties.

2.3   Climatology

Before presenting the variation of SST annual cycle, it would be useful to first characterise the seasonal SST and the average annual cycle in different parts of the subpolar North Atlantic.

2.3.1   Seasonal SST

The subpolar North Atlantic is an area where distinct seasons are found and multiple processes modulate seasonal SST variation. In winter (Figure 2.5a), the transport of

Arctic water into the North Atlantic through the East Greenland Current (EGC) is increased [Woodgate *et al.*, 1999]. As EGC flows around Greenland, the current is usually known as the West Greenland Current (WGC) after turning northward at the southern end of Greenland. WGC is joined by flow from the Davis Strait and both flow towards the Labrador Sea. Here one branch keeps flowing southward forming the Labrador Current (LC). This transports cold water down to the northern wall of the Gulf Stream, forming a strong SST gradient that separates the colder and less saline subpolar water from southern warmer and more saline water, also known as the subpolar front (SPF) [Núñez-Riboni *et al.*, 2012]. SPF is generally considered the southern boundary of subpolar gyre, although its position does not have an agreed numeric definition. It is usually associated with the Gulf Stream and NAC system.

Here, two isotherms were chosen to highlight the difference of SST distribution in winter and summer, following Flatau *et al.*, (2003). Isotherms of 7 and 8 °C were shown in red solid and dashed lines, respectively. The choice of these two isotherms are based on their similarity to the SST gradient that separates the Arctic origin water from the North Atlantic water and their easier application than detailed SST gradient calculation. In this subsection, the aim of showing the two isotherms is to identify the seasonal difference of the isotherm distribution in the subpolar basin. In winter (Figure 2.5a), the two isotherms lay from the Gulf Stream area diagonally towards Iceland while the southern half of the two isotherms lay in the region with strongest SST gradient (black lines). The summer temperature (Figure 2.5b) was higher than winter temperature in most of the subpolar region by over 5 °C, except in the northern Labrador Sea and Greenland shelf where summer SST was only ~2 °C higher than winter SST. The 7 °C and 8 °C contours lay around Greenland and in the Labrador Sea, marking the general pathway of EGC and WGC [De-Jong, 2010]. The southern half of the two isotherms no longer lay in the region with strongest SST gradient. The temperature in SPF area increased from below 9 °C in winter to around 20 °C in summer.

In winter, isotherms lay southwest-northeastwardly to the west of 20 °W and lay northwest-southeastwardly to the east of 20 °W, forming a tongue-shape distribution with warm SST in the southern open ocean. SST in the western open ocean was about 7 °C colder than that in the eastern open ocean, suggesting a stronger influence of warm currents from the south in eastern subpolar and a stronger influence from the north in

western subpolar in winter. In the North Sea, isotherms distribution was southwest-northeastwardly with colder SST towards the continent. This suggests that winter SST in the North Sea was mainly determined by local processes like atmosphere-ocean interaction and runoffs rather than by ocean advection from the North Atlantic. The atmosphere is colder towards the continent influenced by the cold air on land and ice might form in the southeastern North Sea in severe winters. In summer, isotherms lay southwest-northeastwardly across almost the whole basin, including the adjacent North Sea. The only exception was in the Labrador Sea where cold southward LC broke such distribution by pushing isotherms towards the south. SST difference between the two sides of the basin was decreased to about 3 °C, suggesting a stronger impact of warm surface advection in the western subpolar in summer.

2.3.2   Average Annual Cycle

Following the discussion of the distribution of seasonal SST in the subpolar region, the average annual cycle in the four types of locations (eastern shelf seas, eastern open ocean, western shelf seas, and western open ocean, see Figure 2.1 and Table 2.1) were calculated and presented in Figure 2.6. The error bars show the range of one standard deviation (± 1 s. t. d.) of monthly SST over the 140-year time period.

Western shelf seas (magenta line) had the largest mean annual cycle amplitude, ranging around 10 °C. In the eastern shelf seas (red line), the mean annual cycle amplitude was also large, around 5 °C. The peak of the annual cycle in the two shelf areas were similar, about 15 °C, but the winter SSTs in western shelf seas were much lower than that in the eastern shelf seas. This difference in winter SSTs is related to the increased transport of Arctic water into subpolar region in winter and a stronger LC that penetrates and transports cold water into the western shelf seas.

The mean annual cycle amplitude in the two oceanic regions was much smaller than those in the shelf seas (~3 °C), suggesting the influence of deep mixing that extracts heat stored in deeper layers and hence lead to milder cooling in the mixed layer in the two regions. The annual cycle patterns were similar in the two areas, though SST in the western oceanic region (green line) was colder than that in the eastern oceanic region by about 4 °C in all months. In the eastern oceanic region (blue line), the water was characterised by a GS/NAC system circulation and its continuous modification through

interaction with atmosphere in both seasons. The western oceanic region was characterised by recirculation of Arctic water in winter and influenced by North Atlantic water in summer [Holliday, 2002]. Due to the north-westward incline of isotherm distribution, summer SST in the west was lower than that in the east.

The distribution of seasonal SST in the subpolar North Atlantic shows large (~5 °C on average, and larger than 10 °C in some shelf seas) SST difference between winter and summer. These differences result from various reasons: changes in dominating factor or changes in the strength of major currents and gyres. The distribution of seasonal SST could impact the strength of air-sea interaction and thus affect local atmospheric activity. Also, in different parts of the subpolar North Atlantic, climatology annual cycles were not identical, with larger seasonal SST difference in the shelf seas and slightly higher variability in summer months. This indicates that the climatology of ACA and its variability would also be different in different parts of the subpolar basin, and thus leave different impacts on the climate and ecosystem.

2.4   The Observed Variability

In this section, multi-decadal variability of SST annual cycle amplitude (ACA) and seasonal SST are presented. Seasonality can be defined in multiple ways: such as yearly-period sinusoidal curve and difference between yearly-period extremes [Stine *et al.*, 2009; Zveryaev and Gulev, 2009]. The interest of this study is decadal to multi-decadal variation of SST annual cycle, so ACA was defined as in Eq. 2.1

$$ACA = SST_{Max}(i) - SST_{Min}(i), \qquad\qquad i = 1 \cdots 140. \qquad\qquad \text{Eq. 2.1}$$

2.4.1   Decadal to Multi-decadal Variability in SST ACA

As mentioned in section 2.1, along the eastern and western boundaries of the subpolar basin and its adjacent seas, 24 locations were chosen to inspect in detail. These 24 locations were grouped into eastern shelf seas, eastern open ocean, western shelf seas and western open ocean (see Figure 2.1 and Table 2.1). The ACA time series was constructed for each location using original SST data, and then time series belonging to one group was combined to calculate the mean ACA for each group.

This process was done in several steps. First, all 24 time series were standardized to zero following Eq. 2.2, so the amplitude of SST annual cycle calculated from different parts of the subpolar basin could be compared:

$$S_{stand}(i) = \frac{S(i) - \overline{S(i)}}{S_{s.t.d}(i)}, \qquad\qquad i = 1 \cdots 140. \qquad\qquad \text{Eq. 2.2}$$

where S is the original ACA time series, $\overline{S}$ is ACA average over the period of 1870 – 2009, and $S_{s.t.d}$ is the standard deviation of the original time series. Then, higher-than-decadal frequency variability was removed by applying a 9-year running mean to all the 24 time series of standardized ACA. The third step was to calculate the mean values of ACA and associated standard error of the mean (SEM), using Eq. 2.3:

$$SEM(i) = S_{stand_{s.t.d}} \Big/ \sqrt{N_i}, \qquad\qquad i = 1 \cdots 4. \qquad\qquad \text{Eq. 2.3}$$

Where N_i was the number of locations of each group and the 95% confidence interval was calculated by multiplying the resulting SEM by 1.96.

The size of each group could affect the actual value of SEM, so for groups with more than five locations, only five of them were included in the calculation so the size of the biggest group is five and the smallest group is three. Six out of the ten eastern-shelf-sea locations lay in the North Sea, only the location representing the southeast North Sea was included to avoid artificial small error from the autocorrelation between locations that share similar forcing. For the western oceanic region, the locations on both sides of the Greenland were omitted when calculating the average ACA because the two locations include a narrow shelf off the Greenland coast. The final sample size for each group was: five locations for eastern shelf sea, three for eastern oceanic region, four for western shelf sea and five for western oceanic region.

Mean ACA time series of the four groups are shown in Figure 2.7, together with low-pass (9-year running mean) time series (red curves) and SEM on 95% confidence interval shown in grey shades. The width of the grey bands represents the variance of ACA within each group, the narrower the band the smaller variance between the original time series in chosen locations and the group average. Generally, the variance

between chosen locations and the mean ACA was smallest in eastern shelf seas with the narrowest grey band. Mean ACA in eastern oceanic region and western oceanic region also lies within a narrow band. The 95% interval of the western shelf seas was the widest in the four groups, suggesting a weaker homogeneity of amplitude in these locations, though the general pattern remained the same. The long-term variation of ACA in the four groups all showed decadal to multi-decadal variability, though the pattern was not consistent across the basin.

In the eastern shelf region (Figure 2.7a), ACA showed a well-defined multi-decadal variability: ACA was high in the periods of 1890s – 1910s, mid-20th century, and after the 1980s but low in the periods of 1910s – 1930s and the 1950s – late 1970s. From 1870 to 2009, ACA seemed to vary on a period of 40-years and was roughly equally distributed on both sides of zero line. The last period when ACA kept increasing was from the late 1980s to the early 2000s, and the last peak after 1995 was slightly higher than the previous peaks.

In the eastern oceanic region (Figure 2.7b), ACA showed a different pattern compared to eastern shelf seas, which was higher than the long-term average in the 1880s – 1920s and after the late 1970s, while in the 1920s – late 1960s ACA was lower than average. The dominating pattern was the multi-decadal pattern, though during the low-ACA time period the variation showed higher frequency variability imposed on the multi-decadal pattern. Similar to the eastern shelf region, the peak of ACA in the early 2000s was higher than the previous peak.

In the western shelf region (Figure 2.7c), the most noticeable feature was the peak in the mid-1930s, which was about a decade earlier than that in the eastern shelf region and with larger amplitude. Before the late 1920s and during the period of 1950s – late 1980s, ACA was lower than average, followed by a high ACA period from the late 1980s. In the western oceanic region (Figure 2.7d), ACA decreased from higher than average in the 1870s to lower than average in the early 1920s. ACA then varied on a scale of 20-year periods from the early 1920s till the late 1960s, followed by a steady increase from the late 1960s, finally peaking in the 2000s. All three peaks after the 1920s, in the 1930s, 1950s and 2000s, were of similar amplitude. Overridden by the

variability between 1920s and 1960s was a lower frequency variability through the whole time series.

The most obvious difference between the variability of SST ACA in the shelf seas and the oceanic area is the peak in the mid-20th century in the shelf seas (Figure 2.7a and 2.7c), which was absent in the open ocean during this period. In the two open ocean regions (Figure 2.7b and 2.7d), the ACA was at its lowest level in the mid-20th century. Before and after the mid-20th century, shelf and oceanic regions on the same side of the basin displayed similar patterns and the patterns in the two sides of the basin were different. The ACA in the two eastern subpolar regions was roughly higher than average from the 1870s to 1920s, while in the two western regions ACA was lower than average during the same decades. In addition, ACA was larger in the west than in the east, for both shelf seas and oceanic regions. In the two oceanic regions, higher frequency variability overrode the multi-decadal fluctuation between the 1920s and 1960s, shown as two full cycles during the 40-year period.

In the last 140 years, the amplitude of SST annual cycle has varied on decadal to multi-decadal scale, rather than remaining unchanged. In the subpolar North Atlantic, where seasonal SST range larger than 5 °C is found, these changes were not consistent across the whole basin. Shelf seas and the open ocean varied with different patterns and differing timing of peaks and periods, suggesting different mechanisms control the variability in the two types of regions. These results, shown in this section using HadISST1, are different from the "usual" SST time series which presents a general warming trend, especially after the mid-1990s. This might be because the general warming trend was largely removed when subtracting cold extreme from warm extreme, suggesting a comparable warming trend in both extremes. ACA variability might reflect and impact the variation of other parameters such as vertical mixing, and the mechanism of ACA variability in different parts of the subpolar basin requires further investigation.

2.4.2   Evolution of Seasons

ACA, by its definition in this study, is affected by the variability of both warm and cold extreme SSTs. Long-term variability of winter and summer SSTs reveals the underlying controlling processes and could provide possibilities for explaining the observed variability in ACA. In the climatology section (Figure 2.6), average annual cycle was

constructed for four groups of chosen locations representing various bathymetries. On average, March was the coldest month of the year and August was the warmest. September SST was usually higher than June SST. Thus, instead of grouping March into spring, SSTs from January to March were then averaged to produce a wintertime series and SSTs from July to September were averaged to produce a summertime series using original HadISST1 data. The mean standardized (following Eq. 2.2) low-pass filtered winter and summer evolutions of the four groups were produced following the same procedure as producing ACA time series and are presented in Figure 2.8. The grey bands in Figure 2.8 indicate the SEM with 95% confidence intervals (following Eq. 2.3). In the following section, the evolutions of winter and summer over 140 years in each group are described and the potential link between seasonal SST evolution and ACA is discussed.

In the eastern shelf region (Figure 2.8a and 2.8b), summer SST dominated the variability of ACA with a statistically significant correlation between the two time series (r=0.61, p<0.0001), while winter SST just modulated ACA variability, but did not resemble the variation of ACA. For both winter and summer, SST was colder than average before the 1930s. From the late 1930s to the late 1970s, winter and summer SSTs were out of phase, colder than average winter SST and slightly warmer than average summer SST resulted in a peak in ACA (Figure 2.8a). The following warmer than average winter SST and colder than average summer SST were reflected in a lower than average ACA during the 1950s – late 1970s. Seasonal SST started to increase from the early 1990s and after the 1990s, both winter and summer SSTs were warmer than average, though summer SST increased more rapidly and stronger than winter SST, which also led to a peak in ACA from the mid-1990s. The two ACA peaks in the eastern shelf region resulted from two different reasons: the linear regression coefficient is -0.03 for winter SST and is 0.04 for summer SST during 1921-1945 when summer SST started to increase from an earlier cold period but winter SST continued to decrease whilst the coefficient is 0.008 for winter SST and 0.04 for summer SST during 1990-2009. This suggests a change of the influencing factors in the later period from the early 1990s that is manifested in ACA after the mid-1990s.

Winter and summer SSTs evolved in a similar pattern in the eastern oceanic region (Figure 2.8c and 2.8d) and both showed a multi-decadal variability. The multi-decadal

pattern of ACA (Figure 2.7b) was dominated by winter SST, as the two curves were weakly negatively correlated (r=-0.38, p<0.0001), while the shorter-term variability was dominated by the summer SST because correlation between the ACA and summer SST is not significant when using smoothed time series that preserve only signals on the decadal and longer scales. From the 1870s to 1930s, SST was colder than average in winter and summer. After the cold period, winter SST started to increase and exceeded the average during the 1930s – 1970s before another cold winter period from the early 1970s to late 1980s. Major warm summer periods were in the 1950s and after the mid-1990s, with SST during the 1930s – 1940s around average. The lowest point in ACA in the early 1960s resulted from a warmer than average winter SST and colder than average summer SST. Similar to the eastern shelf area, after the mid-1990s, even though winter and summer SSTs were in phase, ACA was higher than average.

In the western shelf area (Figure 2.8e and 2.8f), the multi-decadal ACA (Figure 2.7c) variation was dominated by summer SST (r=0.77, p<0.0001) and winter SST adjusted ACA in shorter-term scale. Both summer and winter SSTs were consistent with a cold period and a warm period. In winter, SST switched from cold phase to warm phase in the 1940s while summer SST switched in the 1930s. Though the variation patterns were similar in both seasons, the delayed arrival of warm phase in winter resulted in the 1930s peak in ACA. The rapid summer SST increase from mid-1990s led to a later peak in ACA.

The most noticeable feature of SST evolution patterns in the western oceanic region (Figure 2.8g and 2.8h) was the very cold period between the 1970s and mid-1990s in winter. The summer SST of the same period was also lower than average (9.6 °C during 1970-1995 and the long-term average SST is 10 °C), but was equivalent to an earlier cold period between the 1910s and 1920s (9.7 °C). The shape of ACA (Figure 2.7d) was dominated by summer SST (r=0.7, p<0.0001 between ACA and summer SST) and the winter SST fluctuated on a similar pattern (r=0.5, p=0.02 between winter and summer SSTs), yet with smaller amplitude compared to summer SST (0.39 °C for winter SST and 0.52 °C for summer SST). From the mid-1990s, both winter and summer SSTs recovered from the very cold phase, with summer SST recovering faster, and led to the small peak in ACA from the mid-1990s.

Summarizing the season evolution patterns in the four regions, in spite of differences in the timing of peaks and the exact patterns, one can still conclude the following similarities: 1) variation patterns in winter and summer were more uniform in the open ocean than in the shelf seas; 2) summer SSTs played a more important role in controlling ACA than winter SSTs, especially in the shelf seas; 3) winter SSTs had a stronger impact on the oceanic region than in the shelf seas; 4) earlier in the time series, the extreme peaks (minimums) in ACA usually resulted from a combination of warmer (lower) than average warm extreme and colder (warmer) than average cold extreme; 5) after the mid-1990s, both winter and summer variations increased rapidly, and the ACA was also higher than average in all four regions, suggesting a change of the controlling factors in the two seasons after 1995.

2.4.3   Changes to Annual Cycle in Recent Decades

The impact of climate change has been found in many parts of the earth system [Levitus *et al.*, 2000; Hoegh-Guldberg and Bruno, 2010]. In the upper ocean, temperature has reached a level higher than historical records in recent decades. In earlier decades, increase in ACA usually resulted from out-of-phase summer and winter SSTs (e.g. the mid-20$^{\text{th}}$ century in eastern shelf seas), but in the more recent decades both winter and summer SSTs increased, along with increasing ACA (Figure 2.7). This change suggested that controlling mechanisms of winter and/or summer SSTs in the more recent decades were not identical to those in the earlier decades. SST variations in the later decades are focused on in the following section to document the more recent changes of SST annual cycle in the subpolar North Atlantic.

2.4.3.1   Choice of period

In this study we also see hints of the impact of climate change in subpolar North Atlantic SST ACA. In both seasons, SST experienced rapid increase from the early 1990s and after 1995; SSTs in all the four types of regions were above average and increased at a rapid rate. At the same time, ACA also exceeded average after 1995 in all regions (Figure 2.7). By the end of the time series, ACA and SSTs in two seasons reached, or exceeded, their respective historical peaks. As mentioned above, in the early decades ACA reached its peaks due to warming in summer and/or cooling in winter (Figure 2.8). From 1995 onwards, however, this was no longer the case. These

differences between later and earlier decades in seasonal SSTs and ACA indicated changes to the annual cycle in the last 15 years. Thus, anomalies of winter and summer SSTs were calculated between the later decades of 1995 – 2009 and earlier decades of 1870 – 1994 for the whole subpolar North Atlantic (Figure 2.9) to first examine its spatial distribution. The associated SEM of each period was calculated following Eq. 2.3 and the total weighted SEM of the anomalies was calculated as shown in Eq. 2.4, using the number of years in both period as weights:

$$SEM_{total} = \sqrt{\left(SEM_{former} \times W_1\right)^2 + \left(SEM_{latter} \times W_2\right)^2}$$

Eq. 2.4

where $W_1 = \dfrac{w_1}{w_{1+}w_2}$, and $W_2 = \dfrac{w_2}{w_1 + w_2}$. w_1 and w_2 are the number of years corresponding to the former and latter time periods. The total weighted SEM of both seasons significant on 95% confidence intervals is shown in Figure 2.10.

2.4.3.2   Seasonal SST anomalies

Despite a general increase in both winter and summer SSTs observed in seasonal evolution, winter SST anomalies (Figure 2.9a) showed a negative center in the northwestern subpolar North Atlantic and both sides of Iceland, meaning that in these areas winter SST was colder in the later period than in the earlier period; the cooling magnitude was around -0.5 ºC. It is worth noting that this cooling signal is related to the cold period since the 1970s in the northwestern basin, especially in winter. From 1995, SST started to recover from the previous cold period, but still at a relatively low level before the 2005 (see Appendix 1). The mechanisms for this cooling signal is still not clear and is beyond the scope of this study, so is not discussed here.

Apart from these areas with negative anomalies, other parts of the subpolar North Atlantic showed a general warming trend in the second period in both seasons, with a magnitude of around 0.5 ºC in summer and around 0.3 ºC in winter in the central subpolar North Atlantic. The warming centers were in the southwestern subpolar around the Gulf Stream, east of Greenland, interior Labrador Sea and southeastern North Sea, where the strongest warming was about 1ºC – 1.5 ºC. The weighted standard error of 0.04 ºC in most of the subpolar region (Figure 2.10) and in regions with strongest winter

warming, the weighted standard errors ranged from 0.12 ºC to 0.18 ºC. The warming signal is of a higher magnitude than the error and hence significant in the second period. The standard error of the cooling area was about 0.05 ºC, and the cooling in the second period was weakly significant in winter.

In summer (Figure 2.9b), the warming signal was observed across the whole basin, except the shelf area west of Greenland, and the signal was stronger on the shelves than in the open ocean. The warming centers were in the southeastern North Sea, along the western boundary of the subpolar basin, the Gulf of St Lawrence and east of Greenland. The warming magnitude was around 1.5 ºC in those centers. On the shelf west of Greenland, the narrow band of the cooling signal was of ~-0.2 ºC magnitude. The central subpolar region showed a general warming signal of 0.5 ºC. In the Gulf Stream and around the Newfoundland shelf, the weighted standard error was $0.18 - 0.2$ ºC (Figure 2.10b) and, compared to the warming magnitude here, the warming was significant after 1995. In the North Sea and the shelf around the basin, the standard error was around 0.14 ºC while in the interior Iceland Basin the standard error was ~0.08 ºC, which was one magnitude lower than the warming signal. The cooling signal in the narrow area in summer anomalies was not significant, as the standard error was 0.12 ºC.

After 1995, warming in the subpolar North Atlantic was ambiguous in summer and in winter, except the area south of Greenland showed cooling SST in winter after 1995. Warming was significant in both seasons and was generally stronger in summer than in winter. Cooling was observed in more regions and was stronger in winter than in summer, with weak but significant winter signal and insignificant summer signal. In the open ocean regions, where warming was observed the warming signal was milder than that in the shelf seas for both seasons. Strongest warming was seen in the Gulf Stream, east of Greenland and the North Sea, where significant warming over 1 ºC was observed in both winter and summer. Largest standard errors were also associated with these areas, and standard errors were higher in summer for the Gulf Stream but were higher in winter for the area east of Greenland and the North Sea.

2.4.3.3   Implication of changes to annual cycle

Comparing the winter and summer SST anomalies between the two periods, one can see that the changes of the annual cycle in the later period are not consistent across the

whole basin. The changes to annual cycle could be to its annual average (the mean value of one cycle) or to its amplitude (the difference between maximum and minimum SSTs during one cycle). These two types of change can be observed together or separately, so within the subpolar North Atlantic basin the annual cycle had changed in various ways in different locations.

The average annual cycles with SEM of the period 1870 – 1994 and 1995 – 2009 at a few locations that present statistically significant warming or cooling signals are shown in Figure 2.11 to indicate changes to the annual cycle in the later period. In the northwestern subpolar basin (Figure 2.11a), cooling in winter and warming in summer were significant, but warming in spring and autumn in the second period was not significant from the first period. This suggests changes mainly to the annual cycle amplitude. Warming in the North Sea (Figure 2.11b) was significant in the warm season from April to September, while warming in the cold season was not significantly different from the former period. The changes in annual cycle here are shown in an increase of annual mean and also an increase of amplitude. In the Gulf Stream (Figure 2.11c), warming in the second period was significant in all months and warming was stronger in winter than in summer. So in this area, annual mean in the second period was increased from the level in the first period, but the amplitude was slightly decreased. In the southern subpolar basin (Figure 2.11d), warming was only significant in winter, but not in summer. Annual mean here in the second period was slightly higher than that in the first period, though the amplitude was slightly lower.

In summary, south of 50 ºN, winter and summer SST anomalies both show warming signals after 1995 and the warming was of similar significance in the region between 50 ºW and 20 ºW, resulting in an increase in annual mean SST. In the Gulf Stream area, warming in winter was slightly stronger than in summer, so the amplitude decreased slightly. North of 50 ºN, the SST anomalies in winter and summer were less consistent. In regions of winter cooling, ACA increased, though the annual mean could stay the same; in regions of stronger summer warming, both ACA and annual mean increased after 1995.

2.4.4   Basin Scale Variability

Empirical orthogonal function (EOF) analysis is a statistical technique that identify and extract signals from a dataset which may contain physically and dynamically independent patterns [Kim and Wu, 1999]. The main steps of an EOF analysis including calculating the covariance matrix of the dataset, working out the eigenvectors with a descending order so the first mode explains the highest percentage of variability, the last step is to calculate the principal component using the eigenvectors, eigenvalues and the covariance matrix (see Appendix 2 for the equations used in this study [Björnsson and Venegas, 1997]). In this study the conventional EOF analysis was applied to SST field, though there are various EOF-related techniques, such as rotated EOF and complex EOF, have been adapted to study the natural variability depending on the features of the patterns of interest. EOF analysis was applied to seasonal averaged SST anomalies after removing the linear trend over the entire time series and to compare the leading modes and their associated time series in each season. The composition of leading modes in each season and the strength of the leading modes could reveal the most important physical processes controlling seasonal SSTs. The differences between the constitution of leading modes and modal strengths in different seasons might provide some explanation to the observed variability in ACA.

2.4.4.1   Significance test of the EOF modes

Before showing the results of seasonal EOF analysis, the significance of the results was tested. First, a Monte Carlo test was carried out to separate real signal from random noise. Then the eigenvalues of each mode were plotted with sampling errors to show the significance of each mode in the four seasons. The core of a Monte Carlo test is to compare the eigenvalues of EOF analysis of seasonal SST to the eigenvalues from large repetition (usually 100 to 1000 times) of EOF analysis of random numbers. All eigenvalues sets were ordered in ascending order and the 95th (99th) set of eigenvalues set the threshold for the 95% (99%) confidence interval. If the eigenvalues of corresponding EOF modes exceed the threshold eigenvalues from the random EOF analysis, then the corresponding EOF modes are significantly different from random noise.

The random dataset should have the same length of rows and columns as the real data. In this study, the experiment was repeated 100 times and these 100 sets of eigenvalues were then listed in ascending order, with the 99th set used as the control eigenvalues. The first four EOF modes were all over the significance threshold set by the 99th eigenvalues from the 100 EOF analyses of random datasets (Figure 2.12). EOF modes derived from finite size dataset are estimates of the "true" EOF that can only be calculated from infinite size dataset [Quadrelli *et al.*, 2005]. The sampling errors estimate how well each mode represents the "true" EOF and two modes with overlapping errors are considered as "effective multiples", suggesting each of these two modes is not representative of two separate physically meaningful modes [North *et al.*, 1982]. Sampling errors were calculated for eigenvalues of real data and threshold eigenvalues, following Eq. 2.5 provided in North *et al.*(1982):

$$\rho\lambda_i = \sqrt{2/N} * \lambda_i \qquad \text{Eq. 2.5}$$

where N was the length of the time series and λ_i was the eigenvalue of each mode. The resulting eigenvalues and associated sampling errors, ρ, are shown in Figure 2.12.

From this simple significance test, one can see that EOF analysis on summer data was the most significant, with the highest eigenvalues of all the 10 modes. Technically, the first 7 EOF modes for summer time series were significantly different from noise (Figure 2.12, red line), while for the EOF modes in the other three seasons the first 5 modes were significantly different from noise (where the lower bar of the mode was above the threshold level). In this study, only the first four EOF modes are presented because the fifth EOF mode explains less than 5% of the total variability in both seasons, which might not contain much physical dynamics though significantly different from noises.

In the following discussion, the focus is only on the first four modes in winter and summer as, in general, the first four modes are all over the threshold with a reasonable difference. For the winter EOF modes, the first mode was significantly different from the second mode, while the second and third modes were not significant from one another, suggesting the two modes could be driven by similar forcing. The first two summer EOF modes were significant from one another and from the third mode, but the

third mode was not significant from the fourth mode. For the two transition seasons, spring and autumn, the first four modes were significant from one another. Though some modes were not significant from their neighbouring modes, all EOF modes were orthogonal and independent from one another; therefore, the modes significantly different from random noise all contribute to a better understanding of seasonal SST variation in the subpolar North Atlantic.

2.4.4.2   Major basin scale signals

Here, the spatial patterns and associated time series of the first four leading modes from winter and summer EOFs are shown (Figure 2.13 for EOF1, Figure 2.14 for EOF2, Figure 2.15 for EOF3 and Figure 2.16 for EOF4). The patterns are first described and then their connection to climate indices and implication to the multi-decadal variability in ACA are discussed.

The spatial patterns of both winter and summer EOF1 (Figure 2.13a and 2.13b for winter, and 2.13c and 2.13d for summer) highlight a positive center in the southwestern subpolar region, with a maximum value at 48 °N, 40 °W. One major difference between the winter and summer EOF1 spatial patterns is that, in winter (Figure 2.13a), the northeastern subpolar and North Sea are occupied by negative values while in summer EOF (Figure 2.13c) the whole subpolar basin shows positive values, suggesting that subpolar North Atlantic is more coherent in summer than in winter. Both winter and summer EOF1 time series (Figure 2.13b for winter and 2.13d for summer) associated with the spatial patterns vary on multi-decadal scale. Positive phases are seen in periods from the 1870s to 1900s, the 1930s to 1970s and after the mid-1990s. The first modes explain about 30% of the total variability in both seasons.

In the North Atlantic, Atlantic Multi-decadal Oscillation (AMO) index is defined by SST anomaly and is a prominent index. Since the first EOF mode displayed a multi-decadal pattern, EOF1 in both seasons were compared to AMO index. AMO index used in this study was downloaded from the website of Earth System Research Laboratory (ESRL)/ Physical Sciences Division (PSD, http://www.esrl.noaa.gov/psd/data/timeseries/AMO/). The index used here is the unsmoothed version calculated from monthly Kaplan SST, covering from January 1856 to present day. Seasonal AMO index was calculated with the same division of seasons as HadISST1, before the seasonal

AMO index was compared to EOF1 time series (see Figure 2.13b for winter, and Figure 2.13d for summer). In Figure 2.13, both time series correlate to the seasonal AMO index with high statistical significance, (r_{winter}=0.58, p_{winter}<0.0001; and r_{summer}=0.77, p_{summer}<0.0001).

Though AMO is a significant climate index and is defined by North Atlantic SST anomaly, the exact physical mechanisms that drive AMO variability are still under debate. Some studies claimed that AMO is driven by thermohaline circulation as it lacked a clear link to known climate indices [Deser *et al.*, 2009]. Another study proposed an atmosphere-ocean-sea ice interaction mechanism in the northern hemisphere that determines AMO variation [Dima and Lohmann, 2007]. Recent studies suggested that the influence from aerosol and its variation could take a more important role in controlling AMO than previously considered [Booth *et al.*, 2012]. Whichever forcing dominated, AMO is clearly the dominating signal in detrended SST variability in both winter and summer. Positive AMO phase suggests higher than average SST anomalies and negative AMO phase suggests lower than average SST anomalies [Knight *et al.*, 2006]. The AMO signal manifested in the subpolar SST shows significant correlation with the AMO signal defined using the SST anomalies over the whole North Atlantic, though there are still differences in the two signals, especially in winter.

Several reasons might explain these features of the correlation. First, there are temporal and spatial differences between the dataset used to calculate the downloaded AMO index and HadISST1. AMO used in this study was calculated from weight-averaged SST in the whole North Atlantic basin from 0 ° to 70 °N since 1856 whereas EOF1 was calculated over the subpolar basin from 1870 to 2009. EOF analysis is sensitive to temporal and spatial domain [Ambaum *et al.*, 2001], thus the differences in these choices could result in differences in the results. Second, the resolution and data resources of the two datasets are different. The ESRL/PSD AMO index used data derived from the Met Office Historical Sea Surface Temperature version 5 (MOHSST5), then several steps of statistical adjustment and interpolation were carried out to fill in missing data and remove bias. The resultant Kaplan SST dataset was on 5°×5° grid. HadISST1 and MOHSST5 had similar data input (Marine Data Bank, MDB) in early decades, but HadISST1 included satellite observation after 1982. The spatial

resolution of HadISST1 was 1° ×1° grid instead of 5° ×5° grid. Though both datasets were intended to keep data consistency and reduce bias as much as possible, it is not surprising that errors still remained in both datasets. Such uncertainties and differences in spatial resolution could both leave traces in the results. These two datasets are not totally independent, which could lead to artificially high correlation coefficients. However, the aim of the correlation analysis is to examine the strength of the AMO signal that is manifested in the subpolar North Atlantic rather than identifying the observed signal because it is not surprising that the first EOF mode captures the AMO signal. Thus, the dependence of the two does not affect the main conclusion that the first EOF mode is the AMO.

The reason for stronger correlation between AMO and EOF1 in summer than in winter could be that the AMO signal was stronger in summer SST anomalies than in winter, as the influence of atmospheric forcing, such as wind and surface buoyancy loss, on SST is stronger in winter, which is different from the two hypothesised mechanisms that result in the AMO signal. However, the results from EOF analysis on seasonal SST confirmed the dominant pattern of SST variability in the subpolar North Atlantic is AMO, both in winter and summer. The AMO signal was clearer in summer than in winter, thus in regions (e.g. western shelf seas) where ACA was dominated by summer SST, summer SST displayed a clear AMO pattern and ACA would also resemble the variation of AMO. In other regions (e.g. eastern open ocean) where winter SST dominates or AMO signal was not clear, processes that drive AMO variability might not play a major role in explaining ACA variability.

The second leading mode in winter (Figure 2.14a) displays a positive variability center in the central subpolar North Atlantic, centered at 55 °N, and 36 ° W, with two negative variability centers in the North Sea and the Gulf of Maine. The time series corresponding to this mode (Figure 2.14b) is negatively correlated to winter North Atlantic Oscillation (NAO, $r_{winter}=-0.54$, $p_{winter}<0.0001$). The EOF mode explains about 16% of the total winter variability. The second mode of summer EOF (Figure 2.14c) displays a negative variability center at 45 °N, and 36 °W and the rest of the subpolar is positive. The corresponding time series (Figure 2.14d) is weakly correlated to summer NAO ($r_{summer}=-0.28$, $p_{summer}<0.0001$). This mode explains about 17% of the total variability in summer.

The NAO index used here is defined by the differences of sea level pressure (SLP) between Azores High and Icelandic Low, typically characterised by a dipole distribution in the North Atlantic [Hurrell and Deser, 2010]. Positive (negative) NAO index is usually associated with stronger (weaker) westerlies in the North Atlantic, especially in winter [Portis *et al.*, 2001; Flatau *et al.*, 2003; Hurrell and Deser, 2010]. In this study, EOF2 displayed a well-developed NAO spatial pattern in winter while in summer the dipole distribution was not clear. However, Portis *et al.* (2001) reported a western and northern shift of their subtropical NAO node during summer months, therefore the negative center in summer EOF2 could be associated with such shift, though the corresponding negative center could not show in winter EOF2 due to geographical constrain. Negative correlation between EOF2 and NAO in winter is strongest from 1960 to 2009, when NAO remained in negative phase from the 1960s to the late 1970s and switched to positive phase from the early 1980s to the early 2000s. In early decades, such negative correlation is less clear. Even though summer EOF2 and NAO show statistically negative correlation, the two time series depict rather similar multi-decadal variability, though not statistically correlated (solid lines in Figure 2.14d). This suggests that such negative correlation is clear only on time scales shorter than decadal, and higher frequency variability dominates summer EOF2 and summer NAO variability.

NAO adjusts SST through wind forcing and wind driven mixing, especially in winter [Henson *et al.*, 2009a]. During positive NAO phase periods, winter westerlies are strong, increasing heat loss and vertical mixing. Vertical mixing brings deeper cold water to the surface, which further cools surface water. In addition to the impact through wind, positive NAO phase is also associated with stronger NAC and subpolar gyre circulation, resulting in a stronger front located further east than during negative NAO phase periods. Flatau *et al.* (2003) found that the differences of subpolar gyre strength during positive and negative NAO phases were similar to those between winter and summer. Such adjustment of NAO is stronger in winter than in summer as correlation between NAO index and average zonal wind is higher in winter, especially for NAO index defined using location specified time series (index used in this study) [Portis *et al.*, 2001]. NAO mainly modulates winter SSTs near action centers through affecting the strength of westerlies while in summer NAO index decreases and thus its impact on summer SST. In both seasons, NAO modulation is strongest on inter-annual to decadal scale.

For the first two leading EOFs, EOF1 in both seasons were AMO patterns and EOF2 was associated with NAO index. Summer EOF1 showed a stronger AMO signal than winter EOF1 while winter EOF2 was correlated more closely to NAO than summer EOF2. These two modes explain about 50% of the total variance in both seasons and the differences between the two seasons could at least partially explain the different seasonal variations in the subpolar North Atlantic. The southwestern subpolar basin was positively correlated with AMO in both seasons and was negatively correlated to NAO index, thus winter and summer SSTs resembled AMO variation, however without strong NAO index modulation, the resulting ACA might resemble AMO variability in this region. Processes controlling ACA variability in the northern subpolar North Atlantic could be more complex, as NAO plays an important role in determining winter SST and AMO dominates summer SST. However, AMO reflects seasonal SST variation on multi-decadal scale and NAO influences seasonal SST on shorter time scales.

Apart from the two major indices discussed above, a few previous works suggested teleconnections between ocean basins, such as Arctic Oscillation (AO) and Eastern Atlantic Pattern (EAP), arguing that variability in other ocean basins or on land could impact variability of physical parameters in the North Atlantic [Deser, 2000; Ambaum *et al.*, 2001; Cannaby and Husrevoglu, 2009]. In the following section, signals from lower ranked EOFs are discussed and compared to climate indices that suggest possible teleconnectivity across ocean basins.

Monthly mean AO index used in this study was downloaded from the website of the University of Washington (http://www.atmos.colostate.edu/ao/Data/ao_index.html). Seasonal mean AO index was calculated by averaging over seasons of the same division as SST. AO is defined as a leading mode in EOF analysis of sea level pressure (SLP) over the Northern Hemisphere, which is significant in any month [Thompson and Wallace, 1998]. It is also known as northern hemisphere "annular mode" (NAM), with Arctic Oscillation as the alternative name [Wallace, 2000]. The spatial pattern of AO highlights three major centers of action: in the Arctic basin and in the North Atlantic and Pacific mid-latitudes with opposite signs. AO index is associated with anti-correlation of zonal wind in both basins between 35 °N and 55 °N, where positive AO suggests a strengthening of subpolar jet in North Atlantic, but a weakening in the North Pacific. The impact of AO is similar to that of NAO, and both time series are highly

correlated. However, NAO is a more regionally-specific index in the North Atlantic while AO could not be fully identified in the North Atlantic sector. AO is less dominant than NAO in the North Atlantic whilst its impact extends to both Atlantic and Pacific basins [Ambaum *et al.*, 2001].

The most noticeable feature in the spatial pattern of the third EOF mode in winter SST (Figure 2.15a) was the contrast between the Gulf Stream area and the remainder of the subpolar North Atlantic. The Gulf Stream area was the only region that showed negative values, ~-0.2. Within the positive value regions, southern North Sea had the highest positive center, about 0.5, while most of the positive values were around 0.2. The associated time series (Figure 2.15b) was weakly correlated to AO (r_{winter}=0.25, p_{winter}<0.05) at 95% significance level. The summer EOF3 (Figure 2.15c) had a different pattern compared to winter EOF3, with a negative band separating the positive areas in the southwestern and eastern subpolar. Negative band values were about -0.2, while the two positive value regions were ~0.3. Similar to winter EOF3 time series, the time series associated with summer EOF3 (Figure 2.15d) was also weakly correlated to AO index (r_{summer}=0.26, p_{summer}<0.01) at 99% significance level. The third EOF mode explains 14% and 12% of total winter variation and total summer variation, respectively.

Though Winter EOF3 is weakly correlated to winter AO index, the spatial does not show typical AO pattern and the 9-year running mean of associated time series does not correlate to the low-pass AO time series, suggesting the weak correlation is only valid on the inter-annual scale. Considering EOF3 is not significantly separated from EOF2, it confirms that NAO is more dominant in the North Atlantic than AO, and it is difficult to fully identify AO in one of the action centers. The time series of summer EOF3 is correlated to AO time series on both inter-annual and longer-term scales (r=0.28, p=0.004 for 9-year running mean); its spatial pattern resembles typical AO pattern better than in winter, possibly relating to reduced NAO impact in summer. However, such signal is weak and AO variability and associated changes in wind strength play a minor role in modulating summer SST.

Winter EOF4 (Figure 2.16a) values were negative along the western subpolar North Atlantic, in the Irminger Basin and northern Iceland Basin. In the southwestern subpolar

near the Gulf of Maine the negative area was separated by a small positive patch just south to Newfoundland Shelf. Central southern subpolar region and the eastern shelf area were occupied by positive values centered around 45 ºN, 30 ºW. The associated time series (Figure 2.16b) was correlated to winter Eastern Atlantic Pattern (EAP) index during the period of 1950 – 2009 (r_{winter}=-0.39, p_{winter}<0.01) when EAP index is available. Monthly EAP index used in this study was downloaded from the website of Climate Prediction Center, NOAA (http://www.cpc.ncep.noaa.gov/data/teledoc/ea.shtml). EAP is defined as the second prominent mode of low-frequency variability in the North Atlantic. It is a significant mode in all months and usually displays a south-north dipole with its center southeast to that of NAO [Barnston and Livezey, 1987]. EAP variation mainly influences surface temperature and precipitation in the eastern North Atlantic and Europe. During years of high EAP, surface temperature and precipitation are usually above average, and vice versa. This pattern also displayed a steady increase during the period 1950 – 2004. Winter EOF4 spatial pattern in Figure 2.16a agrees well with that shown in Cannaby and Husrevoglu (2009) for the region north of 40 ºN.

The spatial pattern in summer EOF4 (Figure 2.16c) did not show a clear EAP pattern, though the corresponding time series (Figure 2.16d) was still negatively correlated to EAP summer index (r_{summer}=-0.35, p_{summer}<0.01). The negative area occupied at the western subpolar boundary in winter expanded to a larger area, covering the whole western subpolar basin west of 36 ºW. To the east of 36 ºW, positive values occupied the region south of 60 ºN. The driving mechanisms of EAP have not been intensively investigated, and are typically understood as a southeast shift of NAO, and thus suggest an atmosphere-ocean teleconnection.

Comparing the first four leading EOFs in winter and summer, it is clear that the first two modes are the dominant modes in both seasons and, combined, explain about 50% of total variance in each respective season. AMO signal is strong in winter, yet NAO influence is almost equally strong, especially in the action centers. In summer, AMO is even clearer and stronger than in winter, while NAO plays a minor role in adjusting summer SST variation. Differences of seasonal SST variation explained by major EOF signals is summarized as: 1) varying importance of AMO and NAO in each season; 2) variation of AMO and NAO strength on seasonal and inter-annual scale; 3) changes of

oceanic responses and action centers of AMO and NAO between two seasons; and 4) AMO reflects mechanisms modulating SST variability on multi-decadal scale, while NAO is typically influential on shorter inter-annual to decadal scales. Differences between shelf seas and open ocean are mainly shown by the reversal of the AMO signal in winter in the eastern subpolar North Atlantic.

The last two modes combined explain about 25% of total seasonal SST variance and play a minor role compared to the first two modes. Differences between the two seasons induced by these two modes are more complicated since the spatial patterns and associated time series were more different between one another. These two modes were weakly correlated to climate indices, especially to AO. Winter EOF2 and EOF3 were not significantly different from one another, suggesting these modes might have a similar driving force, though NAO and AO are known to be highly correlated. The exact interpretation of these two modes and their impact on SST variation, and the interpretation of NAO and AO, were not the focus of this study and thus are not examined in details here.

2.5   Summarising Discussion and Conclusion

The SST annual cycle has been assumed unchanged through time and were removed from datasets in many previous studies [Wallace, 2003; Cannaby and Husrevoglu, 2009]. Results presented in this chapter indicate that the amplitude of SST annual cycle, which is presented as ACA and calculated as the difference between the maximum and minimum SSTs of a year, actually varies on the decadal to multi-decadal scales. In addition, this variability is not consistent across the whole subpolar basin, with shelf regions highlighting a peak in ACA during the mid-20th century, while the peak is absent in oceanic regions. An earlier study suggested that the contribution of annual cycle to the total variability of SST could be up to 80% in the high-latitude regions [Yashayaev and Zveryaev, 2001], thus the long-term variability of SST annual cycle would affect the total variation of SST and climate, both locally and globally. The mechanisms controlling the low-frequency variability of ACA may have changed through time as high-ACA periods were charactersied by colder than usual winter SST and warmer summer SST in early decades, but a stronger increase in summer SST than in winter SST in more recent decades.

After 1995, ACA and seasonal SST show an increased signal in all four groups of locations, though a small patch in the northwestern subpolar actually cooled in winter after 1995 compared to earlier decades. Cooling might be associated with extremely cold periods in the Labrador Sea from the late 1970s to 1990s. In the last 15 years of the time series, summer and winter anomalies suggest different changes to the SST annual cycle occurred at different parts of the basin.

EOF analysis selects major signals in seasonal SST variation. The most dominant signal is a multi-decadal pattern, which correlates well with seasonal AMO index. Though the mechanisms of AMO are still under debate, it is clear that the signal describes the evolution of seasons over the last 140 years, especially in summer. The second EOF modes, in both winter and summer, are well correlated to seasonal NAO index, suggesting the importance of atmospheric forcing in the subpolar North Atlantic. However the major action area in winter is in the interior subpolar while in summer the main action area shifts towards the northeast, with the negative center following and occupying the southwestern subpolar region. The second EOF takes a much more important role in winter than in summer. While summer SST mainly shows AMO index and displays a multi-decadal variability, winter SST is also adjusted by NAO variation, especially in the major action areas. The differences in the importance of major factors in each season, the variation of these factors seasonally and inter-annually and location of the action centers in AMO and NAO, all work to result in different seasonal SST evolution and thus ACA.

In the eastern shelf region, for instance, upon the adjustment of AMO, summer SST was at its peak in the 1940s and winter SST was at its lowest level (negative value suggest opposite sign). NAO index was also in weak positive phase, leading to strong westerly winds and thus colder than average winter SST. The two factors resulted in a peak ACA in the 1940s in eastern shelf locations. From the 1990s, correlation between summer EOF2 and NAO was not as high as earlier decades, and further eliminates the influence of NAO on summer SST in recent decades.

The climatic indices considered in this study were hose known to have close relationship with North Atlantic SST and are only their most direct influence on SST were discussed, e.g. NAO affect SST through affecting the strength of westerlies,

however, these climatic indices may involve in more indirect processes that also changes SST annual cycle on the decadal and longer time scales. For example, there is evidence that NAO has lagged impact on heat flux, precipitation and evaporation in the North Atlantic [Kwon and Frankignoul, 2012]. Variability in other ocean basins, such as north Pacific, may also influence the physical processes in the North Atlantic through inter-basin teleconnection [Cessi and Otheguy, 2003]. All these possibilities can provide further knowledge on the mechanisms controlling the long-term variability of SST annual cycle.

Phytoplankton and higher trophic species respond to SST changes both directly through the relation of photosynthesis and respiration rate and through responding to other SST related parameters. In the subpolar North Atlantic, MLD is an additional important physical parameter for determining nutrient availability for phytoplankton growth, and is related to SST and the timing of re-stratification. Though the actual links between SST and phytoplankton abundance are complex and not consistent in the whole subpolar basin [Longhurst, 2007], the variation of SST annual cycle could imply potential changes to phytoplankton blooms through its impact on the nutrient cycle and light accessibility. The actual mechanisms and evidence are to be discussed in later chapters.

Table 2.1 Location Names Corresponding to the Numbers in Figure 2.1 and equivalent Standard Area

Number/SA	Location	Number/SA	Location	Number/SA	Location
1/B1	NE continental NS[1]	9/D3	Celtic Sea	17/F10	Gulf of Maine
2/B2	Northwestern NS	10/B4	Iceland-Fraoe Ridge	18/B7	Irminger Basin
3/C1	Central eastern NS	11/B5	Northeast Iceland Basin	19/B8	Eastern Labrador Sea
4/C2	Central western NS	12/C5	Rockall Plateau	20/C7	West Reykjanes Ridge
5/D1	Southeastern NS	13/D5	Southern Rockall Trough	21/C8	Labrador Sea
6/D2	Southern NS	14/None	Gulf of St Lawrence	22/D7	South Reykjanes Ridge
7/C3	Irish Sea	15/E9	Newfoundland Shelf	23/D8	Southern Labrador Sea
8/C4	Stanton Bank	16/E10	Scotian Shelf	24/D9	Labrador Shelf

[1] NS stands for North Sea
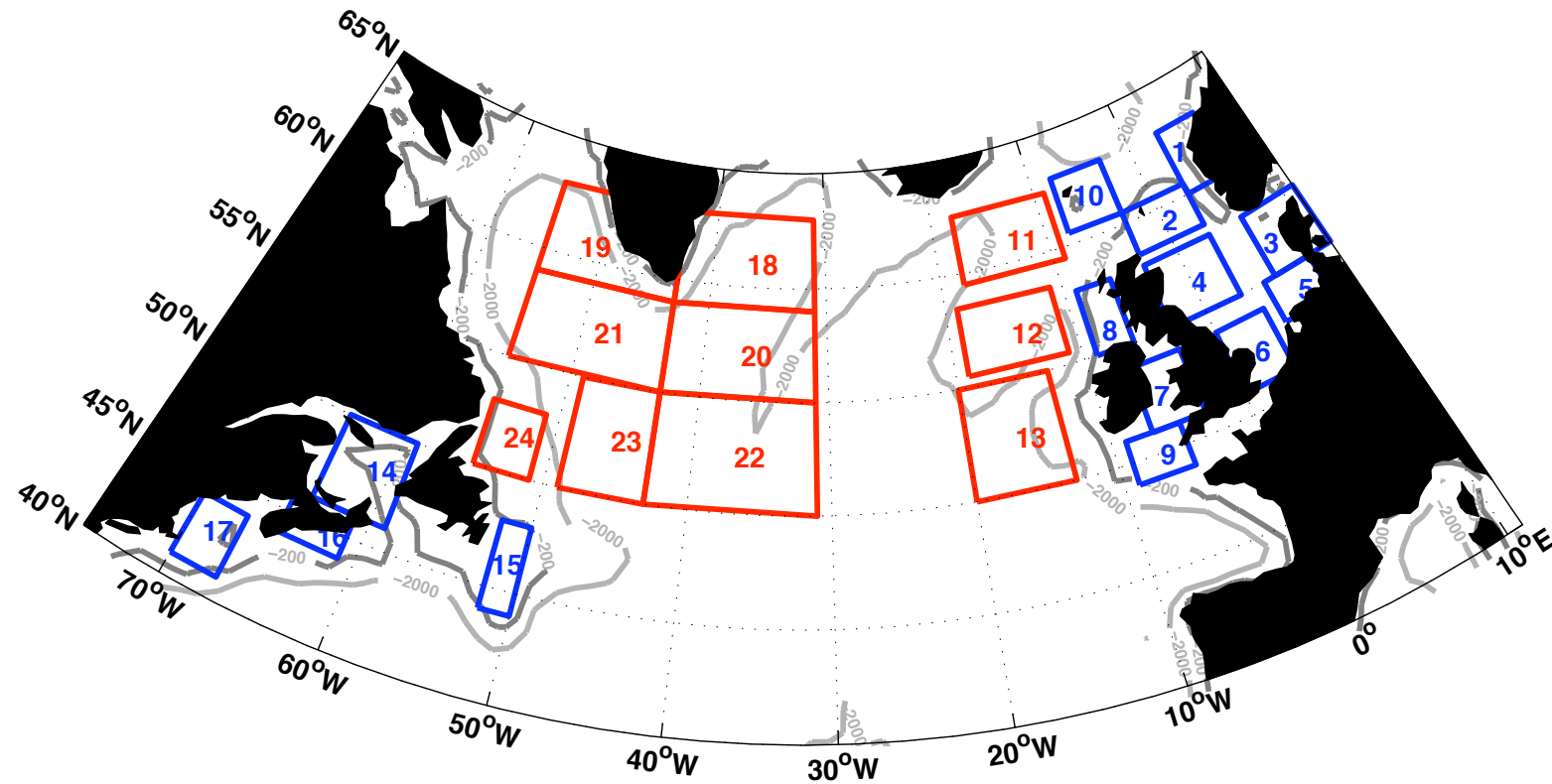
Figure 2.1 The subpolar North Atlantic, dark grey line shows 200m contour and light grey line shows 2000m contour. Shelf regions are shown in blue boxes and open ocean locations are in red boxes for both eastern and western subpolar basin. The names of the locations are listed in Table 2.1 with corresponding numbers.
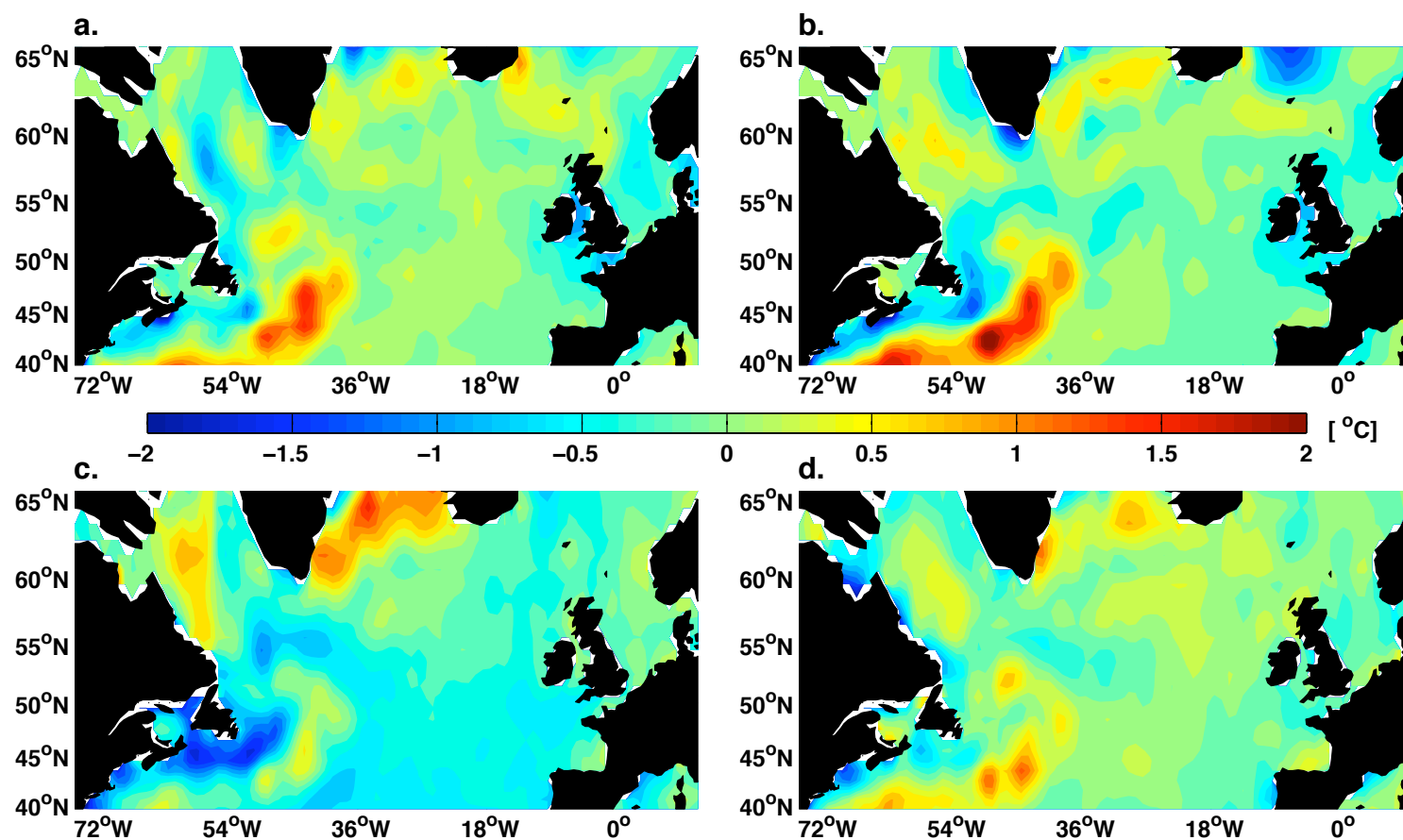
Figure 2.2 The sea surface temperature (SST) climatology (1982 - 2009) differences (OISST v. 2 minus HadISST1) in (a) January, (b) April, (c) July and (d) October.
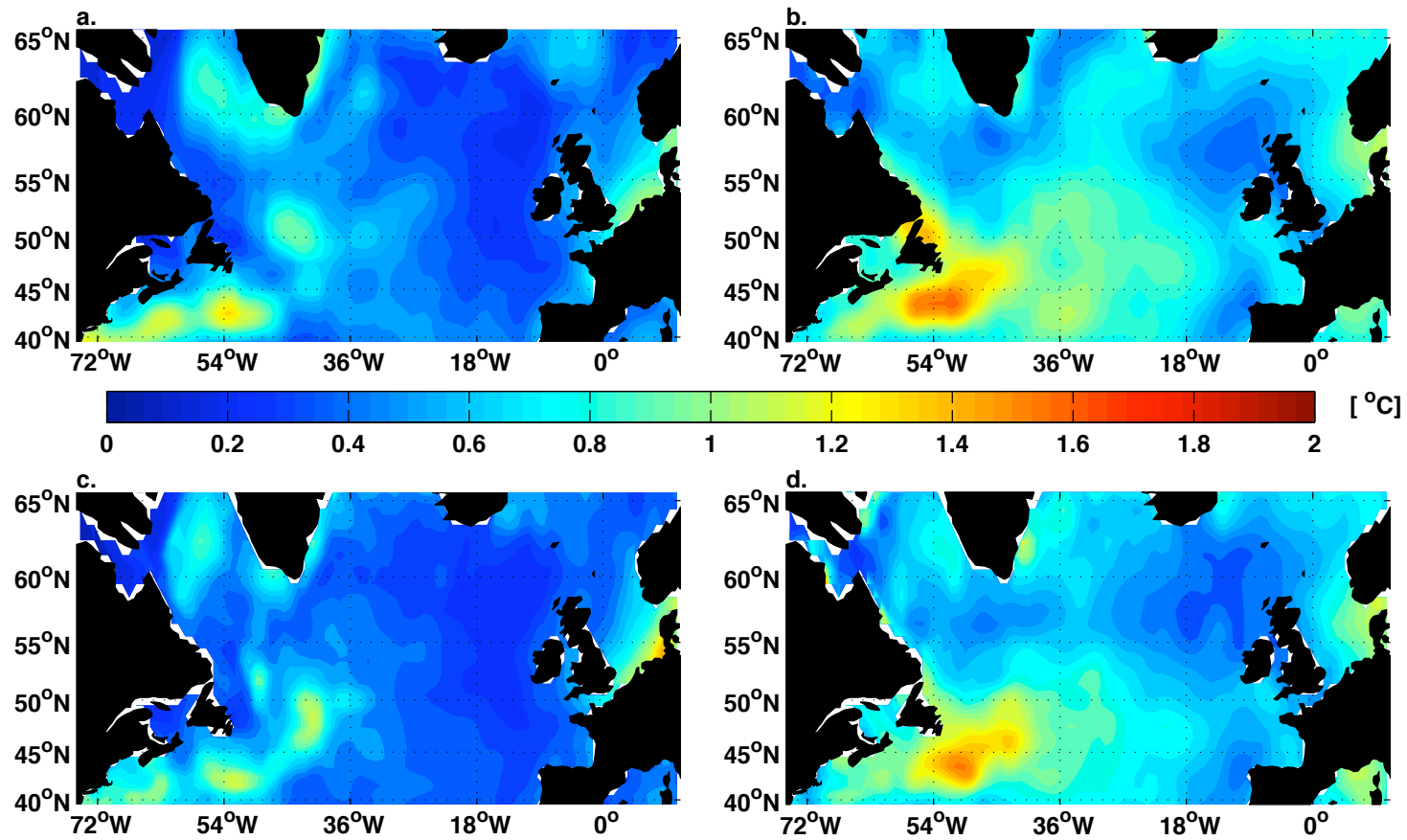
Figure 2.3 SST standard deviation, 1982 – 2009 in: (a-b) OISST v. 2; and (c-d) HadISST1 (left panels: January and right panels: July).
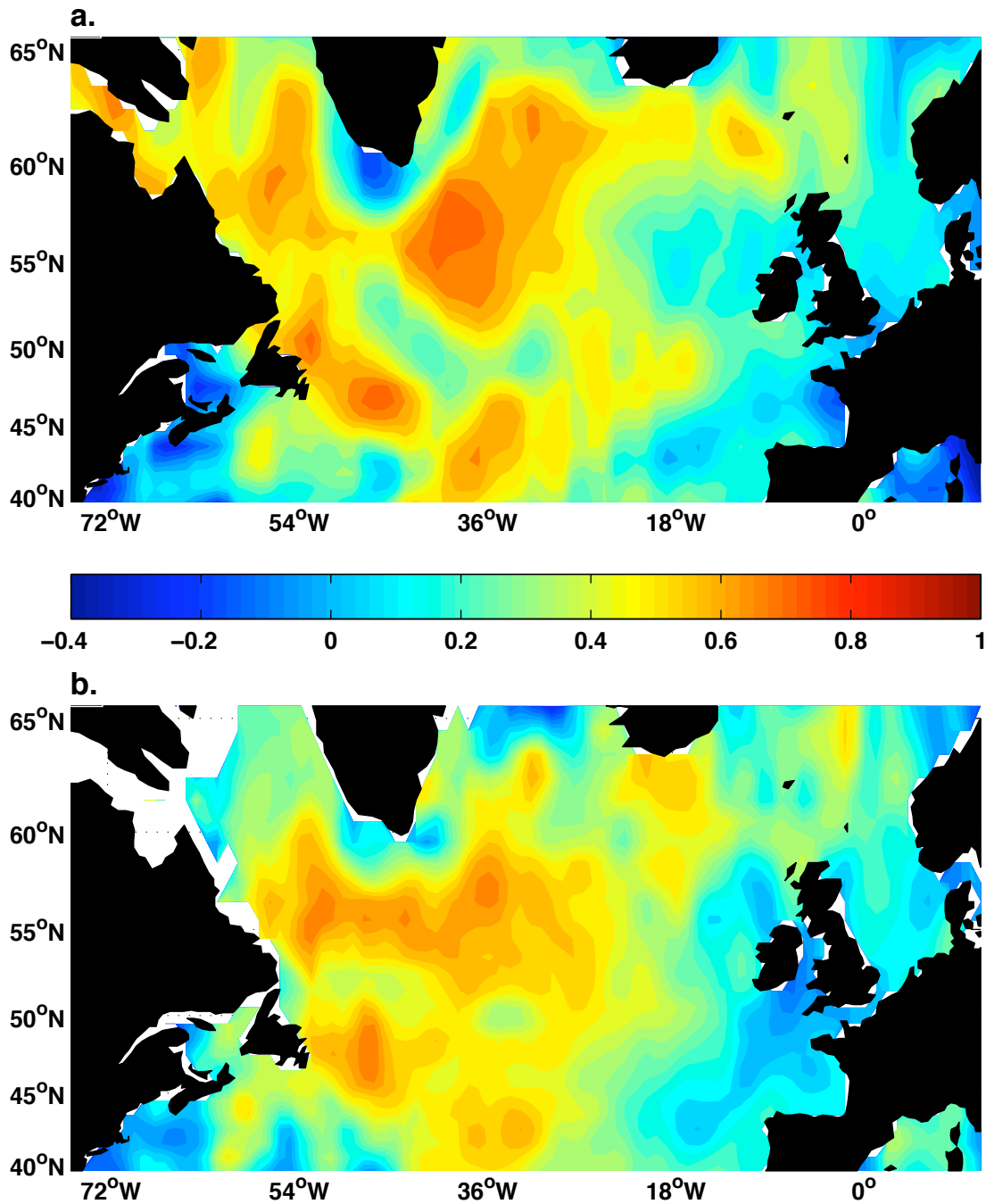
Figure 2.4 One-month lag autocorrelation of detrended monthly sea surface temperature anomalies in each 1 ° area grid box of the period 1982 – 2009, for (a) OISST v. 2 and (b) HadISST1.
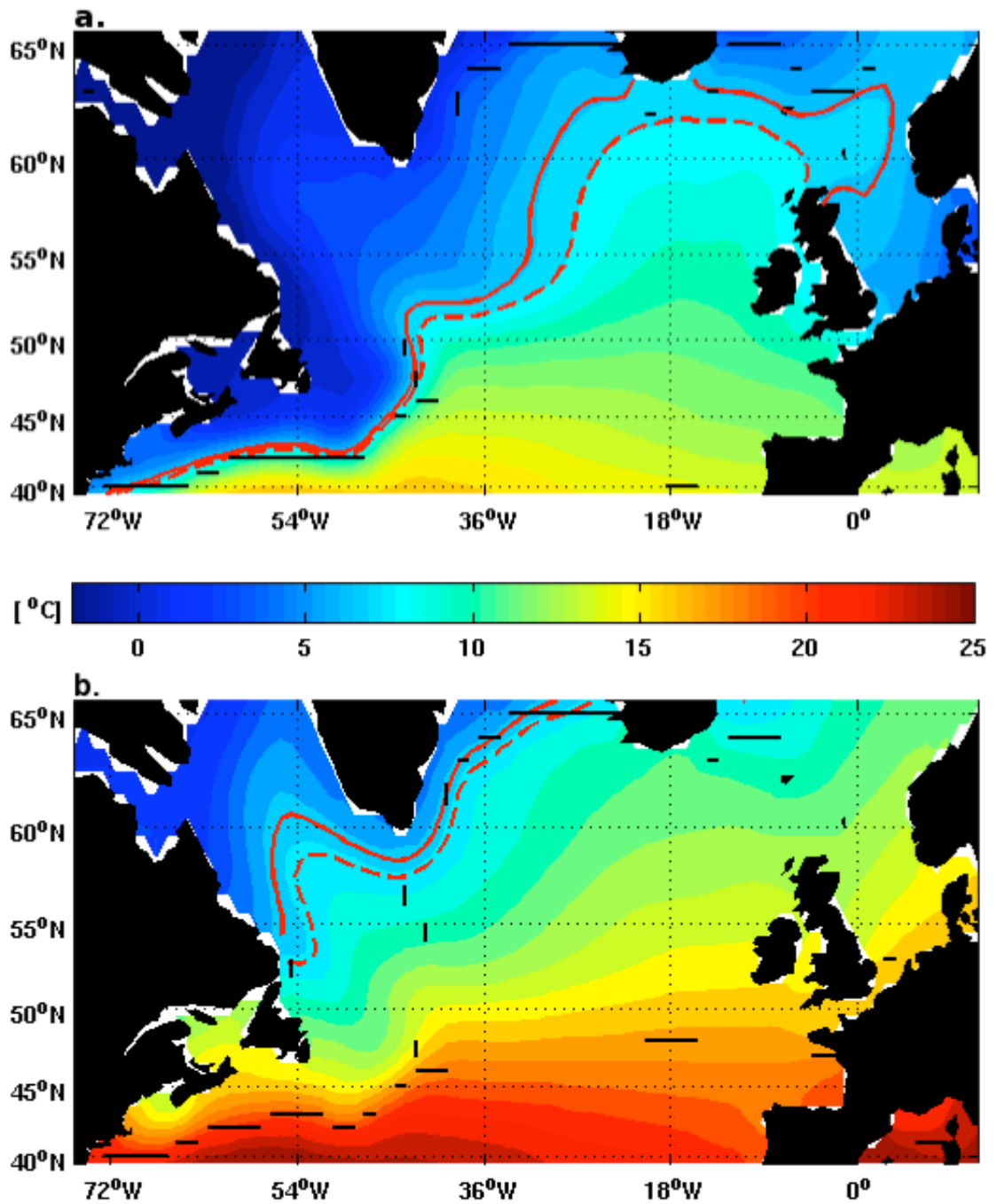
Figure 2.5 The climatology of (a) winter and (b) summer SSTs in subpolar North Atlantic. Solid red lines show the position of 7 °C contour and dashed red lines show the position of 8 °C contour. Solid black lines indicate the position of strongest SST gradient of each latitude determined by the change of temperature per latitude.
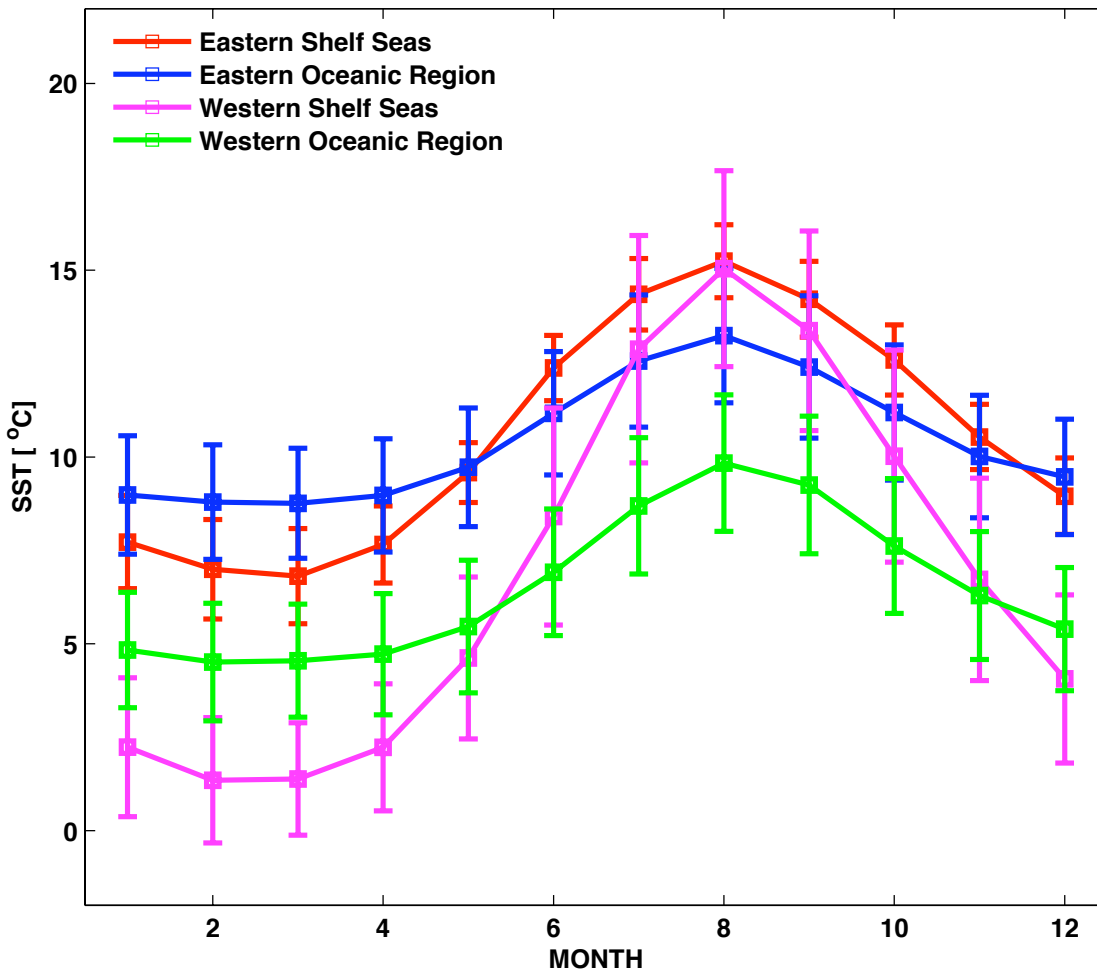
Figure 2.6 The mean annual cycle in four groups of locations: eastern shelf seas (red) that shown as blue boxes in the eastern basin in Figure 2.1, eastern oceanic regions (blue) that shown as the red boxes in the eastern basin in Figure 2.1, western shelf seas (magenta) that shown as the blue boxes in the western basin in Figure 2.1 and western oceanic region (green) that shown as the red boxes in the western basin in Figure 2.1. The error bars denote the standard deviation of each month over 140 years.
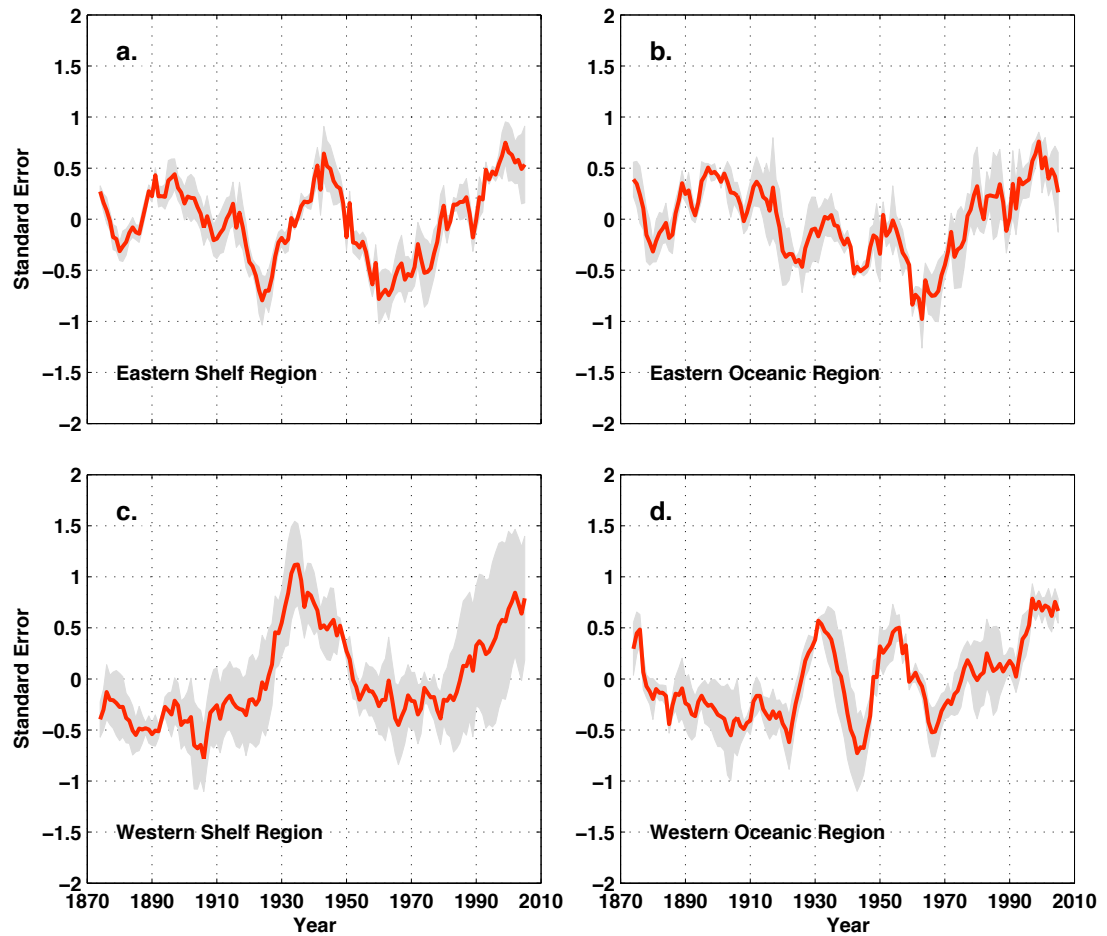
Figure 2.7 The average ACA (Annual Cycle Amplitude) of the four groups: (a) eastern shelf region, (b) eastern oceanic region, (c) western shelf region and (d) western oceanic region. Red lines are the average of 9-year running mean of standardised seasonality in each group and grey shadings highlight the area with 95% of the variation of seasonality of the groups.
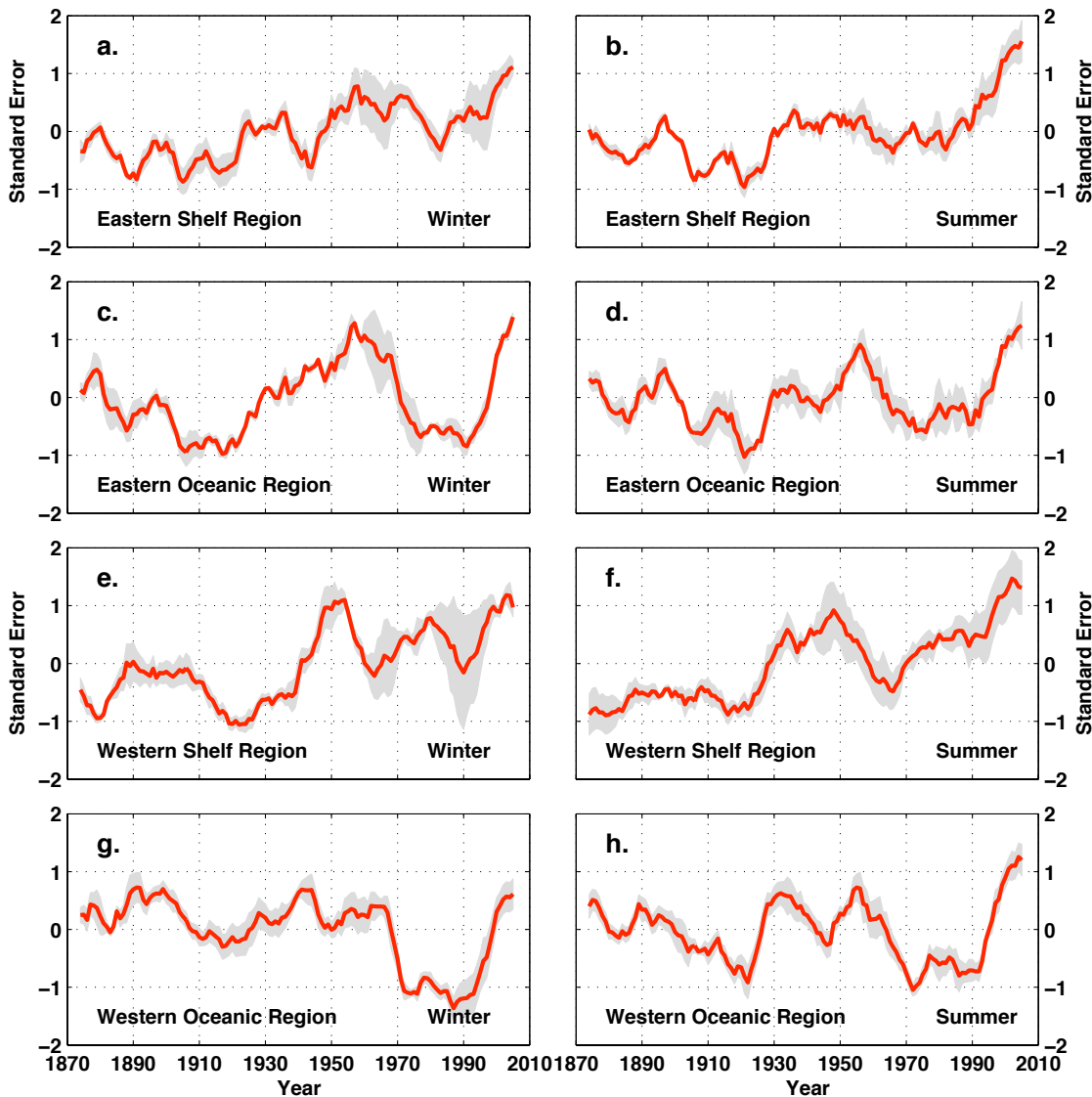
Figure 2.8 The evolution of winter (left panels) and summer (right panels) in four types of regions: (a-b) eastern shelf region, (c-d) eastern oceanic region, (e-f) western shelf region and (g-h) western oceanic region. Red lines show the 9-year running mean of mean season evolution of this region and grey shadows highlight the 95% confidence intervals of the standard error of the mean (SEM) in each grouped region.
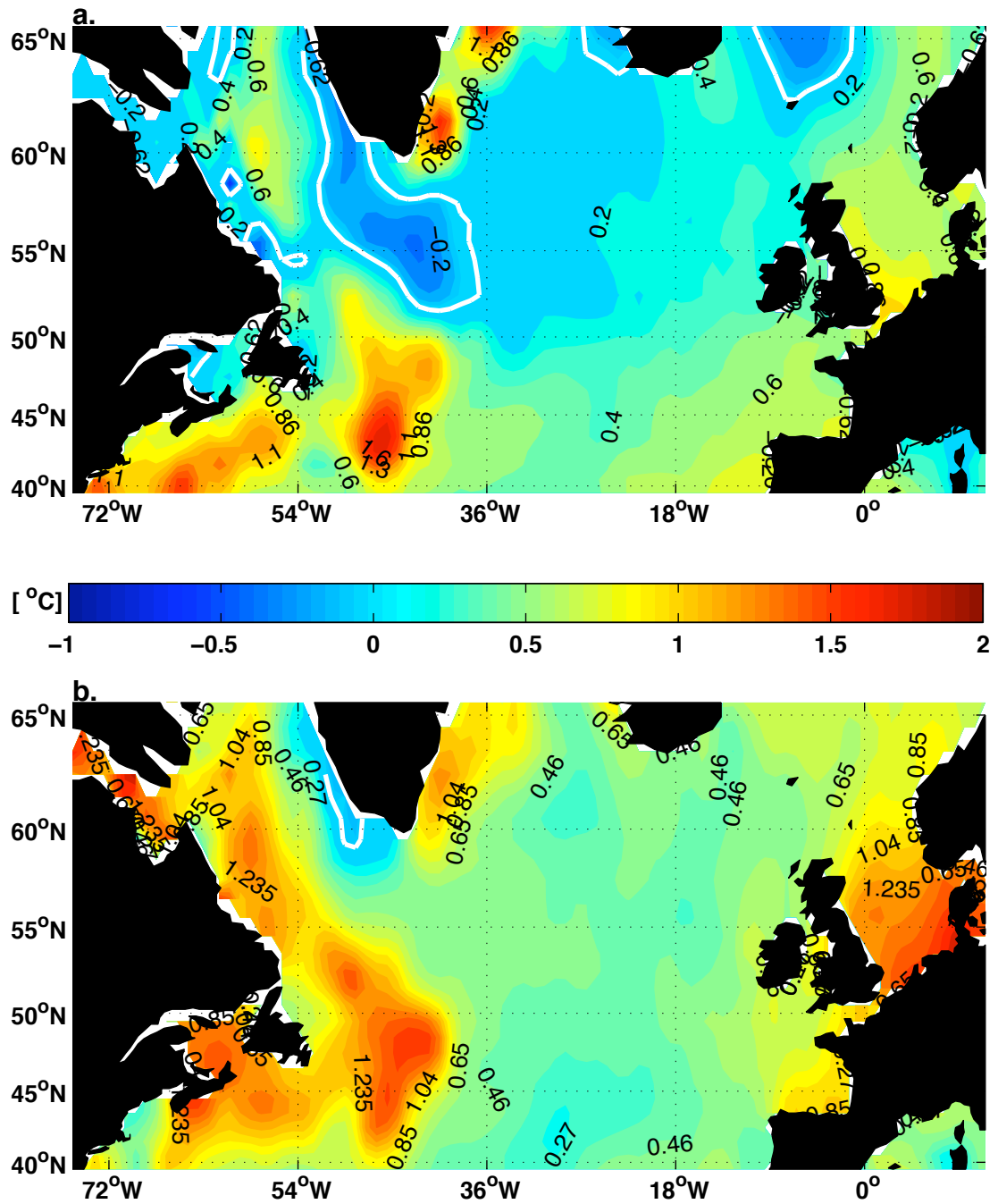
Figure 2.9 SST anomalies in (a) winter and (b) summer North Atlantic between the period 1880 – 1994 and the period 1995 – 2009. White contours indicate zero anomalies. Negative values mean that SST is lower in the later period than in earlier period and positive values mean that SST is higher in the later period than in earlier period.
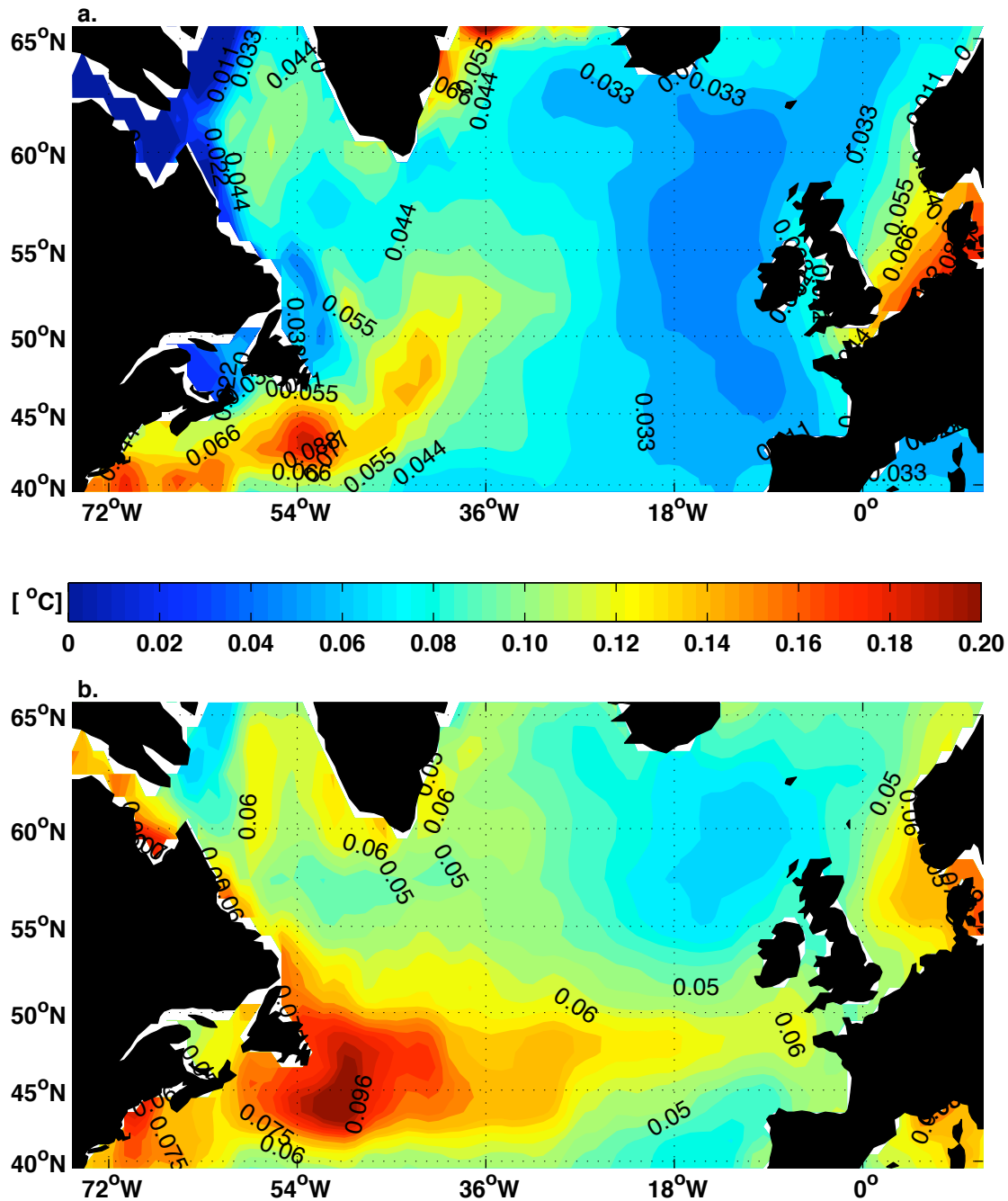
Figure 2.10 The standard error of the mean (SEM) of SST anomalies in (a) winter and (b) summer North Atlantic between the period 1870 – 1994 and the period 1995 – 2009. The values show the threshold of 95% confidence interval.
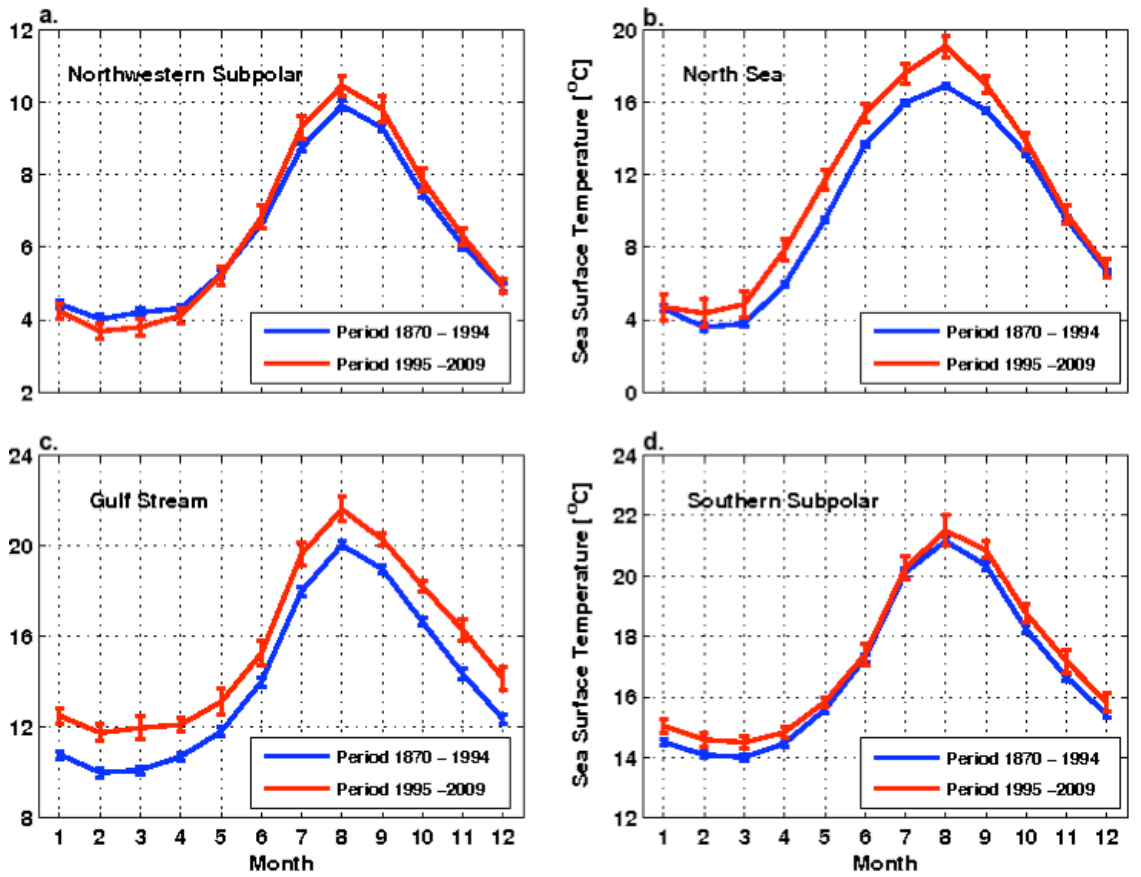
Figure 2.11 Annual cycles in the period 1870 – 1994 (blue lines with error bar) and in the period 1995 – 2009 (red lines with error bar) in four representative locations: (a) northwestern subpolar, (b) North Sea, (c) Gulf Stream and (d) southern subpolar.
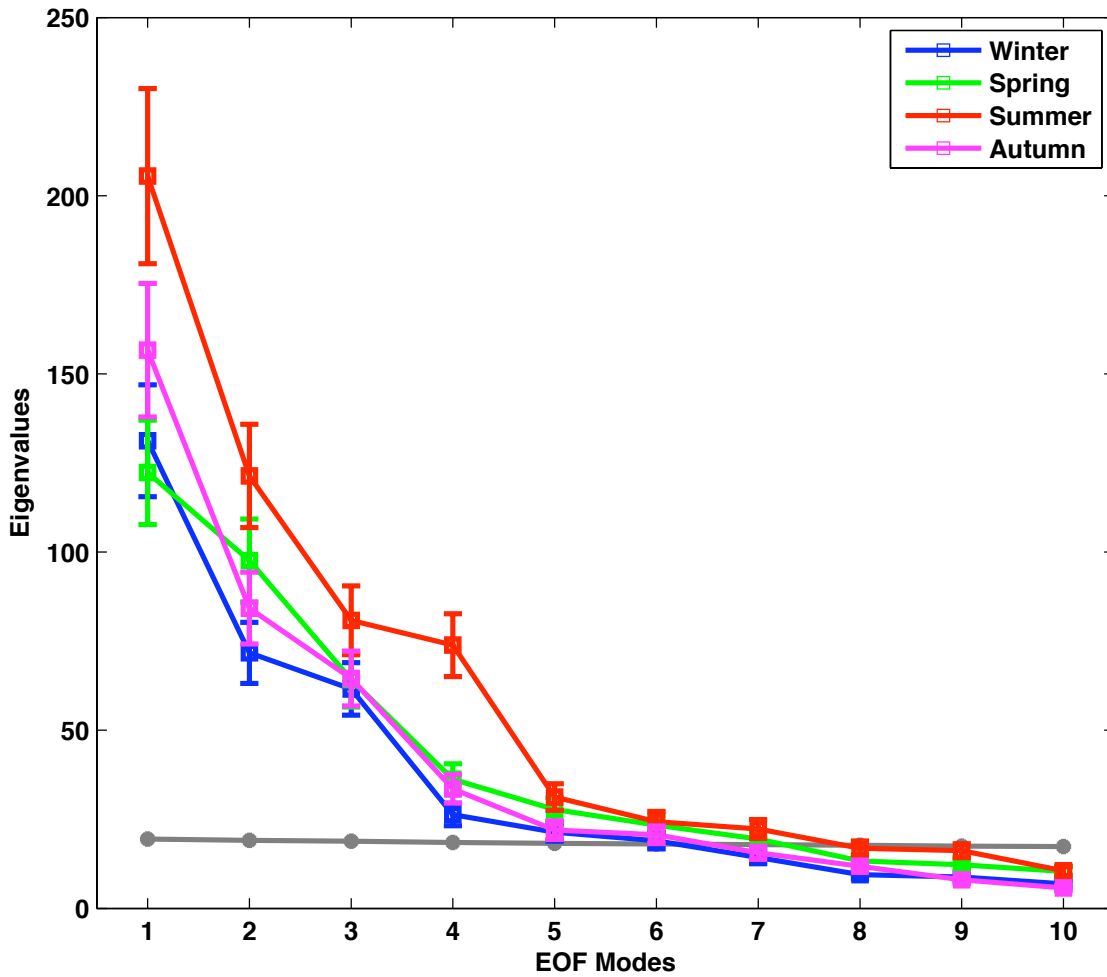
Figure 2.12 The eigenvalues of seasonal EOF analysis. The squares show the values of the eigenvalues and the error bars indicate the sample errors corresponding to each mode. The grey line indicates the threshold level set by the 99th set of eigenvalues from the 100 times of Monte Carlo test, when the resulted eigenvalues are organised in an ascending order. This level suggests 99% confidence interval.
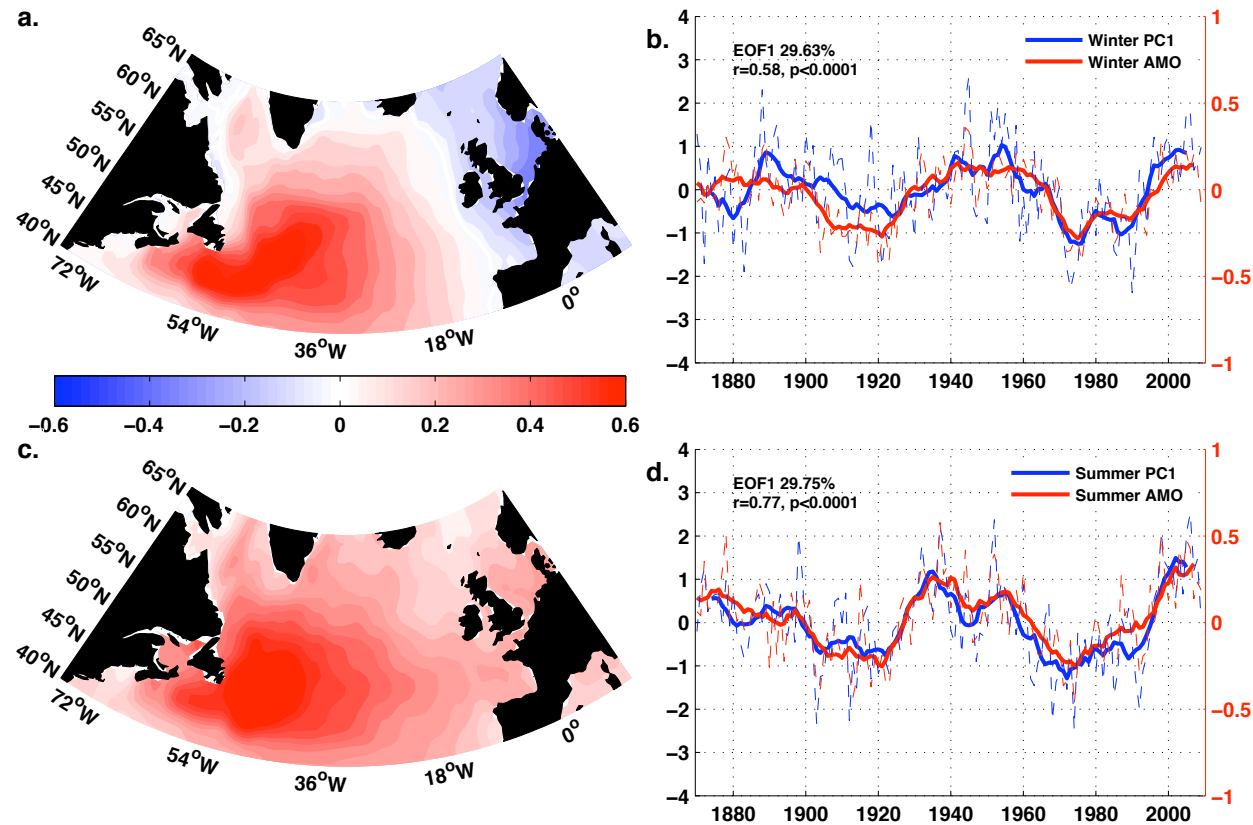
Figure 2.13 The first leading EOF mode spatial patterns (left panels) and associated time series (right panels) of (a-b) winter and (c-d) summer SST. Blue lines are the principal component corresponding to the spatial patterns and the red lines are seasonal averaged Atlantic Multi-decadal Oscillation (AMO) index. Dashed lines are the original time series and solid lines show 9-year running mean.
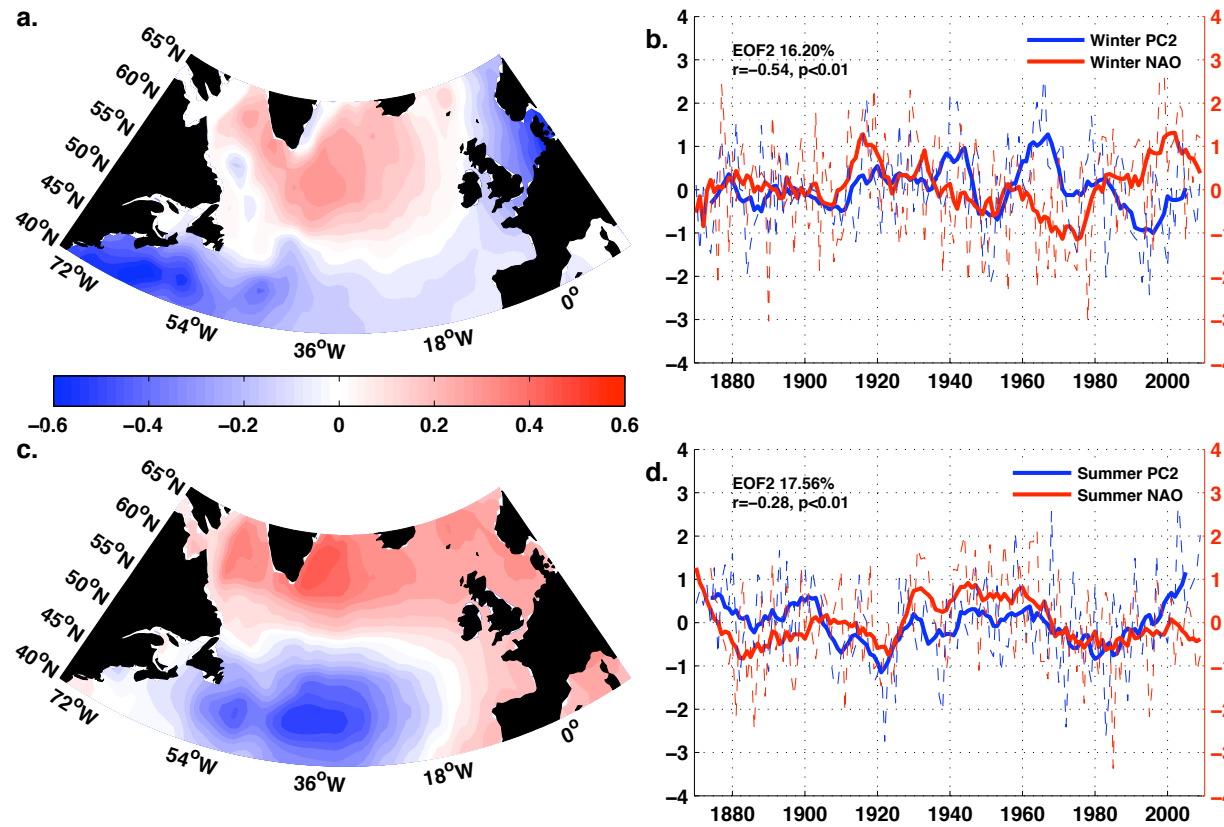
Figure 2.14 The second leading EOF mode spatial patterns (left panels) and associated time series (right panels) of (a-b) winter and (c-d) summer SST. Blue lines are the principal component corresponding to the spatial patterns and the red lines are seasonal averaged North Atlantic Oscillation (NAO) index. Dashed lines are the original time series and solid lines show 9-year running mean.
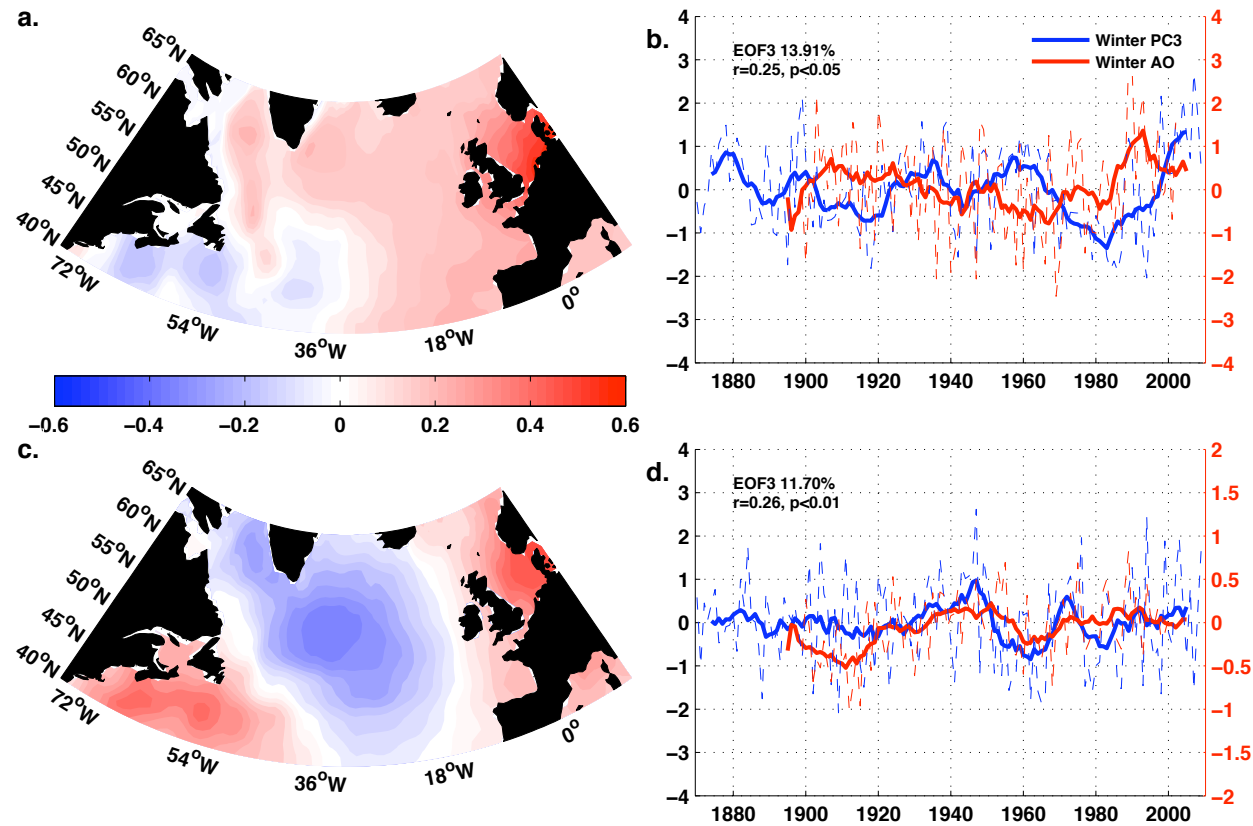
Figure 2.15 The third leading EOF mode spatial patterns (lef panels) and associated time series (right panels) of (a-b) winter and (c-d) summer SST. Blue lines are the principal component corresponding to the spatial patterns and the red lines are seasonal averaged Arctic Oscillation (AO) index. Dashed lines are the original time series and solid lines show 9-year running mean.
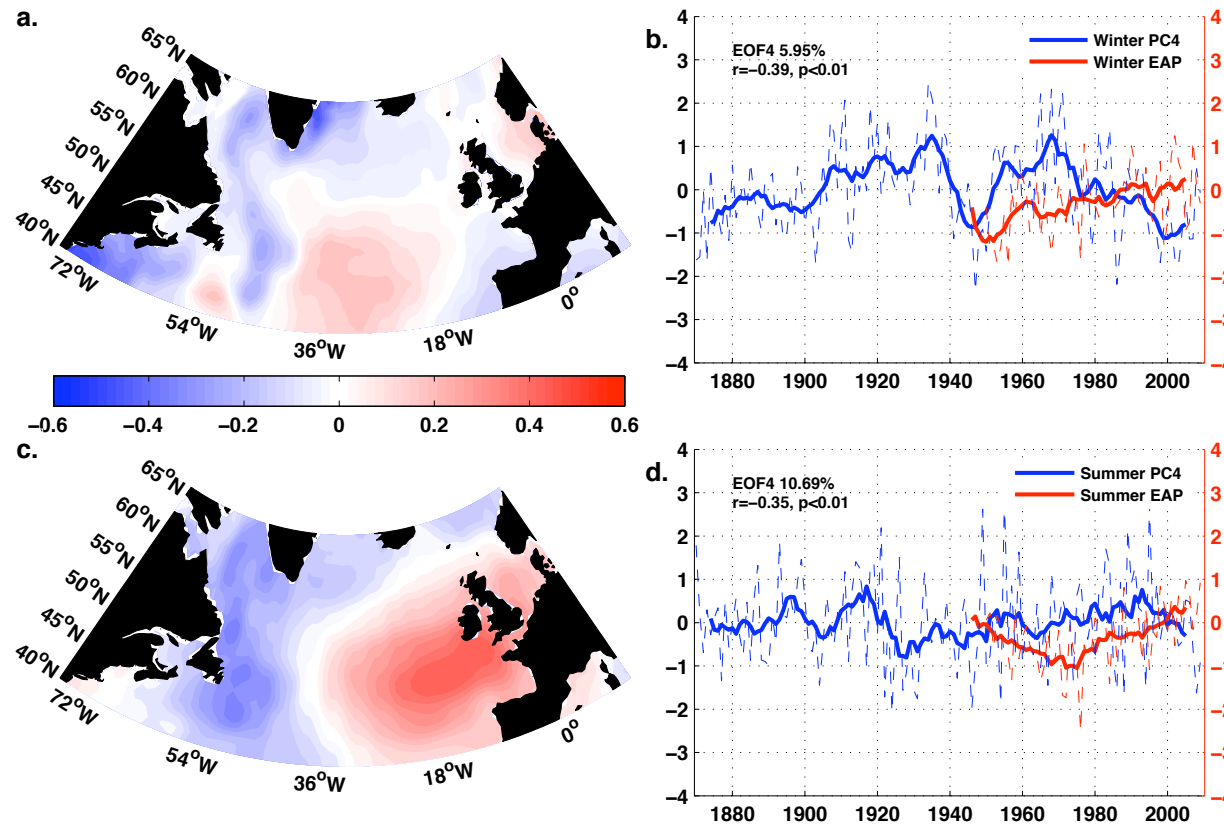
Figure 2.16 The fourth leading EOF mode spatial patterns (left panels) and associated time series (right panels) of (a-b) winter and (c-d) summer SST. Blue lines are the principal component corresponding to the spatial patterns and the red lines are seasonal averaged Eastern Atlantic Pattern (EAP) index. Dashed lines are the original time series and solid lines show 9-year running mean.

Chapter 3

Inter-annual to Decadal Variability of Phytoplankton

in the Subpolar North Atlantic

3.1   Introduction

In the subpolar North Atlantic, changes of phytoplankton abundance have been observed, potentially in response to a warming ocean [Reid *et al.*, 1998]. Since then, many studies have explored the possible explanations in variations of physical parameters [Beaugrand *et al.*, 2000; Edwards *et al.*, 2001; Barton *et al.*, 2003; Beaugrand, 2009; Henson *et al.*, 2009a; Martinez *et al.*, 2009]. The importance of sea surface temperature (SST) in influencing phytoplankton growth was emphasised in existing literature as rapid increase of SST coincides with the changes in phytoplankton abundance, though it might not be the increase of SST that directly drive the increase of phytoplankton growth. Therefore, after describing the variation of SST annual cycle in the previous chapter, observations of decadal phytoplankton variability are presented and the links between SST and phytoplankton are tested in this chapter.

In the marine ecosystem, increasing water temperature normally leads to increased phytoplankton metabolic rates and stronger stratification, which both lead to increased phytoplankton abundance. This positive response of phytoplankton growth to the increase of SST is seen in the northeast North Atlantic north of 50 ºN [Reid *et al.*, 1998; Edwards *et al.*, 2001; Richardson and Schoeman, 2004]. A stepwise increase of phytoplankton abundance and observation of temperate species in cold-water species habitat, the so-called "regime shift", were also reported in the North Sea during 1982—1988 when rapid SST increase was seen [Beaugrand, 2004]. However, for species that are operating on the threshold of their "thermal window", the temperature range within which species can survive, increased water temperature could lead to significant decline in abundance or geographical shift to cooler regions [Pörtner and Farrell, 2008]. Edwards and Richardson (2004) pointed out that the responses to ocean warming are not consistent within the phytoplankton community as some species (e.g. dinoflagellates) are more sensitive to changes in SST and prefer living in stratified conditions than others (e.g. diatoms [Margalef, 1978]). The bloom timing of these sensitive species might shift forward if the current warming continues and such shifts may affect organisms of higher trophic levels through the match-mismatch theory [Cushing, 1990].

In addition to this direct impact, SST also reflects other physical processes that modulate the variation of phytoplankton abundance, such as regional vertical stratification and nutrients distribution. In the parts of the northeast North Atlantic south of 50 º N, where water temperature is higher and water column is more stratified than the north, increase of SST is companied by decrease of phytoplankton due to a further reduction of nutrients associated with strengthened stratification [Richardson and Schoeman, 2004].

It is clear that the impact of SST variation on phytoplankton growth involves complex processes and phytoplankton responses are not consistent on the basin scale. Though a few possibilities have been proposed in previous studies, the exact process of SST modulating phytoplankton growth in the subpolar North Atlantic is still unclear. In Chapter 2, variation of SST annual cycle was discussed in oceanic regions and shelf seas on both sides of the North Atlantic subpolar basin. It would thus be useful to examine whether phytoplankton also varies differently in different groups of locations and if these variability and differences could be explained by the observed SST variation. CPR observation is introduced and used in this study and, with a longer time series compared to the existing literature, more recent changes to phytoplankton abundance can thus be examined.

This chapter is delivered as follows: a detailed introduction to the background and sampling process of CPR observation is presented in section 3.2; observed variability is shown in section 3.3, which includes discussion of the links between SST and phytoplankton. The last section, 3.4, summarises and discuses the major results presented in previous sections.

3.2   Continuous Plankton Recorder

3.2.1   Introduction

The continuous plankton recorder (CPR) survey is a globally-unique plankton-monitoring programme featuring its multi-decadal time span with monthly data available from 1946. The earliest CPR survey was carried out by Sir Alister Hardy in 1931, using a recorder not much different from the ones used in the present day. Historical CPR data from 1931 to 1938 are only currently available in paper form. In the

last 60 years, the sampling methodology has changed little so as to ensure the consistency of the time series. Originally, the CPR survey only sampled in the North Atlantic and the North Sea, but since 1997 sampling has also taken place in the North Pacific. By the end of 2011, sampling was available in almost every ocean basin except the Indian Ocean and a total of 5,961,198 nautical miles have been towed since 1931. By 2011, 245,000 total samples had been analysed and this number is increasing year after year with the extended sampling areas [Edwards *et al.*, 2012].

CPR surveys are carried out by towing the recorder (Figure 3.1) behind commercial ships. Water containing plankton flows through the machine body while the ship proceeds. The machine contains two layers of silk with mesh-size of 270 μm. The filtering silk lies across the tunnel where water flows through (shown in green in Figure 3.1), with the rear impeller moved by the flowing water. This silk is continuously rolled back to the storage space. During the rolling process, the filtering silk meets a second layer of silk, the cover silk (shown in red in Figure 3.1), and the two pieces of silk trap material in between [Richardson *et al.*, 2006].

The commercial ships are ships of opportunity and the routes are changeable. The northeast North Atlantic and the North Sea are well covered with frequent commercial cruises whereas in the northwest Atlantic data coverage is much poorer. In spite of the heavy dependence on ship routes, CPR survey still provides a good opportunity to track the variation of plankton as biomass indicator with its unique long-term continuity.

3.2.2   Sample Processing

When the recorders are returned to the laboratory, the filtering silks are removed from the internal machine and unwound. Typically, a 500 nautical mile tow would use about 5m of silk. These silks are divided into samples each corresponding to 10 nautical miles of tow. With each of the silk samples, four stages are carried out and each stage focuses on one aspect of plankton. The first stage defines the overall phytoplankton, also called phytoplankton colour index (PCI), and this index is used in this study (the actual procedure and description of PCI will be introduced later). The second stage aims to separate large phytoplankton cells. After estimating overall phytoplankton abundance and the abundance of identified species, zooplankton measurement is done by analysing filtering and covering silk. Zooplankton abundance smaller than 2mm total length is

estimated through silk traverse and bigger zooplankton are counted individually for each species. CPR survey on zooplankton is not the main focus of this study, thus the detailed procedure is not introduced here.

PCI is a greenness level visually assigned to each of the samples by comparison with standard colour charts: no colour, very pale green, pale green and green. This index indicates the amount of phytoplankton pigment on the silk. In many studies, PCI has been used as a general indicator of phytoplankton abundance in the ocean (e. g. [Reid *et al.*, 1998]). The four levels are then converted to numerical values (from 0 to 6.5) on a ratio scale based on acetone extracts using spectrophotometric methods [Richardson *et al.*, 2006]. After PCI values are given, 10 fields on each of the diagonals of the filtering silk are counted under microscopes. These 20 fields represent 1/10000 of the area of the silks [Reid *et al.*, 2003]. This count gives an estimate of taxa present for each species on a grid square of the mesh, but does not provide total number of individuals of each species. For each sample, the phytoplankton species are assigned a value between 0 and 20 based on the number of a particular species, these numbers are then multiplied by 10,000 to give the total estimate of phytoplankton abundance on the silks [Richardson *et al.*, 2006].

Phytoplankton cell sizes vary from 2 μm to 2000 μm, so cells smaller than 270 μm (silk mesh-size) might flow through the silk and are not captured by CPR, especially during the period of year when phytoplankton abundance is low in the ocean. Thus CPR measurement is perhaps more accurate for large diatom cells and those phytoplankton that form chains. In the subpolar North Atlantic, where diatom and dinoflagellate dominate, CPR observation could miss small phytoplankton cells, but it provides a good overall estimate of phytoplankton abundance. Phytoplankton data are averaged for each month over large rectangle areas called Standard Areas (Figure 3.2, [Gieskes *et al.*, 2007]) which were first introduced by Colebrook in 1963 to study phytoplankton seasonal and inter-annual variability. In this study, selected standard areas at both sides of the subpolar basin and shelf seas are used to examine phytoplankton variation and possible links to observed physical processes.

3.2.3   Data Pre-analysis

The CPR survey heavily depends on the frequency of cruises and the routes these ships of opportunity take and the typical sampling frequency is once a month [Richardson *et al.*, 2006]. In a particular standard area, there are missing values if no CPR tows were carried out in this area due to changing cruise route or rough sea conditions. Thus, these missing values are first filled using an estimate with available data before examining phytoplankton variation using monthly PCI data. The estimate of PCI missing monthly mean follows the method suggested in Richardson *et al.* (2006):

$$PCI_{estimate} = \overline{M} \times \frac{Y}{\overline{Y}},$$

<div align="right">Eq. 3.1</div>

where $\overline{M}$ is the long-term mean of the estimated month, Y is the annual mean of that particular year and $\overline{Y}$ is the long-term annual mean. In the years with missing values, at least eight months of that particular year need to be sampled to produce a robust estimate otherwise, the missing values in that particular year would be left blank. PCI data with filled missing values were used to analyse phytoplankton abundance variation and will be presented in the following section.

3.3   Observed Variability

In Chapter 2, 24 locations (here after called the SST locations) in the subpolar North Atlantic were chosen to examine the long-term variability in SST annual cycle and are shown in Figure 2.1. To keep consistency, 22 standard areas (where PCI were available) equivalent to those SST locations were selected to study phytoplankton variation in the subpolar basin. The CPR standard area didn't include the Gulf of St. Lawrence and PCI was not available for the Iceland-Faroe Ridge area, so only 22 locations have corresponding SST and PCI data. The numbers of these chosen areas are listed in Figure 3.2 and the names of the 22 areas are shown in Table 3.1.

3.3.1   Greenness Index

The PCI time series shown in pale to dark green colours, often referred to as greenness, is a direct way to visualise the abundance of phytoplankton and has been used to show

decadal variation of phytoplankton in the northeast North Atlantic [Reid *et al.*, 1998; Edwards *et al.*, 2001]. In this study, similar colour plots with longer time series are reproduced using monthly averaged PCI in five locations (two locations from eastern shelf seas), representing the four geographical groups mentioned in Chapter 2, to examine phytoplankton variation at decadal scales on both sides of the subpolar basin. The southern North Sea is dominant by southern origin water and tides so the phytoplankton growth presents a different pattern compared to the northern parts where northern origin water and North Atlantic inflow dominant [Becker and Pauly, 1996]. Thus two locations in the North Sea were selected and presented in Figure 3.3. Considering the data availability at each location, the location with longest data coverage and showing representative bloom patterns in each group was chosen. The selected CPR standard areas do not match the SST locations exactly and all SST locations lay within the CPR standard areas but with rectangle shapes and omit the part on the edge of shelf and oceanic regions.

In the central eastern North Sea (Figure 3.3a), distinct spring and autumn blooms were found in the first few decades before the early 1970s. The spring bloom peaked in April and the second autumn bloom peaked in October. Typically, phytoplankton was observed from March to November, with a low phytoplankton period between two blooms during summer months. In the second half of the 1970s, both blooms were weakened and there were about five years when autumn blooms were absent. The decline of phytoplankton bloom in the mid-1970s has been associated with the decrease in temperature and salinity that appeared in the northeast North Atlantic around similar time. The reduced nutrient-rich North Atlantic advection allows the north-origin cold and low-density waters to penetrate further south and both processes decrease available nutrient for phytoplankton growth [Edwards *et al.*, 2001; Edwards *et al.*, 2002]. The autumn bloom was resumed in the late 1970s, though the spring bloom still remained low. From the mid-1980s, two blooms merged together, and phytoplankton abundance remained high through the summer months. The period when phytoplankton was observed was extended to all months and the intensification was stronger in autumn than in spring.

In the southeastern North Sea (Figure 3.3b), phytoplankton was observed from March to December each year from the beginning of the time series. No distinct spring and

autumn blooms were observed from the beginning of the time series as the decrease in phytoplankton abundance during summer was very brief. The phytoplankton concentrations in April and July are comparable. CPR observation was not available from 1977 till 1985, possibly due to changes of cruise routes. From the late 1980s, phytoplankton blooms intensified, especially during the summer months. The bloom season was also extended and phytoplankton was generally observed in this area all year round. The annual phytoplankton peak shifted toward later season (July—August) in the last two decades.

PCI data in the Rockall Plateau (Figure 3.3b) was only available from 1948 to 1994. Generally, distinct spring and autumn blooms were observed in May and September while the phytoplankton abundance was low in summer months. However, there were periods when the phytoplankton concentration remained relatively high after the spring bloom and the autumn phytoplankton abundance was not significantly higher than that in summer. Such continuous high summertime phytoplankton concentration was observed from 1954 to 1957, from 1966 to 1976 and after 1985. In this location, the timing and strength of the spring bloom stayed stable and the extension of the bloom season also remained relatively stable from late April to early October throughout the time series.

CPR observation was not continuous on the Newfoundland Shelf (Figure 3.3c). Monthly average PCI data was available from 1961 to 1973 and from 1992 to 2006. In the early period, phytoplankton peaked in April and phytoplankton was observed mainly from March to May. Only in three years was phytoplankton captured in the region in November, with low concentration. In the later period, phytoplankton was observed from January to June and from September to December. It is possible that phytoplankton started to accumulate in November/December and the bloom was initiated early the following year, which then peaked in April. Compared to the earlier period, the spring bloom was stronger and the bloom season was also extended. In summer months during both periods, the phytoplankton concentration was very low.

CPR data coverage in the northwestern North Atlantic was very sparse, possibly due to infrequent commercial cruises and rough weather conditions in winter. In the region south of Reykjanes Ridge (Figure 3.3d), observations were available from the early

1960s to the late 1970s and after the early 1990s to 2007. During the earlier period, phytoplankton was observed from April to November, though PCI was very low in summer months. Two distinct blooms were found within this time period; the first, stronger, bloom peaked around June and the second, weaker, bloom peaked in October. In the later decades, the separation of two phytoplankton blooms was unclear, especially after 1998. From 2001, phytoplankton was observed in February and March, though its abundance was low. The major phytoplankton changes in the later period were the merging of two distinct blooms and the extension of phytoplankton observing season.

From the description above, it is clear that phytoplankton bloom patterns are not consistent across the whole subpolar North Atlantic. Phytoplankton concentration is higher in the shelf seas than in the open ocean, both in the eastern and western subpolar basin. In the northern basin (north of 55 ºN), distinct spring and autumn blooms are found in the early decades while in more recent decades two blooms merged and the strength of blooms was enhanced. In the southern basin (south of 55 ºN), the phytoplankton blooms tend to be continuous without separation, which either lasts from early spring to late autumn (Figure 3.3d) or from late autumn to the following summer (Figure 3.3c). From the late 1980s, phytoplankton blooms in these regions intensified and bloom seasons also extended. This change coincided with the SST increase described in Chapter 2. In the next section, the relationship between PCI and SST in selected areas is examined.

3.3.2   Annual Average Time Series of PCI

To quantify the decadal to multi-decadal variation of phytoplankton abundance in the subpolar North Atlantic, the annual mean PCI time series in the five representative locations are shown in Figure 3.4. Annual average values are used because phytoplankton abundance estimated from PCI is more robust when averaged over a large area and a substantial length of time. Annual mean SSTs in the five locations are plotted together with PCI time series to test whether there is a direct relationship between SST and phytoplankton abundance.

In the central eastern North Sea (Figure 3.4a), PCI remained relatively stable from 1946 to the mid-1980s. Within this time period, phytoplankton concentrations were lower than average in the late 1940s and around the mid-1970s (sea the dashed blue line in

Figure 3.4 as a reference for the long-term average PCI). From the mid-1980s, phytoplankton abundance increased to the highest levels of the record. The values were about 1 unit higher than that previously seen, though the inter-annual variability was also higher than that in the previous decades. The annual mean SST in the central eastern North Sea remained around 10 °C from the 1940s to the late 1980s and then SST steadily increased on average. The highest SST is seen towards the end of the time series. PCI and SST time series are positively correlated (r=0.31, p=0.01) on 95% confidence intervals, dominated by the positive trend of both parameters. On the inter-annual scale, PCI does not follow changes of SST closely.

The PCI shows a long-term positive trend in the southeastern North Sea (Figure 3.4b) and the rate of increase was higher after the mid-1980s compared to earlier decades. The inter-annual variability was also highest in the period after the mid-1980s. The annual averaged SST remained relatively stable from the 1940s to the end of the 1980s when a rapid increase in SST occurred. In the 1990s, large inter-annual variability was observed, and after the late 1990s SST increased to a new level that was higher than previously seen. The two time series were correlated (r=0.44, p<0.001) on 99% confidence intervals. On decadal scales, the increase of PCI and SST correlated well while on inter-annual scale, PCI did not follow SST closely.

In the Rockall Plateau (Figure 3.4c) the averaged PCI was lower than long-term mean from the late 1950s to the mid-1960s while PCI was higher than long-term mean from the mid-1980s to the early 1990s, when a decline of PCI is apparent. The annual mean SST here had a high SST period in the late-1950s and after 2000 and low SST periods in between. PCI and SST were negatively correlated (r=-0.33, p=0.02) on 95% confidence intervals, suggesting that the increase of SST in the period after the early 1990s occurred alongside the decrease of phytoplankton and vice versa for the earlier period. Again, correlation was dominated by decadal to multi-decadal scale variability, rather than on inter-annual scale.

On the Newfoundland Shelf (Figure 3.4d), the average PCI after 1995 was about 1 unit higher than the average during 1961-1974. No clear pattern was captured in the SST time series in the Newfoundland Shelf. PCI was not correlated to SST, possibly because continuous PCI was not long enough to give a robust estimate. In the region south of the

Reykjanes Ridge (Figure 3.4e), the average PCI was slightly higher in 1992-2009 than that in 1962-1979. The SST time series here showed multi-decadal variability. The SST decreased steadily from the early 1950s to the early 1970s and a small peak occurred around the early 1980s, followed by an increase from the early 1990s to 2007. SST and PCI showed no clear correlation between one another, possibly because PCI was not available for long enough.

The results can be summarised as follows: 1) in the five representative locations, significant correlations between PCI and SST were only found in the eastern subpolar North Atlantic; 2) in the North Sea the two parameters were positively correlated, while in the Rockall Plateau the two parameters showed negative correlation; 3) these correlations suggest corresponding variation between PCI and SST on decadal to multi-decadal scales, but not on inter-annual scale; 4) in regions where positive correlations were found, increase of phytoplankton abundance occurred alongside SST warming while in regions with negative correlation, the time period of warm (cold) SST corresponded to low (high) phytoplankton concentration.

Similar correlation calculations were done for the other locations and the resulting correlation coefficients and significance levels are shown in Table 3.2 for locations where PCI was available. Not all eastern locations showed correlation between PCI and SST, though 10 out of 12 locations indicated correlations at 95% confidence interval. PCI in most eastern locations was positively correlated to SST and the highest correlation coefficient was found in the Irish Sea. Rockall Plateau was the only location with negative correlation between PCI and SST. In the western subpolar basin, PCI and SST were correlated only in the Scotian Shelf, though PCI was mainly available here after 1992. Lack of consistent CPR observation was the major obstacle in producing a reasonable estimate of direct impact of SST on phytoplankton using PCI data.

The correlations described above only suggest an overall similarity between PCI and SST on decadal to multi-decadal scales. Due to the nature of the two datasets, especially CPR survey, it is difficult to depict the finer relationship between temperature and phytoplankton abundance. However, a high percentage of chosen locations, particularly on the eastern side of the basin, showing statistically significant correlations between PCI and SST confirms that there are factors that could link the variation of

phytoplankton and temperature on decadal and longer time scales. This provides a good foundation for further more detailed analysis of physical impact on biological processes.

3.3.3   Annual Cycle of PCI

As suggested by the greenness variation, phytoplankton concentration has changed in multiple aspects, such as intensified summer growth, extended bloom season and potential shift of bloom peak (see Figure 3.3 for details). The aim of this subsection is to compare the annual cycles between earlier and more recent decades. PCI time series were divided into two periods with the same division point as the SST time series described in Chapter 2. Average annual cycles and standard errors of the first period (1946 – 1994) and the second period (1995 – 2007) were calculated for all the locations. In the 22 chosen locations, average annual cycles in 19 locations were available in both time periods while in B8 (Southeastern Labrador Sea), C8 (South to Labrador Sea) and D9 (Labrador Shelf) average annual cycles were available for only one or neither time periods.

In a few eastern North Sea locations, northeastern continental North Sea (Figure 3.5 B1), central eastern North Sea (Figure 3.5 C1) and southeast North Sea (Figure 3.5 D1), the strongest increase in phytoplankton abundance in the second period was in summer-autumn months. Significant increase in phytoplankton was seen from May to October in these three locations and also from December to the following February in C1 and D1, though increase was weaker. In the early period, two distinct blooms were observed in the three locations while in the later period the bloom pattern had switched to a single summer peak in C1 and D1. Three bloom peaks were observed in B1, where a summer month peak was observed in July. Note that even though the summer phytoplankton increase was stronger than in winter months, the standard error was also higher, suggesting higher inter-annual variability in the summer.

A significant increase in phytoplankton abundance in the second period was mainly seen in spring and autumn in the three western North Sea locations: northwestern North Sea (Figure 3.5, B2), central western North Sea (Figure 3.5, C2) and Southern North Sea (Figure 3.5, D2). The timing of bloom peaks in the two periods was similar, especially in B2 and C2, in May and August/September. Phytoplankton remained at a high level in D2 from March to December in both periods. In the adjacent shelf regions

west to the North Sea, statistical significant phytoplankton increases were observed in summer and early autumn in Stanton Bank (Figure 3.5, C4) and the Celtic Sea (Figure 3.5, D4). Whereas in the Irish Sea (Figure 3.5, C3), significant increases were observed mainly in winter months. In both periods, phytoplankton bloomed in April/May in C4 and D4 and kept at a relative high level from June to October while in C3 a single bloom peak was observed in late spring and early summer.

Phytoplankton increase in the oceanic locations was very limited in the second period and the timing of annual cycles remained similar in all locations, except in the northeastern Iceland Basin (Figure 3.5, B5) where significant increases were observed from April to December. The bloom timing was not uniform in all the oceanic locations. In B5, PCI was very low in winter months and PCI was above zero with no distinct peak from April to November in the period of 1946—1994 while a single late spring peak was shown in the average annual cycle from 1995 to 2007. In the rest of the oceanic locations, there was generally no statistical significant increase in the later period and the timing and strength of phytoplankton abundance remained unchanged.

Data coverage was very poor in the region southwest of Greenland (Figure 3.5, B8), southern Labrador Sea (Figure 3.5, C8) and Labrador Shelf (Figure 3.5, D9). It was thus impossible to compare the average annual cycles of the two periods in these locations. CPR observation was also sparse in the Gulf of Maine (Figure 3.5, F10) in the first period, indicated by its large monthly standard error. The resulting annual cycle was thus less robust than that in the second period, when monthly standard error was largely reduced. A spring bloom peak in March and a weak autumn bloom in September/October were depicted by the second annual cycle, though it is difficult to estimate the actual phytoplankton increase in the second period. The Newfoundland Shelf (Figure 3.5, E9) and Scotia Bank (Figure 3.5, E10) were the only shelf regions where annual cycles with reasonable uncertainty were available. In these locations, a strong spring bloom in April was seen in both periods and phytoplankton increase was statistically significant through winter months from November to the following May.

In summary, phytoplankton abundance increased in the later period of 1995 – 2007 compared to the earlier period of 1946 – 1994 in various locations in subpolar North Atlantic. Shelf seas showed a greater overall increase than in the open ocean. In the

eastern shelf seas, especially in the eastern North Sea, the increase in phytoplankton abundance was strongest in summer months and weaker significant increase was seen in winter. In the western shelf seas, the only significant increase in phytoplankton abundance was in winter and early spring.

In the oceanic regions, the increase of phytoplankton abundance in the second period was less significant than that in the shelf seas. The strength of phytoplankton increase declined towards the south. In the northernmost location, the northeast Iceland Basin, a statistically significant increase in phytoplankton abundance was found from spring to autumn. In the Rockall Plateau, where CPR observation was very limited in the second period, only two months showed significant changes from the first period and phytoplankton abundance decreased in June compared to the first period. In the south-Reykjanes Ridge, a statistically significant increase was found in late winter and late summer. Timing of phytoplankton blooms in the second period remained similar to that in the first period.

3.3.4   Statistical Analysis

In the previous section, PCI dataset was presented using simple methods. To test whether these simple methods provide robust results, a series of statistical analyses was carried out following Colebrook (1979), focusing on links between SST and PCI annual cycles. It was also a good opportunity to reproduce these analyses and present a more robust estimate of annual cycles using longer time series. A set of parameters that depicted the major features of annual cycles was first established using monthly HadISST1 and PCI data in each of the 22 chosen locations over the period from January 1946 to December 2007. Then Principal Component Analysis (PCA, also known as EOF analysis) was applied to SST and PCI data to extract the dominant signals in both parameters. The analysis procedure is first described, followed by results from each of these analyses.

In this and following equations, x_i represents the monthly value for PCI or SST. The first parameter is the annual average of PCI and SST. The second parameter calculated was the timing of spring increase in phytoplankton (S_p) and SST (S_T), following Eq. 3.2:

$$S = \sum (i \cdot x_i) / \sum x_i, \qquad\qquad i = 1 \cdots 6. \qquad\qquad \text{Eq. 3.2}$$

In this study, the timing of spring increase was estimated as the month coordinate of the centre of gravity of the area below x-axis when graphing monthly mean SST or PCI for January to June on an x-y coordinate. This method effectively selects the month corresponding to the start of SST increase from the colder half during January to June. Duration of growing (increasing) season for phytoplankton (SST) was estimated as the standard deviation of the timing of spring increase and was calculated following Eq. 3.3:

$$L = \sqrt{\left\{ \sum \left[x_i \cdot (i - S)^2 \right] / \sum x_i \right\}}, \qquad\qquad i = 1 \cdots 12. \qquad\qquad \text{Eq. 3.3}$$

Season duration was calculated for both PCI and SST and S is the timing of spring increase estimated using equation (3) for phytoplankton and SST, respectively.

The timing of spring increase and the growing season duration of phytoplankton were calculated for all locations, together with equivalent SST parameters (Figure 3.6, a, c, e and g); these resulting time series are presented in Figure 3.6. In the open ocean, the timing of annual SST increase (Figure 3.6a) was very stable from 1946 to 2007, occurring in March with limited inter-annual variability. SST kept increasing for about four and half months (Figure 3.6c) when water temperature started to decrease around early to mid-September. The range of the timing of phytoplankton spring increase (Figure 3.6b) was larger than SST warming and PCI started to bloom from late April to mid-May in most years. Its inter-annual variability was also larger than that for SST, though no decadal to multi-decadal signal can be identified. The phytoplankton blooming season (Figure 3.6d) lasted about three months in this area, the duration kept relatively stable without obvious long-term pattern.

In the shelf seas, the increase of SST (Figure 3.6e) occurred in late March to early April and the timing was relatively stable with small inter-annual variability. The increase of SST (Figure 3.6g) lasted about four and half months and no decadal to multi-decadal change was observed. The timing of the spring phytoplankton increase (Figure 3.6f) was delayed by about one month during the period from 1970s to mid-1980s. In most years,

the PCI spring increase started in early April and during the delayed period PCI started to increase from mid to late April. In normal years, the growing season (Figure 3.6h) lasted about four months and about three months during the period of delayed phytoplankton increase. Thus in the shelf seas, the phytoplankton spring bloom generally ended in August.

In Figure 3.7, the direct impact of SST on the timing of SST increase and phytoplankton bloom initiation is tested. On the shelves, the timing of SST increase is significantly correlated to the average winter SST (Figure 3.7a, blue circles, r=-0.94, p<0.01), meaning spring warming occurs earlier after warmer winters and vice versa. The timing of the increase of phytoplankton and SST shows negative correlation (Figure 3.7b, blue circles, r=0.81, p<0.01), suggesting the increase of phytoplankton starts earlier in colder shelf region. Figure 3.7c further confirms that on cold-water shelves, phytoplankton starts to accumulate in March and occurs a month earlier than the start of SST increase whilst on warmer shelves, SST starts to increase in March, leading the initiation of phytoplankton accumulation by one month. This early phytoplankton accumulation on cold-water shelves may result from the prohibited heterotrophic consumption in cold environment [Colebrook, 1979; Townsend et al., 1994], however it is difficult to rule out the possibility that this correlation reflects the response of phytoplankton growth to nutrients concentration, which is usually abundant in the late winter as a result of active vertical mixing in winter, rather than directly to SST. The influence of vertical stability and the timing of phytoplankton spring increase are shown in Figure 3.7d. In this study, a simple estimate of vertical stability was calculated as the average standard deviation of SST annual cycle, with bigger (smaller) standard deviation suggesting a more (less) stable vertical water column [Colebrook, 1979]. The timing of PCI spring increase is negatively correlated to SST annual standard deviation (r=-0.81, p<0.01) on the shelves, so phytoplankton grows earlier regions with bigger SST differences during January-June, suggesting a stronger stratification in the late spring. Overall, phytoplankton grows earlier in the shelf regions with cold winter SST but stronger stratification process during spring.

In the oceanic regions, SST also starts to increase earlier after a warmer winter (Figure 3.7a, red circles, r=-0.9, p<0.01), though not as significant as on the shelves. There is no significant correlation between the timing of phytoplankton increase and SST in the

oceanic region (Figure 3.7b, red circles), though the linear regression suggests phytoplankton accumulation may start earlier in warmer open ocean than in colder regions. Figure 3.7b indicates that SST warming occurs in late March and phytoplankton starts to accumulate in May. However, there is no direct link between the timing of the increase of phytoplankton and SST or between the timing of phytoplankton increase and the water column stability. All oceanic locations remain actively mixed over a longer time as the winter convection extends to a deeper depth and requires more heat to stabilise the water column compared to in the shelf seas. The overall light level is lower in an actively mixing layer and phytoplankton cells might be brought to depths with insufficient light though vertical mixing, both processes lead to a later phytoplankton bloom in the open ocean.

Monthly PCI (SST) was then rearranged into a 12×22 ($row \times column$) table, with each column representing a location shown in Figure 3.5 and each row representing the average value over the period of 1946—2007 for each month. The table was then subjected to PCA analysis in two ways:

PCA1: Each row of the table was standardised to zero, removing the differences between months and effectively removing the differences between phytoplankton and SST. Only differences between locations remained in the resulting table. A normal PCA was then applied to this table and the eigenvectors contained values for months and associated principal components (hereafter PC) indicated geographical distribution of PCI (SST).

PCA2: Each column of the table was standardized to zero, leaving only differences between months in the resulting table. A conventional PCA was applied to this table and the eigenvectors contained information for the locations and the associated PCs indicated the average annual cycle of PCI (SST).

Note the PCA procedure introduced here is slightly different from that used in recent studies, as the applied data is tables summarising information of groups of locations instead of grid points. Therefore, the resulting eigenvalues are also in table form and could not be visualised in the same way, as in more recent studies. The PCs indicate different information in the two PCA analyses, rather than providing temporal pattern corresponding to the spatial distributions in recent studies. The methods of presenting

these eigenvectors and PCs were introduced in Colebrook (1979) and were adapted in this study.

PCA was used to extract the dominant signals in the variation of phytoplankton and SST annual cycles. Firstly, the first two eigenvectors of PCA1 represent the two dominant signals controlling the annual cycles. Therefore, the relative distribution of the first two eigenvectors statistically divides the year into two halves for both phytoplankton (blue circles) and SST (red squares) and is shown in Figure 3.8. The first two eigenvectors explain 54% and 25% of total variability in phytoplankton, respectively while for SST the first two modes explain 75% and 23% of its total variability, respectively. For both phytoplankton and SST, there is a common element that determines the variability of these two parameters all year round (the first eigenvector). The second mode, however, shows a changing pattern of phytoplankton and SST with seasonal succession. On average, phytoplankton is low from November to April and is abundant from May to October, while sea surface is cold from December to May and warm from June to November. This division corresponds very well to the annual cycles of both parameters.

To visualize the distribution of phytoplankton in winter and summer, the weighted sum of the first two PCs of PCA1 was calculated for two groups of months using mean eigenvector values of November—April (months with negative second eigenvector) as winter weight and June—September (months with positive second eigenvector) as summer weight. In winter (Figure 3.9a), phytoplankton abundance is above its annual average in most shelf seas while phytoplankton abundance is below average in most of the open ocean areas. In summer (Figure 3.9b), this distribution is reversed, with overall higher than average abundance in the open ocean and lower than average abundance on the shelves. This result agrees with the observation in Colebrook (1979), though the seasonal contrast is larger, confirming the observed stronger increase of phytoplankton abundance in summer in more recent decades.

The first two eigenvectors of PCA2 statistically separate the locations showing shelf and oceanic features (Figure 3.10a). The first two modes explain 60% and 21% of its total variability, respectively. With the exception of F10, a common element determines the variation of phytoplankton at all locations. There is a changing element that separates

shelf seas (blue circles) from open ocean areas (red circles), though the Irish Sea (C3) seems to show oceanic character in this aspect and the Rockall Plateau (C5) and southern Rockall Trough (D5) present weak shelf characteristics. The average annual cycles (Figure 3.10b) of the shelf seas and the open ocean were calculated as the weighted sum of the first two PCs from PCA2, using the mean eigenvalues for shelf seas and open ocean as weights; however, the three locations (C3, C5 and D5) mentioned above were removed from the calculation. Phytoplankton annual peak was observed in the shelf seas in April—May and in June in oceanic regions. A second weak increase in PCI was observed around September in shelf seas while in the open ocean areas phytoplankton only had a single early-summer peak.

Compared to earlier equivalent results shown in Colebrook (1979) using all available PCI data from 1946 to 1976, the results shown here confirm that the timing of phytoplankton annual cycle has kept relatively stable. The geographical distribution of phytoplankton in extended winter and summer suggest that the amplitude of phytoplankton bloom has increased, especially in southwestern shelves. The annual cycles were similar in the two studies, though a slight shift of phytoplankton peak towards summer is seen in oceanic regions. The timing of spring increase of phytoplankton shows similar relationship with SST increase and vertical stability as in Colebrook (1979), with slightly more significant coefficients. This means that a similar conclusion could be drawn from these results that SST increasing plays a minor role (the fact that phytoplankton can start to accumulate before, during or after SST increases) in controlling phytoplankton growth, while phytoplankton is more sensitive to the impact of vertical mixing in the shelf seas. Phytoplankton growth occurs earliest in cold shelf seas where cold SST prohibits heterotrophic consumption [Colebrook, 1979]. Latest phytoplankton growth occurs in the open ocean (Figure 3.7b), where low vertical stability and active mixing delay the onset of spring bloom. These results agree very well with the findings presented in previous sections using simple methods, and hence enhance confidence in the robustness of the observed variability.

3.4   Summarising Discussion and Conclusion

The long-term variability of the primary producer in marine ecosystem, phytoplankton was examined using CPR observation in the subpolar North Atlantic. CPR observation

was first operated in 1931, it was then paused during WWII and continuous plankton measuring was carried out from 1946 onwards [Reid *et al.*, 2003]. Various datasets were produced from CPR observation. For phytoplankton, PCI was produced by estimating the greenness of the filtering silk under a consistent standard and then averaging over the standard areas (Figure 3.2 and Section 3.2). In this study, PCI time series in 22 standard areas were selected, corresponding to most of the SST locations in Chapter 2, to carry out analysis focusing on the decadal to multi-decadal variability.

The greenness in five representative locations suggests that in regions where two distinct blooms were observed in early decades, the two blooms merged together and the overall strength intensified after the mid-1980s, confirming the findings in Reid *et al.* (1998). In regions where phytoplankton blooms continuously from spring to autumn, the blooming season extended and the abundance increased after the mid-1980s. In the two western locations, observation was available from the early 1960s to mid 1970s and from the early 1990s onwards. Phytoplankton bloom in the second period was much more intense than in the earlier period, which suggests there could be an expanded regime shift in the North Atlantic [Reid, 2005], though the lack of significant signal in the open ocean and poor data coverage on the western shelves make this suggestion less exclusive.

In the southeastern North Sea, the decadal variability in annual average phytoplankton is correlated to the annual mean SST. In the Rockall Plateau, phytoplankton variation is statistically negatively correlated to SST, though in most of the locations surrounding Rockall Plateau positive correlation is found between SST and PCI. One feature of the Rockall Plateau is that the bottom depth is shallower than its surrounding regions, but whether this difference can alter the phytoplankton response to increasing SST and its mechanism is not clear. In the western basin, however, there is no correlation between SST and PCI, possibly due to a lack of continuous observation here. In summary, in some of the eastern subpolar regions, phytoplankton abundance varies corresponding to the long-term variation of SST, but for most oceanic regions, there is no direct relationship.

The comparison between the average annual cycle over the period 1995—2007 and over the period 1946—1994 suggests that in the eastern shelf seas statistically significant

increase in phytoplankton abundance observation was seen mostly in spring to summer months, especially in the North Sea, whereas in the western shelf seas statistically significant increase was seen in winter to early spring. In most of the oceanic regions, however, annual cycles in both periods were very similar and the timing of spring bloom remains stable. Only in the northern oceanic regions, northeastern Iceland basin and the Irminger basin, were statistically significant increases in the second period observed in warm seasons.

The timing of spring increase and season duration of phytoplankton and SST were identified following the methods introduced in Colebrook (1979) in both shelf and oceanic regions. For both PCI and SST, the timing of spring increase and season duration remains relatively stable during the period from 1946 to 2007 in the oceanic region while in the shelf seas the timing of spring phytoplankton bloom shows a weak decadal pattern and was delayed from the early 1960s to the mid 1990s by one month. Considering the documented bio-geographical shifts in the subpolar North Atlantic in many existing literature [e.g. Beaugrand *et al.*, 2001; Beaugrand *et al.*, 2008; Hátún *et al.*, 2009] it is surprising that the timing of both phytoplankton and SST increases have remained relatively stable over the last 60 years. One possible reason is the resolution of the datasets is not high enough to capture the shift of the bloom initiation, as the change would be a few days if existing. Scatter plots between PCI and SST suggest that spring increase of phytoplankton is more associated to the water column stability than to the timing of SST increase. Spring phytoplankton increase occurs before the SST warming in shelf seas with cold SST, which could result from the prohibited growth of heterotrophic organisms.

In conclusion, using CPR observation from 1946 to 2007 in the subpolar North Atlantic, significant increase in phytoplankton abundance has been observed mainly in the shelf seas and the northern oceanic regions after mid-1990s. In the eastern subpolar basin, significant increase is observed during warm months from May to September and in the western basin, significant increase is seen during cold months from December to April. Clear differences in phytoplankton annual cycle features are presented between shelf seas and open ocean. In the eastern shelf seas, major changes include increased abundance and merger of previously distinct spring and autumn blooms, which coincide with the increasing SST. By contrast, in the open ocean and western shelf seas such

correlation is weak or insignificant, which is because phytoplankton is more sensitive to water column stability and because of poor data coverage in these regions. However, with the resolution of current data, it is difficult to distinguish the two effects. One potential solution in the future is testing the relationship between SST and satellite derived chlorophyll-a to eliminate the influence of the poor data coverage. Overall, significant changes in phytoplankton abundance have been observed corresponding to a changing climate and potential changes to the structure of functional groups within the local ecosystem could occur if such changes in the physical environment continue.

Table 3.1 Standard Area in the Subpolar North Atlantic and its Corresponding SST
Location Number in Figure 2.1

SA/Number	Location	SA/Number	Location
B1/1	Northeast Continental NS[1]	D5/13	Southern Rockall Trough
B2/2	Northwest NS	D9/None	Labrador Shelf
C1/3	Central East NS	E9/15	Newfoundland Shelf
C2/4	Central West NS	E10/16	Scotian Shelf
D1/5	Southeast NS	F10/17	Gulf of Maine
D2/6	Southwest NS	B7/18	Irminger Basin
C3/7	Irish Sea	B8/19	Northeastern Labrador Sea
C4/8	Stanton Bank	C7/20	West Reykjanes Ridge
D4/9	Celtic Sea	C8/21	Southern Labrador Sea
B5/11	Northeast Iceland Basin	D7/22	South Reykjanes Ridge
C5/12	Rockall Plateau	D8/23	South of Labrador Sea

[1]NS stands for North Sea

Table 3.2 Correlation Coefficients between PCI and SST in the Chosen Locations

Location	R[1]	Location	R
Northeast Continental NS	**0.31**	Southern Rockall Trough	0.01
Northwest NS	**0.26**	Labrador Shelf	None
Central East NS	**0.31**	Newfoundland Shelf	0.27
Central West NS	**0.28**	Scotian Shelf	**0.47**
Southeast NS	**0.44**	Gulf of Maine	0.19
Southwest NS	**0.43**	Irminger Basin	0.17
Irish Sea	**0.66**	Northeastern Labrador Sea	None
Stanton Bank	-0.05	West Reykjanes Ridge	0.21
Celtic Sea	**0.37**	Southern Labrador Sea	-0.03
Northeast Iceland Basin	**0.45**	South Reykjanes Ridge	0.19
Rockall Plateau	**-0.33**	South of Labrador Sea	0.24

[1] Bold number suggests significant correlations on 95% confidence interval
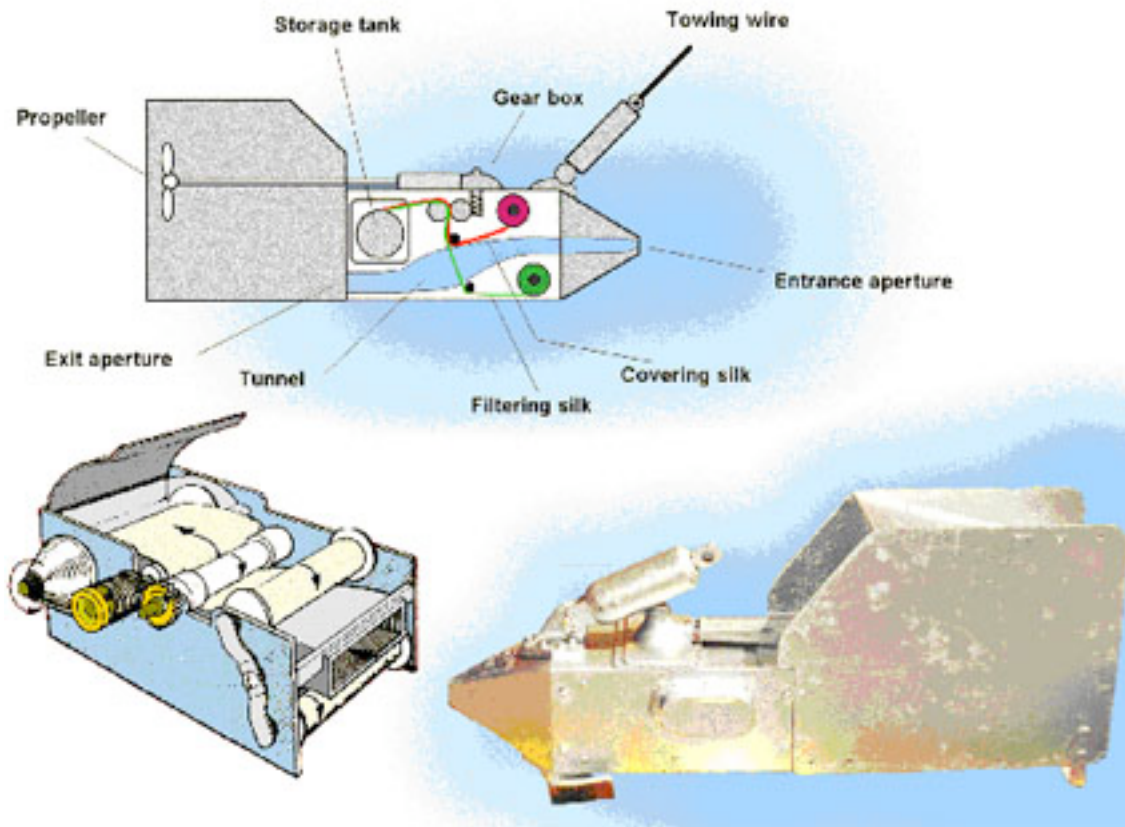
Figure 3.1 Example of cross-section of continuous plankton recorder (CPR, top), its internal mechanism (bottom left) and CPR body (bottom right, [Richardson *et al.*, 2006]).
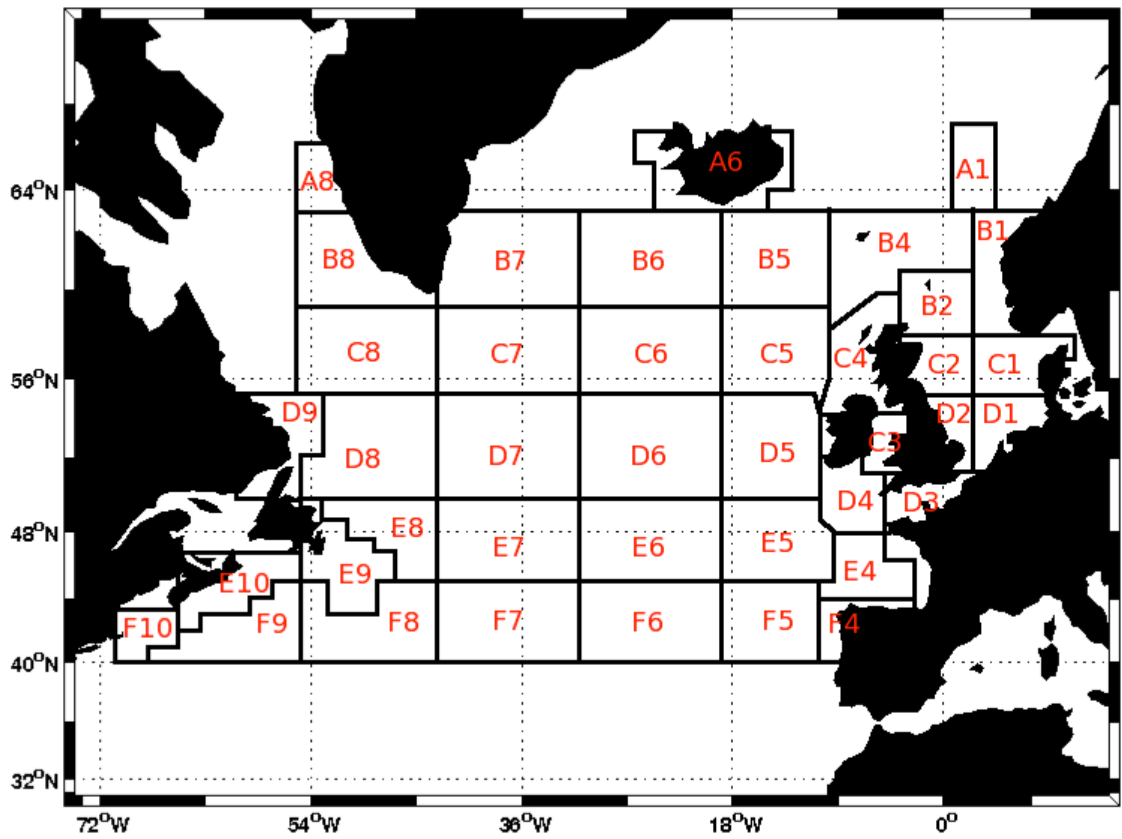
Figure 3.2 CPR standard area.
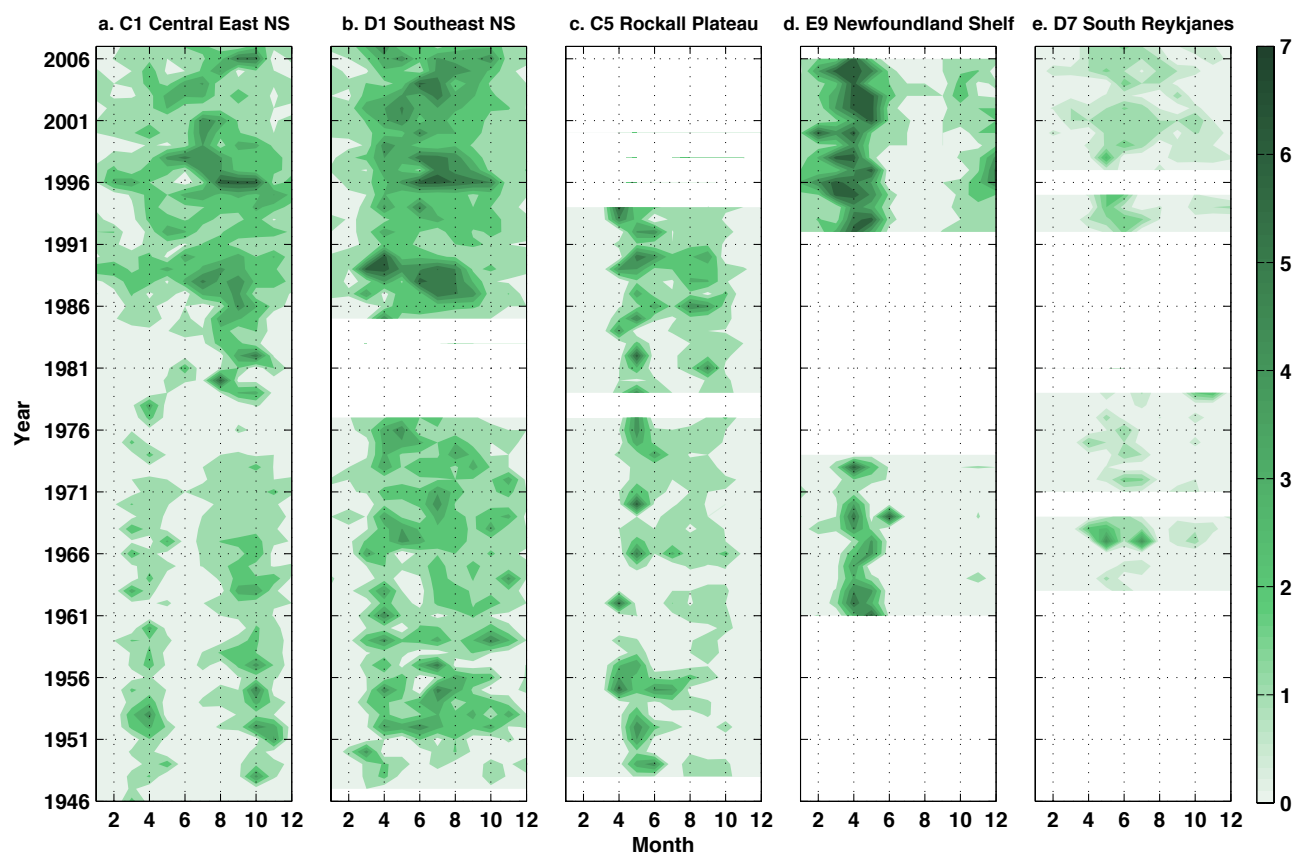
Figure 3.3 Monthly Phytoplankton Colour Index (PCI) from 1946 to 2007 in five representative locations shown in the form of greenness: (a) C1 central eastern North Sea, (b) D1 southeast North Sea, (c) C5 Rockall Plateau, (d) E9 Newfoundland shelf and (e) D7 south of Reykjanes Ridge. The blank area suggests no observation was carried out that month or year at the particular location.
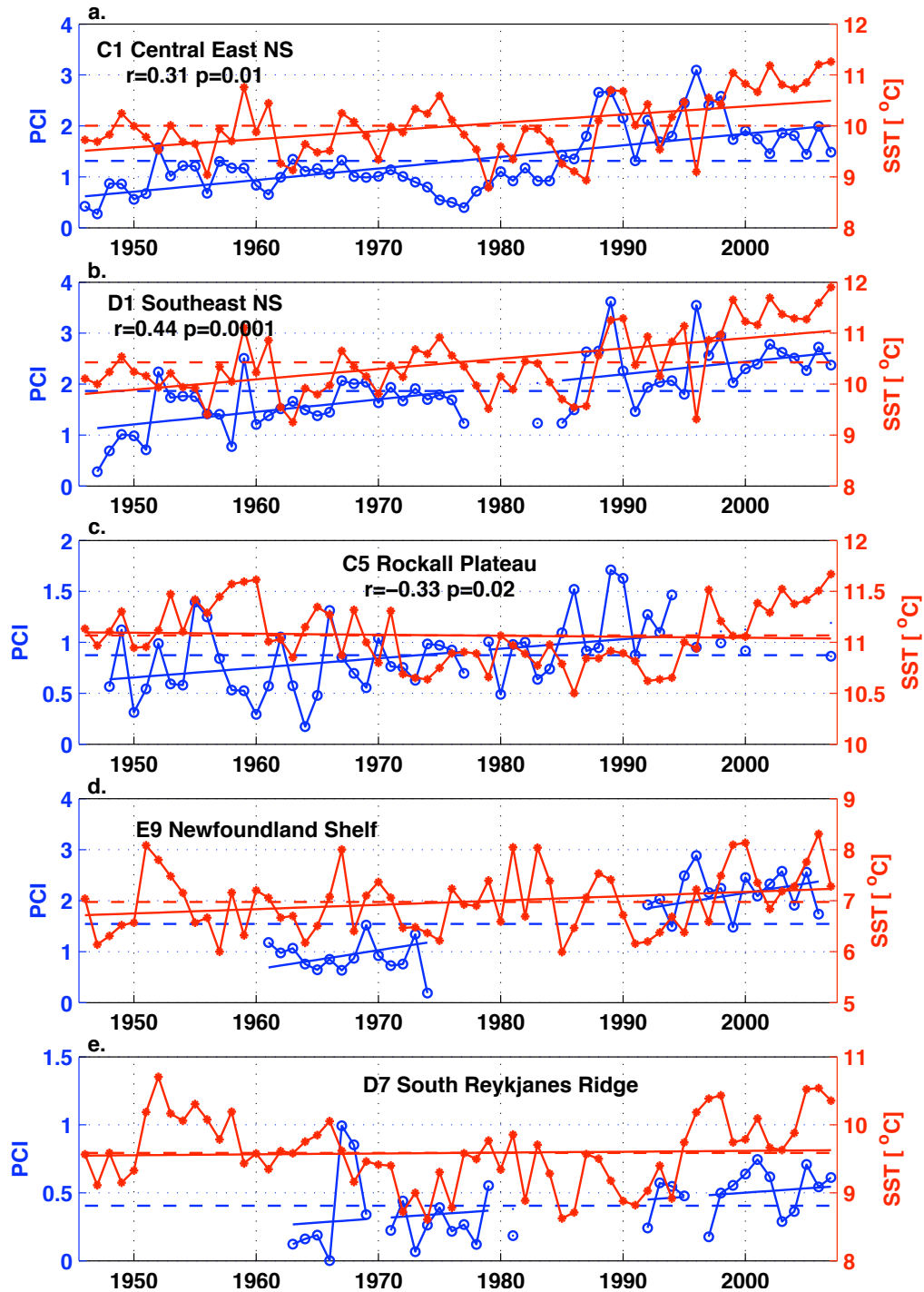
Figure 3.4 Annual mean PCI from 1946 to 2007 in the five representative locations (blue lines with open circles) and annual mean SST (red lines with filled circles) during the same period: (a) C1 central eastern North Sea, (b) D1 southeast North Sea, (c) C5 Rockall Plateau, (d) E9 Newfoundland shelf and (e) D7 south of Reykjanes Ridge. The blue (red) lines indicate the linear trend of the annual PCI (SST) and dashed blue (red) lines indicate the long-term average PCI (SST).
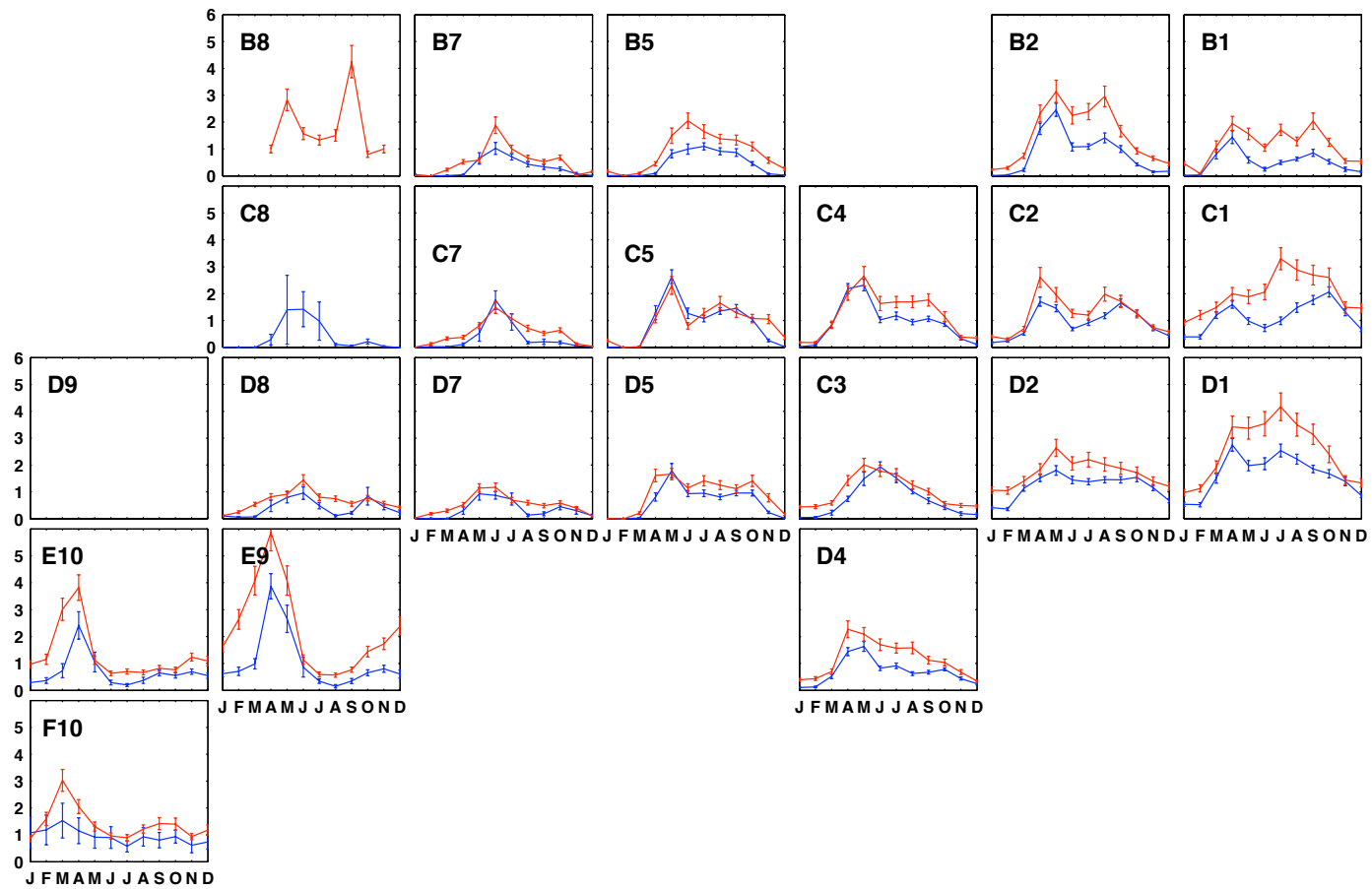
Figure 3.5 Changes of the PCI annual cycles in the 22 chosen locations between the period 1946 – 1994 (blue lines) and the period 1995 – 2007 (red lines). The error bars show the range of the standard error of the mean (SEM) for each month in the two periods.
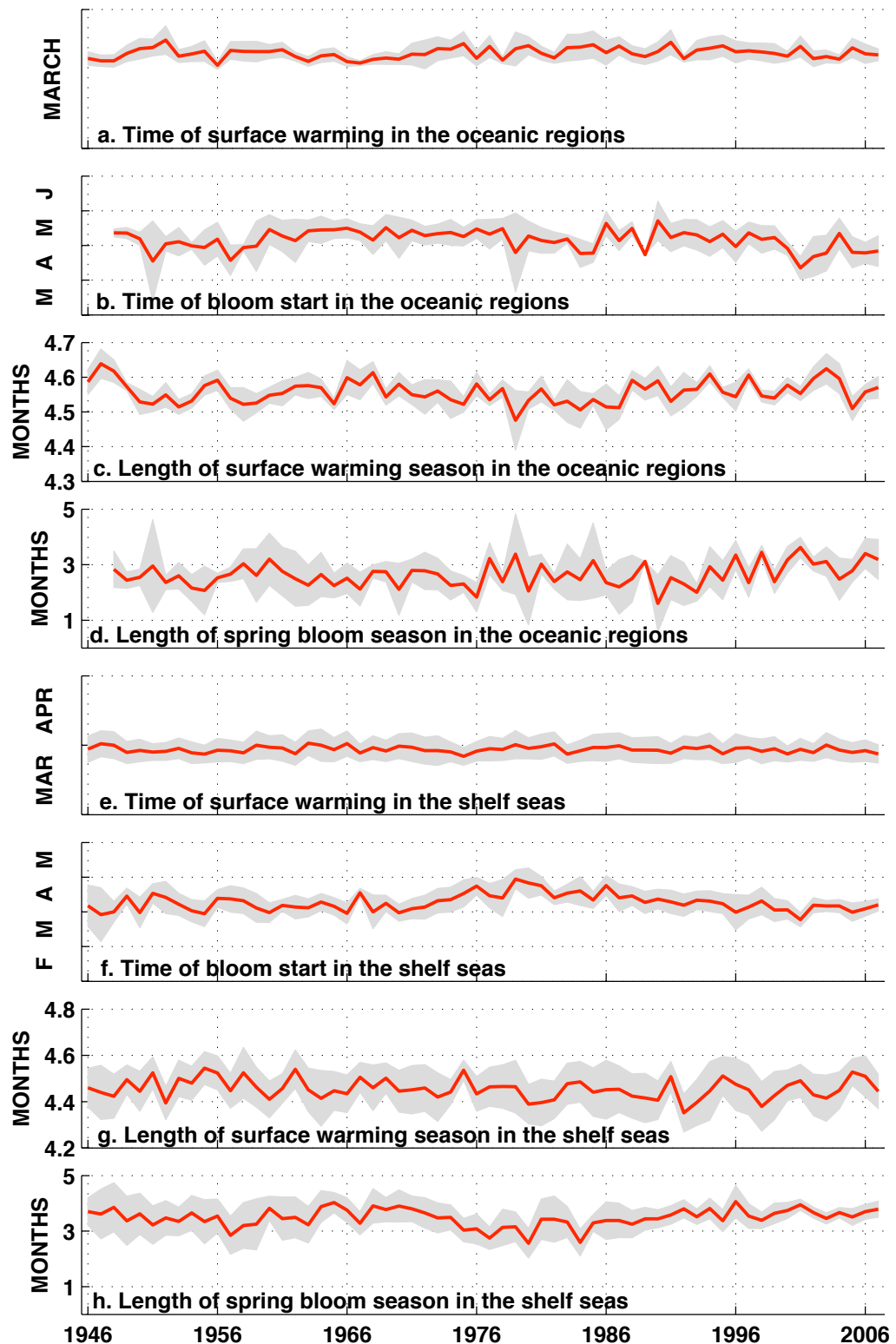
Figure 3.6 The initiation date and the length of the warming season of surface water (a, c, e and g) and the initiation date and the length of the spring bloom of phytoplankton (b, d, f and h) in (a-d) oceanic regions and (e-h) shelf seas. The grey areas mark the range of ± standard deviation between locations in the oceanic and shelf regions.
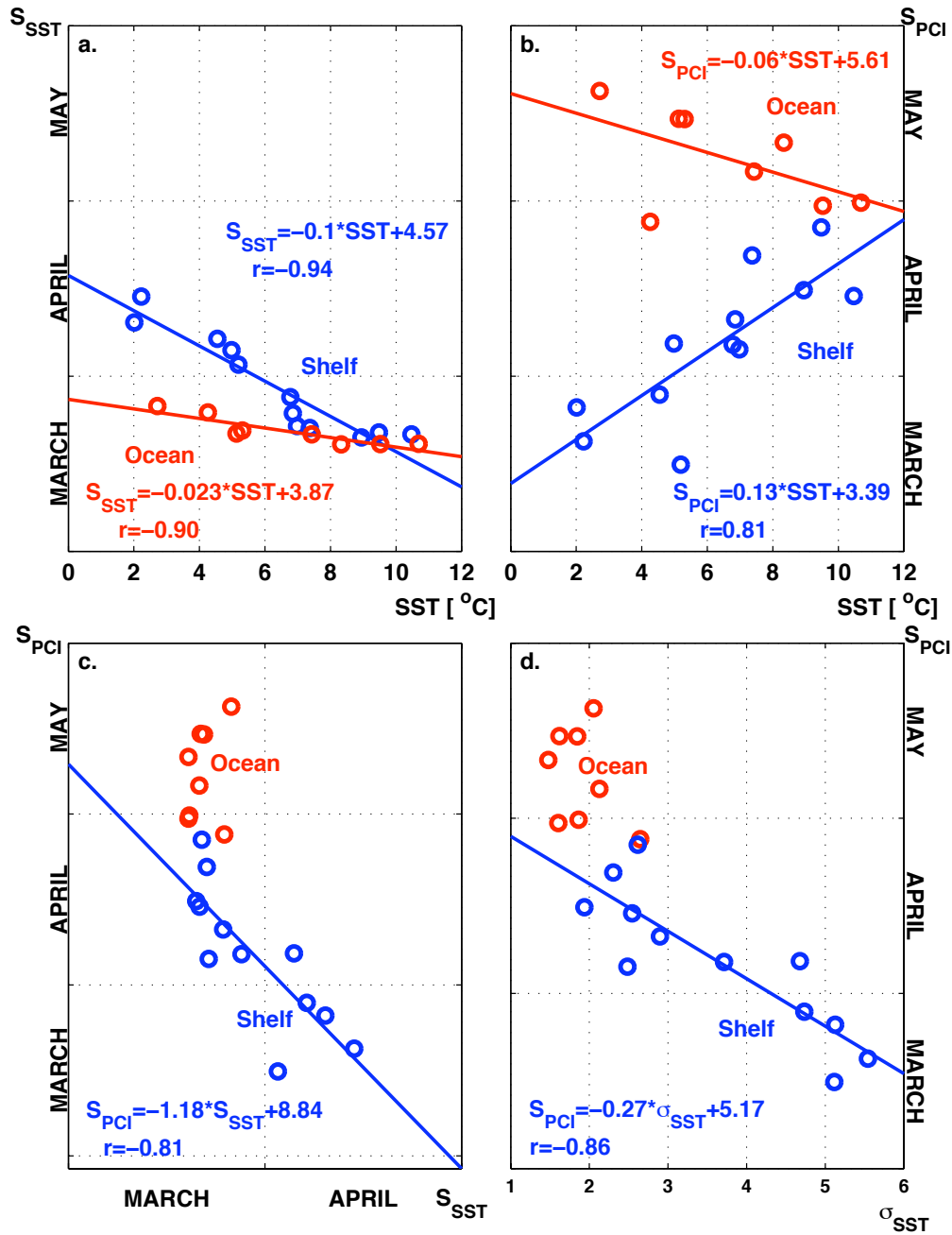
Figure 3.7 Scatter of (a) the timing of SST spring increase (S$_{SST}$) against winter (January—March) SST, (b) the timing of phytoplankton spring increase (S$_{PCI}$) against winter SST, (c) the timing of phytoplankton spring increase (S$_{PCI}$) against the timing of SST spring increase (S$_{SST}$) and (d) the timing of phytoplankton spring increase (S$_{PCI}$) against the water column stability represented by the standard deviation of SST during January—June (σ_{SST}). Blue circles represent shelf locations and red represent ocean locations. The least-square fit lines are presented with corresponding colours and correlation coefficients (significant at 99% level) are presented where applicable.
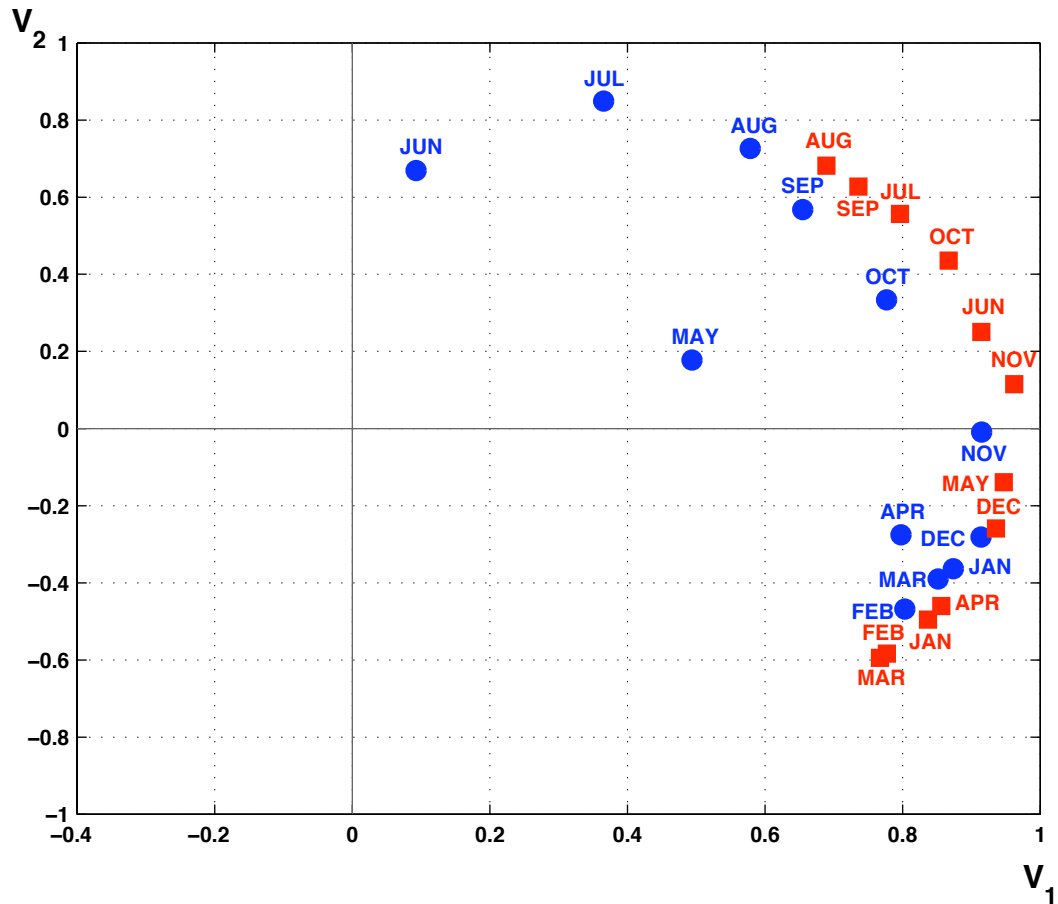
Figure 3.8 Scatter diagram of the first two eigenvectors of PCA1, showing the distribution of each month in the $V_1 - V_2$ coordinates for phytoplankton (blue circlues) and SST (red squares).
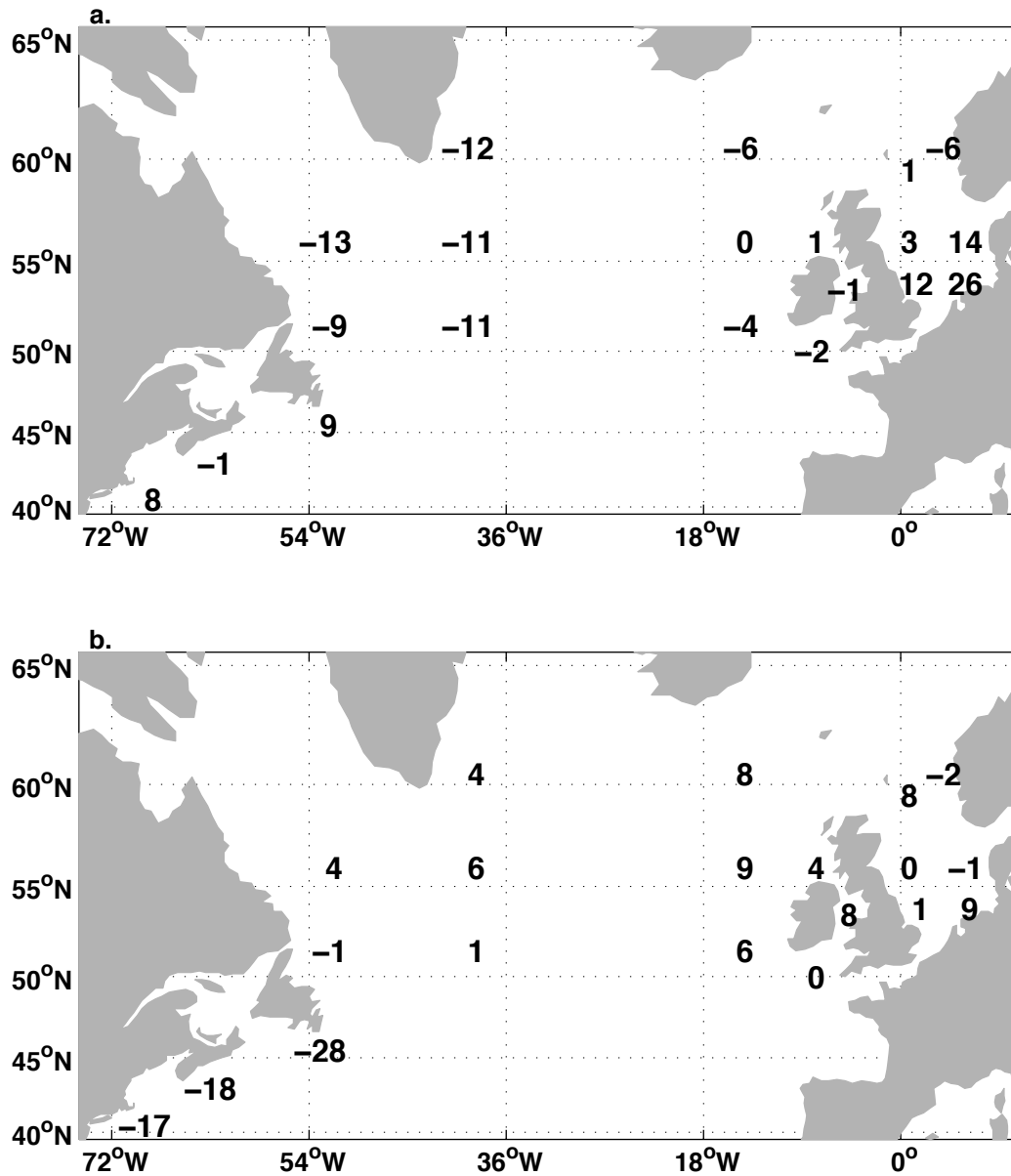
Figure 3.9 The average geographical distribution of phytoplankton in groups of months, calculated as the sum of the weighted first two principal components of PCA1. The mean eigenvector values are used as weights for each corresponding month group, the initial results are standardised to zero and multiplied by 10 before presenting. The month groups are (a) winter (November to April) and (b) summer (June to September).
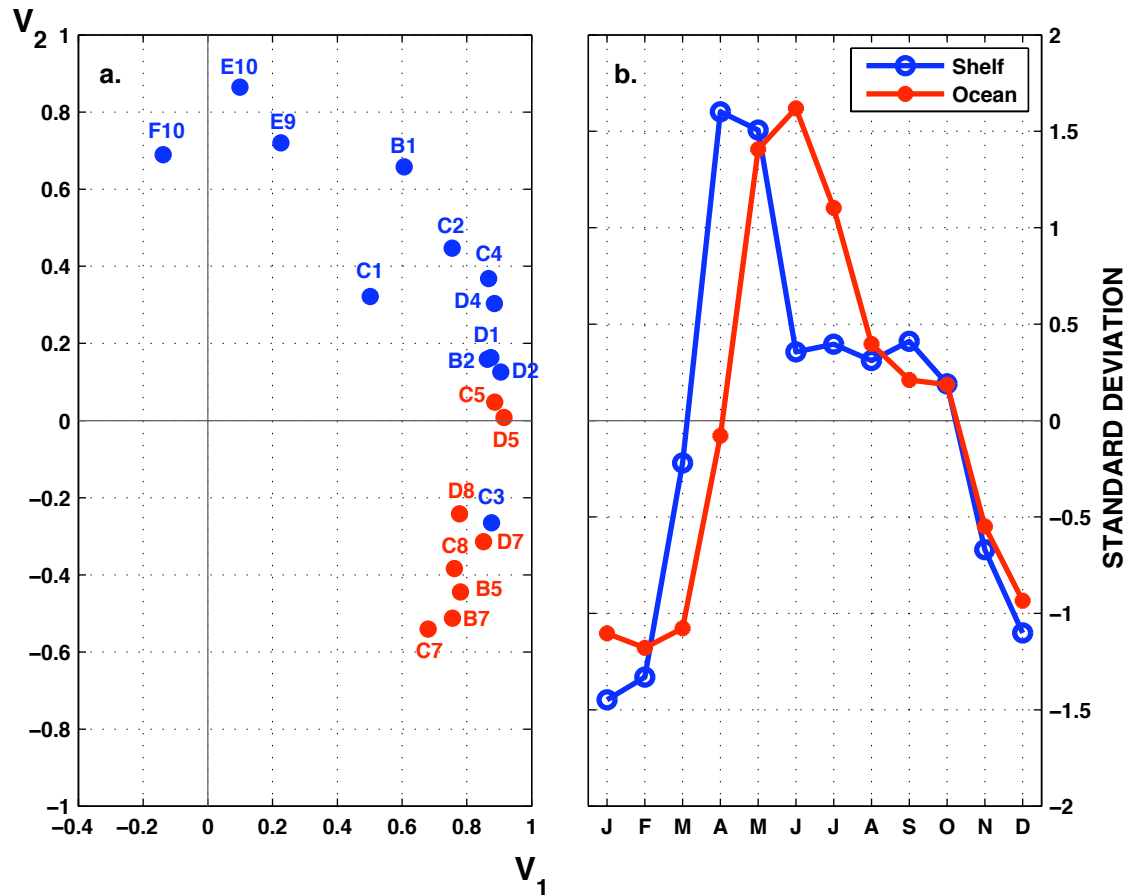
Figure 3.10 (a) scatter diagram of the first two eigenvectors of PCA2, showing the distribution of the shelf (blue circles) and oceanic (red circles) locations in the $V_1 - V_2$ coordinates for phytoplankton; (b) the average annual cycle in the shelf and oceanic regions, calculated as the sum of the weighted first two principal component of PCA2. The mean eigenvector values are used as the weights for each location group and the initial results were standardised to zero.

Chapter 4

Simulation of Physical Influences on Phytoplankton Variability, Part One: Model Validation

4.1   Introduction

Studying oceanic processes in the ocean using numerical models has developed on various aspects since the late 1960s [Bryan and Cox, 1967; Manabe and Bryan, 1969; Herring and Mellor, 1970]. Since these early studies, the performance of the numerical models has improved, partially due to increased model resolution and a better understanding of physical processes. Model simulations have proved to be effective tools to investigate the physical mechanisms behind observations in the present day, on paleo-timescales and for future predictions, especially in regions and periods with sparse observations (e.g. [Yang and Huang, 1996; Zhang and Wu, 2010]). Biogeochemical models, embedded into physical models, have also been used to study the variation and interaction between physical and biological processes [Henson *et al.*, 2009b; Popova *et al.*, 2010; Popova *et al.*, 2012], supplementary to satellite and *in situ* observations.

In previous chapters, the decadal to multi-decadal variability in sea surface temperature (SST) and phytoplankton abundance were discussed. No direct links between the two parameters could be established using monthly HadISST1 and CPR observations. These results lead to a further investigation of mixed layer depth (MLD, also known as upper mixed layer, UML) for the potential mechanisms of physical control of phytoplankton growth. However, MLD observations in the high latitude North Atlantic are very limited and restricted to the regional scale. Basin-scale observation of MLD can be constructed following the increased deployment of Argo floats since 2001 [Hosoda *et al.*, 2008], though the duration of these observations is insufficient to address decadal to multi-decadal variability. Thus, simulation of MLD from an ocean model is an ideal tool to examine its variability and interaction with SST. However, simulated MLD has discrepancies with observation, especially in the Labrador Sea and Irminger Sea where sea ice and freshwater influences the development of MLD [De-Jong, 2010]. Hence, a validation of simulated MLD is conducted in this study before further analysis.

In the subpolar North Atlantic, the coverage of decadal observation of phytoplankton abundance (continuous plankton recorder, CPR, introduced in Chapter 3) is not balanced across the whole basin, with intensive observation in the east and very sparse observation in the west. In the northern part of the subpolar basin, satellite observation

of chlorophyll-a suffers from the limitation of satellite swathe so there is no data beyond 60 °N in winter and the atmospheric particles might adjust the signal received by the satellite sensors [McClain, 2009]. The overall error in the satellite-derived chlorophyll-a is assumed as ±35% [Lavigne *et al.*, 2011]. Thus, outputs from biogeochemical models appear to be a good choice for studying the variation of phytoplankton at basin-scale, as well as testing the role of MLD in regulating phytoplankton growth.

In the following chapters, the effects of physical parameters, focusing on MLD and SST, as controls on phytoplankton abundance in the subpolar North Atlantic are investigated using a global 3-D high resolution coupled physical and biogeochemical model. In this chapter, the selected models are first introduced and the simulated physical and biological parameters are then validated by comparing them to the available observations. The chapter is structured as follows: section 4.2 presents the brief model description, section 4.3 presents the comparison between observations and model outputs and section 4.4 provides summarizing discussion and conclusions.

4.2   Physical and Biogeochemical Models

4.2.1   NEMO

The Nucleus for European Modelling of the Ocean (NEMO) is a primitive equation model, composed of an ocean general circulation model, OPA [Madec, 2012], interfaced with the Louvain-la-Neuve Ice Model v3, LIM3 [Vancoppenolle *et al.*, 2012]. The NEMO model used in this study is version 3.4, with a horizontal resolution of $1/4°$ and a vertical resolution of 64 levels. The vertical spacing ranges from 6m at the surface to 250m at depth of 6000m. The model outputs are available on 5-day, monthly and annual scales.

The primitive equations are Navier-Stokes equation and a nonlinear equation of state coupling temperature and salinity with the fluid velocity. Basic assumptions are made mainly from scale consideration, namely the direction of gravity parallels to the earth's radius and ocean depth is neglected compared to the earth's radius. Small-scale fluxes are expressed in terms of large-scale features and density variations are only considered if they contribute to the changes of buoyance force: the flux exchange of heat, salt, fresh

water and momentum between the ocean and various interfaces, such as the land-ocean interface, atmosphere-ocean interface and sea ice-ocean interface. A more detailed list of the equations and the time and space domain within which the equations are solved can be found in Madec (2012).

The surface forcing used in NEMO is the DFS 4.1 fields, developed by the European DRAKKAR collaboration [DRAKKAR-Group, 2007]. These fields also combine the CORE dataset [Large and Yeager, 2004] and ERA40 reanalysis and the former provides precipitation and downward short and long-wave radiation, while the latter provides 10m wind and 2m air humidity and temperature for the period of 1958 —2001. For precipitation, the DFS4 forcing is monthly and the forcing for radiation and turbulent variables are daily and 6-hourly, respectively. A monthly climatology is used as the initial condition and, in high latitudes, this climatology combines Levitus World Ocean Atlas climatology with the Polar Science Center Hydrographic Climatology (PHC2.1) database, which contains temperature and salinity data available as monthly, seasonal and annually products [Steele *et al.*, 2001; Madec, 2012]. The vertical mixing is parameterised using a turbulent kinetic energy scheme, which was developed by Gaspar *et al.* (1990) for oceanic case and significantly modified by Madec *et al.* (1998). All parameters included as the input data in the model contain climatological values or inter-annual values when applicable.

4.2.2   MEDUSA

The Model of Ecosystem Dynamics, nutrient Utilisation, Sequestration and Acidification (MEDUSA) is a unique intermediate complexity plankton ecosystem model. It is coupled with NEMO and is developed to simulate biogeochemical parameters on the global scale [Popova *et al.*, 2010; Yool *et al.*, 2011]. Within MEDUSA, the plankton ecosystem is divided into small and large portions and different planktonic components and processes are organised corresponding to each portion. The small class includes nanophytoplankton, microzooplankton and small detrital particles that sink relatively slowly. The large class includes diatom phytoplankton, mesozooplankton and large detrital particles that sink relatively quickly, the sinking speed is not defined in the model because the detrital particles are not properly resolved within model time-stepping [Yool *et al.*, 2011]. Altogether 11 state variables are

resolved in the model and are distributed between the nitrogen (six variables), silicon (two variables) and iron (one variable) cycles. The two remaining state variables represent chlorophyll for each of the two phytoplankton classes. The 11 state variables are listed in Table 4.1. A schematic diagram showing the components and interactions in the MEDUSA model is adapted from Yool *et al.* (2011) and shown in Figure 4.1. The 11 state variables are indicated in solid boxes.

The differential equations for these 11 state variables are applied within every ocean grid cell in the physical model regardless of horizontal or vertical position, which is similar to the implementation of ecosystem models in some general circulation models. The equations describeing light and nutrient limitation of chlorophyll accumulation and phytoplankton growth are applied to non-diatom and diatom separately. An extra silicon limitation is applied to diatoms. In addition to the physical limiting factors, phytoplankton population is also adjusted by zooplankton grazing, which are governed by separate equations for non-diatom and diatom. Detailed equations and description are presented in Yool *et al.* (2011).

In MEDUSA, two forms of detrital material represent particles of different sizes, which are also associated with phytoplankton and zooplankton of corresponding sizes. Small particles are assumed to sink slowly relative to the model time step and sink under gravity down the water column. These particles are remineralised back to nutrients at a constant rate, which may be consumed by both micro- and meso-zooplankton and accelerate the return of nitrogen and iron to utilisable forms. The sinking rate of the large particles of detritus is more complex as they may sink at a rate that cannot be resolved given the time and space scales of NEMO. The concentration of the large particles is hence modelled in an implicit manner and a ballast model [Armstrong *et al.*, 2002] was used to calculate the redistribution of these particles between the vertical levels. This model posits that a fraction of organic material is quantitatively associated and hence "protected" by sinking inorganic materials (e.g. fluxes of biogenic opal and calcium carbonate), thereby allowing the organic material to penetrate deeper into the water column than the conventional Martin Curve [Martin *et al.*, 1987].

4.3   Comparison between Model Outputs and Observation

Model outputs are produced based on a series of artificial choices, such as initial and boundary conditions, geographical domains, resolution, numerical methods, parameterizations and external surface forcing. Thus the results vary significantly between models and some observable features are not guaranteed to be reproducible in models. It is hence essential to evaluate the robustness of the model outputs before in-depth analysis. In this particular section, the simulated monthly SST and MLD at quarter degree spatial resolution from NEMO are compared to observations on various scales to provide an overall evaluation.

4.3.1   Sea Surface Temperature

Firstly, average SSTs in winter and summer over the period 1990—2007 between NEMO SST and HadISST1 in the subpolar North Atlantic were compared (Figure 4.2). In winter (Figure 4.2, a-b), the distribution of isotherms generally agrees well between HadISST1 (Figure 4.2a) and NEMO SST (Figure 4.2b). SST is about 1 °C lower along the Labrador shelf and Newfoundland shelf and in the eastern subpolar basin in NEMO than in HadISST1. In summer (Figure 4.2, c-d), the distribution of isotherms agree between HadISST1 (Figure 4.2c) and NEMO SST (Figure 4.2d) in the majority of the basin, except in the Labrador Sea where the "warm tongue" into the central Labrador Sea seen in HadISST1 is absent in NEMO SST. Overall, NEMO has satisfyingly reproduced the typical features of seasonal SST distribution in the subpolar North Atlantic, except a few locations on the western shelves where known difficulties of model simulation have been reported previously [De-Jong, 2010]. A more statistical comparison between simulated SST and observations, such as satellite-derived SST, may provide more detailed assessment of NEMO SST than comparing it to HadISST1 that also included model simulation. An updated validation of NEMO performance can be found in Yool *et al.* (2013).

Secondly, the SST anomalies of the coldest and warmest months, which are March and August in both SST datasets, between the period of 1990—1994 and the period of 1995—2007 were calculated by subtracting the average highest (lowest) SSTs of the earlier period from the corresponding extreme SSTs of the later period. The purpose of this calculation was to examine the strength and pattern of SST warming (or cooling) in

recent decades simulated in NEMO and to retain consistency with the previous chapter by selecting 1995 as the division year. In winter (Figure 4.3, a-b), strongest warming in the later period is seen in the interior subpolar and along the western off-shelf area in both time series. However, the warming signal is about 1°C stronger in NEMO SST (Figure 4.3b) than in HadISST1, especially in the Irminger basin and Iceland basin. The boundaries separating the warming centres from the rest of the subpolar basin are clearer in NEMO. The cooling along the Gulf Stream area is also stronger in NEMO than in HadISST1.

In summer (Figure 4.3, c-d), warming centres occur in the central subpolar basin, with strongest warming off the Newfoundland shelf in HadISST1. The warming centres in NEMO occur east of those in HadISST1, with strongest warming at ~35 °W, 53 °N. In regions around the warming centres, SST is about 1°C higher in HadISST1 than in NEMO, thus overall the warming centres are more distinct from the rest of the subpolar basin in NEMO. The surface warming in the North Sea shown in HadISST1 is absent in NEMO as NEMO simulation focuses more on global open ocean rather than the shelf seas, so simulation on the shelves is less accurate compared to the open ocean.

In HadISST1, surface warming is stronger in summer than in winter, while in NEMO winter warming is stronger. In both extreme anomalies, the patterns of the main warming centre are similar in NEMO, where a "cold tongue" roughly along the Reykjanes Ridge between the Irminger and Iceland basins is shown. In HadISST1, no such "cold tongue" presented and the main warming centres in both anomalies are lacking a similarity. Overall, the SST anomalies between two periods in cold and warm extremes show stronger warming in the central subpolar than the regions around the basin in both HadISST1 and NEMO. Warming signals in the Irminger and Iceland basins are stronger in NEMO than in HadISST1, suggesting that SST patterns seen in these regions in NEMO should be treated with more caution. Considering the model run used in this study is only 18-years long, the presented results are generally satisfactory.

Conclusions drawn from the comparison between HadISST1 and NEMO SST are summarised as follows: 1) isotherms are more smooth in HadISST1 as a result of averaging while NEMO SST isotherms show finer scale gradients due to a higher resolution; 2) NEMO SST simulated the typical seasonal SST distributions very well; 3)

the overall pattern of the anomalies of the cold and warm extremes between two periods are generally agreed between the two datasets, though the anomalies are higher in NEMO than in HadISST1, especially in winter; 4) NEMO SST has provided a satisfying simulation in the subpolar basin, though the results in the shelf seas should be used with caution.

4.3.2   Mixed Layer Depth

NEMO generated MLD using two definitions: 1) the depth where potential density is higher than that of the reference depth (10 m) by 0.01 kg/m^3; and 2) the depth of turbocline where turbulent mixing coefficient is zero (also referred to as the turbocline depth). The two parameters present very similar results in the subpolar North Atlantic and the turbocline depth is favoured as it indicates MLD based on the coefficient directly associated with mixing. In this subsection, MLD defined using the second criterion (the turbocline depth) is compared to the Levitus MLD climatology, defined using three criteria, to evaluate the accuracy of NEMO MLD. These three criteria are: 1) the depth where its temperature is colder than SST by 0.5 ℃ (hereafter δ_θ criteria), 2) the depth where its potential density is higher than that of the surface by 0.125 kg/m^3 (hereafter δ_σ criteria) and 3) the depth where its potential density is higher than the surface potential density by a value that corresponds to a temperature difference from the surface by 0.5 ℃. The third definition is also referred to as "variable potential density" [Waniek, 2003].

Maximum MLD influences the amount of nutrients available for the coming phytoplankton-growing season. Thus a good simulation of the maximum MLD is a desirable feature of the selected model. The long-term average of the maximum MLD in NEMO is presented in Figure 4.4, together with the MLD climatology using the three criteria. In NEMO (Figure 4.4a), vertical mixing over 200m is observed generally north of 55 ℃N and the deepest mixing is seen in the Labrador Sea to about 1000m. In the Irminger basin, northern Iceland basin and Rockall Plateau, average maximum MLD is about 500m. The MLD in the Labrador Sea is much deeper in the MLD climatology using δ_θ criteria (Figure 4.4b), which is about 3000m, while in the northeastern subpolar basin, maximum MLD is about 500m. With the δ_σ criteria (Figure 4.4c), the deepest vertical mixing is seen in the eastern Labrador Sea, about 2000m. In the

northeastern subpolar basin, average maximum MLD is about 800m. Deepest vertical mixing, about 750m, is seen in the Faroe Front area using the variable potential density criteria (Figure 4.4d), instead of in the Labrador Sea where average maximum MLD is about 500m. In the Irminger basin and eastern subpolar basin, the average maximum MLD is about 400—500m.

The overall range of maximum MLD in NEMO agrees with the climatology using the variable potential density criteria but with spatial differences. The spatial distribution of maximum NEMO MLD agrees best with the climatology using δ_θ criteria and it generally agrees with the climatology using δ_σ criteria except in the Labrador Sea NEMO MLD shows a bigger area with mixing deeper than 500 m. The vertical mixing in the Labrador Sea has the largest uncertainty and the distribution and deepest mixing vary between observations and model output, where the biggest difference is 2000m. In the northeastern subpolar basin, average maximum NEMO MLD agrees with the climatology using the δ_θ and variable potential density criteria, though the MLD climatology using δ_σ is about 500m deeper than NEMO MLD. This comparison confirms that the observation of MLD is a difficult process and MLD defined using different criteria can provide different results. A detailed hydrographic comparison between observation and a series model simulation has confirmed that in the Labrador and Irminger Sea, NEMO simulation proves to be closer to *in situ* observation than the other eight chosen coupled ocean-atmosphere climate models (CCMs) and two reanalysis datasets [De-Jong, 2010]. These results enhance the confidence of NEMO's performance in simulating maximum MLD in the northwestern subpolar basin and a general agreement between NEMO MLD and MLD climatology in the eastern and southern subpolar basin indicate that NEMO MLD provides a good simulation of average maximum MLD over the 18-year period.

In addition to the maximum MLD, the minimum MLD in NEMO is also compared to the MLD climatology using three criteria and presented in Figure 4.5. All MLD data show deeper mixing in the interior subpolar basin than in the shelf seas and the annual minimum MLD is deeper in the MLD climatology (deepest MLD is between 40 m and 55 m depending on the criteria concerned) than in NEMO MLD (deepest MLD is about 35 m). The spatial distribution of the minimum MLD agrees best between NEMO MLD

(Figure 4.5a) and the MLD climatology using δ_θ criteria (Figure 4.5b), both highlight the deeper mixing in the Iceland basin, along Greenland and around the Iceland-Faroe Ridge but the deeper mixing extends further south in the southern Labrador basin in the climatology compared to NEMO MLD. The MLD climatology using δ_σ criteria (Figure 4.5c) presents an enhanced mixing in the Irminger Sea and Iceland-Faroe Ridge but shallower mixing along the Greenland compared to the NEMO MLD. The deeper mixing is also restricted to the Iceland basin and southern Irminger Sea using the variable density criteria (Figure 4.5d), which gives an average annual minimum MLD 5 m deeper than the NEMO MLD. The increase of nutrients associated with deepening of MLD can give a more exclusive explanation of MLD controlling phytoplankton growth through adjusting nutrients concentration. This study

NEMO MLD agrees generally well with Levitus climatology for the minimum MLD and the deepest vertical mixing occurs in the central subpolar basin and shallower MLD around the centre. On the shelves, the average minimum MLD is between 5m and 15m. The better agreement between the climatology using three definitions in minimum MLD than in maximum MLD suggests that the distribution of potential density is influenced more by the temperature structure in summer than in winter. The overall similarity between NEMO MLD and Levitus MLD climatology presented in Figure 4.5 enhanced the confidence in the simulated MLD in warm months.

In conclusion, the comparison between NEMO MLD and Levitus MLD climatology for the maximum and minimum MLDs shows that: 1) the maximum MLD climatology using three definitions is different in terms of the distribution of the maximum MLD and the depth of deepest mixing; 2) the maximum NEMO MLD presents similar distribution as the MLD climatology using δ_θ and δ_σ criteria, with deepest vertical mixing in the Labrador Sea and shallower mixing in the Irminger basin, Iceland basin and Rockall Plateau region; 3) the distribution of the minimum MLD agrees well between NEMO MLD and MLD climatology, with deeper-than-20m MLD and a mixing centre of about 35m in the open ocean, while in the shelf seas, the MLD is between 5m and 15m; 4) NEMO MLD captured the general features of deep mixing, though the exact values could be different in a few locations, where large differences can be seen in observations using different definitions. Overall, NEMO MLD provides a good simulation of MLD in the subpolar North Atlantic.

4.3.3   Statistical Comparison

In addition to the visual comparison for SST and MLD, the basin-scale spatial pattern and associated time series between NEMO SST and HadISST1 over the period from 1990 to 2007 were compared using EOF analysis. The EOF analysis was also applied to NEMO MLD and presented together with the two SST datasets. Levitus MLD climatology was not subjected to further analysis using statistical method as it could not provide a time series comparable to the other datasets. The aim of this analysis is to compare the underlying spatial and temporal signals included in the three datasets. In this subsection, the first EOFs of NEMO SST, HadISST1 and NEMO MLD are shown, followed by a discussion of the leading EOFs after the first mode from previous EOF analysis was removed.

The time series of wintertime average NEMO SST, HadISST1 and NEMO MLD were first constructed and then subjected to EOF analysis. The first leading mode of the three datasets and associated time series are shown in Figure 4.6. For the NEMO SST (Figure 4.6a), positive values are seen in the majority open ocean with its centre in the Irminger basin and central subpolar gyre. Negative values are mainly seen on the eastern shelves, Labrador shelf and the Gulf Stream area. The first leading mode in HadISST1 (Figure 4.6b) shows positive values in almost the entire subpolar basin except a few locations on the eastern continental shelves and near the Gulf Stream area. For the NEMO MLD (Figure 4.6c), the spatial pattern of EOF1 presents negative values in the majority subpolar basin and the negative centre is located south of Greenland. EOF1 explains 41% of NEMO SST total variability, 43% of HadISST1 total variability and 46% of NEMO MLD total variability.

The associated principal components (PCs) of the three EOF1s are shown together with wintertime AMO index over the same period (Figure 4.6d). All the four time series present an overall increasing trend from 1990 to 2007. For the two SST datasets, the first PCs indicate general warming in the subpolar basin over the period while for NEMO MLD the first PC indicates a general shoaling of MLD over the period. These changes coincide with the variation of AMO index on decadal and inter-annual scales (r=0.89, p<0.0001 for NEMO SST, r=0.84, p<0.0001 for HadISST1 and r=0.89, p<0.0001 for NEMO MLD. The two SST datasets show similar spatial pattern and time

series (r=0.95, p<0.0001), both on decadal and inter-annual scales, which suggests that NEMO has successfully simulated the dominant signal of SST variability.

The first leading modes (Figure 4.6) shown previously presented a linear increasing trend and these dominant signals were removed from the corresponding datasets. EOF analysis was then applied to the three datasets with linear trends removed. The resulting EOF1s are shown in Figure 4.7. For NEMO SST (Figure 4.7a), negative values are seen mainly in the open ocean regions and positive values are seen in the shelf seas. The negative centre is located at 50 °N and 35 °W and the positive centre is located in the southern North Sea. For HadISST1 (Figure 4.7b), the spatial pattern shows negative values in the northern subpolar basin while positive values are shown in the southern basin and North Sea. For NEMO MLD (Figure 4.7c), positive values are seen in the majority subpolar basin, while negative values are seen in the Gulf Stream area and shelf seas. The three corresponding PCs are presented together with NAO index in Figure 4.7d. The two PCs from EOF analysis on the two SST datasets agree very well in most years (r=0.55, p=0.02), though from 1999 to 2001 the PCs are of opposite signs. The variation of SSTs coincide the changes of NAO on decadal scale but not on inter-annual scale (r=0.61, p=0.007 for NEMO SST and r=0.45, p=0.06 for HadISST1). The PC representing variation of NEMO MLD shows no clear connection to SST variations whilst its variations coincide with the NAO index prior 1999 (r=0.75, p=0.01 for the first 10 years). These modes explain 34% of the total variability for the de-trended HadISST1, 27% for NEMO SST and 23% for NEMO MLD.

The second leading EOF modes after the linear trend was removed are shown in Figure 4.8. For NEMO SST (Figure 4.8a), the spatial pattern of EOF2 shows general negative values south of 55 °N, west of 18 °W and positive values are seen north of 55 °N, east of 18 °W. The negative centre is located around the Gulf Stream area and the positive centre is located east of Iceland. For HadISST1 (Figure 4.8b), the subpolar basin south of 50 °N and west of 18 °W is occupied by negative values with its centre along the Gulf Stream and its extension. In the subpolar basin north of 50 °N and east of 18 °W, positive values are seen and centres are located east of Iceland and in the southern North Sea. The spatial pattern for NEMO MLD (Figure 4.8c) shows negative values in the subpolar basin south of 55 °N and along the Labrador-Newfoundland shelf. Positive values are distributed in the northern subpolar basin without a noticeable centre. The

variability of the two PCs corresponding to EOF2 of the two SST datasets (Figure 4.8d) agrees well (r=0.55, p=0.02), especially after 1997. The Eastern Atlantic Pattern (EAP) index coincides the two SST PCs (r=0.50, p=0.03 for NEMO SST and r=0.78, p=0.0001 for HadISST1) and overall it agrees better with HadISST1 than NEMO SST. The PC corresponding to EOF2 of NEMO MLD shows opposite signs to SST PCs and EAP index in some years, but none of the time series are statistically significant correlated to PC2 of NEMO MLD. The choice of climate indices are based on the results of EOF analysis on HadISST1 presented in Chapter 2. In the 18-year period, the influence of the Arctic Oscillation (AO) has been supressed while the atmospheric forcing plays a more important role.

These statistical analyses show that NEMO SST has successfully simulated the major signals controlling SST variability during the 18-year period. The leading modes discussed above explain 73% of total variability in NEMO SST and 68% of total variability in HadISST1. In addition to agreeing PCs, the spatial patterns corresponding to the discussed three modes in the two SST datasets also show general similarity and close action centres. These results suggest that NEMO has successfully simulated the main underlying physical mechanisms that control SST variation in the subpolar North Atlantic. For NEMO MLD, the first two EOF modes discussed above coincide with changes of AMO and NAO indices, especially prior to 1999. The dominant AMO signal shown in MLD suggests that the mechanisms, though still under debate, might modulate MLD on multi-decadal variability in a similar way as modulating SST variability. It further suggests a possible connection of SST and MLD, especially around the action centres. The importance of NAO in modulating MLD is possibly conducted through its impact on the strength of westerly wind, and hence vertical mixing [Hurrell and Deser, 2010]. Overall, this statistical analysis confirms the robustness of NEMO in simulating SST and MLD and enhances the confidence of further analysis using these model outputs.

4.3.4   Surface Chlorophyll-a

Two types of surface chlorophyll-a corresponding to non-diatom and diatom are simulated in MEDUSA. In this subsection, the total surface chlorophyll-a (simply a sum of non-diatom and diatom chlorophyll-a, hereafter Chl-a) is compared to satellite

observation during the Sea-viewing Wide Field-of-view Sensor (SeaWiFS) mission over the common period from December 1997 to December 2007. Monthly SeaWiFS data on 9km spatial resolution is used in the following comparison. The aim of this comparison is to evaluate the performance of the model simulation in the subpolar basin. In all the figures, logarithmic colour scale is used to present the large range in Chl-a.

The average summer (June – August) and winter (December—February) distributions of Chl-a in the subpolar basin were compared first (Figure 4.9). In summer (Figure 4.9, a-b), simulated Chl-a concentration (Figure 4.9b) is higher in the northern subpolar basin (north of 50 ºN) than in the observation (Figure 4.9a) by ~ 0.6 mg/m^3, especially in the Labrador Sea, Irminger basin and southeast of Iceland. In the shelf seas, simulated Chl-a concentration is much lower than the observation. Around the Newfoundland shelf and southern North Sea, observational Chl-a is ~ 2.5 mg/m^3 in summer, while the simulated Chl-a is ~ 0.1 mg/m^3. This difference is perhaps related to the fact that the physical model (NEMO) in which MEDUSA is embedded focuses on the simulation of processes in the open ocean while its simulation in the shelf seas is less accurate. Overall, the distribution of average summer Chl-a concentration agrees between observation and model in the open ocean.

In winter (Figure 4.9, c-d), observational Chl-a concentration (Figure 4.9c) is only available generally south of 60 ºN. In the open ocean, Chl-a concentration is very low north of 55 ºN in both datasets, while in regions south of 55 ºN, simulated Chl-a concentration is about 1 mg/m^3 and observation is about 0.25 mg/m^3. In the shelf seas, observational Chl-a concentration is higher than the simulated concentration, especially in the southern North Sea. The differences of Chl-a concentration between open ocean and shelf seas are clearer in observational data.

The zonally averaged annual cycle (also known as the Hovmöller diagram) of Chl-a concentrations in observation and simulation is shown in Figure 4.10. Compared to observation (Figure 4.10a), the increase of Chl-a concentration in April/May is less rapid in simulated data (Figure 4.10b). The amplitude of the annual cycle, however, is larger in simulated data than in observation, with a lower concentration in summer months, especially in the southern subpolar basin south of 50 ºN. The simulated bloom

peak is also higher than that in observation, which is about 0.6 mg/m^3 higher in the region around 60 ºN and about 0.4 mg/m^3 in the southern areas. The lower summer concentration is partially related to the assumption of geographically invariant nutrient kinetics, which might prevent phytoplankton adapting to seasonally low-nutrient conditions in the model [Yool *et al.*, 2011].

Figure 4.10 also show that in the subpolar basin south of 50 ºN, seasonal low Chl-a condition occurs and lasts about 3-5 months, which is different to the typical annual cycle in the northern basin. Surface Chl-a is hence averaged over the two halves of subpolar basin, separating at 50 ºN, for both NEMO and SeaWiFS Chl-a to compare its inter-annual variability. The spatial variability is calculated as the SEM of each half of the basin and is indicated as the error bar in all panels of Figure 4.11 and 4.12. The monthly time series averaged over the northern half of subpolar basin (Figure 4.11a) generally agrees between NEMO (black) and SeaWiFS Chl-a (red line), with observed Chl-a higher than the simulation in summer and shows stronger inter-annual variability. The shape of Chl-a annual cycle is also more stable in the simulation as the observed Chl-a has anomalous high Chl-a in winter months in some years (e.g. December 1999 and January 2001), but remains at similar low levels in all 18 years in NEMO. In 2006, SeaWiFS Chl-a shows an exceptional high Chl-a concentration in January, but the model did not reproduce this. Overall, the two time series show statistically significant correlation in the 10-year period with r=0.65 and p<0.0001, dominated by the annual cycle.

In Figure 4.11b-e, the time series is obtained by first calculating the parameter of interest at each grid point (e.g. maximum Chl-a minus minimum Chl-a at each grid point for each year in Figure 4.11b), then average over the northern basin with error bars indicating the spatial variability. The seasonal range of surface Chl-a is usually higher in NEMO than in SeaWiFS, except in 1998 and 1999. The two time series shows no statistically significant correlation, which is dominated by the disagreement between the two in 2002. The timing of bloom initiation (Figure 4.11c), which is defined as the first month when Chl-a exceeds the annual median by 5%, remains relatively stable in the late March or early April during the 10-year period for both observation and simulation and the two time series show statistically significant correlations in the last 9 years (r=0.74, p=0.02). In the northern basin, the average bloom peak (Figure 4.11d) is

higher in SeaWiFS than in NEMO simulation in most years except 1998,1999 and 2002. The differences between the two bloom peak time series get smaller towards the end of the period, especially between 2004 and 2006 the differences is within the spatial variability range. The bloom peak (Figure 4.11e) is reached in early June in the observation but about a month earlier in NEMO. The inter-annual variability of the timing of bloom peak remains within 15-days/half month for both time series. Weak correlation is found between the timing of bloom peaks in the last 6 years (r=0.78, p=0.04).

In the subpolar basin south of 50 ºN, the Chl-a annual cycle is different between NEMO and SeaWiFS Chl-a (Figure 4.12a): the observation shows a stronger spring bloom around April/May and a weaker bloom in October, then Chl-a decreases again and annual minimum is seen in winter months; simulated Chl-a starts to increase in November/December and keeps accumulating through winter, the annual peak is seem around April/May with annual minimum in summer months. This possibly because the nutrient-limitation is too strong and the rate of phytoplankton making use of recycled nutrients is too low in the model compared to real life in the southern subpolar basin. Thus phytoplankton starts to grow when the MLD is deepest and nutrients are most abundant in NEMO. The seasonal range (Figure 4.12b) of surface Chl-a is also bigger in the model due to the exaggerated annual minimum. The bloom initiation (Figure 4.12c) is constantly one month earlier in the model than in the observation during the 10-year period and the two time series are significantly correlated (r=0.67, p=0.03). The inter-annual variability of the maximum Chl-a (Figure 4.12d) shows no significant correlation between NEMO and SeaWiFS, SeaWiFS maximum Chl-a is higher than NEMO Chl-a in the first two years but is lower in the last 8 years. The maximum Chl-a is reached about ¼ month earlier in NEMO than in SeaWiFS, except in 2002 and 2007. The two time series also shows statistically significant correlation with r=0.81, p=0.004.

Overall, the model simulation agrees with SeaWiFS observation in the subpolar basin over the period from January 1998 to December 2007. In the basin north of 50 ºN, the general annual cycle is well simulated during the 10-year period. The timing of bloom initiation agrees between the two time series, the timing for bloom peak is about one month earlier for NEMO Chl-a and the spatial variability for both time series is 15 days. In the basin south of 50 ºN, the nutrient-limitation assumed in the model is too strong

compared to reality as its annual minimum still remains around 0.4 mg chl/m^3 rather than close to zero in the model. Even the Chl-a values have bigger discrepancies between NEMO and SeaWiFS in the southern basin, the inter-annual variability of the time of bloom initiation and peak are more significantly correlated. However, NEMO blooms lead SeaWiFS blooms by ~½ month at the initiation and peak stages, which is also associated with the assumption that phytoplankton starts to accumulate when nutrients is most abundant in this region. Other differences between observation and simulation are seen in the shelf seas in both summer and winter. In the open ocean, the datasets agree better in summer than in winter, where simulated Chl-a concentration is much higher than the observed concentration in winter. This comparison suggests that, even though the simulated Chl-a concentration shows discrepancies with observations, its performance in capturing Chl-a seasonal distribution and average annual cycle in the subpolar basin is generally satisfactory. The satellite observation contains ~31% errors on the global scale due to the influence of atmosphere and algorism used to correct the received signals, which is lower in the open ocean (~28%) and higher on the shelves (~33%) [Gregg and Casey, 2004]. The high latitudes also suffers from sampling biases that is 20% higher than the global annual mean and could be up to 80% in some months [Gregg and Casey, 2007]. This uncertainty should be bear in mind when considering the comparison between NEMO Chl-a and satellite derived Chl-a.

4.4   Summarising Discussion and Conclusion

In this chapter, the coupled model used in the study, the physical model NEMO and the biogeochemical model MEDUSA, were introduced. The simulated MLD, SST and surface Chl-a were then compared to observations, focusing on its spatial distribution and decadal variability. The aim of this comparison was to assess the performance of the models and prepare for the further detailed analysis of physical mechanisms controlling phytoplankton variability in the following chapter using the outputs from these models.

The seasonal mean SSTs were very well simulated in NEMO over the period of 1990 – 2007. For the seasonal SST anomalies between the period of 1990—1994 and the period of 1995 – 2007, simulated SST anomalies presented more pronounced regional boundaries, especially in the Irminger basin and Iceland basin. The overall patterns of

SST anomalies were generally reproduced. Averaged long-term simulated maximum MLD, defined using turbulence criterion, over the period from 1990 to 2007 was compared to Levitus MLD climatology defined using three criteria. The three types of MLD climatology showed major differences in the Labrador Sea, where the maximum MLD was ~ 1000 (2000)m deeper using the potential temperature difference criterion than using the potential density difference (variable potential density) criterion. It is, therefore, difficult to quantitatively evaluate MLD simulation using the climatology. However, NEMO successfully simulated the distribution of maximum MLD pattern, which showed deep mixing in the Labrador Sea, Irminger basin, northern Iceland basin and Rockall Trough. This pattern agrees well with all three types of maximum MLD climatology. For the minimum MLD, three types of MLD climatology showed similar patterns, with MLD of ~ 35m in the central subpolar region and shallower minimum MLD towards the shelves. The simulated minimum MLD agrees very well with the three types of MLD climatology for both the distribution pattern and range of depths.

A statistical comparison of simulated winter SST and MLD and observed winter SST was performed using an EOF analysis. The first leading modes of the two SST datasets presented positive values in the majority of subpolar basins and negative values for MLD. The corresponding principal components of the three datasets showed a gradual increasing signal, which was significantly correlated to AMO index. These signals suggested an increasing SST trend and a shoaling MLD trend over the period. This linear trend was then removed from the datasets and EOF analysis was applied to the three resulting datasets. The EOF1s of the two SST datasets after linear trends were removed presented positive values in the open-ocean and negative values in the shelf seas; values of opposite signs were seen for the EOF1 of MLD after the linear trend was removed. All three principal components corresponding to these EOF1s after the linear trends were removed were linked to the NAO index. This suggested that lower (higher) SSTs and deeper (shallower) MLD was associated to positive (negative) NAO, especially for the first 10 years. For the EOF2 after linear trends were removed, all three datasets presented similar distribution in the subpolar basin, with positive values located north of 55 ºN and negative values south of 55 ºN. The two principal components corresponding to SST EOF2s showed significant correlation to EAP and no correlation was found between EAP and MLD.

This analysis suggests that simulated SST time series has successfully reproduced the major variation signals in SST observation on decadal scale. Though it is difficult to compare the resulting major signals in simulated MLD variability to observation on decadal scale in the same manner as for SST, the similarity between the variability of leading MLD and SST EOF modes, as well as with major climate indices, enhances the confidence in MLD simulation. Overall, the statistical comparison confirms the agreement previously seen in visual comparison.

Seasonal distribution of simulated surface Chl-a agrees generally well with SeaWiFS Chl-a, with major discrepancies seen in the shelf seas in summer and southern open ocean in winter. The comparison of the zonally averaged annual cycle suggests that simulated surface Chl-a concentration is higher than observation in winter and spring, but lower than observation in summer. The region potentially influenced by nutrient depletion is also larger in the model than in the observed data. The values of surface Chl-a agrees well in the subpolar basin north of 50 °N but the inter-annual variability only shows statistical significant correlation between NEMO and SeaWiFS Chl-a for the timing of bloom peak. The actual values of surface Chl-a and timing of bloom initiation and peak show bigger difference between model and observation in the subpolar basin south of 50 °N but the inter-annual variability shows more significant correlation for the timing of bloom initiation and peak. The main reasons for these model-data mismatches are twofold: (1) the physical processes in the open ocean are better understood and reproduced in the physical model; and (2) the assumption that the nutrient kinetics' impact on phytoplankton growth increases the Chl-a concentration in the southern subpolar in winter with relatively deep mixing and limits the ability of phytoplankton to adapt to seasonally low-nutrient conditions in summer because the model assumes a weaker nutrient recycling ability than in reality.

In conclusion, NEMO and MEDUSA have reproduced the major distribution and variability seen in the parameters of interest. Simulation of SST is closest to observation, possibly due to a better understanding of the processes affecting SST variation. The simulation of MLD successfully reproduced the distribution of maximum and minimum MLDs in the subpolar basin. A glimpse of the difficulty in measuring MLD in the ocean can be seen from the discrepancies in the MLD climatology using three criteria. The simulation of surface chlorophyll-a presents seasonal distribution and

average annual cycle generally agrees with satellite observation, though the limitation of model simulation in the shelf seas should be considered in future analysis. The model simulations of SST, MLD and Chl-a present spatial distribution and temporal variability that agrees well with observations. Thus, model outputs are proved to be an ideal tool for analysing physical and biological processes in the subpolar North Atlantic, where observations of MLD and chlorophyll-a concentration are limited spatially and temporally.

Table 4.1 Model State Variables from MEDUSA

Symbol	Name	Units
P_n	Non-diatom phytoplankton	mmol N m^{-3}
P_d	Diatom phytoplankton	mmol N m^{-3}
Chl_{Pn}	Chlorophyll in non-diatoms	mg chl m^{-3}
Chl_{Pd}	Chlorophyll in diatoms	mg chl m^{-3}
Pd_{Si}	Diatom phytoplankton (silicon)	mmol Si m^{-3}
$Z\mu$	Microzooplankton	mmol N m^{-3}
Zm	Mesozooplankton	mmol N m^{-3}
D	Slow-sinking detritus	mmol N m^{-3}
N	Dissolved Inorganic Nitrogen (DIN)	mmol N m^{-3}
S	Silicic acid	mmol Si m^{-3}
F	Iron nutrient	mmol Fe m^{-3}
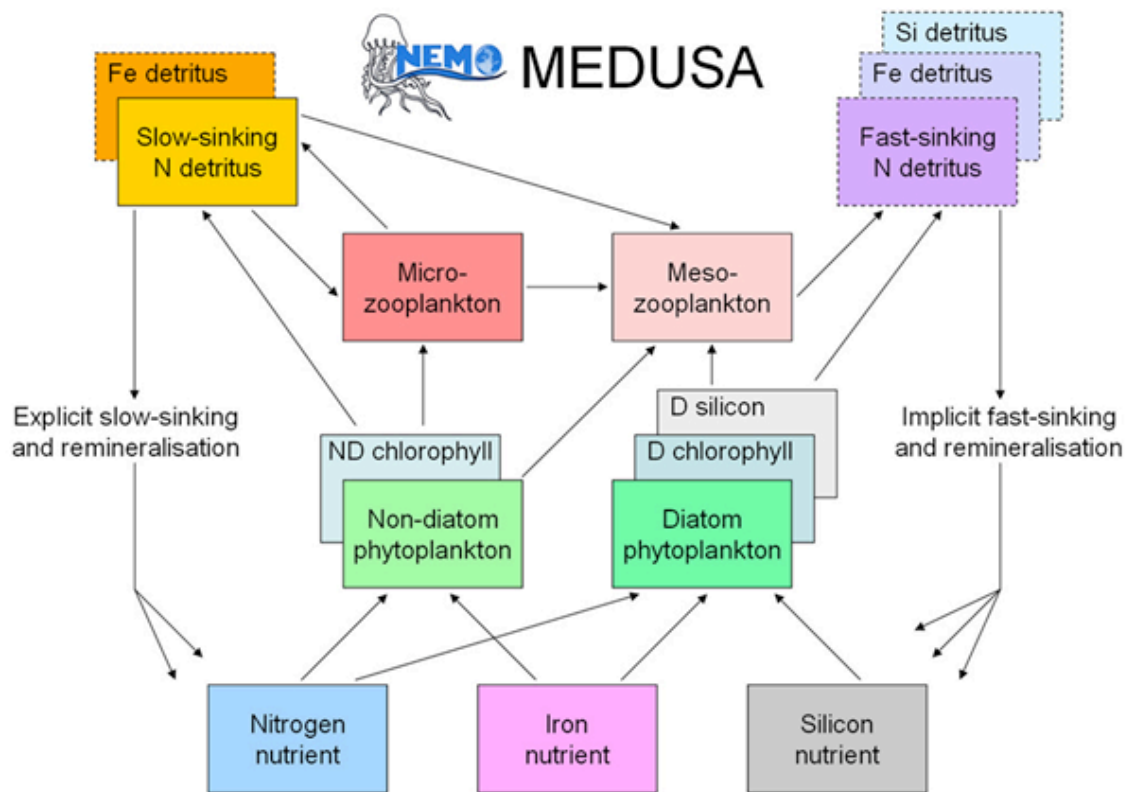
Figure 4.1 Schematic diagram of the components and interaction of these components across the trophic levels in the MEDUSA model. Boxes with solid boarders indicate explicitly modelled state variables and boxes with dashed borders indicate implicitly modelled state variables [Yool *et al.*, 2011].
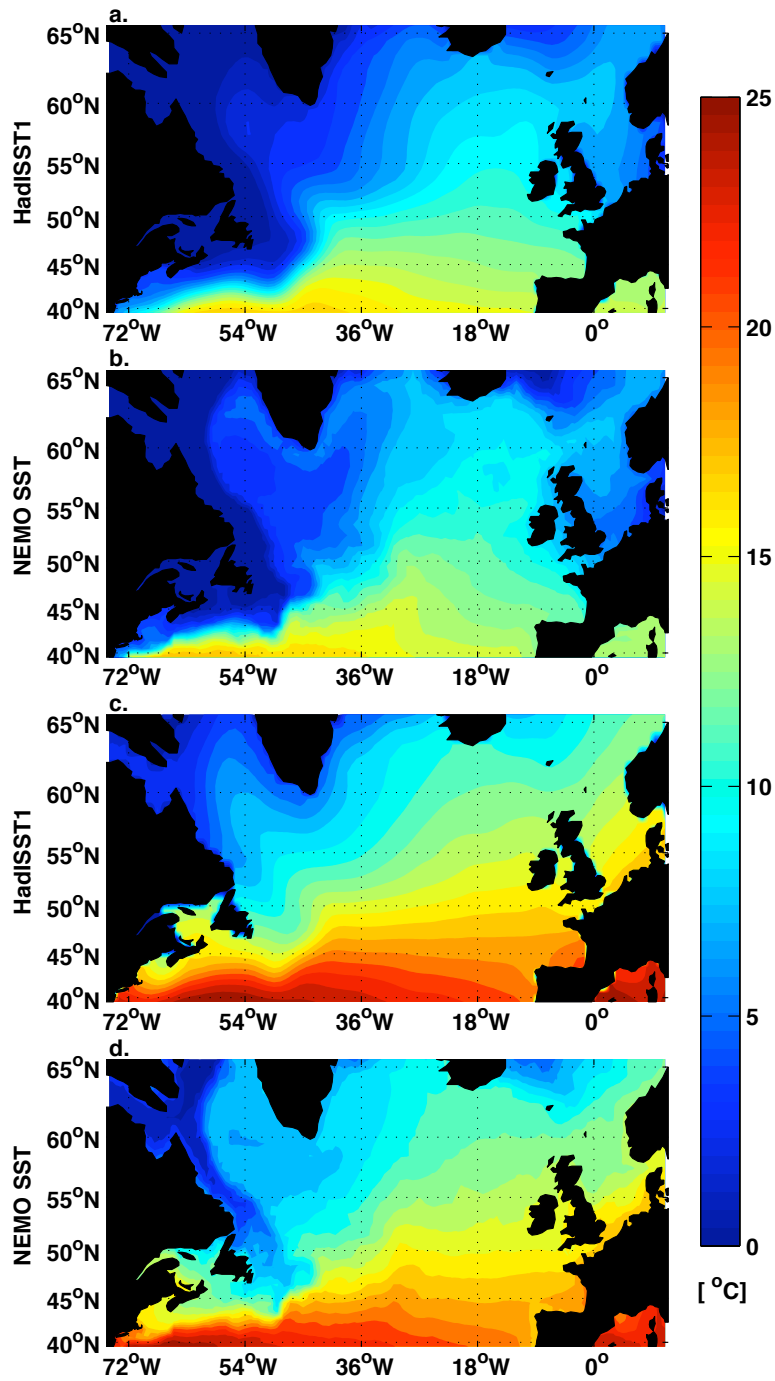
Figure 4.2 The average (a-b) winter and (c-d) summer SSTs over the period 1990 – 2007 using (a and c) HadISST1 and (b and d) NEMO SST.
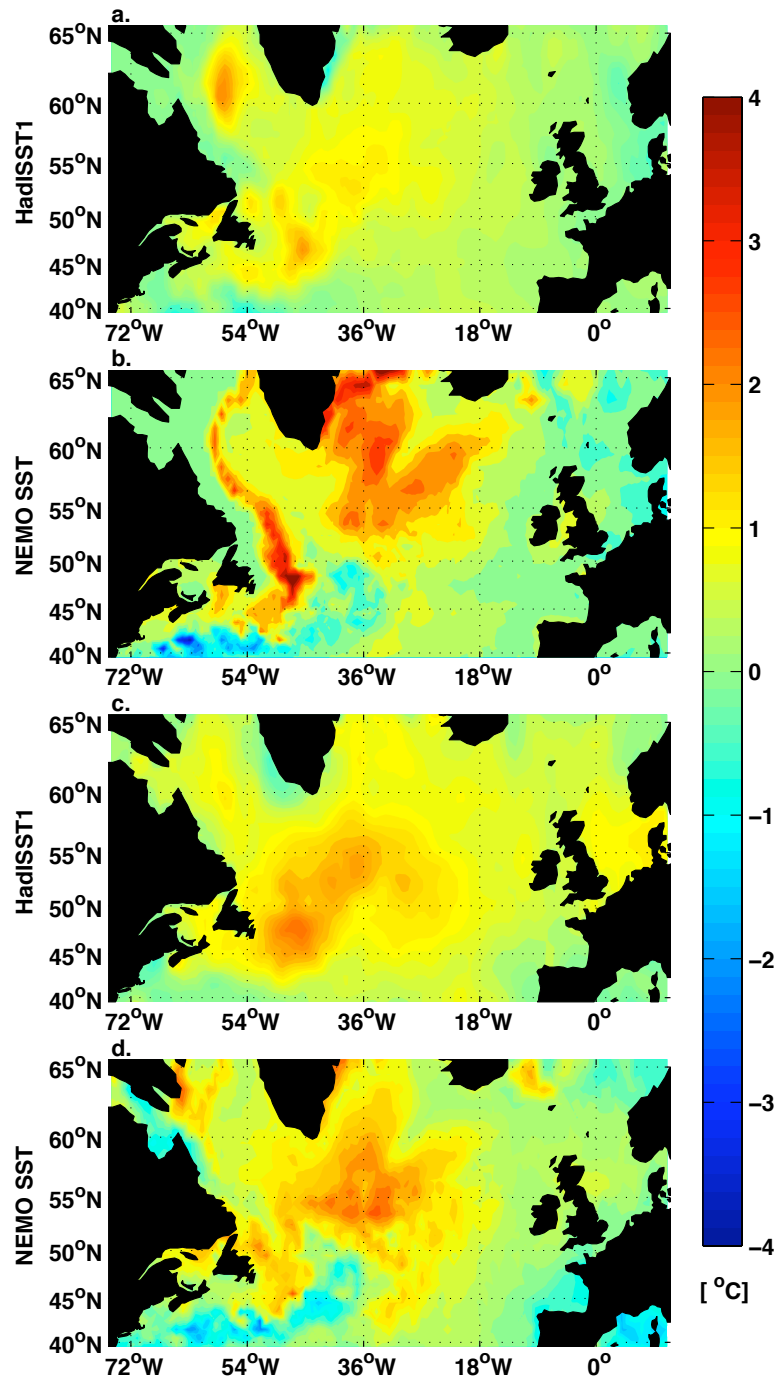
Figure 4.3 The SST anomalies in (a-b) cold and (c-d) warm extremes in the period 1995 – 2007 compared to the period 1990 – 1994, using (a and c) HadISST1 and (b and d) NEMO SSTs. The anomalies are calculated by subtracting the average extreme SST of the earlier period from the average extreme SST of the later period. Positive values indicate warming signal in the later period and negative values indicate cooling signal in the later period.
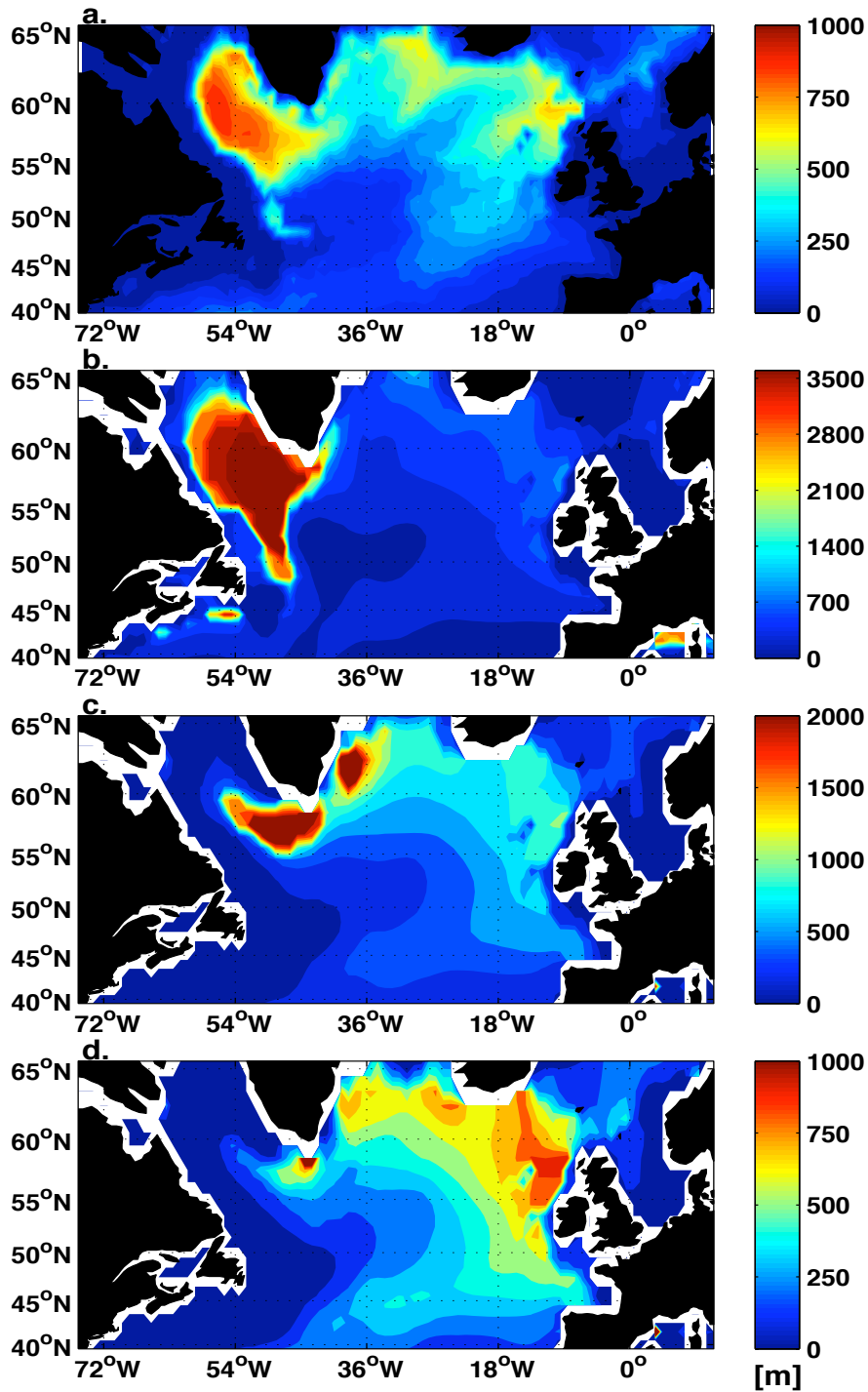
Figure 4.4 The long-term average of the maximum MLD over the period 1990 – 2007 in (a) NEMO MLD, (b) Levitus MLD climatology using δ_θ criterion, (c) Levitus MLD climatology using δ_σ criterion and (d) Levitus MLD climatology using variable potential density criterion. Please note the colour scales in the four panels are different.
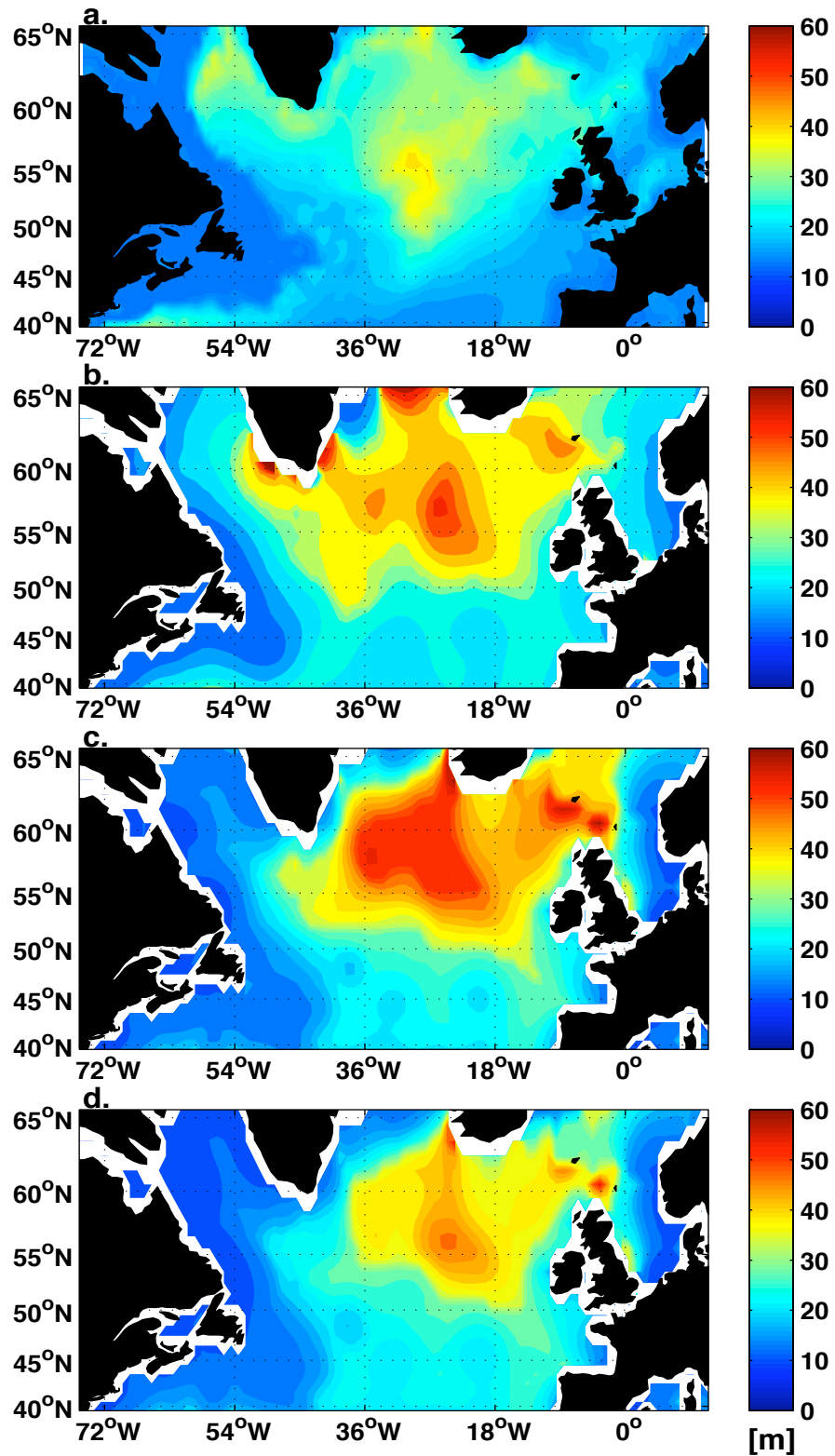
Figure 4.5 The long-term average of minimum MLD over the period 1990 – 2007 in (a) NEMO MLD, (b) Levitus MLD climatology using δ_θ criterion, (c) Levitus MLD climatology using δ_σ criterion and (d) Levitus MLD climatology using variable potential density criterion.
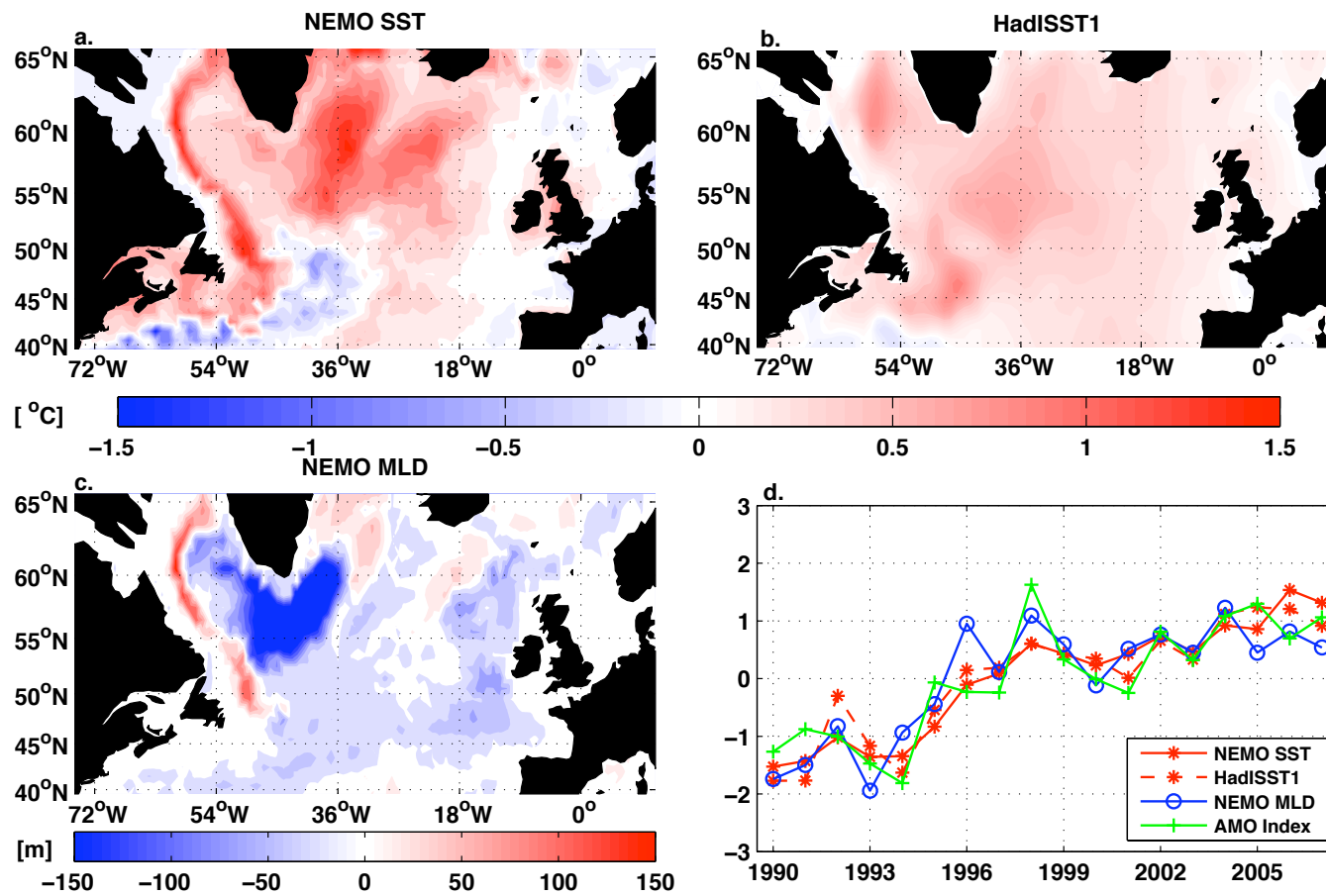
Figure 4.6 The first leading EOF mode on (a) NEMO SST, (b) HadISST1 and (c) NEMO MLD over the period 1990 – 2007. The associated Principal Components (PCs) and AMO index are shown in (d).
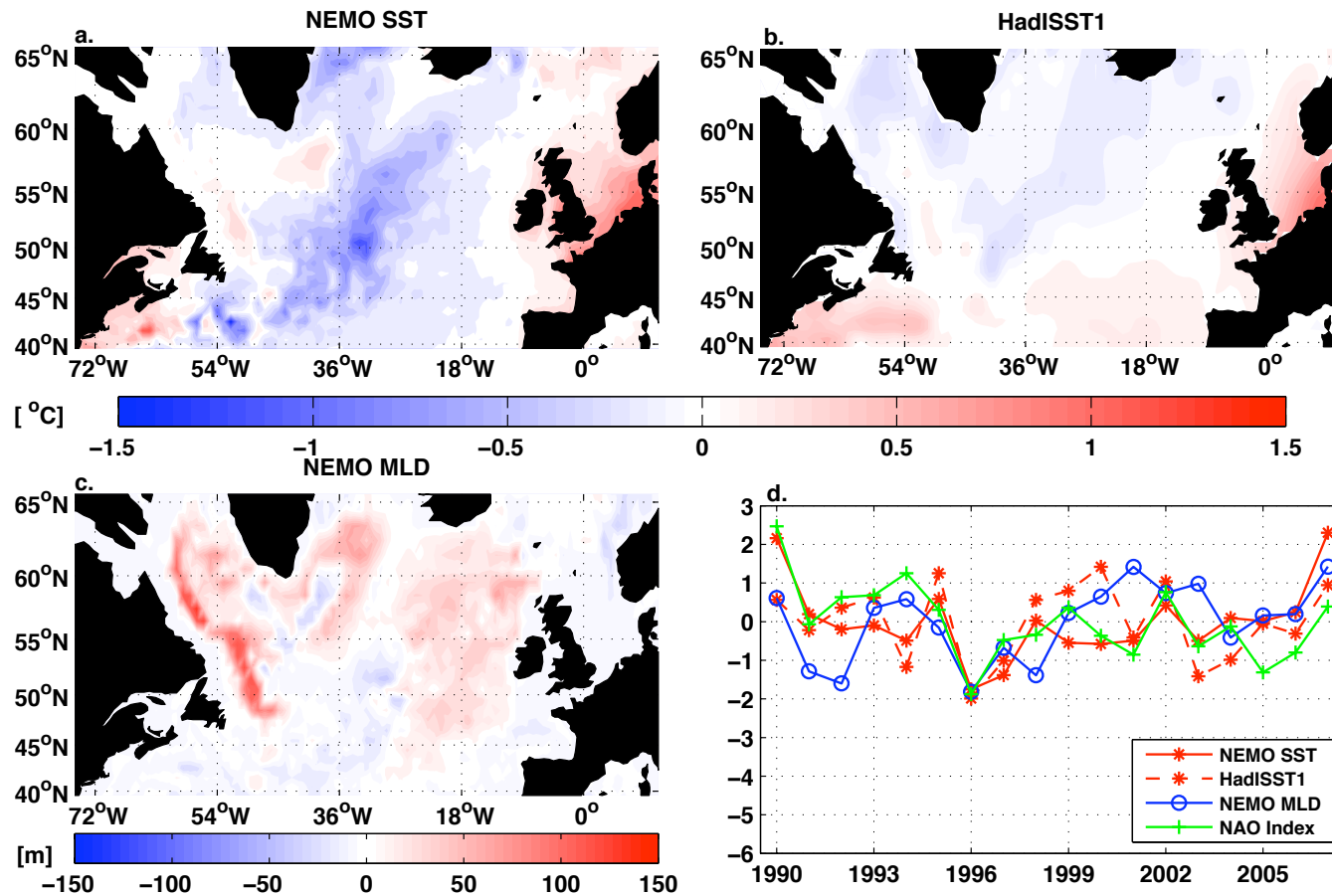
Figure 4.7 The first leading EOF mode on (a) NEMO SST, (b) HadISST1 and (c) NEMO MLD over the period 1990 – 2007, with the linear trend removed. The associated PCs and NAO index are shown in (d).
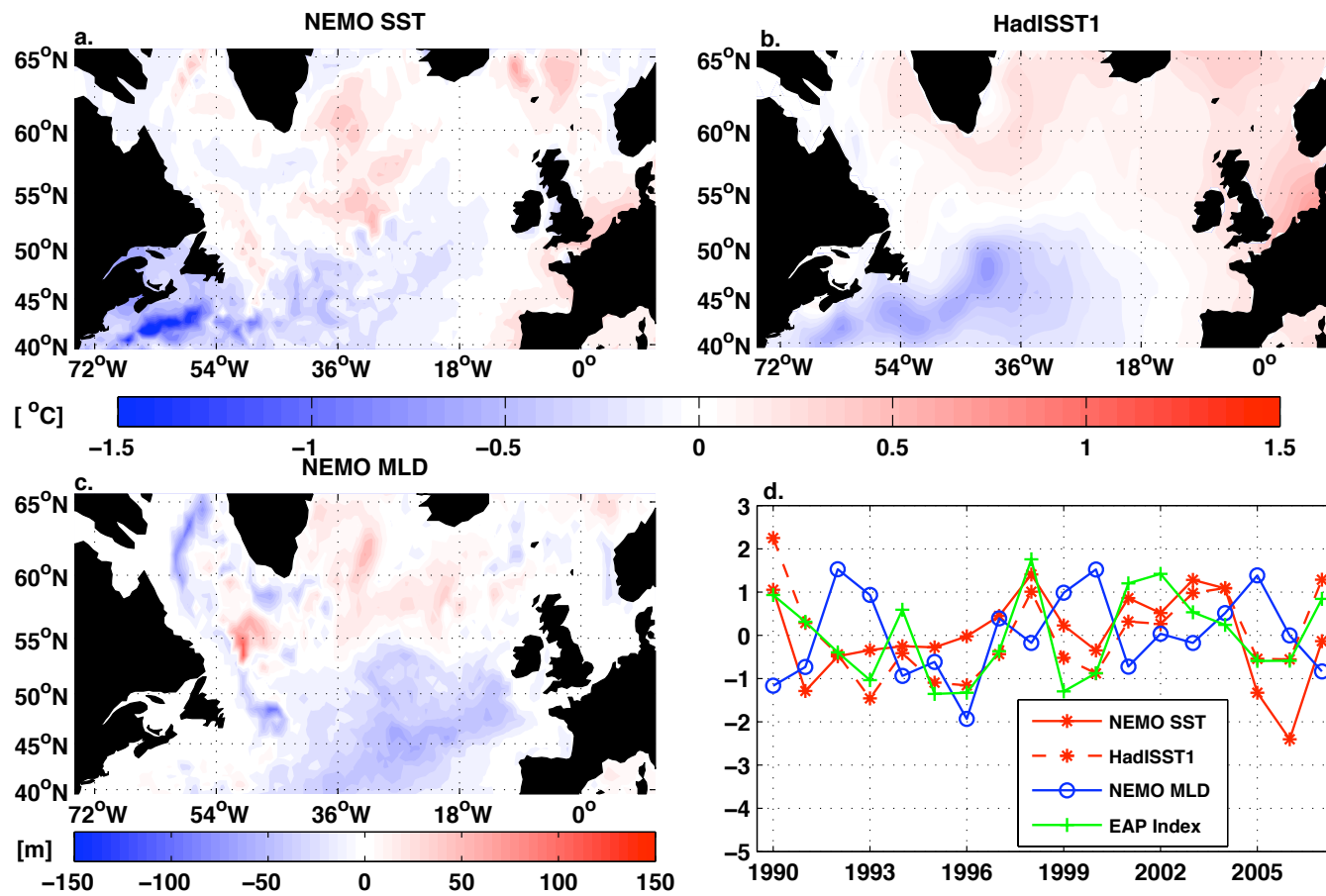
Figure 4.8 The second leading EOF mode on (a) NEMO SST, (b) HadISST1 and (c) NEMO MLD over the period 1990 - 2007, with the linear trend removed. The associated PCs and EAP index are shown in (d).
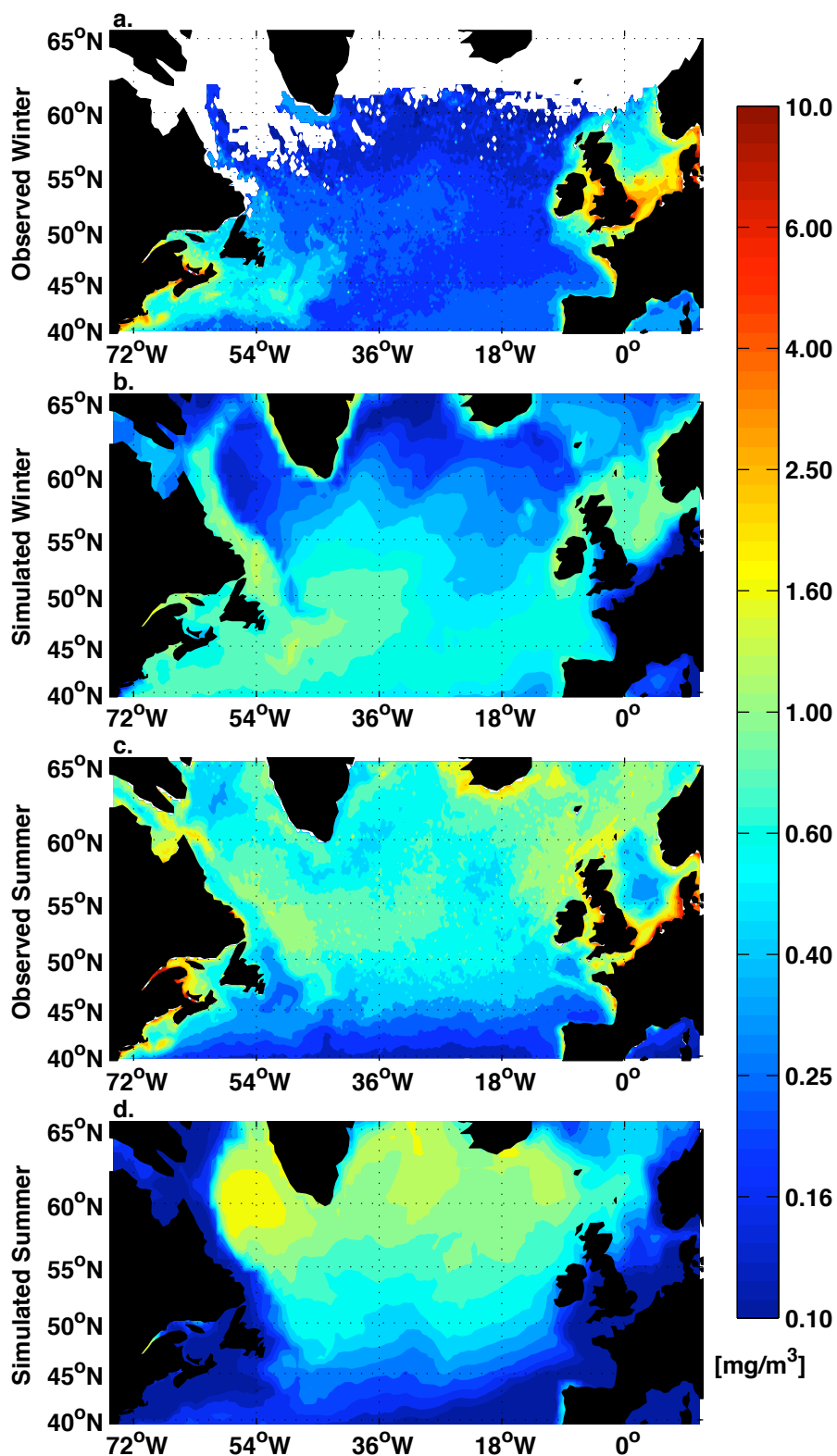
Figure 4.9 Observed (SeaWiFS, a and c) and simulated (b and d) surface Chl-a for northern winter (a-b, December – February) and northern summer (c-d, June – August) in the subpolar basin. The unit is mg chl. m^{-3} and plotted on a logarithmic scale.
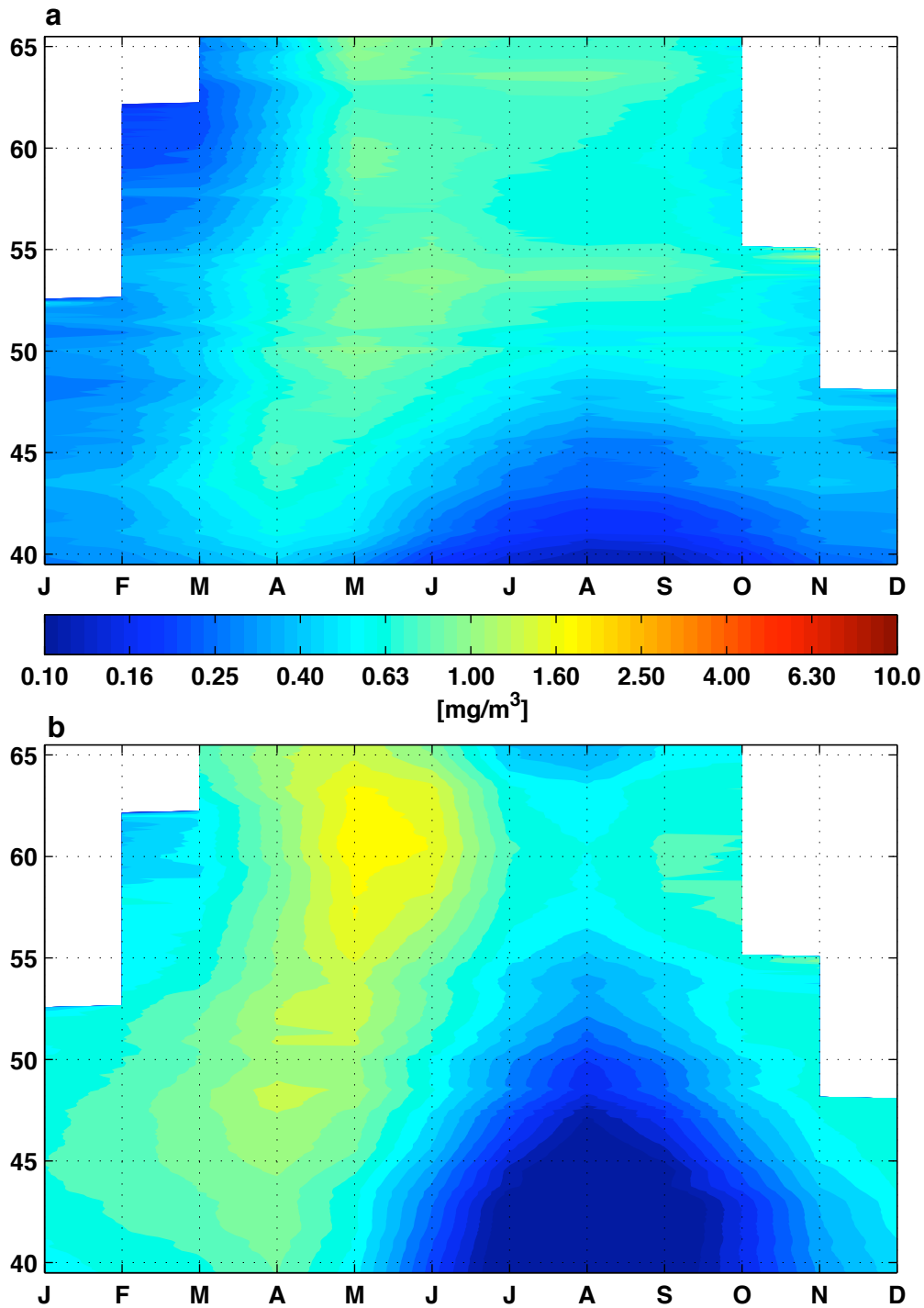
Figure 4.10 Hovmöller diagrams of observational (a, SeaWiFS) and simulated (b, MEDUSA) monthly surface Chl-a, averaged zonally for the subpolar basin. The unit is mg chl. m^{-3} and plotted on a logarithmic scale.
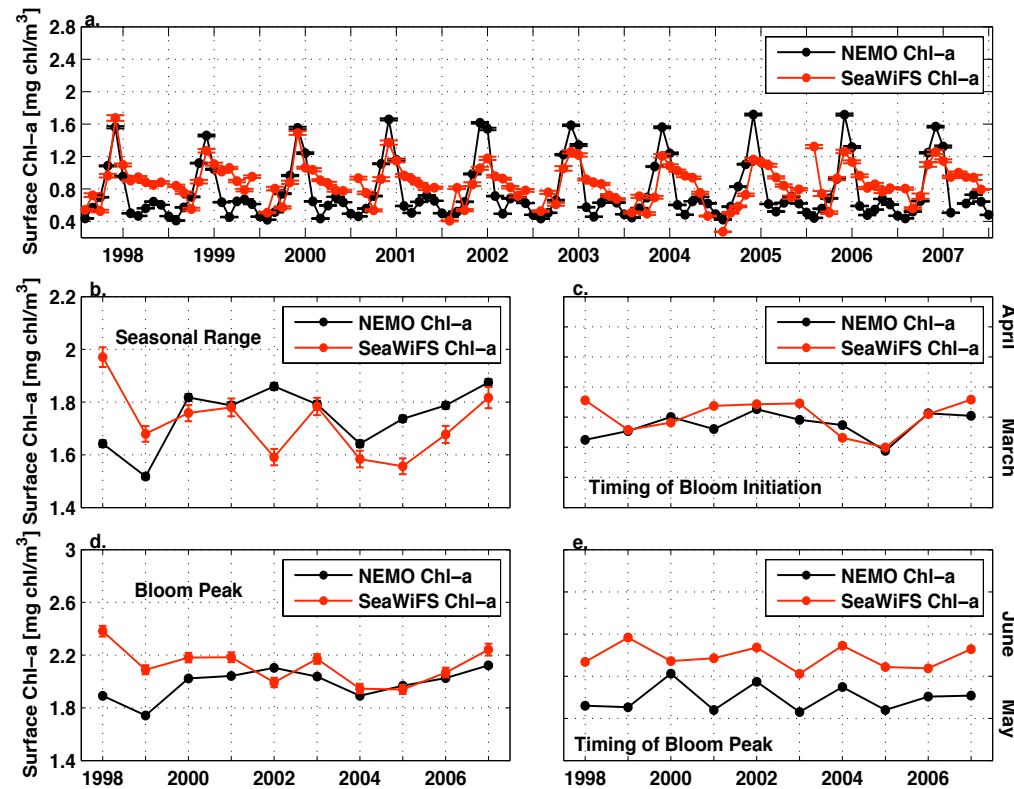
Figure 4.11. The comparison between NEMO surface Chl-a (black lines in all panels) and SeaWiFS Chl-a (red lines in all panels) in the suboplar basin north of 50 °N from January 1998 to December 2007: (a) average inter-annual variability over the northern basin; (b) seasonal range of Chl-a annual cycle; (c) the timing of spring bloom initiation; (d) the maximum Chl-a and (e) the timing of bloom peak. The errorbars in all panels indicate the spatial variability over the basin north of 50 °N.
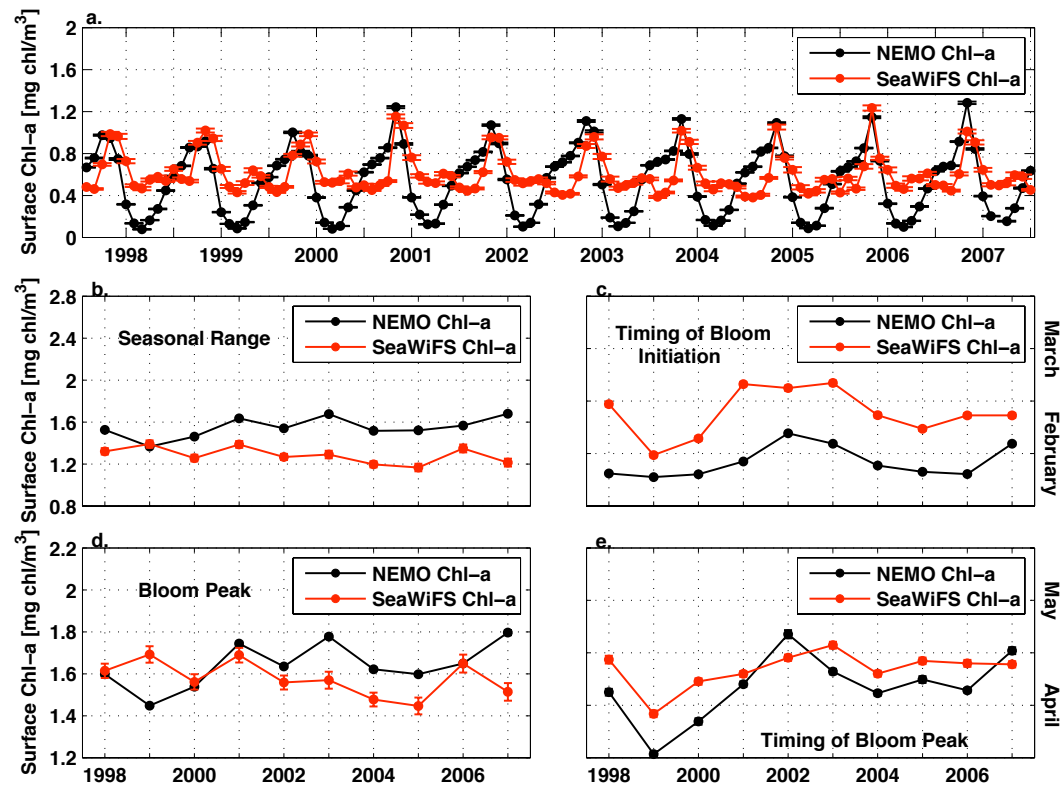
Figure 4.12. The comparison between NEMO surface Chl-a (black lines in all panels) and SeaWiFS Chl-a (red lines in all panels) in the suboplar basin south of 50 °N from January 1998 to December 2007: (a) average inter-annual variability over the northern basin; (b) seasonal range of Chl-a annual cycle; (c) the timing of spring bloom initiation; (d) the maximum Chl-a and (e) the timing of bloom peak. The errorbars in all panels indicate the spatial variability over the basin south of 50 °N.

Chapter 5

Simulation of Physical Influences on Phytoplankton Variability, Part Two: Model Result

5.1   Introduction

In Chapter 2, decadal to multi-decadal variability of SST annual cycle was described. On decadal and longer scales, increased phytoplankton abundance coincides with the surface warming in cold and well-mixed regions, suggesting an impact of SST on surface Chl-a. Comparatively, a decrease of the phytoplankton abundance has been found in warm and stratified regions, suggesting that SST also impacts phytoplankton indirectly through stratification [Reid *et al.*, 1998; Edwards and Richardson, 2004; Häkkinen and Rhines, 2004; Richardson and Schoeman, 2004; Sarmiento *et al.*, 2004; Martinez *et al.*, 2009]. However, such connection between SST and phytoplankton could only be found in a few locations in the subpolar basin, while in the interior subpolar gyre no direct links were established. This indicates that SST possibly impacts phytoplankton variation mainly through indirect processes, though such links have not been proved.

In Chapter 4, the physical and biogeochemical models used in this study were introduced. Model performances were validated by comparing model outputs to available observation data. The comparison confirmed that NEMO (Nucleus for European Modelling of the Ocean) and MEDUSA-1.0 (Model of Ecosystem Dynamics, nutrient Utilisation, Sequestration and Acidification) can reproduce the major variation pattern in the subpolar North Atlantic for sea surface temperature (SST), mixed layer depth (MLD) and surface chlorophyll-a (Chl-a). In the following section, the links between physical and biological processes in the subpolar basin are analysed and discussed using model outputs.

In the water column, the upper layer where light is higher than 1% of light at surface is usually referred to as the "euphotic zone" (or photic zone) [Margalef, 1978]. Physical modulation of phytoplankton variation is mainly through adjusting the availability of nutrients and the accessibility to light [Lévy *et al.*, 2005]. In the subpolar North Atlantic, both conditions are closely related to thermal stratification: the stratified water column inhibits bringing nutrients from depth, but is exposed to sufficient light whereas active vertical mixing brings nutrients from deeper layers but the mean light level in the mixed layers is reduced. Thus, under shallow stratification, phytoplankton grows rapidly with sufficient light, but consumes nutrients quickly and nutrient limitation curtails further

bloom. Under a deep convection period, surface nutrients are sufficient for phytoplankton growth, but vertical mixing can bring phytoplankton cells out of the euphotic zone and disturb photosynthesis through light-limitation, which could cease phytoplankton bloom [Taylor and Ferrari, 2011a]. In the ocean, stratification can be described using MLD and this parameter has been studied as an important factor affecting phytoplankton growth in addition to SST [e.g. Sverdrup, 1953; Henson *et al.*, 2009b; Boss and Behrenfeld, 2010].

In the following section, the relation between SST and MLD in the subpolar North Atlantic on an inter-annual scale is first discussed using model MLD with SST from both model and observation (HadISST1). The impact of MLD on phytoplankton growth is then examined, focusing on its modulation through nutrient availability. The needs and methods used to define ecological provinces in the subpolar region are discussed, followed by the resulting province scheme. Model biological parameters are then compared to available CPR observation in each province, aiming to select the province(s) with the most reliable data to study the physical mechanism controlling phytoplankton growth in each province. The resulting locations and more detailed analysis of the controlling mechanism are presented next. The chapter ends with a summarising discussion and conclusion.

5.2   Links between SST and MLD

In the northern and eastern subpolar North Atlantic, SST and MLD are amongst the most important physical parameters that determine phytoplankton bloom dynamics. Both parameters are influenced by atmospheric and oceanic processes, such as surface heat fluxes, wind and circulation; the two parameters also interact between one another [Carton *et al.*, 2008]. In winter, large buoyancy loss occurs in this region, which decreases SST and also leads to deep convection. Deep mixing brings cold deeper water to the surface, which further reduces SST. In summer, insolation increases significantly and wind weakens, which combines with increased SST and leads to stratification. It is highly possible that the variability of SST and MLD is connected. Some phytoplankton species, e.g. diatoms, are less sensitive to SST than to MLD, whilst most species are sensitive to MLD. Once the connection between SST and MLD is established, the influence of SST on phytoplankton through modulating MLD can be estimated.

In Chapter 2, four representative locations were selected to show annual cycle amplitude (ACA) variability. Here, the direct links between SST and MLD are firstly examined at these four locations. SST and MLD anomalies in winter and summer are shown in Figure 5.1 and 5.2, respectively. In winter, the North Sea shows the smallest MLD anomalies (less than ± 1m) while in the south Reykjanes Ridge anomalies are of ~ ± 240m. The two SST time series are in good agreement in temperature range and pattern, though in the south Reykjanes Ridge, NEMO SST is ~ 0.5 ºC colder than HadISST1 before 1997 and warmer after 1997. In the two oceanic locations, the southern Rockall Trough and south Reykjanes Ridge, shallower than average winter MLD occurs during warmer than average SST. The correlation coefficients between MLD and NEMO SST (HadISST1) are r=-0.64, p=0.005 (r=-0.45, p=0.06) in the southern Rockall Trough and r=-0.88, p<0.0001 (r=-0.8, p=0.0001) in the south Reykjanes Ridge. Such a link is less clear in the two shelf locations, which could be either because the whole water column is well mixed during winter in the shelf seas so further decrease in SST is not manifested in MLD or because the MLD anomalies in the shelf seas are too small to be reflected in SST.

In summer, MLD anomalies are less than ± 10m in all the four locations and anomalies are slightly bigger in the oceanic locations than in the shelf seas. The two SST anomalies agree very well in both temperature range and pattern in all locations. SST anomalies are bigger in the shelf seas than in the oceanic locations. Warmer (colder) than average SST now corresponds to shallower (deeper) than average MLD better than in winter for the Newfoundland Shelf, perhaps because summer mixing is not through the whole water column so the change of SST manifested in MLD. The correlation coefficients using NEMO SST (HadISST1) are r=-0.75, p=0.0007 (r=-0.71, p=0.0009) on the Newfoundland shelf. Major forces for turbulence in the shelf regions include wind, density gradient and tides [Han *et al.*, 2008]. All these variations are connected with SST, so the link between MLD and SST is clearer in summer. The main driving force of turbulence in the open ocean is heat flux and wind stress, in summer the heat loss is largely reduced as a result of the increased air and ocean temperatures and the wind is also weaker. The connection between SST and MLD is not clear and the two time series are not correlated in the south Reykjanes Ridge.

A linear regression analysis was then applied to winter and summer NEMO MLD and SST anomalies at each grid point, following Eq. 5.1:

$$Y = X \times b \qquad\qquad\qquad \text{Eq. 5.1}$$

where Y and X are matrices of average MLD and SST anomalies, respectively, and b is the vector of regression coefficient in this linear model. The resulting coefficient shows the change of MLD corresponding to 1 ℃ SST increase with a unit of $m\,^{\circ}C^{-1}$.

In winter (Figure 5.3a), clear negative MLD change corresponding to SST increase is found in the area south of Greenland, Rockall Trough and the Porcupine Abyssal Plain. In the shelf seas, no MLD change is seen with changing SST. This suggests that in NEMO, SST is modulated strongly by MLD in regions where deep winter mixing occurs, whilst in regions where winter MLD is shallow other parameters such as surface currents, may play a more important role. In summer (Figure 5.3b), negative coefficient is found in the eastern subpolar basin, where MLD is ~100m deep, whilst no linear connection between MLD and SST is seen in the western basin where MLD is much shallower and surface current (e.g. the Labrador Current) plays an important role (see Figure 4.5).

From this analysis, direct connections between MLD and SST are only established in regions with deep mixing. In these areas, colder than average SST usually corresponds to deeper than average MLD and vice versa. The regression coefficient is equivalent to an MLD anomaly of ~ -200m in winter and ~ -10m in summer with 1 ^{o}C SST increase. In the rest of the subpolar basin, however, the direct connection between SST and MLD is invalid and SST is mainly modulated by other parameters than MLD in these regions.

5.3   Links between MLD and Biological Parameters

5.3.1   Mechanisms

The upper mixed layer is considered to be neutrally stable and phytoplankton distributes evenly within the whole layer [Townsend *et al.*, 1994]. As briefly introduced in section 5.1, the seasonal variation of MLD, especially the maximum MLD, determines the nutrients available for phytoplankton consumption in the upper mixed layer [Henson *et*

al., 2009b]. Deeper than average maximum MLD increases available nutrients, which can support more phytoplankton growing and potentially stronger spring-summer phytoplankton concentration, when other factors remain unchanged. Conversely, deeper than average maximum MLD reduces average light level and it takes longer for stratification to establish and thus may delay phytoplankton bloom and hence lower overall phytoplankton production [Henson *et al.*, 2009a]. The actual ecological response of the variation of maximum MLD may vary under different conditions.

In the North Atlantic, MLD is also a critical parameter that affects the initiation of the phytoplankton spring bloom. Following Sverdrup (1953), the most accepted hypothesis states that a bloom occurs when the average growth rate exceeds the loss rate and such condition is only met when MLD is shallower than a "critical depth". The "critical depth" refers to the depth above which the rate of photosynthesis exceeds the rate of respiration, which could be calculated using various methods [Lalli and Parsons, 1997; Frajka-Williams and Rhines, 2010; Taylor and Ferrari, 2011b]. When MLD is shallower than the critical depth, it elevates the average light within the mixed layer, and hence the average rate of production.

However, such mechanism has been proven to be invalid in nutrient-limited environments, e.g. the North Atlantic subtropical area where phytoplankton bloom occurs in autumn/winter when deepening MLD increases nutrient concentrations in the upper layer [Lévy *et al.*, 2005]. More recent studies also reported pulses of rapid phytoplankton growth when MLD is still deeper than critical depth in the light-limited subpolar regions [Townsend *et al.*, 1994; Waniek, 2003; Carcia-Soto and Pingree, 2009; Taylor and Ferrari, 2011b]. These early blooms are associated with short-term calm and clear atmospheric conditions, which result in a temporary shallow stratification before the shoaling of the MLD. In addition to the impact on nutrient concentration and average light, MLD variation can lead to early blooms by affecting the grazing rate. The "dilution-recoupling" hypothesis proposes that a deep MLD and associated vertical mixing dilutes the distribution of zooplankton and hence reduces the grazing pressure on phytoplankton whereas under stratified conditions the recoupling of phytoplankton and zooplankton increases grazing rate [Behrenfeld, 2010; Boss and Behrenfeld, 2010]. The variability of MLD is mainly driven by thermal forcing, such as the surface heat loss and associated deep convection in winter. In the region along the storm track in the

subpolar basin, wind-driven vertical mixing brings equivalent amounts of nutrients into the upper layer as through winter entrainment (can be indicated by the maximum MLD) [Longhurst, 2007] whilst in near-Arctic areas sea-ice-melt contributes to modulating MLD by freshening the surface waters and reducing the saline contribution to the MLD.

In the North Atlantic, the impact of MLD on phytoplankton variation can be briefly summarized as follows: 1) annual maximum MLD indicates the amount of nutrients available for the following growing season through entrainment; 2) under nutrient-rich but light-limited conditions, deepening of MLD reduces light in the upper layer and decreases phytoplankton production. Shoaling of MLD elevates the average light level in the upper layer and hence the phytoplankton production; 3) under nutrient-poor but light-rich conditions, deepening of MLD increases nutrient concentrations and leads to higher phytoplankton production. Shoaling of MLD further reduces available nutrients and constrains phytoplankton growth; 4) MLD controls phytoplankton growth through the "dilution-recoupling" hypothesis: deep MLD and active vertical mixing reduces the chance of zooplankton encountering its prey and hence releases phytoplankton from grazing pressure, so phytoplankton accumulation starts [Behrenfeld, 2010].

5.3.2   Results

In this section the direct impact of varying MLD on biological parameters (surface chlorophyll-a, Chl-a and depth-integrated primary production, PP in the top 100m) is examined, following the hypothesis that the maximum MLD indicates the nutrients available in the upper layer and deeper maximum MLD leads to a higher spring-summer phytoplankton concentration. The linear trend is removed from the maximum MLD and biological parameters before a correlation analysis. The correlation coefficient between annual maximum MLD and averaged spring-summer (May – August) surface Chl-a and PP are shown in Figure 5.4. Monthly correlation between MLD and biological parameters were calculated, which presented very similar spatial patterns and coefficients as using seasonally averaged data. Considering no additional information is provided by monthly correlation, only the results using seasonally averaged data are shown and coefficients over the 95% significance are indicated in black lines.

Positive statistically significant correlation between MLD and Chl-a is observed mainly in the southern subpolar basin in both figures, suggesting that deeper than average

winter maximum MLD leads to higher than average spring-summer Chl-a and PP here. In the Iceland basin, northern Irminger basin and east of Iceland patches of positive coefficient are found for Chl-a and PP. Differences between Chl-a and PP correlation patterns are seen south of Greenland, where maximum MLD is deepest in the subpolar basin. In this area, patches of positive coefficient occupy larger areas for Chl-a and significant negative correlations are observed only between MLD and PP. This is possibly because PP is a measure of phytoplankton growth, which responds to variation of nutrients and sunlight. Chl-a represents phytoplankton standing stock or biomass and is also controlled by grazing, in addition to nutrients and sunlight. Deeper than average maximum MLD may delay the shoaling of MLD in spring, thus the average MLD during May-August is also deeper and the average light level is lower. Low average light would then lead to low photosynthesis rate and production. Overall, Chl-a and PP respond to changes of the maximum MLD in a similar manner and the maximum MLD is not the major driver of phytoplankton variability due to the lack of a consistent correlation pattern on the basin-scale.

This simple analysis shows no clear correlation pattern between maximum MLD and spring-to-summertime Chl-a and PP in the subpolar North Atlantic. In the area south of Greenland, deeper (shallower) than average maximum MLD leads to larger (smaller) than average phytoplankton standing stock, possibly responding to more nutrients, though such correlation is limited in patches. In the southern subpolar basin, positive correlation is observed between maximum MLD and Chl-a and PP, suggesting nutrient limitation of phytoplankton growth. The lack of a basin-scale pattern indicates discontinuity of biological response to the variability of MLD. The subpolar basin is thus divided into various ecological provinces to reveal the underlying physical control of biological processes on the regional scale.

5.4   Ecological Provinces

5.4.1   Definition of Ecological Provinces

Discontinuity in phytoplankton annual cycle and ecological structure have been observed in the global ocean, e. g. distinct spring and autumn blooms in the subpolar North Atlantic, while in the equatorial Atlantic phytoplankton shows no clear annual

bloom peak [Lalli and Parsons, 1997]. These ecological differences are determined by the discontinuity in physical forcing, especially the physical processes controlling the stability of the upper layers and the mixing of deeper water into the euphotic zone [Longhurst, 2007]. The analysis of the physical mechanisms controlling phytoplankton variability is hence more meaningful in regions where the physical forcing and ecological responses are relatively uniform. The term "ecological province" is thus introduced to define the region within which the annual cycles of phytoplankton and associated organisms of higher trophic levels are controlled by similar physical forcing. Between ecological provinces, the development of phytoplankton and zooplankton should present clear differences, responding to the differences in the determining physical forcing.

5.4.2   Division of Ecological Provinces

Various methods have been used to divide the world ocean into ecological provinces. Longhurst (2007) used various parameters to define ecological provinces worldwide, including biological and physical criteria. In the subpolar North Atlantic, the major parameters used were three main frontal systems (Gulf Stream-North Atlantic Current system, polar front and Icelandic-Faroe Island front) and one arbitrary zonal line from the south of Iceland to the edge of the Shetlands shelf separating the Atlantic Subarctic Province and North Atlantic Drift Province. Comparatively, Sarmiento *et al.* (2004) divided the world ocean using vertical velocity, maximum MLD and wind stress. In this study these two methods were combined to divide the subpolar basin into ecological provinces. In the following section, the method is first described and then the result is shown in Figure 5.6a.

The ecological provinces in Longhurst (2007) in the subpolar basin is presented in Figure 5.6b. In Sarmiento *et al.* (2004), the whole region of interest is defined as the subpolar province with no detailed subdivision, so their ecological provinces are not compared in details in this study. Figure 5.6a generally agrees with the previous two divisions. However, due to both previous works targeting the global ocean, their equivalent provinces include areas outside the region considered subpolar basin in this study. Only the southern parts of Longhurst's Atlantic Arctic Province (ARCT, Figure 5.6b) and Atlantic Subarctic Province (SARC, Figure 5.6b) are located in the subpolar

basin and the two parts agree well with the mixed Atlantic Arctic Province and the mixed Atlantic Subpolar Province, respectively. Longhurst's Northwest Atlantic shelves province (NWCS, Figure 5.6b agrees well with a combination of western shelf and stratified Arctic province in Figure 5.6a. The Gulf Stream Province in Figure 5.6a generally agrees with Longhurst's Gulf Stream province. Longhurst's Northeast Atlantic shelves province is included in the eastern shelf region in Figure 5.6a and the North Atlantic Subtropical Province resembles the northern part of Longhurst's North Atlantic subtropical gyre province-east (NASE, Figure 5.6b), but with a southwest-northeast boundary instead of a line along the latitudes. The largest province in both studies is the North Atlantic Drift Province, which is located in the central subpolar basin.

Before the main analysis, shelf regions where topography was shallower than 200m were omitted because the simulated properties in the shelf regions are not accurate and equations that governing processes in the open ocean are used on the shelf seas too, which might not match the real shelf processes. Frontal systems were defined using gradient in the annual climatology of NEMO SST. SST gradient of each 1-degree pixel was identified and then the pixels with the biggest SST gradients per latitude/longitude were connected with direct lines. This gradient generally lies along the southwest-northeast direction, including the Labrador Sea, south of Greenland, the Irminger Sea and east of Iceland.

Regions where maximum MLD was shallower than 150m were considered stratified and regions with maximum MLD deeper than 150m were considered mixed, following the threshold set in Sarmiento *et al.* (2004). On both sides of the SST gradient line, boundaries between stratified and mixed areas were drawn based on the average maximum MLD. Annual climatology of the modelled vertical velocity was used to separate upwelling and downwelling regions, where positive vertical velocity indicates upwelling and negative vertical velocity indicates downwelling. Regions where both negative and positive vertical velocities distributed equally indicate that no large-scale downwelling or upwelling dominates there and vertical mixing is relatively active in these regions. In the interior of ocean basins, nutrients are more abundant in regions of upwelling induced by basin scale gyres than in the downwelling regions [Sarmiento *et al.*, 2004].

The variability of dissolved inorganic nitrogen (DIN) in each ecological province was analysed to further examine the division of these provinces. Firstly, the median annual cycle of DIN using 5-day model data was produced for the subpolar basin. Usually limitation of phytoplankton growth is reached when DIN concentration drops below 0.5 mmolN/m^3. The number of days during which average DIN concentration was below 0.5 mmolN/m^3 at each grid point was calculated and is shown in Figure 5.5a. The frequency of DIN depletion during the 18-year period (Figure 5.5b) is summarised in four bins: 1) nutrient depletion occurs in less than three years out of the 18-year period; 2) nutrient depletion occurs in more than three years but less than nine years; 3) nutrient depletion occurs in more than nine years but less than16 years; and 4) nutrient depletion occurs in more than 16 years. The determining physical forcing is summarised in Table 5.1 and ecological (including DIN) responses are summarised in Table 5.2.

5.4.3   Defining Characteristics and Ecological Responses

A total of seven ecological provinces were determined for the subpolar North Atlantic (Figure 5.6a). The defining characteristics of each province based on physical processes are shown first and the ecological responses are discussed, focusing on DIN, surface Chl-a and depth-integrated PP (100 m) shown in Figure 5.7 – Figure 5.11. The shelf and stratified Atlantic Arctic province are not shown because the model simulations on the shelves are not accurate.

5.4.3.1   Mixed Atlantic Arctic Province

The mixed Atlantic Arctic Province (mAAP, Figure 5.6a) includes the Labrador Sea, Irminger Basin, area south of Greenland and a small region northeast of Iceland. One dominating characteristic of these regions is the cyclonic gyres and associated strong eddy fields[Lillya *et al.*, 2003; Rykova *et al.*, 2009; Fan *et al.*, 2013]. This province is located to the west of the SST gradient where SST (see Figure 2.5) is much colder than regions in the east of equivalent latitudes and winter convection is as deep as 2000m under severe conditions as a result of large surface buoyancy loss and relatively low water column stability [Våge *et al.*, 2009]. The Arctic water influences the Labrador Sea water masses through entrainment around the Labrador and Irminger gyres and is modified by Atlantic water with eddies across the SST gradient [Longhurst, 2007; Vage *et al.*, 2011]. The North Atlantic water is then transported northward toward the western

part of the gyre in the Irminger Current [Longhurst, 2007]. This province is separated from the stratified Atlantic Arctic Province to its west off the Labrador shelf, on which cold Arctic-origin water flows southward. The southern boundary of mAAP extends to the extension of the northern wall of the Gulf Stream and along the cold side, relatively cold (0-4 °C) and low-salinity (34.6-34.9) water recirculates within the Labrador-Irminger basin [Swift, 1986; Longhurst, 2007].

Under normal conditions (Figure 5.5a), surface DIN concentration is above 0.5 mmolN/m^3 all year round in mAAP. During the 18 years period (Figure 5.5b), nutrient depletion does not occur in mAAP. From late winter (March—April), the insolation starts to increase and surface DIN concentration is high due to deep convection. Once the water column is stabilized, phytoplankton accumulation occurs generally in late April to early May, peaking in May-June, corresponding to the MLD shoaling (Figure 5.7a). In the northeast Labrador Sea and northeast of Iceland, the appearance of Arctic origin fresh water stabilizes the water column and phytoplankton accumulation can occur earlier than in the rest of the province [Longhurst, 2007; Frajka-Williams and Rhines, 2010]. As DIN is above depletion level in summer (Figure 5.7b), phytoplankton concentration remains relatively high through the summer months, though a brief decrease in Chl-a is seen in July—August (Figure 5.7c) before a slight increase in September, possibly due to the migration of zooplankton to deeper depth that releases the grazing pressure [Longhurst, 2007]. In October, Chl-a decreases rapidly as MLD deepens and light limitation curtails further phytoplankton accumulation.

The two Chl-a products, modeled Chl-a (Figure 5.7c, black line) and SeaWiFS Chl-a (Figure 5.7c, red line), present similar cycles during the period from January 1998 to December 2007. Modeled and observed Chl-a have a consistent offset, where modeled Chl-a is higher than the observation by ~0.7 mg chl/m^3 at bloom peak in May/June. The summertime Chl-a decrease is much clearer in the model, except in 1998 when the two annual cycles agree very well. The timing of bloom peak is slightly earlier in the model than in observation, especially during the second half of the time period. Depth-integrated PP (Figure 5.7d) resembles modeled Chl-a, as under a light-limited environment, maximum growth of phytoplankton is seen close to the surface.

5.4.3.2   Mixed Atlantic Subarctic Province

Mixed Atlantic Subarctic Province (mASP, Figure 5.6a) is the region where one branch of the warm and salty North Atlantic Current (NAC) starts flowing towards the Nordic seas. The other branch of the NAC continues its gyral circulation [Hansen and Østerhus, 2000; Curry and Mauritzen, 2005]. The SST gradient lies to its west separating mASP from the mixed Atlantic Arctic Province. In this province, winter mixing is deep, especially around the SST gradient and south of Iceland and the average MLD is ~500m [Montegut *et al.*, 2004; Reid and Valdés, 2011]. The average annual vertical velocity suggests that upwelling dominates the variation of water masses along water columns. The DIN concentration is relatively abundant in the province and the DIN concentration in the western and northern parts of the province is above 0.5 mmolN/m^3 all year round, though in the rest of the province DIN concentration is below 0.5 mmolN/m^3 for about 20 days. In the central province, DIN could be a limiting factor to phytoplankton growth during summer months under common conditions. The occurrence of DIN depletion is not consistent in the province, which varies from infrequent (occurs in less than nine and more than three years) in the west, to almost every year in the east. For the majority of this province, DIN depletion frequency falls in the frequent bin (occurs in more than nine and less than 16 years) during the 18-year period.

In mASP, average surface Chl-a (Figure 5.8c, black line) remains at relatively low levels until April whilst, in May, Chl-a increases rapidly as MLD shallows universally in the province. Shortly after the Chl-a peaks in May, Chl-a starts to decrease from June and remains low until August due to low DIN concentration (Figure 5.8b). In September—October, a second weak peak is seen as MLD deepens (Figure 5.8a) and replenishes the surface with more DIN, and also due to the migration of zooplankton to deeper depths that releases the grazing pressure on phytoplankton [Longhurst, 2007]. In this province, the highest annual phytoplankton concentration (~4 mg chl/m^3) in the subpolar basin is observed, especially in the eastern mASP where maximum MLD is deeper and summer DIN concentration is lower than in the western mASP.

SeaWiFS Chl-a (Figure 5.8c, red line) shows stronger inter-annual variability than the modeled Chl-a. As DIN limitation occurs in some years during the 18 years period when summertime decrease in phytoplankton abundance is clearer than in other years.

The bloom peak is higher in the model than in observation by ~ 0.7 mg chl/m^3. PP (Figure 5.8d) closely follows the variation of modeled phytoplankton concentration.

5.4.3.3   North Atlantic Drift Province

The North Atlantic Drift Province (Figure 5.6a, NADP) includes the region where winter wind stress is comparable to that in the Southern Ocean [Trenberth et al., 1990; Longhurst, 2007] and the wind driven deep mixing, together with thermal convection, contributes to the circulation within the subpolar basin [Häkkinen and Rhines, 2004]. In this study, NADP is the biggest province, which extends from 40°N to 57°N, where a line separates the upwelling-and-downwelling-evenly-distributed NADP from the upwelling-dominated mASP. To the west, SST gradient separates mAAP and NADP and the well-mixed NADP is separated from the stratified Gulf Stream & Extension Province in the southwest. To the east, NADP is separated from the shelf seas at the edge of the continental shelf. The seasonal SST differences are large (>5°C) in some parts of the province [Longhurst, 2007], which is also characterized by the presence of mesoscale eddies, possibly generated in the more active Gulf Stream and along the path of NAC [De-Mey, 1992; Richardson, 1993]. The average winter mixing varies from 200m to 500m and MLD is deeper in the north than in the south. In this province, DIN depletion lasts about 50 days in the northern part and gradually increases towards the south. At the southern boundary of NADP, nutrient depletion lasts about five months. In this province, DIN depletion occurs frequently.

In NADP, modelled surface Chl-a (Figure 5.9c, black line) starts to increase patchily along the pathway of NAC from December to March while Chl-a in the rest of the province remains relatively low. By April, shallow stratification is established in the majority of NADP and spring bloom occurs almost simultaneously. The early surface bloom are likely related to the increased irradiance on cells brought to the surface by meso-scale eddies rather than the establishment of stratification [Longhurst, 2007]. From June to September, Chl-a decreases steadily as nutrient depletion occurs frequently in summer and from October surface Chl-a starts to increase again, as MLD deepens through winter months (Figure 5.9a). The variation of depth-integrated PP (Figure 5.9d) follows the changes of surface Chl-a. Compared to model Chl-a, observed Chl-a (Figure 5.9c, red line) was lower from winter to later spring but higher in summer.

The timing of spring bloom agrees well between the modeled and observed surface Chl-a.

5.4.3.4   Gulf Stream Province

The Gulf Stream Province (Figure 5.6a, GFSP) is located east of the SST front, including the main pathway of the Gulf Stream and its extension towards the Newfoundland shelf where the stratified GFSP is separated from NADP. The maximum MLD (Figure 5.10a) is around 120m in most years and the region is characterised by predominately downwelling activity. The Gulf Stream area is known for active meso-scale eddies which form domes or dips in the centers based on eddy characteristics and the direction of their rotation; however, the relatively small scale movement of water masses usually would not lead to consistent upwelling or downwelling [Longhurst, 2007]. The observed dominant downwelling is more likely due to other processes. In this province, nutrient depletion occurs every year and lasts ~5 months.

GFSP is the region with highest winter Chl-a concentration in the subpolar basin, with model Chl-a (Figure 5.10c, black line) starting to accumulate in November and peaking in February and March. High Chl-a is concentrated along the Gulf Stream pathway. After May, model Chl-a starts to decrease and remains low during summer, before it increases again when MLD deepens. The SeaWiFS Chl-a (Figure 5.10c, red line) agrees very well with modeled Chl-a, both for the strength and the timing of the winter-spring bloom. Depth-integrated PP (Figure 5.10d) follows the variation of surface Chl-a closely.

5.4.3.5   North Atlantic Subtropical Province

North Atlantic Subtropical Province (Figure 5.6a, NASP) is stratified with maximum MLD about 90m and is characterized by downwelling. The DIN concentration at the surface is very low and DIN depletion occurs every year, from May to November. The dissolved carbon material (DCM) is not reproduced in the model, so its influence on the phytoplankton dynamics is examined here. In the NASP, surface Chl-a (Figure 5.11c, black line) is very low all year round. Chl-a increases in December and peaks in February—March, when MLD is deepest in a year and DIN is at its peak. From April, Chl-a starts to decrease and reaches its minimum in August, following the variation of

DIN. The depth-integrated PP (Figure 5.11d) follows the changes of Chl-a. The timing and strength of the simulated Chl-a agrees very well with the SeaWiFS Chl-a (Figure 5..11c, red line), though SeaWiFS Chl-a is slightly higher than modeled Chl-a during summer months (~0.1 mg chl/m^3).

The stratified Atlantic Arctic and eastern shelf provinces lay in the regions where model simulation is less accurate, so the ecological responses in these provinces are not discussed here.

In summary, the general timing and peaks of phytoplankton cycle in the five major provinces agree well between the observations and the modeled Chl-a. In the two northern mixed provinces (mAAP and mASP), phytoplankton peaks occur when MLD is shallow and DIN is relatively abundant, suggesting light-limitation. DIN depletion seldom occurs in mAAP, so Chl-a remains at a moderate level in summer months, which results in a single bloom from late spring to late summer. Inter-annual variability in the Chl-a annual cycle is large in mASP, in some years when DIN depletion occurs Chl-a decreases rapidly in summer and a second bloom peak emerges as MLD deepens. In other years, when DIN remains above depletion threshold, the second autumn bloom is less distinguishable from the spring bloom. In NADP, phytoplankton starts to accumulate from early spring along the NAC pathway and in the rest of the NADP spring bloom occurs in April—May, which is curtailed in early summer by frequent DIN depletion. Phytoplankton continues to accumulate at deeper depth where DIN is more abundant and hence the accumulation of PP. In GFSP, the phytoplankton bloom occurs in the late winter when MLD is still relatively deep and the bloom is curtailed by DIN depletion by June. Clear nutrient-limitation on phytoplankton growth is observed in NASP, where a short and weak bloom peaks in winter when MLD is deepest, the Chl-a concentration remains very low from June to November due to DIN depletion.

5.5   Physical Mechanism in The Northern Subpolar Atlantic

In section 5.3.2, it is proved that there is no basin scale DIN limitation controlling the timing of phytoplankton growth, though nutrient limitation scheme can explain Chl-a variation in stratified and downwelling provinces in the subpolar basin (NASP, see Figure 5.6a). Hence, the impact of maximum MLD on phytoplankton growth by altering the amount of nutrients entrains into the upper layer seems to play a minor role in the

subpolar North Atlantic. In the following section, three mixed provinces are focused on and the influence of MLD on phytoplankton under different conditions (nutrient-rich, low-light and nutrient-poor, high-light) and through "dilution hypothesis" process are examined (the other three mechanisms in section 5.3.1). A case study is selected based on the resemblance of phytoplankton colour index (PCI) produced by Continuous Plankton Recorder (CPR) and NEMO Chl-a in equivalent areas. One possible physical mechanism controlling the timing and strength of phytoplankton bloom in the northern subpolar North Atlantic is discussed.

5.5.1   Comparison between PCI and NEMO Chl-a

CPR observation and PCI were introduced in detail in Chapter 3. Here PCI data in a few locations are compared to model biological parameters, as the ultimate goal of this study is to propose physical mechanisms that control the observed variability in CPR observation. PCI is a useful tool recording the long-term variation of phytoplankton variability, but is limited by its low temporal resolution. With the high-resolution model outputs, parameters related to phytoplankton growth can be tested and the underlying mechanisms can be revealed. The first step, however, is to examine whether model outputs reproduce the observed variability. Through this comparison, the accuracy of model Chl-a and PP can be further examined. PCI is a direct measurement of greenness pigment in the ocean, while satellite sensors estimate Chl-a concentrations through measuring the water-leaving radiance, resulting from scattering and reflection, at blue-green wavelengths [Martin, 2004]. Though the three products are not measuring exactly the same parameter and are not compared quantitatively, the comparison between these three products provides a chance to qualitatively evaluate the performance of the model. The more similar model outputs are compared to the observation, the more likely that the model has assumed the right mechanisms.

Three Standard Areas (SA) locations were chosen to compare to model outputs. Each of these three SA boxes was located completely in one of the three mixed provinces: C8 locates in mAAP, B5 locates in mASP and D5 locates in NADP (please refer to Figure 3.2 for the exact location of the three SA boxes). In the following analysis, all model outputs were calculated over the areas that match the three SA boxes exactly to maintain comparability between the two datasets.

5.5.1.1   Annual cycle

The average annual cycle of PCI and modeled surface Chl-a in the three chosen locations in the overlapping time period 1990-2007 are shown in Figure 5.12. In mAAP (Figure 5.12a), PCI is only available from April to November. Both annual cycles highlight a strong spring bloom, though bloom peak is reached in May in model and in June in PCI. Model surface Chl-a shows a clearer autumn bloom in September—October compared to PCI. The 95% confidence intervals of the standard error of the mean (SEM) are much bigger in PCI than in model, which could be related to smaller effective sampling size of a particular month during the period 1990—2007. SEM is calculated following Eq. 5.2:

$$SEM_i = \sigma_i \Big/ \sqrt{N_i} \qquad\qquad i = 1,...,12 \qquad \text{Eq. 5.2}$$

where σ_i is the monthly standard deviation of PCI and model time series at each location and N_i is the number of years over the overlapping period.

The most continuous CPR observation in the three locations was in mASP (Figure 5.12b), where PCI is available all year round. Spring blooms are distinguishable in both annual cycles, but the standard errors of the mean (SEM), calculated following Eq. 5.1, in PCI are much bigger than in the model, especially in May and June when PCI peaks. Average bloom peak during 1990—2007 is seen in May in the model but is seen in June in PCI. During summer months, model Chl-a decreases to ~1/4 of its peak level, though PCI stays relatively high. Thus, the second autumn bloom in September—October is more noticeable in the model than in PCI. Overall, model Chl-a annual cycle agrees with PCI annual cycle and captures the main features of the observation.

In NADP (Figure 5.12c), the first half of model Chl-a annual cycle agrees well with PCI annual cycle, highlighting the early spring bloom peak in April—May. After June, however, model Chl-a decreases to ~1/6 of its peak level in August, though the decrease in PCI is brief, and remains at a relatively high level through summer months. Similar to previous locations, the error bars of PCI are much bigger than that in the model Chl-a.

Overall, both model Chl-a and PCI captured phytoplankton spring bloom in these three locations. The bloom peak is earlier in the model than in PCI observation. This could be

related to the fact that CPR observation is carried out monthly and the sampling usually occurs during a short period in a month, and hence it could miss the actual annual peak [Richardson *et al.*, 2006]. In addition, the SEMs of PCI are larger in all three locations and in almost every month available. This is possibly related to a smaller effective sample size in observation than in the model, as CPR observation is heavily dependent on cruise routes, and because the observation is more variable than the model. The general agreement of annual cycle between model Chl-a and PCI indicates that the model has reproduced some features of phytoplankton bloom in these locations, though there are discrepancies between the two datasets and the missing data in the observation makes it difficult to fully evaluate the performance of the model.

5.5.1.2   Longer-term time series

Monthly time series from January 1990 to December 2007 of model Chl-a and PCI in these three locations are shown in Figure 5.10. In mAAP (Figure 5.13a), the coverage of CPR observation is very poor. Continuous sampling was only available in 2003—2004, while before and after this period PCI data was only collected in three separate months. The average annual cycle in Figure 5.12a mainly represents the annual cycle in 2003. It is difficult to judge if this annual cycle is representative in this location and the comparison at annual scale is not robust due to the poor data coverage of PCI in this location.

CPR observation coverage was much better in mASP (Figure 5.13b) than in mAAP during the period 1990—2007 and continuous monthly sampling was carried out almost throughout the whole period. The bloom timing agrees well between model Chl-a and PCI. Inter-annual variability of maximum Chl-a/PCI generally agrees, though PCI data is more variable than model Chl-a on this scale. The average annual cycle (Figure 5.12b) is more representative than that in mAAP. However, there are no statistically significant correlations found between the timing of phytoplankton bloom or peak, suffering from the missing data in CPR observation. Because of the nature of CPR observation, it is not suitable for identifying the timing of a particular event but is more suitable for providing an overall trend. The annual peaks of simulated surface Chl-a, depth-integrated PP (total annual PP in this case) and PCI were well correlated (Figure 5.14). In all the three time series, a slight overall increasing trend (see Table 5.3 for the linear regression coefficients) is seen from 1990 to 2007, though inter-annual variability

is clear too. The values in 2002 are the highest in this 18-year period in all the three time series. All three-time series are positively correlated between one another at 95% confidence intervals. The correlation coefficients are shown in Table 5.3. However, PCI is more closely correlated to PP compared to surface Chl-a. This might be because PCI measures all the green pigment on the surface and PCI is closer to PP than Chl-a when averaged over a large area.

These three sets of comparison confirm that at least in some parts of the subpolar North Atlantic model surface Chl-a and PP agree well with CPR observation. In the western subpolar, however, such comparison is not possible due to a lack of continuous CPR sampling. These results also enhance the confidence of studying physical mechanism using the model in regions showing good agreement with observation. An additional assessment of the simulated Chl-a and PP could be a comparison between model outputs and satellite-derived Chl-a and PP. This study aims to explain the observed variability in CPR data using the mechanism established from model outputs, so the ability of model to reproduce the signal seen in CPR data was the priority.

Regular CPR observation was carried out in NADP during the period of 1994—1996 (Figure 5.12c). Before 1994, CPR sampling was only seen in a few months from 1990 to 1993 and after 1997 data coverage was mainly in winter months. Due to the lack of continuity of CPR data in spring/summer months, it is difficult to compare the inter-annual variability of bloom peaks between model Chl-a and PCI. The timing of PCI blooms agreed well with model when observations were available. This suggests that the physical forcing considered in the model is generally accurate on the annual scale.

Though there are discrepancies between model simulation and CPR observation, they are partially due to the poor data coverage of the observation, either intra- or inter-annually. The province mASP has longest observation and model has simulated similar trend for Chl-a and PP peak as seen in PCI, this location is selected as a case study and is subjected to further analysis.

5.5.2   Physical Mechanism in mASP

In the northern subpolar North Atlantic, the most important processes controlling phytoplankton growth include: variability of MLD, seasonality of light and zooplankton

grazing [Townsend *et al.*, 1994; Boss and Behrenfeld, 2010]. In section 5.3.2, no clear correlation between maximum MLD and spring-summer Chl-a or PP was found in this region, though connection between MLD and biological parameters has been suggested by many other studies [Dutkiewicz *et al.*, 2001; Waniek, 2003; Henson *et al.*, 2009a]. In the subpolar North Atlantic, MLD could modulate phytoplankton variation during its growth other than through affecting maximum nutrient concentration. Thus in the following section, connections between MLD and biological parameters (including zooplankton grazing rate) are examined focusing on particular stages of the phytoplankton growth cycle at the location representing mASP.

5.5.2.1   Time series at key bloom stages

In this section, the direct impact of MLD on surface chlorophyll-a and PP are examined. The average annual cycles of MLD, DIN, total surface Chl-a, Chl-a from diatoms and non-diatoms, depth-integrated PP and the relative strength (relative to depth-integrated PP) of three types of zooplankton grazing (meso-zooplankton on diatom, meso-zooplankton on non-diatom and micro-zooplankton on non-diatom) on 5-day resolution are shown in Figure 5.15. Within one annual cycle, major phytoplankton bloom stages include: spring bloom initiation, spring bloom peak, spring bloom termination and autumn bloom termination. These bloom terms were defined using model data at 5-day resolution: spring bloom initiation was defined as the first day when Chl-a exceeded the annual median by 5% consistently for 15 days, following previous studies [Siegel *et al.*, 2002; Henson *et al.*, 2009b; Frajka-Williams and Rhines, 2010]. Spring bloom peak was defined as the day when chlorophyll-a reached its maximum level whilst spring bloom termination was defined as the last day of rapid Chl-a decrease in late spring or early summer; and the autumn bloom initiation was defined as the last day when Chl-a exceeded the annual median by 5%. MLD, DIN concentrations and grazing strength relative to depth-integrated PP at these bloom stages were plotted along since Chl-a time series for the period of 1990—2007 (Figure 5.16).

Under normal conditions, non-diatom Chl-a (Figure 5.15b, blue line) starts to increase first from late winter to early spring when MLD (Figure 5.15a, blue line) is still ~400m deep and DIN is very abundant in the surface layer (Figure 5.15a, red line). The rapid accumulation of phytoplankton occurs during the MLD shoaling period and, potentially, the increase of irradiance. This early phytoplankton accumulation triggers an early peak

in micro-zooplankton grazing on non-diatom (Figure 5.15d, blue line), though it only consumes ~6% of the total PP. This suggests that under low-light conditions, small non-diatoms survive better than bigger phytoplankton cells. From early May, diatoms form a bigger portion of the phytoplankton community structure (Figure 5.15b, green line) and hence an increase in meso-zooplankton grazing on diatoms (Figure 5.15d, magenta line). Spring bloom peaks in late May/early June and is contributed almost entirely by diatoms, meso-zooplankton consumes ~11% of total depth-integrated PP at its peak. Chl-a declines rapidly after the peak and through June as a result of gradually increased grazing rate and declined DIN concentration (Figure 5.15a, red line). The total grazing rate peaks in summer when the three types of zooplankton grazing consumes ~25% of total PP in July-August and the post-spring-bloom standing stock of non-diatom is high. Both micro- and meso-zooplankton grazing on non-diatom are at their peaks and much higher than the grazing rate on diatoms. In September-October, a weak autumn bloom occurs following the decrease of grazing rate and increase of nutrients concentration, before light-limitation curtails further cell accumulation [Longhurst, 2007].

The spring bloom is initialised around late-April (Figure 5.16e, solid blue line). Surface Chl-a (red line) is negatively correlated to MLD (r=-0.63, p=0.005) and deeper (shallower) than average MLD leads to lower (higher) than average Chl-a concentrations at initiation stage. The model results support the "dilution-recoupling" hypothesis as spring bloom is initiated before stratification and deeper (shallower) MLD leads to weaker (stronger) micro-zooplankton grazing (r=-0.65, p=0.004). However, on the inter-annual scale, deeper MLD, and hence lower grazing rate, coincides with lower Chl-a rather than higher Chl-a, thus the influence of MLD on phytoplankton through modulating light intensity could not be eliminated. It is also worth noting that shallower than average MLD does not lead to higher PP (see Table 5.4), suggesting that the photosynthesis rate is still low and is determined more by irradiance than by MLD [Martin, 2004].

Spring bloom peaks (Figure 5.16b) usually occur at the end of May and surface Chl-a (red line) is not significantly correlated to MLD. DIN (dark green line) is largely reduced, resulting from rapid phytoplankton growth, and is also modulated by MLD where shallower (deeper) MLD leads to lower (higher) DIN concentration (r=0.65, p=0.004). Under turbulent conditions in spring, diatoms dominate the phytoplankton

community structure when MLD is still shoaling. The strength of spring bloom peaks is not modulated by MLD-related processes, but is likely related to other factors, such as self-shading and the development of the zooplankton population.

From mid-June, Chl-a (Figure 5.16c, red line) remains at a moderate level as DIN concentration (dark green line) is low and the overall grazing rate is at its annual high level, removing >20% of total PP. The three types of grazing are of equivalent strength, which suggest that the population of diatoms, small non-diatoms and large non-diatoms are comparable. In some years, especially from 1999 to 2005 (Figure 5.16e), summertime Chl-a drops below its annual median, following the nutrient depletion during these years. This inter-bloom Chl-a trough lasts ~15 days and Chl-a starts to increase again, coinciding with the replenishment of nutrients in the surface layer in early September. At the end of the weak autumn bloom (Figure 5.16d), deepening MLD and decreasing irradiance curtails further phytoplankton growth. Non-diatoms dominate the phytoplankton standing stock, suggested by the stronger micro- and meso-zooplankton grazing on non-diatoms. Light limitation is indicated by statistically significant negative correlation between MLD and Chl-a, and deeper (shallower) than average MLD is associated with lower (higher) than average Chl-a level (r=-0.59, p=0.01). The inter-annual variability also modulates zooplankton grazing with MLD deepening leading to reduced grazing rates and vice versa. The statistical correlations between the discussed parameters are summarized in Table 5.4.

In summary, MLD impacts the strength of spring bloom initiation and autumn bloom termination, when DIN is adequate, directly through light-limitation. Deeper MLD leads to weaker spring bloom initiation and autumn bloom termination and vice versa. The results also suggest that MLD has a direct negative impact on grazing rate at various stages of phytoplankton bloom development. However, the results could not eliminate the possibility that the influence of MLD on light intensity and nutrient concentration plays an important role in determining the development of phytoplankton blooms. At spring bloom peak, surface Chl-a negatively correlates with micro-zooplankton grazing, which is possibly related to the change of the dominant functional group from small non-diatoms to diatoms as the latter prefer turbulent condition. Thus stronger diatom spring bloom peak indicates a lower small non-diatom standing stock and hence weaker

micro-zooplankton grazing. These results, however, provide limited information about the timing of phytoplankton bloom dynamics.

5.5.2.2   Bloom types in mASP

Firstly, time series of MLD, DIN, surface Chl-a, depth-integrated PP and the relative strength of three types of zooplankton grazing (relative to depth-integrated PP) are examined year by year (only two representative years are shown in Figure 5.17). Two different types of spring bloom can be observed: an intense but short spring bloom in 2000 (Figure 5.14 a-d) and a weak but long spring bloom in 2005 (Figure 5.17 e-h).

In the first situation (Figure 5.17, a-d), MLD starts to shoal from late April (Figure 5.17a, blue line) and stable stratification is established by mid-May. Surface Chl-a (Figure 5.17b, red line) follows MLD closely and a strong Chl-a diatom spring bloom (~5 mg chl/m^3, see Figure 5.17, green and red lines) occurs in May, though an earlier non-diatom accumulation is seen in late April (Figure 5.17b, blue line). The depth-integrated PP (Figure 5.17c, red line) steadily increases from January, possibly related to low grazing rate (Figure 5.17e, red line) that allows non-diatom to reach a high production rate. Grazing rate increases more rapidly from late April, following the peak of non-diatoms and removes ~30% of total depth-integrated PP (Figure 5.17d, blue line). Diatom outcompete non-diatom around mid-May and so as PP from diatoms (Figure 5.7b-c, green lines) Meso-zooplankton grazing on diatoms (Figure 5.17d, magenta line) follows the main spring bloom closely, removing ~20% of annual total depth-integrated PP at its peak. The post-spring-bloom phytoplankton abundance remains low, as DIN concentration is low and zooplankton population is well developed. Non-diatoms dominate phytoplankton community structure again from early July, though both non-diatoms and diatoms concentrations are below 1 mg chl/m^3. A second, much weaker autumn bloom occurs in September-October following the DIN replenishment when MLD deepens. By the late October, further phytoplankton accumulation is curtailed by light-limitation.

In the second situation (Figure 5.17, e-h), MLD (Figure 5.17e, blue line) starts to shoal from mid-March and stable stratification is finally established by mid-June. During the three months, multiple episodes of MLD-shoaling processes occur but are disturbed by vertical mixing and associated MLD deepening. A pulse of phytoplankton accumulation

(Figure 5.17f, blue line) starts almost instantly after each episode of MLD-shoaling, but is also affected by the frequent vertical mixing. Early Chl-a increase is due to the non-diatom accumulation and diatoms become more abundant after early May. The phytoplankton bloom after the establishment of stable spring stratification is of comparable strength to the previous pulses of phytoplankton accumulation and is consisted by both diatoms and non-diatoms. The dominance of diatoms is weak under this condition and diatoms and non-diatoms coexist almost all year round (Figuer 5.17f). Pulses of early phytoplankton accumulation trigger early development of zooplankton population and by mid-June these zooplankton are ready for grazing (Figure 5.17h). Depth-integrated PP (Figure 5.17g, red line) increases slowly from January and a relative high production period lasts from late March to late June. Micro- and meso-zooplankton grazing on non-diatoms takes place even during the major diatoms bloom in late spring. The autumn bloom is not distinctive from the summer low concentration as the summertime Chl-a is ~0.8 mg chl/m^3. By mid-November, zooplankton migrates to deeper depth and phytoplankton accumulation is restrained by light-limitation.

The two types of phytoplankton bloom development can be summarised as follows: 1) MLD starts to shoal earlier under the interrupted condition, but a stable vernal stratification is established earlier under the continuous condition; 2) phytoplankton starts to accumulate earlier under the second condition, though the strengths of phytoplankton and depth-integrated PP spring blooms are weaker compared to under the first condition; 3) non-diatoms dominate phytoplankton composition pre and post the main diatom spring bloom under the first situation, whilst the two groups coexist during most of the year without clear dominance under the second condition; 4) distinct micro-zooplankton grazing and meso-zooplankton grazing are seen under the first condition and such separation is less noticeable under the second condition. This suggests that, at this location, the process of MLD shoaling and establishing stratification is one physical mechanism that could change the timing and strength of the phytoplankton spring bloom. Such impact can transfer to higher trophic levels through a potential bottom-up controlling chain by changing the food availability of zooplankton. A similar mechanism was proposed by Waniek (2003) and here further statistical analysis to justify this potential mechanism using model outputs is shown below.

5.5.2.3   Physical mechanism in mASP

The length of MLD-shoaling period (T_{MLDS}) was defined as the time period between continuous deep MLD (within the range of ($Max_{MLD} - 50m$)) and continuous shallow MLD (shallower than 50m). Time series of relevant physical and biological terms, such as the winter and summer SSTs, the length of spring bloom and the average bloom strength, were also constructed. In this subsection, the modulation of the T_{MLDS} of phytoplankton blooms and observed variability in phytoplankton abundance in the subarctic province is investigated.

Stable stratification is established within a period ranging from 10 days to 90 days (blue lines in Figure 5.15) and, in most of the years, MLD shoals to stratification in 30—60 days. In the late winter, if calm weather lasts for a few days, temporary stratification or large MLD-shoaling occurs, which could start as early as mid-March [Townsend *et al.*, 1994]. But during this time of year, storms are still frequent and the just-established stratification is vulnerable to disruption and MLD deepens again. Episodes of MLD-shoaling processes and vertical mixing repeat the same cycle until calm weather lasts and stable stratification is established. Conversely, when winter mixing is strong and stable, MLD only starts to shoal in spring when insolation increases steadily and storm events are not frequent. MLD shoaling is not disturbed by external forcing and stable stratification can establish quickly in early spring. Thus, in general, the T_{MLDS} indicates the type of stratification process: long period leads to early but disturbed shoaling process and hence late stable stratification whilst short period leads to late, fast shoaling process and hence early stable stratification (r=0.87, p<0.0001 between T_{MLDS} and the timing of stable stratification).

In Figure 5.15a, the T_{MLDS} is negatively correlated (r=-0.62, p=0.006) to spring bloom initiation date (the date on which surface Chl-a excess the annual median by 5%). Early yet long MLD-shoaling leads to early phytoplankton accumulation, as under nutrient abundant condition changes of light intensity become the key-limiting factor. The reproduction time for phytoplankton is in terms of hours to days and, hence, soon after short-term stratification (or significant MLD shoaling) is established Chl-a increases rapidly, the first sign of spring bloom appears as early as late winter [Townsend *et al.*, 1994; Waniek, 2003]. If the water column remains well mixed through winter without

calm weather long enough to initiate MLD shoaling, then phytoplankton starts to accumulate once mixing is reduced and light intensity is increased in spring. In the period 1990—2007, spring bloom mainly initiated in late-April, though bloom can be initiated within the range of ~26 March to ~15 May.

The variation of the T_{MLDS} is positively correlated to the length of spring bloom (r=0.76, p=0.0002, Figure 5.15b). This suggests that early and long MLD-shoaling process indicates a long spring bloom season and vice versa. Two reasons could explain this connection: 1) as discussed above, long and early MLD-shoaling process leads to early spring bloom initiation and hence longer spring bloom season in this generally nutrient-rich region, Tchanges to the spring bloom termination date is ~8 days at this particular location; and 2) vertical mixing caused by storm events disturbs the short-term stratification, which leads to phytoplankton cell loss to deeper layers but simultaneously replenishes upper layer nutrients, which can support a longer bloom season. Under the late and rapid MLD-shoaling conditions, phytoplankton accumulation starts later and hence there is a shorter bloom season. The rapid phytoplankton growth after vernal (spring) stratification consumes DIN quickly. With low DIN concentration and strong zooplankton grazing following phytoplankton bloom, Chl-a decreases rapidly and spring bloom terminates.

The strength of main spring bloom is much stronger under the late and rapid MLD-shoaling process compared to under the early and lengthy MLD-shoaling process. The T_{MLDS} is negatively correlated to spring bloom peak Chl-a (r=-0.44, p=0.06, Figure 5.15c red line) and to average spring bloom Chl-a (r=-0.56, p=0.02, Figure 5.15c green line). This is related to the development of zooplankton and its grazing pressure on phytoplankton under the two conditions. When episodes of MLD-shoaling occur before the establishment of stable vernal stratification, on-and-off phytoplankton growth provides early food for zooplankton, which starts to accumulate earlier than usual, especially for micro-zooplankton that graze on small non-diatoms (also see Figure 5.14h). When stable stratification is finally established, the zooplankton population is ready to graze, which removes 5-10% and 40% of total and surface PP respectively, during the development of the main spring bloom. This early grazing limits the accumulation of phytoplankton standing stock. However, when MLD starts to shoal later yet more rapidly, intense phytoplankton bloom develops while zooplankton

population is very low and the grazing rate is <3% for both total and surface PP. The growth cycle is much longer for zooplankton, thus intense grazing occurs following the phytoplankton bloom. Before the main spring bloom, DIN concentration is relatively high in the upper layer, which can support a large phytoplankton standing stock. With sufficient light, nutrient and a low grazing rate, spring bloom can reach a much higher peak and average level compared to the former condition.

The total depth integrated PP during spring and autumn blooms, however, is higher with long but weak phytoplankton spring bloom and lower with short but intense spring bloom (r=0.6, p=0.009, Figure 5.15d). This is likely related to the higher total nutrient and longer growing season during the year under early and disturbed MLD-shoaling process. Summertime nutrient depletion lasts for a shorter period after a mild spring bloom, which also contributes to the overall higher annual PP.

At this particular location, the T_{MLDS} presents no significant correlation with maximum winter MLD (Figure 5.15e) or winter and summer SSTs (Figure 5.15f solid green line and dashed green line). This indicates that the atmospheric and oceanic conditions that lead to deep convection are not linked with the conditions in the following spring. Hence large heat flux loss between the ocean and atmosphere, which is the main force for deep convection, has no impact on MLD-shoaling in the following spring. In addition, winter and summer SSTs are not indicators of the MLD-shoaling process: colder (warmer) than average winter SST does not suggest longer (shorter) than average MLD-shoaling process and rapid (lengthy) MLD-shoaling does not suggest warmer (colder) than average summer SSTs. SST is determined by both atmospheric and oceanic forcing, within which the annual cycle of MLD contributes to the variation of SST, but the combination of other factors plays a more important role in determining seasonal SSTs.

The SST annual cycle amplitude (ACA), which is calculated as the difference between maximum and minimum SSTs for a single year, is negatively correlated to the T_{MLDS} on an inter-annual scale (r=-0.54, p=0.02, Figure 5.15g). This indicates that in years with relative large ACA, shallow stratification is established rapidly whilst in years with relative small ACA shallow stratification occurs over a longer period. It is possibly because there are common factor(s) contributing to the variability of SST annual cycle

and MLD-shoaling process and the strength of SST annual cycle is more relevant to MLD-shoaling than extreme SST values.

Phytoplankton abundance measured using CPR observation presents negative correlation with the T_{MLDS} before 2001, but presents positive correlation after 2001. Before 2001, rapid MLD-shoaling triggers a relatively strong phytoplankton abundance peak (r=-0.65, r=0.03, Figure 5.15h red line) and the annual average abundance (r=-0.55, p=0.09, Figure 5.15h green line). The mechanism is likely the same as that linking MLD-shoaling with model Chl-a. However, after 2001 rapid MLD-shoaling seems to result in weak phytoplankton abundance peak (r=0.80, p=0.03) and annual average abundance (r=0.70, p=0.08). There is no simple explanation to the dramatic turn, though this coincides with the change of the ratio between total diatom and total dinoflagellates from ~2 to ~1 (see Appendix 4). A bigger ratio suggests a higher proportion of total diatom and vice versa. As discussed above, diatom is more competitive under turbulent and nutrient-adequate conditions, whilst dinoflagellates survive better under stratification when recycled nutrients are the main nutrient resources; many dinoflagellates are also heterotrophic. The shifts of diatoms dominance to diatom-dinoflagelates coexistence around 2001 might alter the spring bloom response to the MLD-shoaling process. Previous study has suggested that changes of the transport through the Rockall Trough may have some impact on the ecological shift in the North Sea [Holliday and Reid, 2001]. Similarly, changes of the hydrographical conditions in the northeastern subpolar basin around 2001 may be responsible to the observed community structure, though the exact mechanism remains unclear.

To further explore the mechanisms that control MLD-shoaling and the amplitude of the SST annual cycle, the number of atmospheric blocking days is calculated for the region 45 ° – 75 °N, 30 °W – 10 °E. Atmospheric blocking events occur when a persistent high-pressure system develops, which adjusts the track, frequency and intensity of storms in the North Atlantic [Häkkinen *et al.*, 2011]. The occurrence of atmospheric blocking can influence local weather and winter climate [Serreze *et al.*, 1997]. Time series of the number of blocking days in spring and extended winter (December to March) are generated using the 60-year National Centers for Environmental Prediction/National Center for Atmospheric Research (NCEP/NCAR) reanalysis. The blocking events are identified using the blocking definition (see Eq. 5.3 and Eq. 5.4)

based on reversal of the north-south geopotential height gradient at 500 hPa within the targeted region in the North Atlantic [Häkkinen *et al.*, 2011]. A blocking grid is counted here only if the reversal lasts for five or more days. These time series are then correlated to simulated and observed biological and physical parameters. The climatic influence of atmospheric blocking is discussed in association with climatic indices.

$$GHG_N = \left(Z(\lambda, \phi_N) - Z(\lambda, \phi_0)\right)\big/\left(\phi_N - \phi_0\right) < -10 \text{ (m/ degrees of latitude)}, \qquad \text{Eq. 5.3}$$

$$GHG_S = \left(Z(\lambda, \phi_0) - Z(\lambda, \phi_S)\right)\big/\left(\phi_0 - \phi_S\right) > 0, \qquad \text{Eq. 5.4}$$

GHG stands for geopotential height gradient, Z is the 500 hPa geopotential height, λ is longitude, ϕ_0, ϕ_N and ϕ_S are the center, northern and southern latitudes, respectively and $\left|\phi_0 - \phi_{N/S}\right| = 15$ degrees as the NCEP/NCAP reanalysis has 2.5 degree resolution. With this choice the blocking days for the range from 45 °N to 75 °N can be computed and the results can be compared to those (calculated over 34 ° – 74 °N, 30 °W – 10 °E) in Häkkinen *et al.* (2011) to test the accuracy of the calculation. The chosen region objected to atmospheric blocking calculation is bigger than the mASP because the scale for atmospheric circulation can be ~1000 km [Lutgens and Tarbuck, 2000] and the observed variability in mASP can be responding to atmospheric changes that occur over a larger area.

The number of days of atmospheric blocking in spring (April-June, Figure 5.16a, blue line) is negatively correlated to phytoplankton colour index (PCI) from 1948 to 2007 (r=-0.31, p=0.02 for the average spring-summer PCI and r=-0.26, p=0.05 for PCI peak). This correlation is dominated by the anti-correlation on the decadal scale, which lacks a close connection on shorter scales. More blocking days coincide with low phytoplankton abundance whilst fewer blocking days coincide with high phytoplankton abundance (Figure 5.16a). The long-term variation of atmospheric blocking is accompanied by the shifts of AMO index from positive phase in the 1950s to negative phase between the 1960s and the 1980s, before switching to positive phase again in the early 1990s (Figure 5.17a). High atmospheric blocking activity corresponds to a cold ocean surface, potentially because the blocking system disturbs the warming process over the ocean surface, though it is difficult to separate the cause and effect. Springtime

atmospheric blocking events are also weakly correlated to EAP (Figure 5.17a), possibly due to its influence on wind stress and associated teleconnection.

The number of atmospheric blocking days in the extended winter (December – March) is presented in Figure 5.16b (blue line). Previous studies have shown that high blocking activity coincides with negative NAO phases, which is also confirmed here (Figure 5.17b), though in Western Europe blocking activity shows positive correlation with NAO [Scherrer *et al.*, 2006; Häkkinen *et al.*, 2011; Häkkinen *et al.*, 2013]. Wintertime atmospheric blocking is negatively correlated to the amplitude of the SST annual cycle (Figure 5.16b, r=-0.27, p=0.08), meaning active blocking activity corresponds to a small amplitude for the SST annual cycle and vice versa. This supports the observation that active blocking activity usually occurs when the ocean surface is warm in winter. Warm winter SST potentially reduces the amplitude of SST annual cycle when summer SSTs show no significant change.

From 1990 to 2007, blocking activity is positively correlated to the simulated T_{MLDS} (Figure 5.16b, r=0.45, p=0.06; for blocking activity during February-March, r=0.56, p=0.02). As discussed above, active wintertime blocking activity coincides with negative NAO phase and warm ocean surface, which are also accompanied by weakening of the westerly wind and ocean circulation. These processes all contribute to stabilising the water column during blocking events, which lead to early MLD-shoaling. The blocking events typically last four to eight days and wind stress increases locally after these events, which may disturb the temporary stratification. In years with high blocking activity, more episodes of early-but-disturbed MLD-shoaling develop before the stable spring stratification and hence there is a longer MLD-shoaling process. In years with low blocking activity, stronger westerly winds and ocean circulation keep the water column well mixed through winter, so rapid MLD-shoaling process occurs in spring. The only exception is seen in 2000 when rapid MLD-shoaling occurred in a year with high blocking activity, which might be due to the differences in the distribution of blocking events and the timing of such events in that year compared to others. The correlation between wintertime atmospheric blocking and EAP is stronger than in winter, but still weaker compared to its connection with NAO (Figure 5.17b).

It is worth noting that the North Atlantic SST has been increasing rapidly since the 1990s, with SST equaling or exceeding historical records after the early 2000s [Cattiaux *et al.*, 2011]. The AMO set a historical high record around 2005 (e.g. [Häkkinen *et al.*, 2011]), which corresponds to the warm ocean surface in the North Atlantic. In Figure 5.15 and Figure 5.16, some parameters show extreme values coinciding with this SST extreme whilst other parameters are unaffected. For instance, MLD shoals over an extremely long period and surface chlorophyll-a and PP vary accordingly in 2005 (Figure 5.15). The atmospheric blocking was active, with blocking events occurring over 75 days during the 2004/2005 winter, though not the most active year since 1948 (Figure 5.16b). This also supports the fact that more blocking events occur when the ocean surface is relatively warm, though SST might not be the only factor associated with atmospheric blocking. Seasonal SSTs and maximum winter MLD at this particular location, however, did not react to the SST extreme in 2005. It is possible that the extreme warm state is true for the large-scale average, but is not strongly manifested at some particular locations. The slight decrease of SST ACA is associated with rapid increase of winter SST and as summer SST is also at its high level, the variability of SST ACA is small around this period.

In conclusion, the T_{MLDS} determines the development of the phytoplankton spring bloom and zooplankton population in mASP. An early but disturbed MLD-shoaling process lasts from late March to late June and leads to a weak but continuous spring bloom whilst the late and rapid MLD-shoaling process results in an intense and short spring bloom. Early bloom initiation triggers early zooplankton growth, allowing zooplankton accumulation before the main spring phytoplankton bloom and the resulting spring bloom peak is low. A late and intense spring bloom develops when the zooplankton population is low and zooplankton grazing increases after the main spring bloom, thus the spring bloom can reach a much higher level. The annual PP is perhaps more related to the length of bloom season and overall nutrient concentration rather than to the intensity of spring bloom. The overall energy passed on to higher trophic levels is higher under a weak and long bloom as more phytoplankton is consumed by zooplankton.

Maximum winter MLD and winter and summer SSTs provide no direct implication for the MLD-shoaling process. The strength of the SST annual cycle, calculated as the

amplitude of the annual cycle, is potentially controlled by similar parameters to those that determine the MLD-shoaling process such as heat flux and wind stress. The control of observed variability of phytoplankton abundance (as measured by the CPR observation) through the MLD-shoaling process is not consistent through time: a late and rapid (early but disturbed) process leads to a stronger (weaker) spring bloom before 2001 and the reverse after 2001. The mechanism behind this change is not understood but it may be due to the change of surface circulation and associated water properties, e.g. the dominance of North Atlantic Water or northern origin water and its associated temperature and salinity (pers. comm. P. Chris Reid, 2013). CPR observation is, however, negatively correlated to the number of blocking days in spring on the decadal scale. A greater (fewer) number of blocking days in spring coincides with the negative (positive) phase of AMO and occurs when phytoplankton abundance is relatively low (high). The MLD-shoaling process and SST ACA are related to the number of blocking days in the extended winter, which suggests that the variability of atmospheric forcing from late winter to early spring plays an important role in determining MLD and SST annual cycle in the northeastern North Atlantic. It is not known if the physical mechanisms that control phytoplankton growth in this ecological province also apply in other provinces, which should be tested in the future work.

5.6   Summarising Discussion and Conclusion

Physical and biological characteristics from the NEMO and MEDUSA models were used to analyse the mechanisms controlling phytoplankton growth. The most important physical parameters determining phytoplankton variability were SST and MLD [Waniek, 2003] and the examined biological parameters included surface Chl-a, surface and depth-integrated PP and DIN. All model outputs were of ¼° spatial resolution from January 1990 to December 2007. Monthly data were used to compare model outputs with observations and to define ecological provinces and 5-Day outputs were used to study the physical mechanisms. Due to the length of the simulation, only inter-annual variability can be examined whilst variability on longer scales is suggested but not verified.

It is presented in previous chapters that the direct SST increase only plays a miner role in determining the timing of phytoplankton spring bloom whilst the variation of MLD

modulating phytoplankton accumulation by changing the distribution of light and nutrients. The link between MLD and SST is tested first because if this connection is true then the observed long-term variability of SST and phytoplankton can be linked via MLD. Linear regression analysis suggested that in the Rockall Trough, Porcupine Abyssal Plain and Labrador Sea-south Greenland area, a negative connection between SST and MLD was found in winter while in summer, a negative connection was seen in the eastern subpolar and no statistical significant connection was seen in the rest of the subpolar basin. These results suggest that previously observed variability in SST could indicate variability in MLD in parts of the subpolar North Atlantic and mainly in winter. Though higher SST is often accompanied with stronger stratification (shallower MLD), this link between MLD and SST might not be significant at basin sale. In addition, only inter-annual variability between MLD and SST is tested in this study due to a short model simulation. However, the most influential climatic indices are AMO and NAO for both SST and MLD (see Chapter 4.3.3 for details), which are also the two leading modes controlling the longer-term variability of SST, suggesting SST and MLD at least share similar controlling mechanism that may also work on the decadal to multi-decadal scales.

A deep MLD provides abundant nutrient but reduces average light intensity while a shallow MLD limits nutrient availability, but the stratified upper layer is well-lit. Winter mixing is the major process that replenishes the nutrient concentration in the upper layer and the maximum MLD indicates available DIN and, potentially, the strength of spring bloom. However, no basin-scale pattern was found in the subpolar basin, though deeper than average maximum MLD leads to higher than average Chl-a and PP in the southern subpolar basin. This region is sometimes regarded as the transition zone between the subpolar and subtropical gyres [e.g. Henson *et al.*, 2009a; Zhai *et al.*, 2013] and the bloom type is between typical subpolar and subtropical types. In the model, the region south of 45 °N, phytoplankton growth is controlled by the nutrients concentration and is closer to the subtropical bloom type. In the northern subpolar basin, the relationship between simulated Chl-a and maximum MLD is less consistent and is unlikely driven by the same mechanism. The discontinuity in phytoplankton response to MLD reflects the inconsistency of physical forcing and the driving mechanisms across the basin. The subpolar basin is then divided into seven ecological provinces based on discontinuity in temperature, vertical velocity and maximum MLD.

In the Atlantic Arctic Province (mAAP), DIN depletion seldom occurs and DIN is not a limiting factor. In the Atlantic Subarctic Province (mASP), DIN depletion occurs infrequently and lasts ~ 20 days, which could limit phytoplankton spring bloom in some years. In the North Atlantic Drift Province (NADP), DIN depletion occurs frequently, which lasts ~5 months in the south and ~3 months in the north, limiting phytoplankton growth. In the two stratified provinces, Gulf Stream Province (GFSP) and North Atlantic Subtropical Province (NASP), nutrient depletion occurs every year during the 18-year period and a clear nutrient limitation controlling phytoplankton bloom presents here. In these two provinces, phytoplankton bloom in late autumn—early winter when nutrient is relatively abundant.

To further analyse the physical mechanisms controlling phytoplankton growth in mAAP, mASP and NADP, model outputs were compared to CPR data that corresponds to the same provinces. The annual cycle and long-term monthly data were in best agreement in the location representing mASP, this location was thus selected as a case study. The 5-Day data suggested that variation of MLD at bloom initiation stage determined the strength of bloom initiation, with deep (shallow) MLD corresponding to a low (high) Chl-a at bloom initiation. MLD and DIN did not control phytoplankton bloom directly at the bloom peak stage. The Chl-a concentration at autumn bloom termination was weakly correlated to MLD and DIN, but large inter-annual variability was seen in Chl-a concentration. The phytoplankton concentration at bloom peak and spring bloom termination is affected perhaps more directly by other factors than by MLD and DIN.

At this location, phytoplankton starts to accumulate before shallow stratification in a typical annual cycle, which contrasts the critical depth theory [Sverdrup, 1953] and supports more recent findings, such as the dilution-recoupling hypothesis [Behrenfeld, 2010]. However, model simulation rules out the dilution-recoupling as the primary mechanism here because deeper MLD actually coincides with lower Chl-a rather than higher Chl-a expected under low grazing pressure. The impact of zooplankton grazing on phytoplankton abundance seems to be stronger in the model towards the end of the spring bloom, when three types of zooplankton grazing remove ~85% of surface PP and terminating surface bloom together with natural mortality. Phytoplankton growth can continue at depth as grazing removes ~30% of total depth-integrated PP and nutrients

are above depletion level. In autumn, MLD deepening is accompanied by a very weak increase in phytoplankton and grazing as a result of the replenished nutrients in the upper layer.

In order to address the mechanism controlling phytoplankton spring blooms, the characteristics of MLD-shoaling, phytoplankton accumulation and zooplankton grazing are summarised as follows:.

1. An early but disturbed MLD-shoaling process takes up to three months to establish vernal (spring) stratification and leads to pulses of phytoplankton accumulation, which is disturbed by storm events and vertical mixing. This early phytoplankton accumulation triggers early growth of zooplankton and zooplankton removes ~8% (~40%) of total annual depth-integrated (surface) PP during the development of the main spring bloom following the vernal (spring) stratification.

2. In some other years, a late and rapid MLD-shoaling process takes 10—30 days to establish stable stratification and leads to a short but intense phytoplankton bloom as the major spring bloom occurs soon after stable stratification is established and grazing rate of total annual depth-integrated PP is close to zero during its development (~3% of surface PP). Zooplankton grazing peaks after the spring bloom and removes ~15% of total annual depth-integrated PP. This mechanism might apply to the whole mASP where the physical forcing and ecological responses are uniform as the average spatial variability is ~65 m for MLD and ~0.2 mg Chl/m^3 for surface Chl-a. Though it might not be valid in other parts of the subpolar basin. In the period 1990—2007, no decadal shift between the two physical and biological conditions is seen, rather a change from one condition to the other is evident at an inter-annual scale. Based on model outputs, two types of spring bloom occurred for an equivalent length of time during this 18-year period.

The main hypothesis presented in this study is that the timing and characteristics of the MLD-shoaling period determines the timing, duration and strength of the phytoplankton spring bloom through altering the timing and development of zooplankton grazing. The role of MLD differs from that in the dilution-recoupling hypothesis because: the

variation of MLD changes the timing of the zooplankton growth rather than affecting the grazing pressure in the late winter. It was the accumulated zooplankton population in spring that matters to the strength of the main spring bloom instead of the grazing pressure during the MLD-shoaling period.

Waniek (2003) proposed a similar hypothesis for the spring bloom development in the northeast North Atlantic using observation from scientific cruise and a numerical biological-physical model. Disturbed bloom started also earlier than a continuous bloom and with lower biomass, similar to what is found in this study. The disruptive vertical mixing was explained as a consequence of storms occurring at a frequency of once a week in early spring. However, in this study, it is argued that the anomalously early and calm condition in the late winter leads to early phytoplankton bloom, which is disturbed by the resumed vertical mixing. The calm weather condition is explained by the temporary atmospheric blocking in the northeast North Atlantic that shifts the wind patterns and modulates the heat fluxes at the ocean surface.

The combination of reduced wind and increased net heat flux in the late winter has been proposed as the controlling factor of spring bloom initiation. [Taylor and Ferrari, 2011a; Taylor and Ferrari, 2011b]. They argued that the switch of net heat flux from negative to positive is a better indicator of spring bloom initiation than MLD shoaling, because the change net air-sea flux allows the establishment of a shallow mixing layer. This layer is nutrient abundant and well-lit, which lead to phytoplankton accumulation. The timing of the disturbed spring bloom initiation in this study agrees with their results, but it is unclear whether the differences between the two types of spring bloom can be fully explained by the net air-sea flux changes. Later study also suggested that eddy induced slumping of the north-south density gradient can reduce the vertical sheer and lead to patchy bloom about 20-30 days before the restratification caused by surface warming. This eddy restratification is associated with the lateral density gradient, MLD, surface cooling that is lower than a certain threshold and is affected by wind direction as well as its speed [Mahadevan *et al.*, 2012]. It is not tested here whether the atmospheric blocking and associated temporary MLD-shoaling is associated with eddies in this study, the two processes at least share some similar factors such as the change of wind speed, direction and potentially surface heat cooling.

Other studies pointed out the influence of NAO to the timing of spring bloom initiation and phytoplankton community structure with negative NAO leading to earlier spring bloom and higher ratio of dinoflagellate [Henson *et al.*, 2012; Zhai *et al.*, 2013] Though the study areas are not necessarily identical to the location discussed in this study, the link between spring bloom dynamic and NAO is suggested through its influence of the number days with atmospheric blocking. In years when NAO index is at negative phase, more atmospheric blocking occurs in the eastern subpolar basin, leading to an early but weak spring bloom. The potential influence of atmospheric blocking on phytoplankton community structure is not discussed here but the response of phytoplankton to temporary MLD shoaling shows a drastic turn around 2001 were coincided with the change from diatoms dominance to dinoflagellates dominance.

Inter-annual variability of maximum winter MLD and seasonal SSTs were not linked directly with the MLD-shoaling process, though the SST annual cycle amplitude (ACA) showed a negative correlation with the MLD-shoaling. This suggests that there might be parameters or processes influencing both the variability of ACA and MLD-shoaling. The number of days of atmospheric forcing was calculated for the extended winter to examine the physical mechanisms that control ACA and MLD-shoaling. In years with high atmospheric blocking activity, ACA was relatively low (for the period 1948-2007) and MLD shoals over a long period (for the period 1990-2007). This is likely due to the fact that more blocking activity in winter coincides with a shifted storm track and relatively warm ocean surface. Temporarily reduced wind stress and warm winter SST both contribute to temporary MLD shoaling, especially towards the end of winter. Higher than average winter SST also tends to decrease SST ACA.

Potential physical mechanisms controlling the observed CPR variability is one of the focus of this thesis. In this particular location in mASP, the MLD-shoaling process is negatively related to phytoplankton abundance before 2001 and positively related to phytoplankton abundance after 2001. This observed shift may be related to the change in surface circulation and associated water properties and/or the proportional increase of the non-diatom population in the local functional group structure, with the exact process and mechanism remaining unclear. This correlation suggests that MLD is one factor that controls phytoplankton variability and the effect of MLD could manifest itself in other parameters. On the decadal scale, the strength of the spring bloom is also related to the

number of blocking days in spring, with a greater (fewer) number of blocking events coinciding with low (high) phytoplankton abundance.

In the Labrador Sea, the earliest bloom was observed in the northeast and was most intense there. This early bloom was associated with early stratification caused by offshore-directed freshwater in that region and its intensity was correlated to ocean processes. In the central Labrador Sea the bloom was later and weaker and correlation was only found between the bloom timing and irradiance [Frajka-Williams and Rhines, 2010]. This agrees well with modelled Chl-a variability in mAAP and this mechanism might apply to the ecological province where freshwater was an important factor. In autumn, phytoplankton accumulation is curtailed by light-limitation. The phytoplankton development in NADP and GFSP is closely related to the frontal system, where early phytoplankton accumulation is observed along the pathway of the Gulf Stream and North Atlantic Current. The difference between these two provinces is that nutrient-limitation occurs soon after the late-winter-to-early-spring bloom in GFSP whilst phytoplankton growth lasts longer in NADP as the nutrient brought into the upper layer by wind-driven mixing is considerable in this area [Edwards and Richardson, 2004]. In NASP, the development and inter-annual variability of the phytoplankton bloom is mainly determined by the variation of the maximum MLD, which controls the amount of available nutrients.

In conclusion, the physical mechanisms controlling phytoplankton growth were examined using data outputs from the NEMO and MEDUSA models. The model outputs captured the basic physical and biological features within the subpolar North Atlantic. The development of phytoplankton spring blooms in different parts of the basin are controlled by different physical processes and ecological provinces are defined using NEMO outputs. In mASP, modeled Chl-a agrees with CPR observations on both annual and inter-annual scales. At this location, the MLD-shoaling process determines the timing, length and strength of the phytoplankton spring bloom and the development of the zooplankton population. An early, long and disturbed MLD-shoaling process leads to early but disturbed phytoplankton accumulation, which gives more time for zooplankton to grow and results in weak spring bloom but high annual PP. A late and rapid MLD-shoaling process leads to an intense and short spring bloom but lower annual PP. MLD-shoaling processes are correlated to the number of blocking days in

winter, particularly in late winter, whilst spring CPR abundance and bloom peak are negatively correlated with the number of blocking days in spring on decadal scale. This province lay within the region where negative correlation was found between SST and winter MLD in both cold and warm seasons. The blocking events in late winter and early spring are also related to the variability of the amplitude of the SST annual cycle, which is potentially due to the warm ocean surface and negative NAO phase during high blocking activity years. The proposed hypothesis explains the observed CPR variability to some extent through the interaction of phytoplankton and zooplankton development' however, other parameters such as concentration of nutrients might have a greater impact on phytoplankton bloom dynamics, especially under a warming climate.

Table 5.1 Determining Physical Parameters in the Major Ecological Provinces

	SST	Maximum MLD	Vertical Velocity	DIN Depletion Length	DIN Depletion Frequency
mAAP	< 7 °C	Mixed	Upwelling	0	Seldom
mASP	> 7 °C	Mixed	Upwelling	< 20 Days	Frequent
NADP	> 7 °C	Mixed	Upwelling & Downwelling	50-150 Days	Very Frequent
GFSP	> 7 °C	Stratified	Downwelling	50-150 Days	Very Frequent
NASP	> 7 °C	Stratified	Downwelling	> 200 Days	Every Year

Table 5.2 Phytoplankton Responses in the Major Ecological Provinces

	Bloom Initiation	Bloom Peak	Second Bloom	Bloom Termination	Zooplankton Control[1]
mAAP	Mid-April, with increasing isolation and shoaling MLD	May—June	Occasionally, associated with zooplankton migrating to deeper depth	~ October, light limited	Associated to the occasional second bloom
mASP	Early April, with increasing irradiance and shoaling MLD	Late April—May	Associated to nutrient replenish and zooplankton migration	September—October, light limited	Associated to the second bloom
NADP	Along NAC pathway: March; the rest NADP: April	April—May	No	Nutrient limited	Post-spring bloom—summer Chl-a distribution
GFSP	December—January with relatively deep MLD	March	No	Nutrient limited	Post-bloom—summer Chl-a distribution
NASP	December when MLD is deep	February—March	No	Nutrient limited	Balance phytoplankton production

[1] The zooplankton control is adapted from Longhurst (2007).

Table 5.3 The Correlation Coefficient between Simulated Biological Parameters and CPR Observation

	PCI	Model Chl-a	Model PP
PCI		r=0.53, p=0.02	r=0.64, p=0.004
Model Chl-a	r=0.53, p=0.02		r=0.8, p=0.0001
Model PP	r=0.64, p=0.004	r=0. 8, p=0.0001	
Linear Regression	gradient=0.2, intercept=0.5	gradient=3.9, intercept=144	gradient=0.06, intercept=2.0

Table 5.4 The Correlation Coefficients[1] of Simulated Parameters at Four Stages of the bloom within One Annual Cycle

		DIN	Chl-a	INT_PP[2]	GMIPN/ INT_PP	GMEPN /INT_PP	GMEPD /INT_PP
Spring Bloom Initiation	Chl-a	-0.73		0.67	0.41		
	MLD		-0.63		-0.65		
Spring Bloom Peak	Chl-a	-0.79		0.68	-0.63		
	MLD	0.65					
Spring Bloom Termination	Chl-a			0.63			0.41
	MLD	0.68		0.57	-0.59		
Autumn Bloom Termination	Chl-a	-0.79		0.44	0.65	0.59	0.73
	MLD	0.72	-0.59		-0.88	-0.85	-0.66

[1] Shown correlation coefficients are significant at 95% interval levels and crossed boxes indicate no significant correlation was found between the two regarding parameters.

[2] INT_PP stands for depth-integrated primary production, GMIPN stands for micro-zooplankton grazing on non-diatom, GMEPN stands for meso-zooplankton grazing on non-diatom and GMEPD stands for meso-zooplankton grazing on diatom.
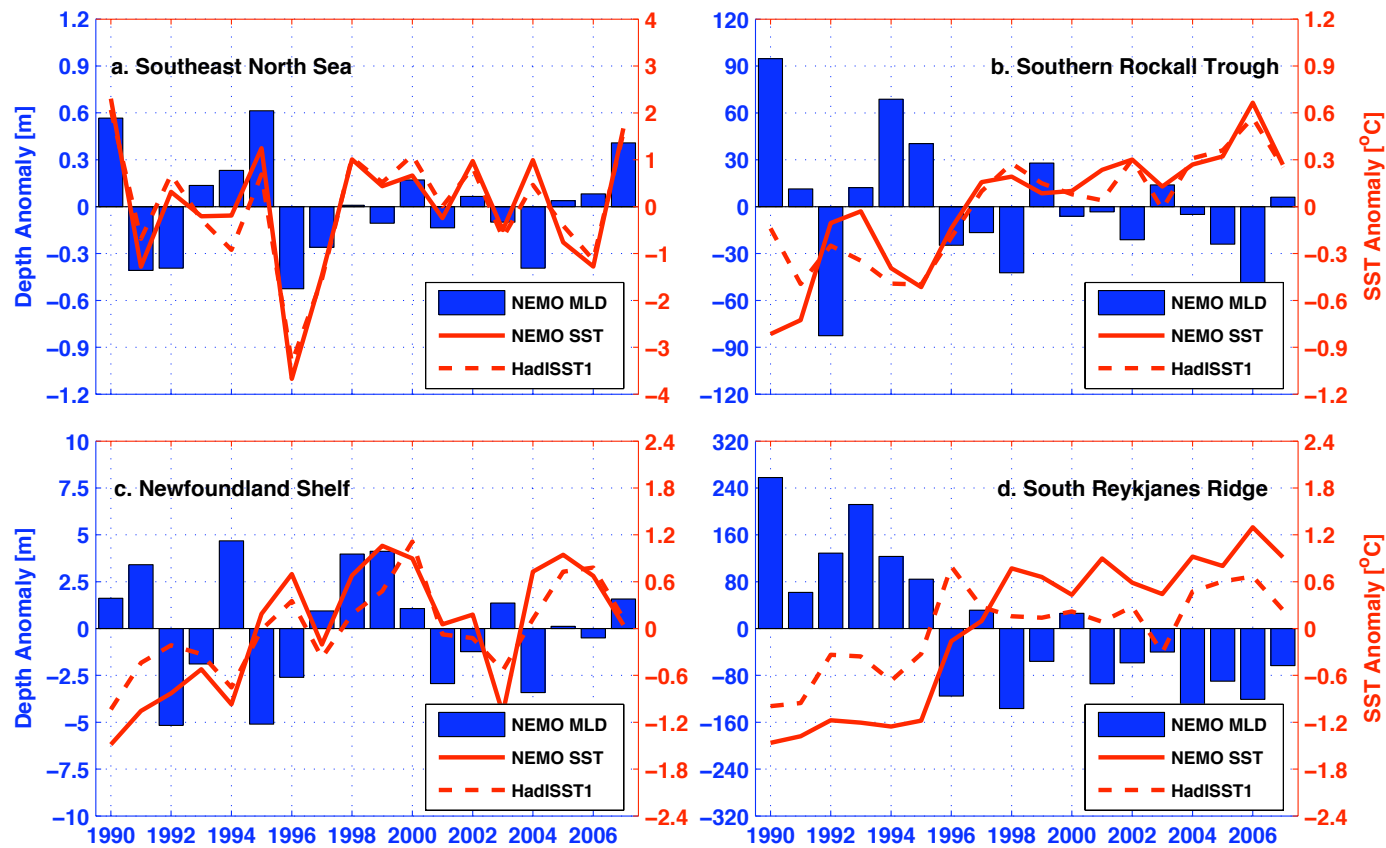
Figure 5.1 The anomalies of winter (January – March) NEMO MLD (blue bars), NEMO SST (solid red lines) and HadISST1 (dashed red lines) in (a) Southeast North Sea, (b) Southern Rockall Trough, (c) Newfoundland Shelf and (d) South Reykjanes Ridge over the period 1990 – 2007. Note the vertical scales are different in different panels.
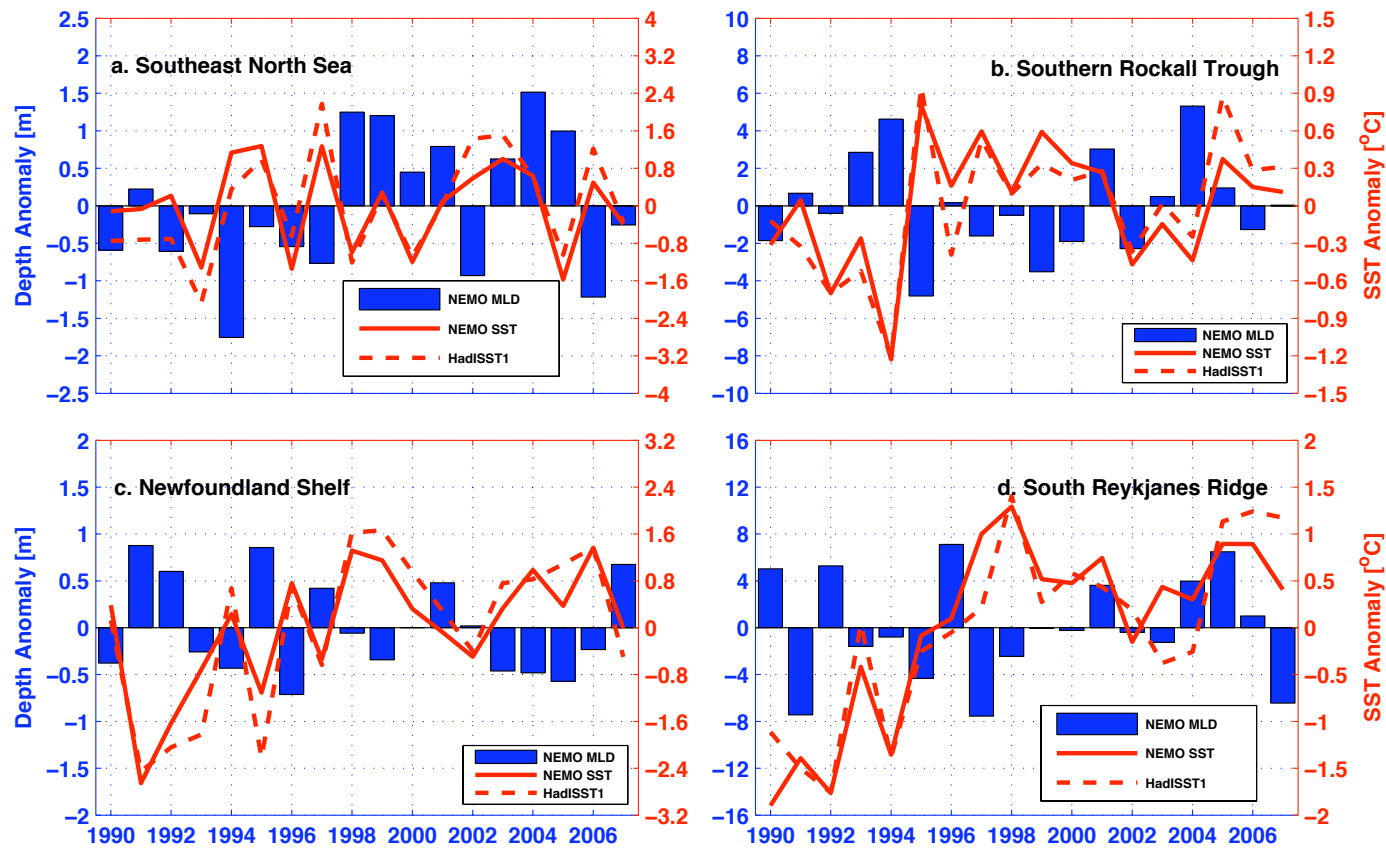
Figure 5.2 The anomalies of summer (July – September) NEMO MLD (blue bars), NEMO SST (solid red lines) and HadISST1 (dashed red lines) in (a) Southeast North Sea, (b) Southern Rockall Trough, (c) Newfoundland Shelf and (d) South Reykjanes Ridge over the period 1990 – 2007. Note the vertical scales are different in different panels.
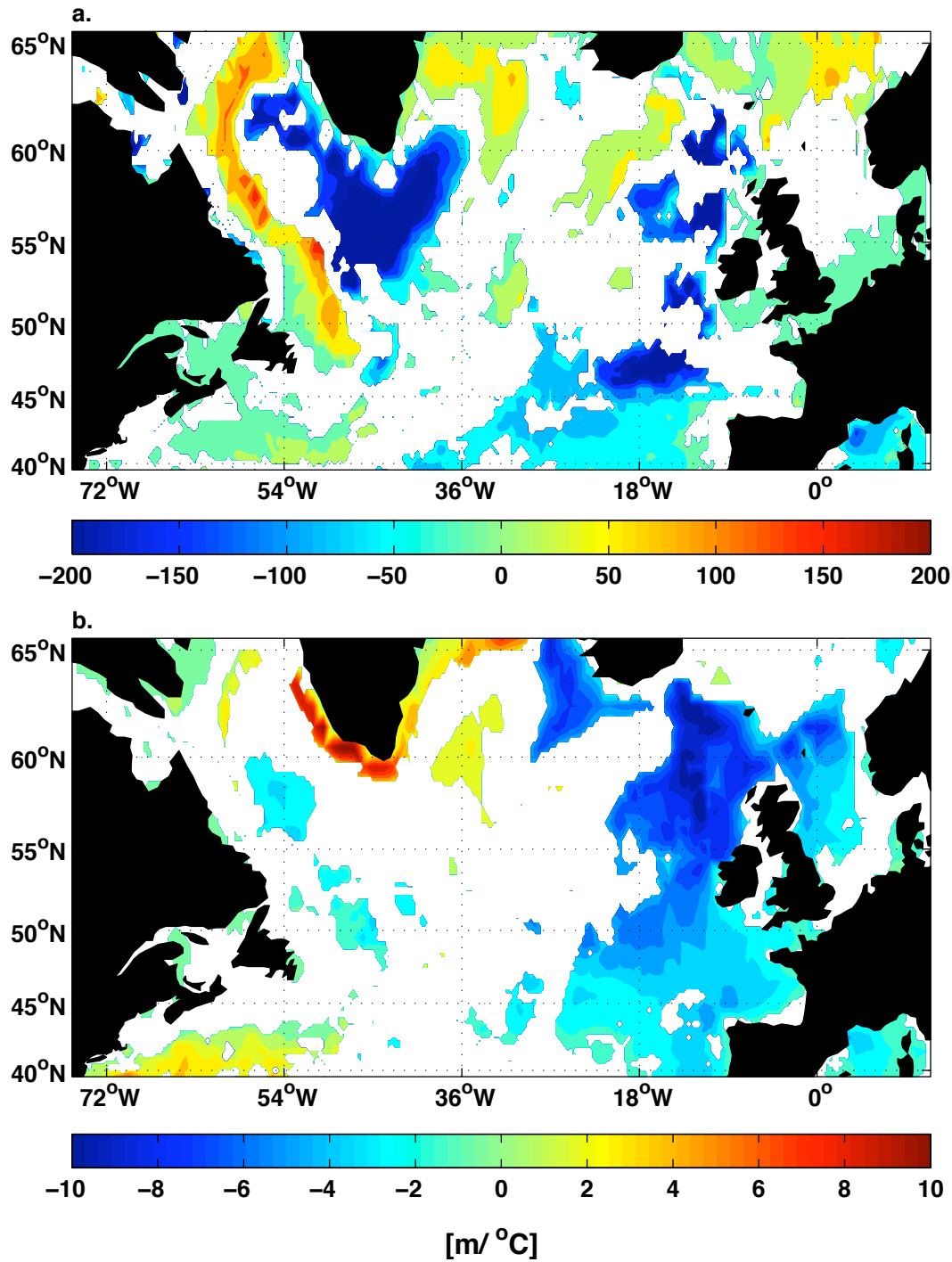
Figure 5.3 Linear regression coefficient of NEMO MLD on NEMO SST in the subpolar North Atlantic in (a) winter and (b) summer over the period 1990 – 2007. Only coefficients significant at 90% confidence intervals are shown.
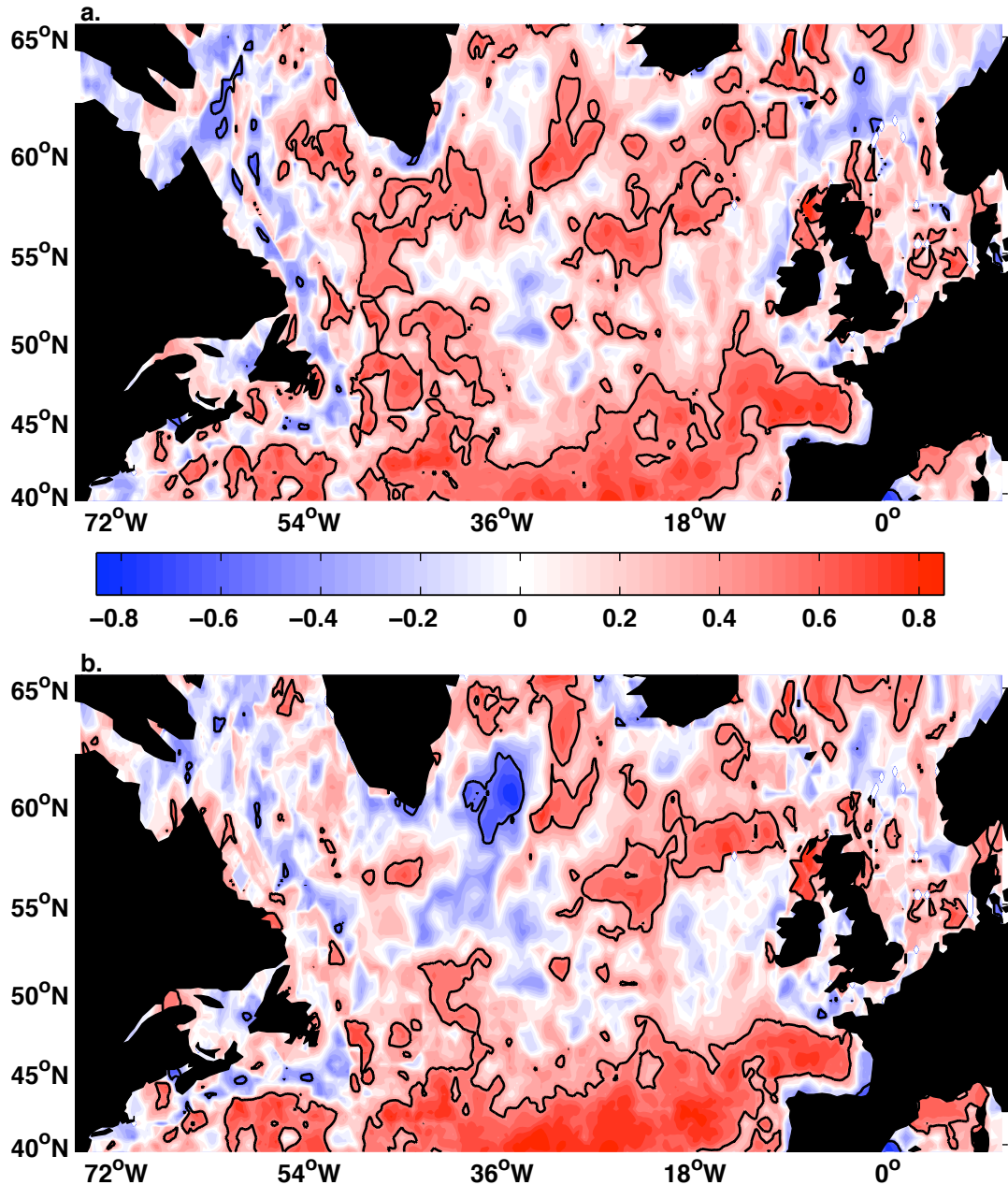
Figure 5.4 The correlation coefficients between the maximum NEMO MLD and (a) the average simulated spring-summer surface Chl-a and (b) the average simulated spring-summer surface PP over the period 1990 – 2007. All three time series are detrended and black lines indicate areas with coefficients of 95% significance.
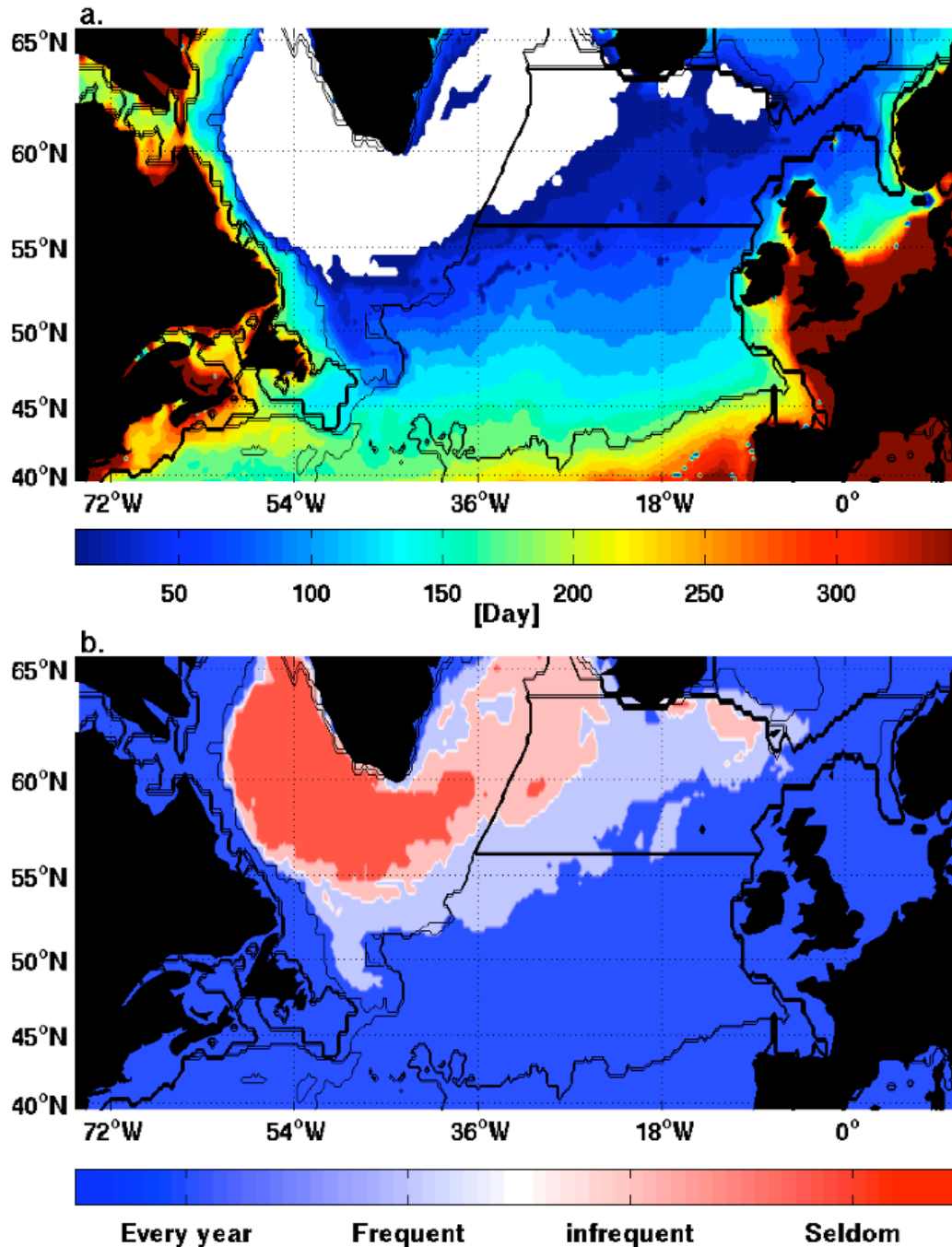
Figure 5.5 (a) The average length of nitrate depletion in the subpolar basin, the blank area indicate the region where average nitrate never falls below 0.5 mmol-N/m^3; (b) the frequency of occurrence of nitrate depletion. Seldom: nitrate depletion occurs in less than 3 years during the 18-year period; infrequent: nitrate depletion occurs in more than 3 years but less than 9 years; frequent: nitrate depletion occurs in more than 9 years but less than 16 years; every year: nitrate depletion occurs in more than 16 years.
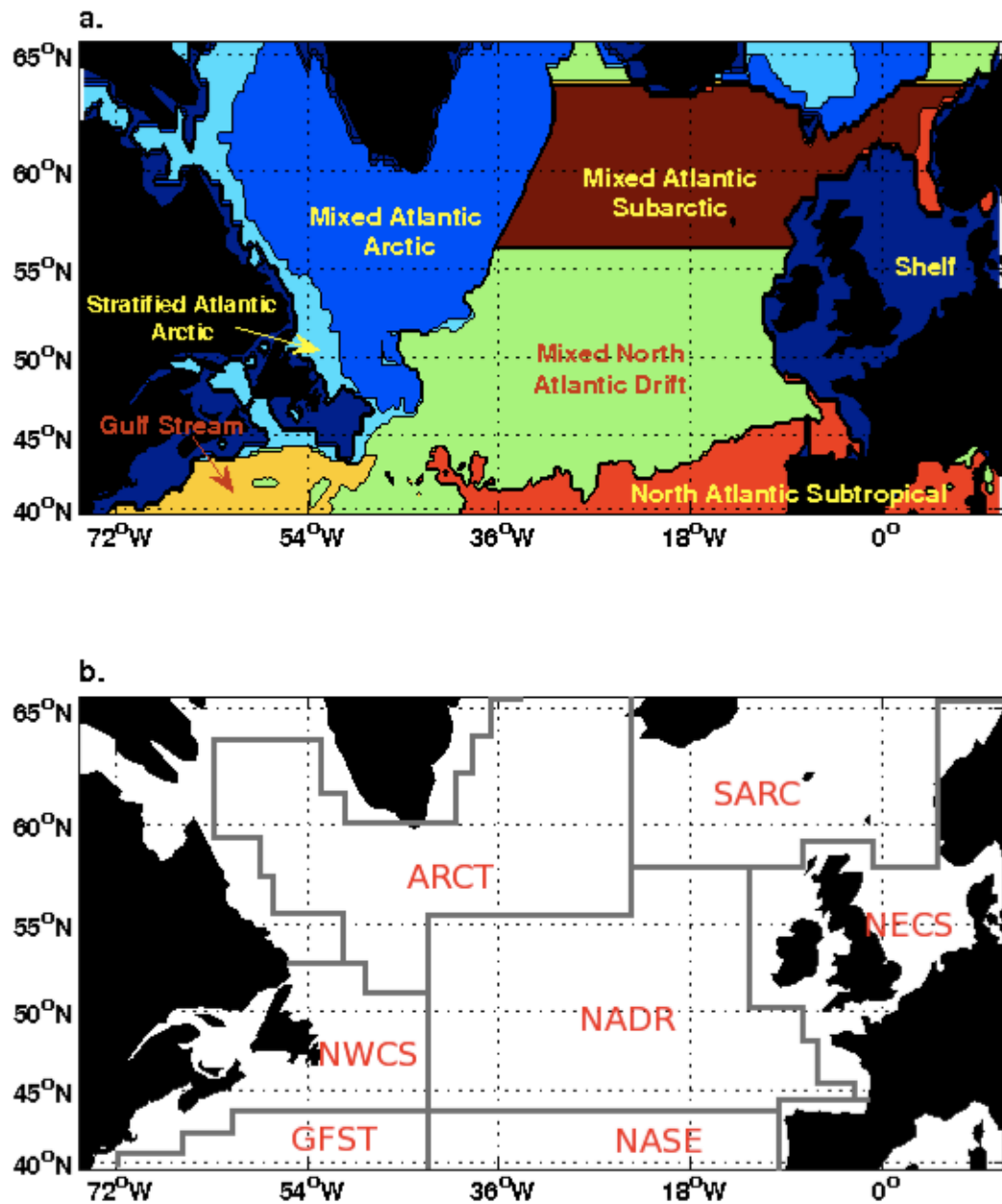
Figure 5.6 (a) The ecological provinces scheme in this study; (b) the ecological provinces in the subpolar North Atlantic in Longhurst (2007).
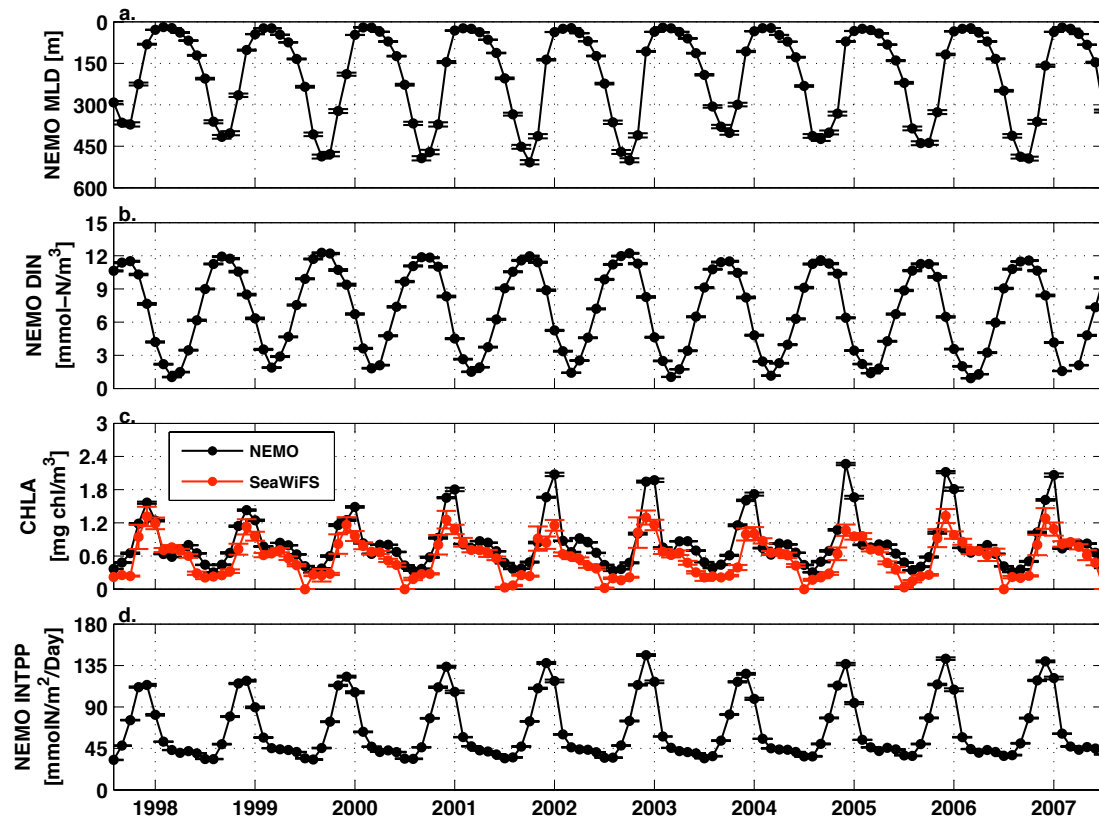
Figure 5.7 Monthly variation of simulated (a) MLD, (b) DIN, (c) surface NEMO Chla (black line) and SeaWiFS Chla (red line) and (d) depth-integrated PP in Atlantic Arctic province from September 1997 to December 2007. The error bars indicate the spatial variability within the province.
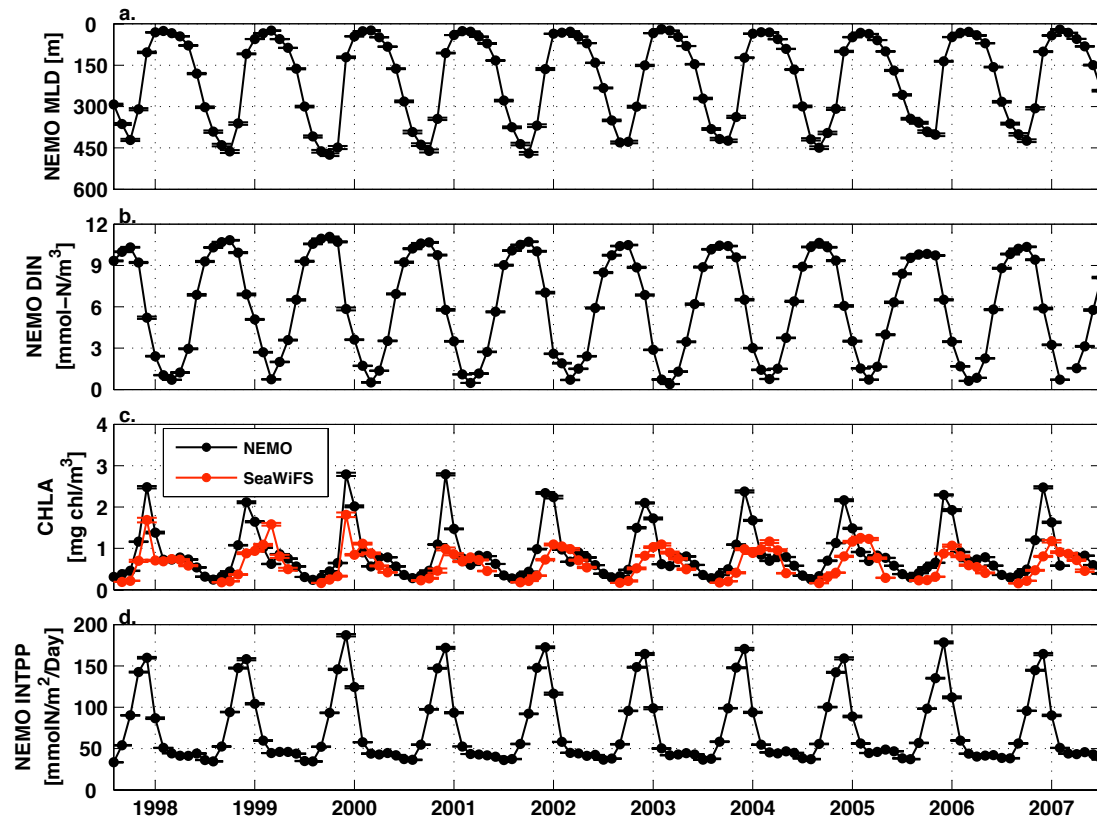
Figure 5.8. Monthly variation of simulated (a) MLD, (b) DIN, (c) surface NEMO Chla (black line) and SeaWiFS Chla (red line) and (d) depth-integrated PP in Atlantic subarctic province from September 1997 to December 2007. The error bars indicate the spatial variability within the province.
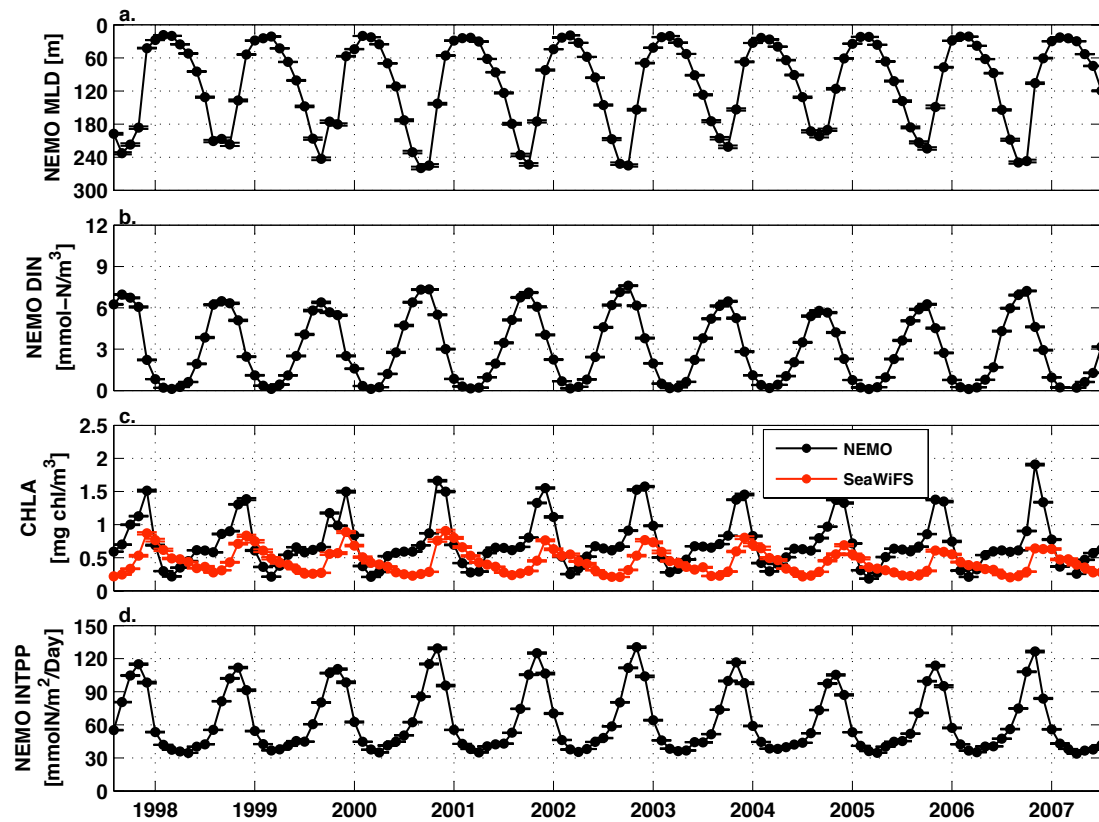
Figure 5.9. Monthly variation of simulated (a) MLD, (b) DIN, (c) surface NEMO Chla (black line) and SeaWiFS Chla (red line) and (d) depth-integrated PP in North Atlantic Drift province from September 1997 to December 2007. The error bars indicate the spatial variability within the province.
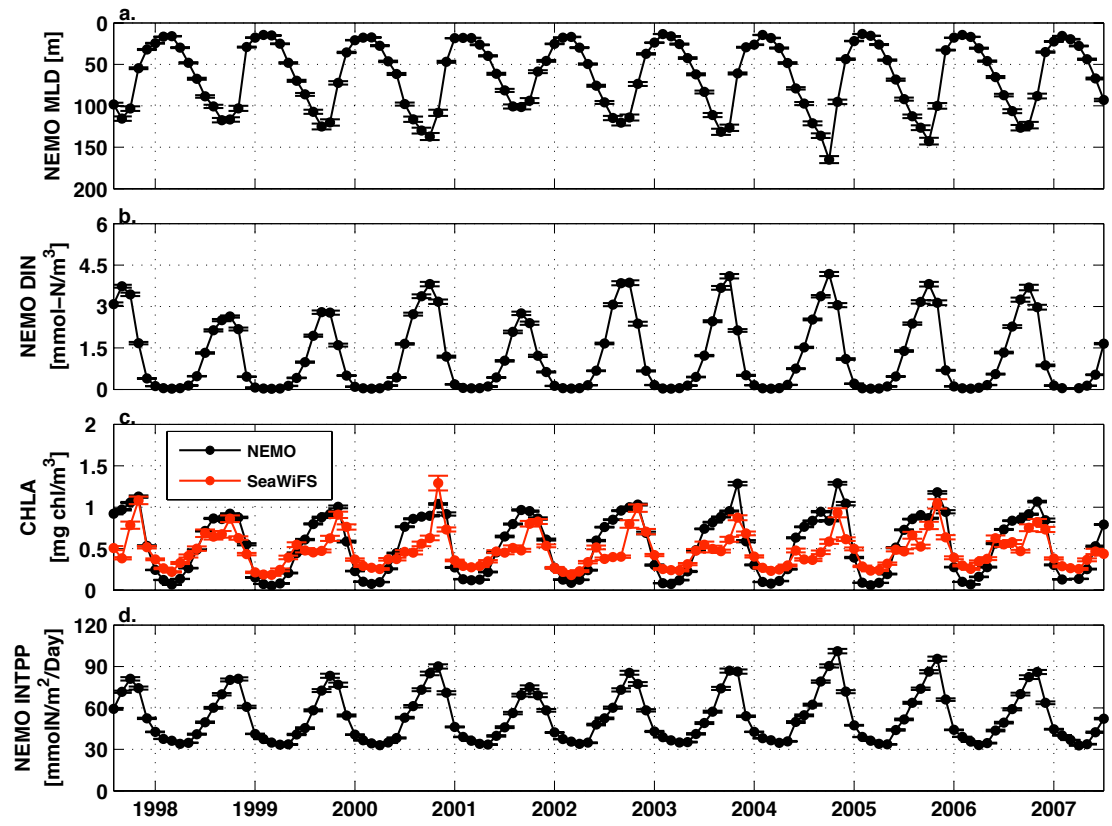
Figure 5.10. Monthly variation of simulated (a) MLD, (b) DIN, (c) surface NEMO Chla (black line) and SeaWiFS Chla (red line) and (d) depth-integrated PP in Gulf Stream & Extension province from September 1997 to December 2007. The error bars indicate the spatial variability within the province.
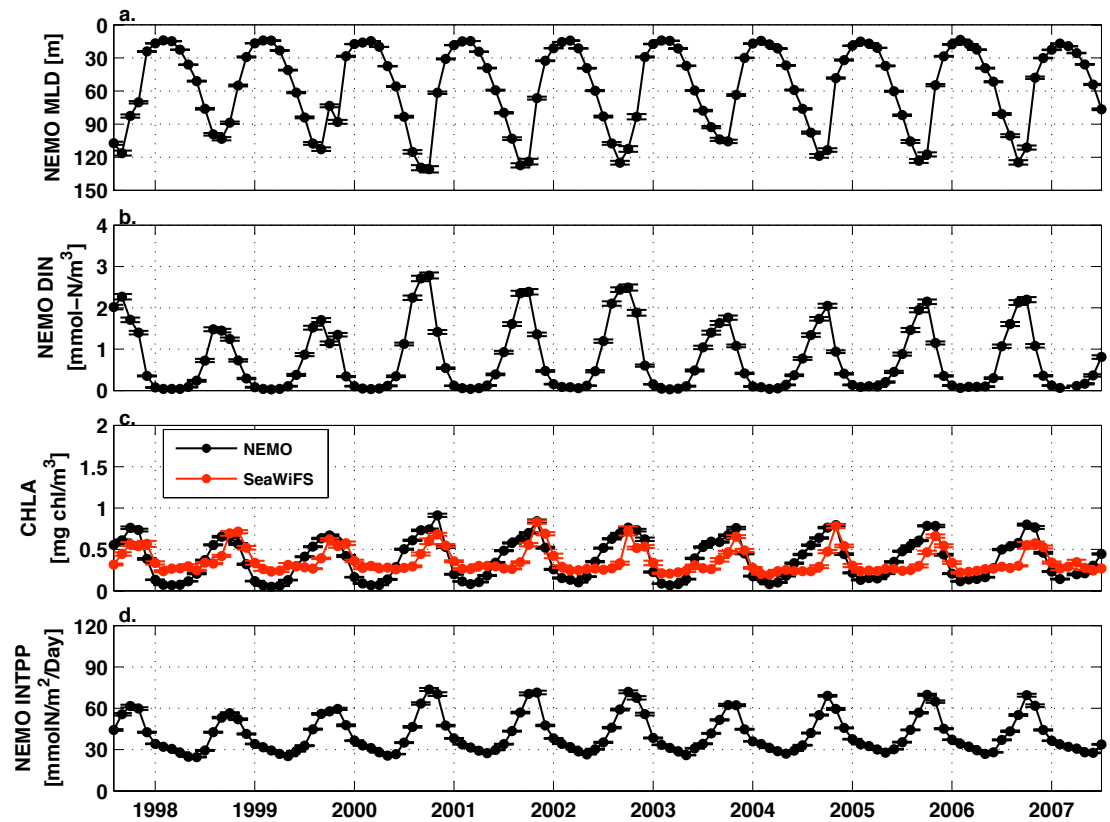
Figure 5.11. Monthly variation of simulated (a) MLD, (b) DIN, (c) surface NEMO Chla (black line) and SeaWiFS Chla (red line) and (d) depth-integrated PP in North Atlantic Subtropical province from September 1997 to December 2007. The error bars indicate the spatial variability within the province.
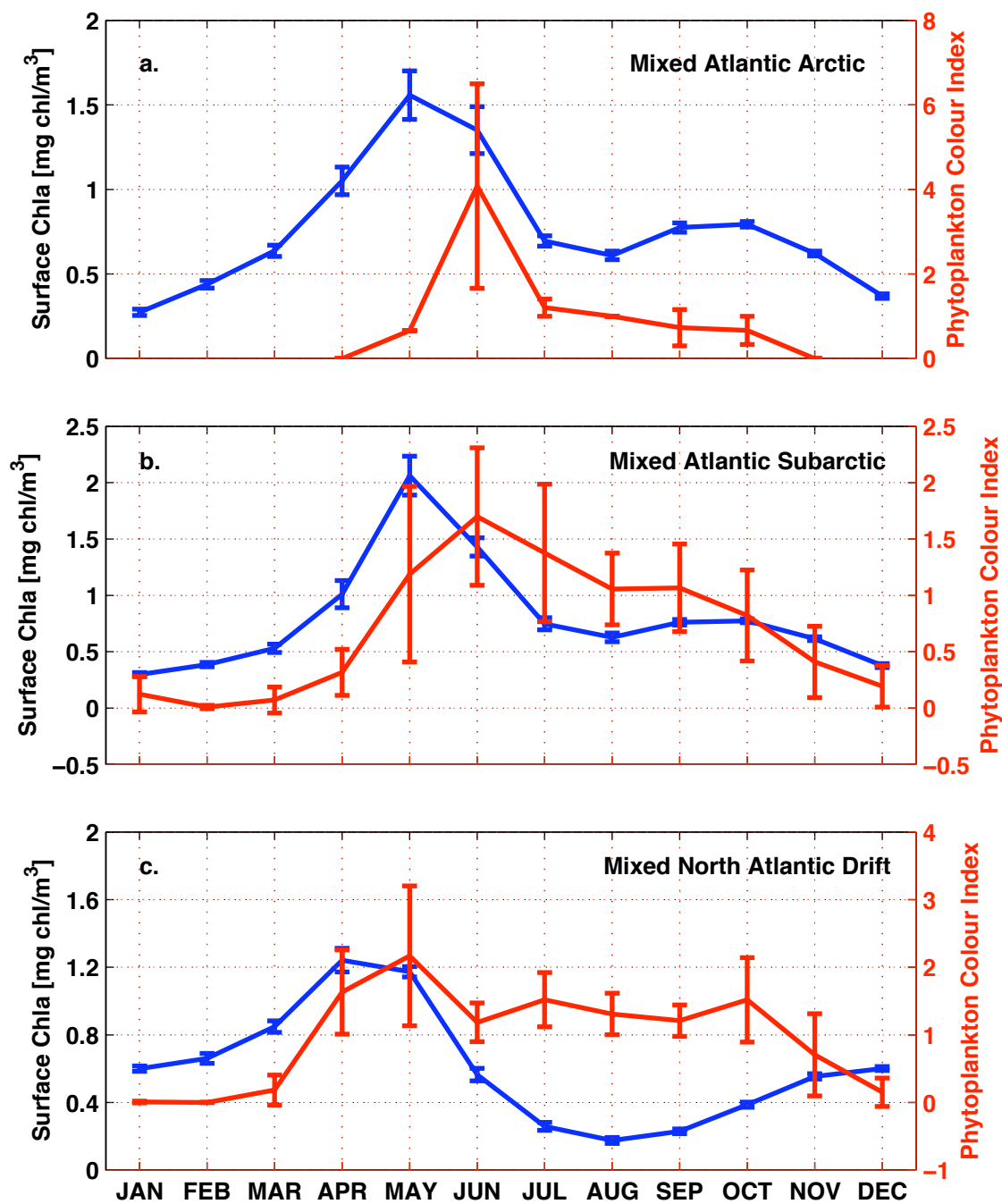
Figure 5.12 The average annual cycle of PCI (red lines) and simulated surface Chl-a (blue lines) over the period 1990 – 2007 in (a) mixed Atlantic Arctic province, (b) mixed Atlantic Subarctic province and (c) mixed North Atlantic Drift province. The error bars indicate the standard error of the mean (SEM) on 95% confidence intervals.
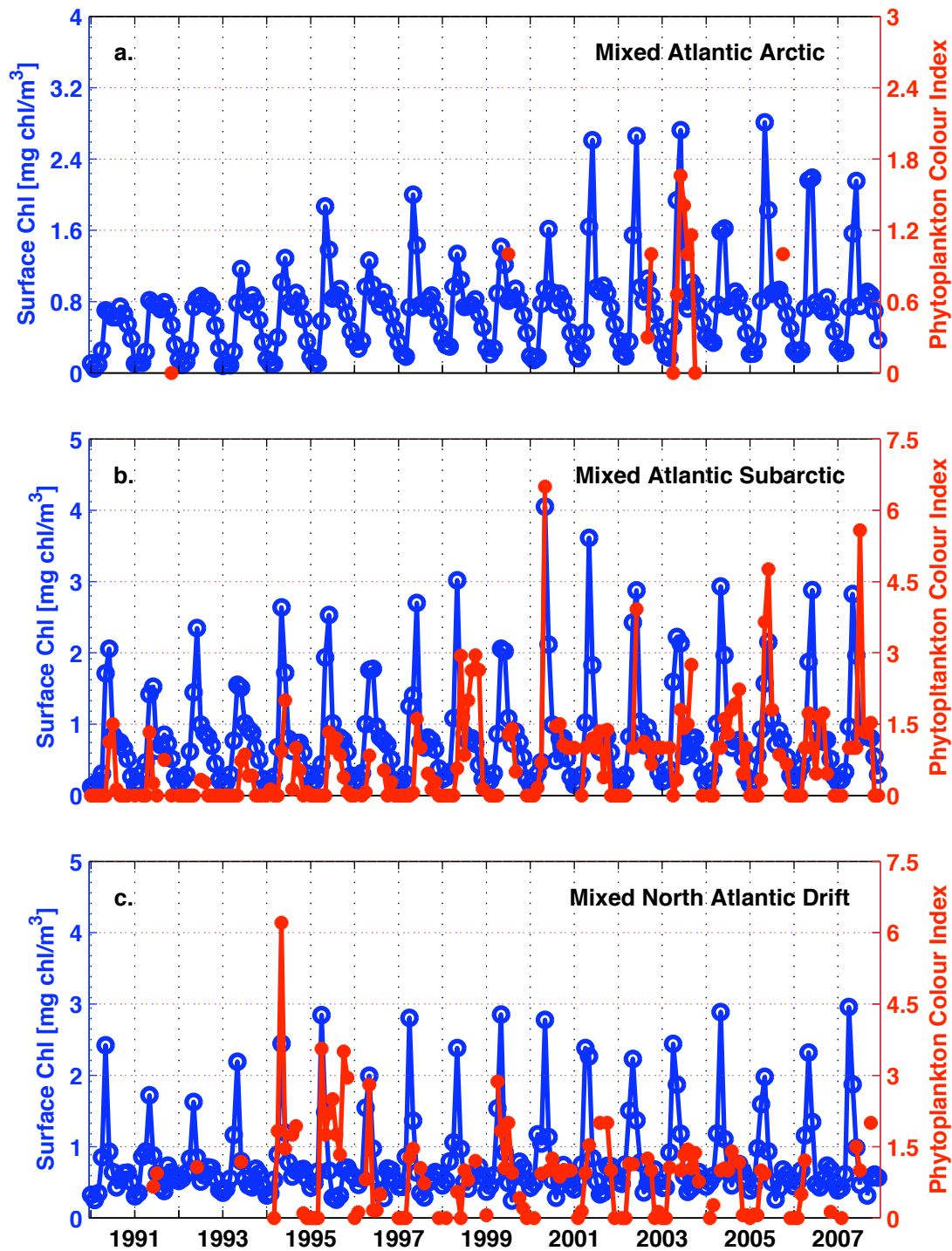
Figure 5.13 Monthly time series of simulated surface Chl-a (blue lines) and PCI (red lines) over the period 1990 - 2007 in (a) mixed Atlantic Arctic province, (b) mixed Atlantic Subarctic province and (c) mixed North Atlantic Drift province.
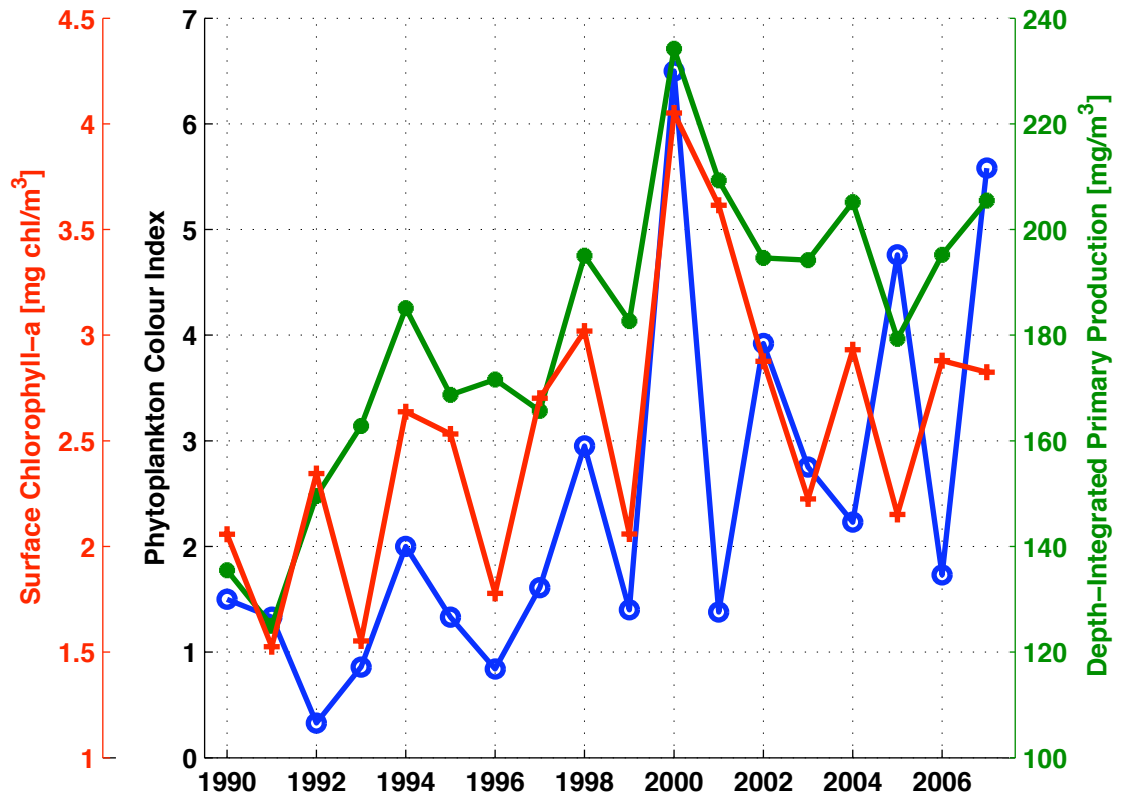
Figure 5.14 The simulated annual maximum surface Chl-a (red line), depth-integrated PP (green line) and PCI (blue line) in the location (CPR B5) representing the mixed Atlantic Subarctic province from 1990 to 2007.
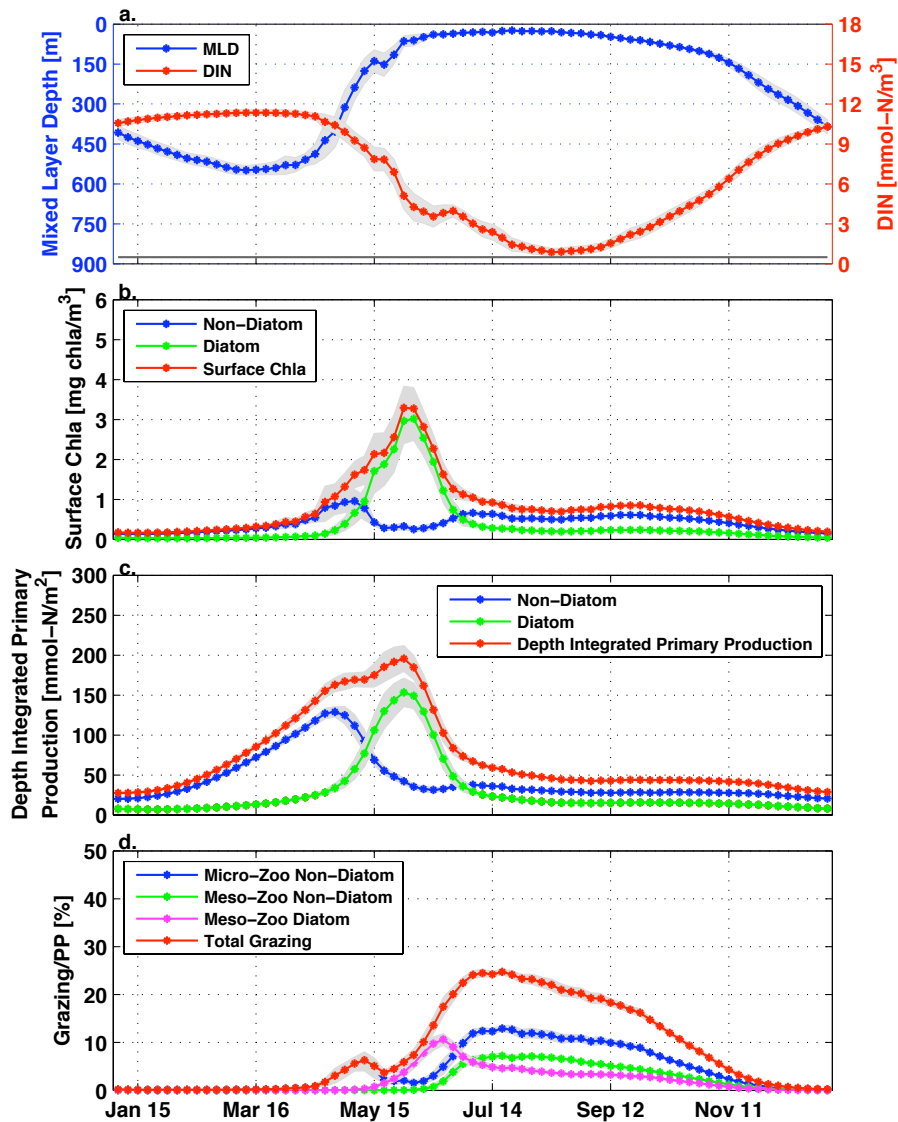
Figure 5.15 The average annual cycle of (a) MLD (blue line) and DIN (red line), (b) surface Chla from non-diatom (blue line), diatom (green line) and combined (red line), (c) PP from non-diatom (blue line), diatom (green) and combined (red line) and (d) microzooplankton grazing on non-diatom (blue line), mesozooplankton grazing on non-diatom (green line), mesozooplankton grazing on diatom (magenta line) and total grazing (red line) at the location representing mASP. All grazing rate is plotted related to the depth-integrated PP. The grey shades indicate the variability over the 18-year period at this location.
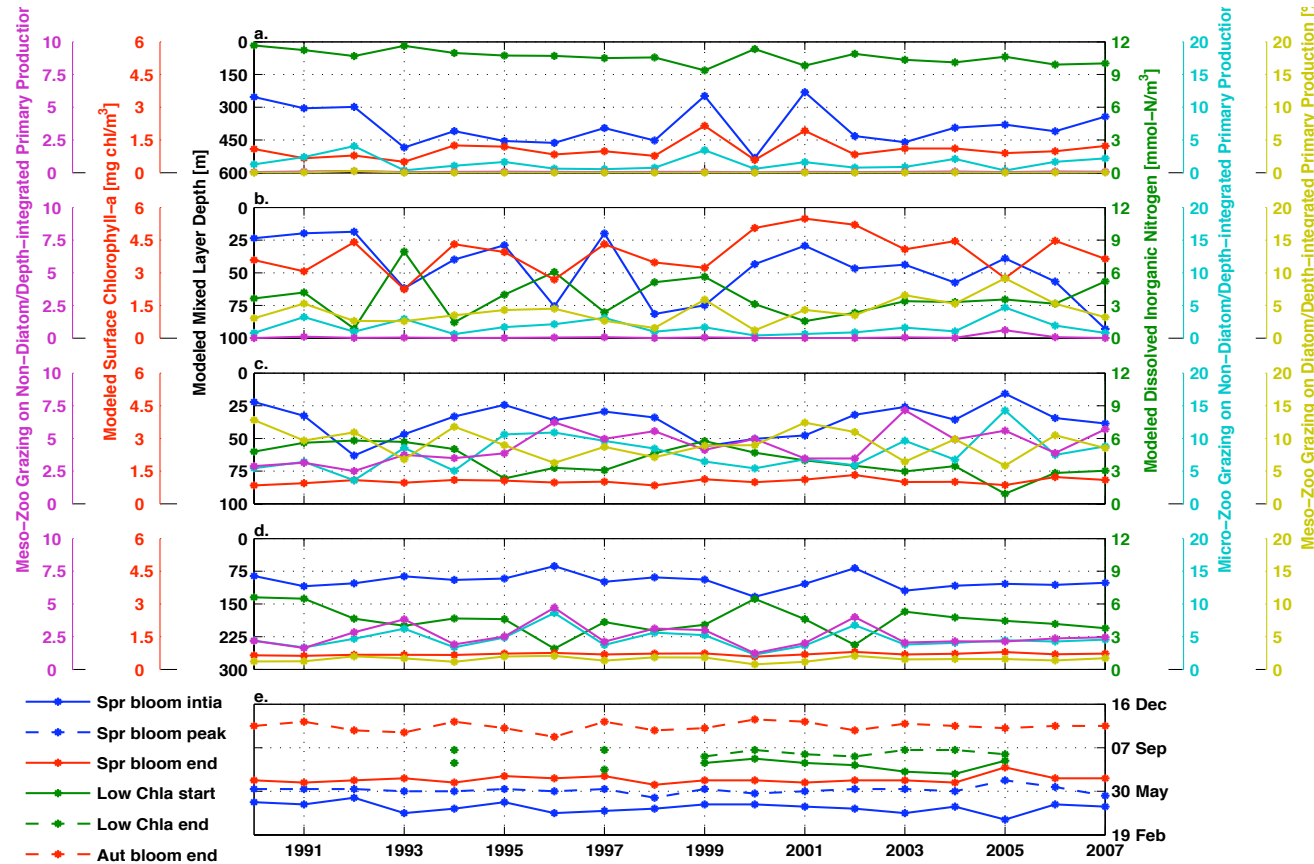
Figure 5.16 The time series of simulated surface Chl-a (red lines), MLD (blue lines), DIN (green lines), three types of zooplankton grazing relative to depth-integrated PP (blue-green, purple and yellow-green lines) at (a) spring bloom initiation, (b) spring bloom peak, (c) spring bloom termination and (d) autumn bloom termination. Panel (e) indicates the timing of bloom stages.
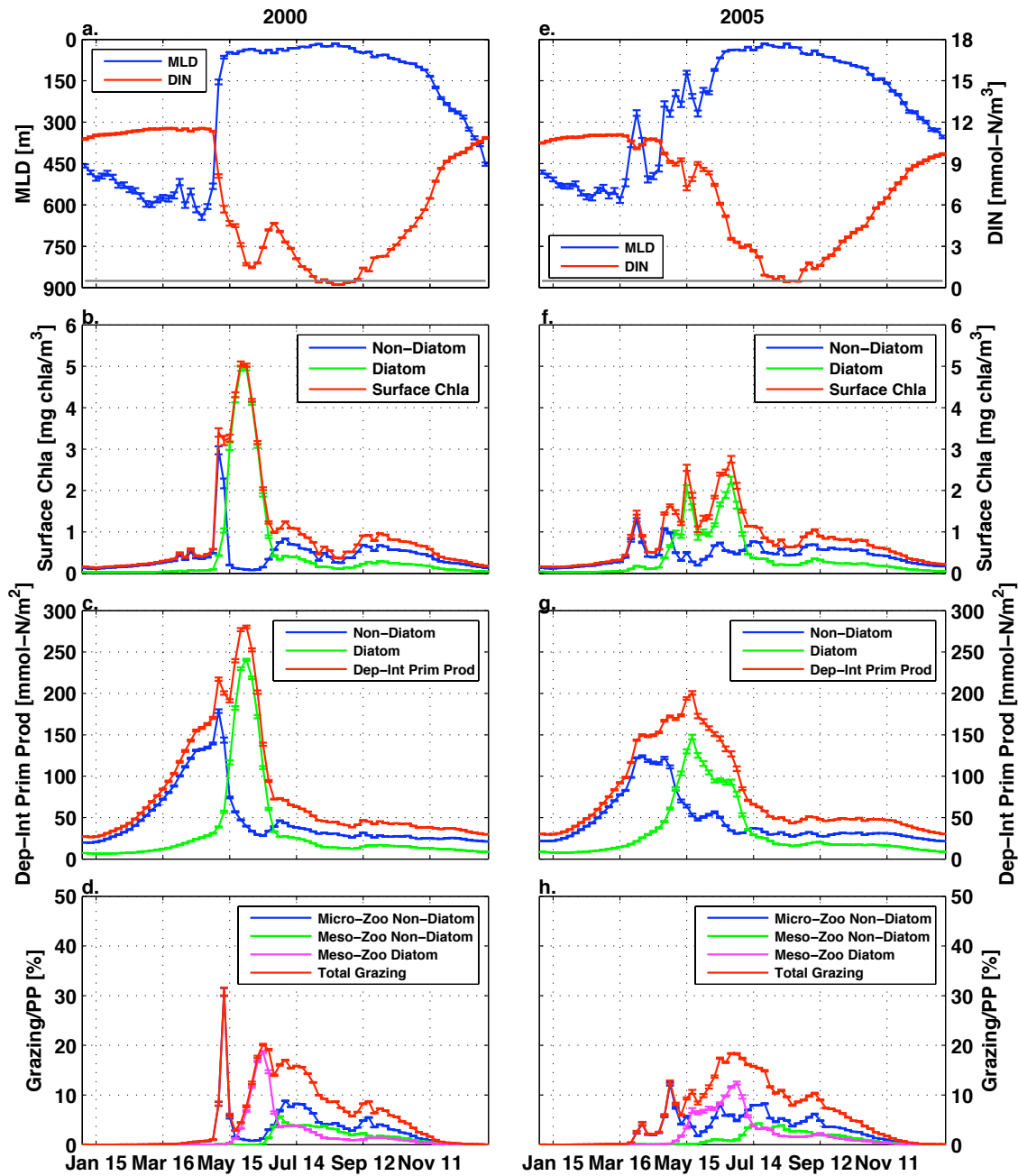
Figure 5.17 The annual cycle of simulated physical and biological parameters in two representative years (a-d for 2000 and e-h for 2005): (a and e) MLD in blue and DIN in red, (b and f) surface Chl-a from non-diatom (blue), diatom (green) and combined concentration (red), (c and g) depth-integrated PP from non-diatom (blue), diatom (green) and combined (red) (d and h) three types of zooplankton grazing in relation to depth-integrated PP. All error bars indicated the spatial variability within this location representing mASP.
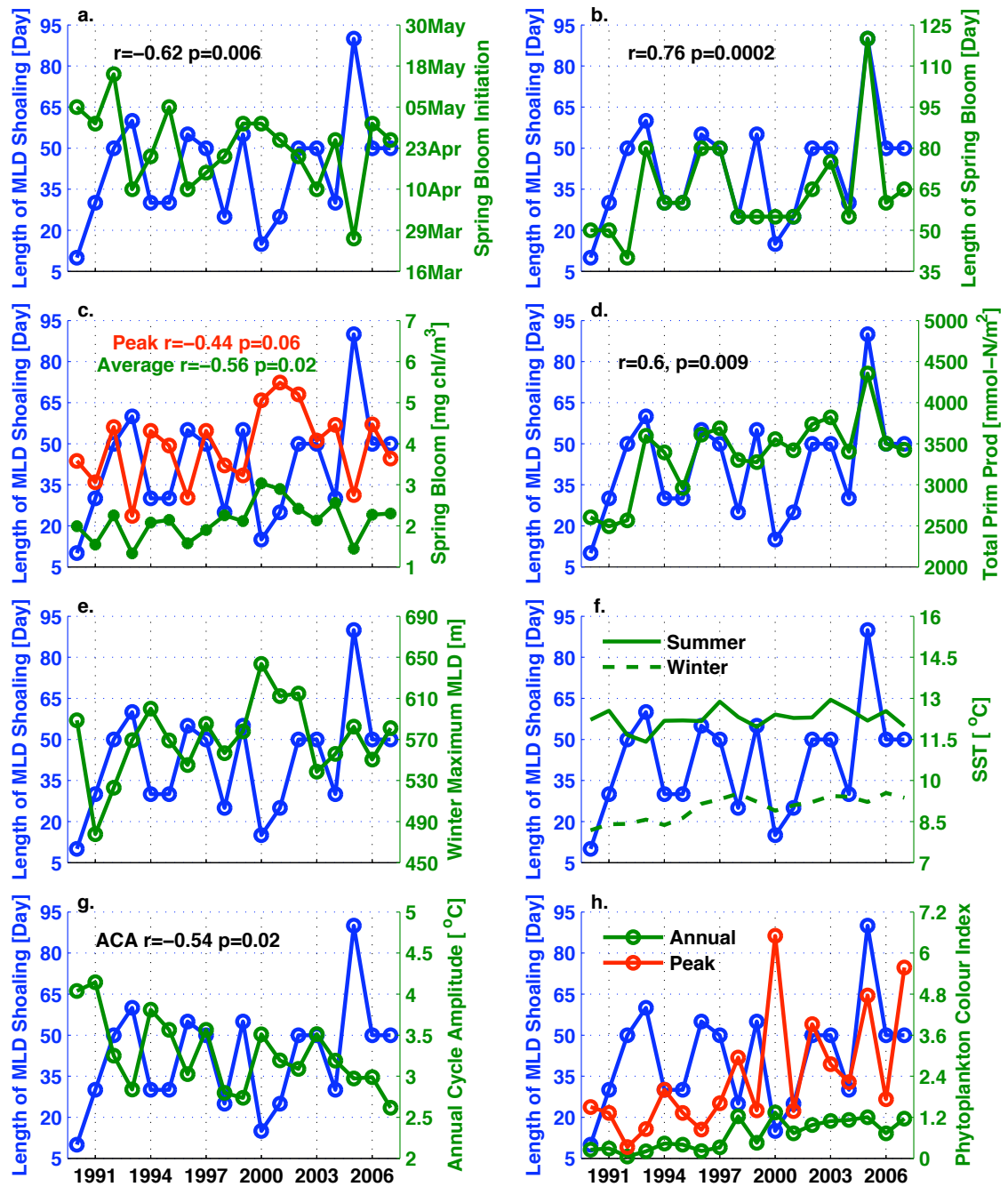
Figure 5.18 The length of MLD-shoaling period (blue lines) in relation to (a) spring bloom initiation date, (b) length of spring bloom, (c) spring bloom peak (red) and bloom average Chl-a (green), (d) depth-integrated PP in spring and autumn blooms, (e) the maximum MLD, (f) summer (solid line) and winter (dashed line) SSTs, (g) SST annual cycle amplitude and (h) PCI bloom peak (red) and annual average (green).
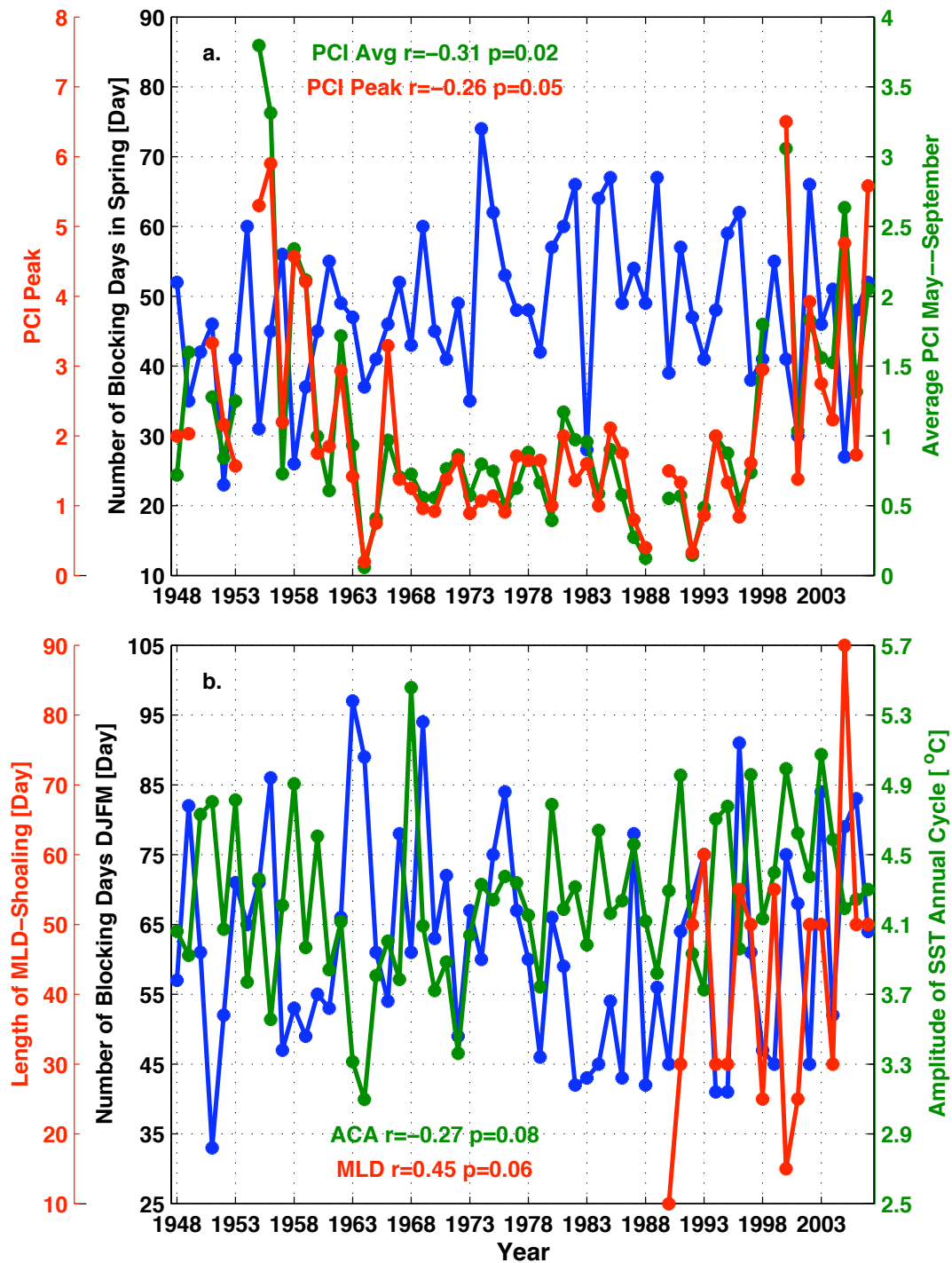
Figure 5.19 The number of atmospheric blocking days in the northern subpolar basin (blue lines) in relation with physical and biological parameters for 1948 – 2007: (a) the number of blocking days in spring (blue line), averaged spring-summer PCI (green line) and annual PCI peak (red line); (b) the number of blocking days in the extended winter (blue line), the SST annual cycle amplitude (green line) and the length of MLD-shoaling period (red line).
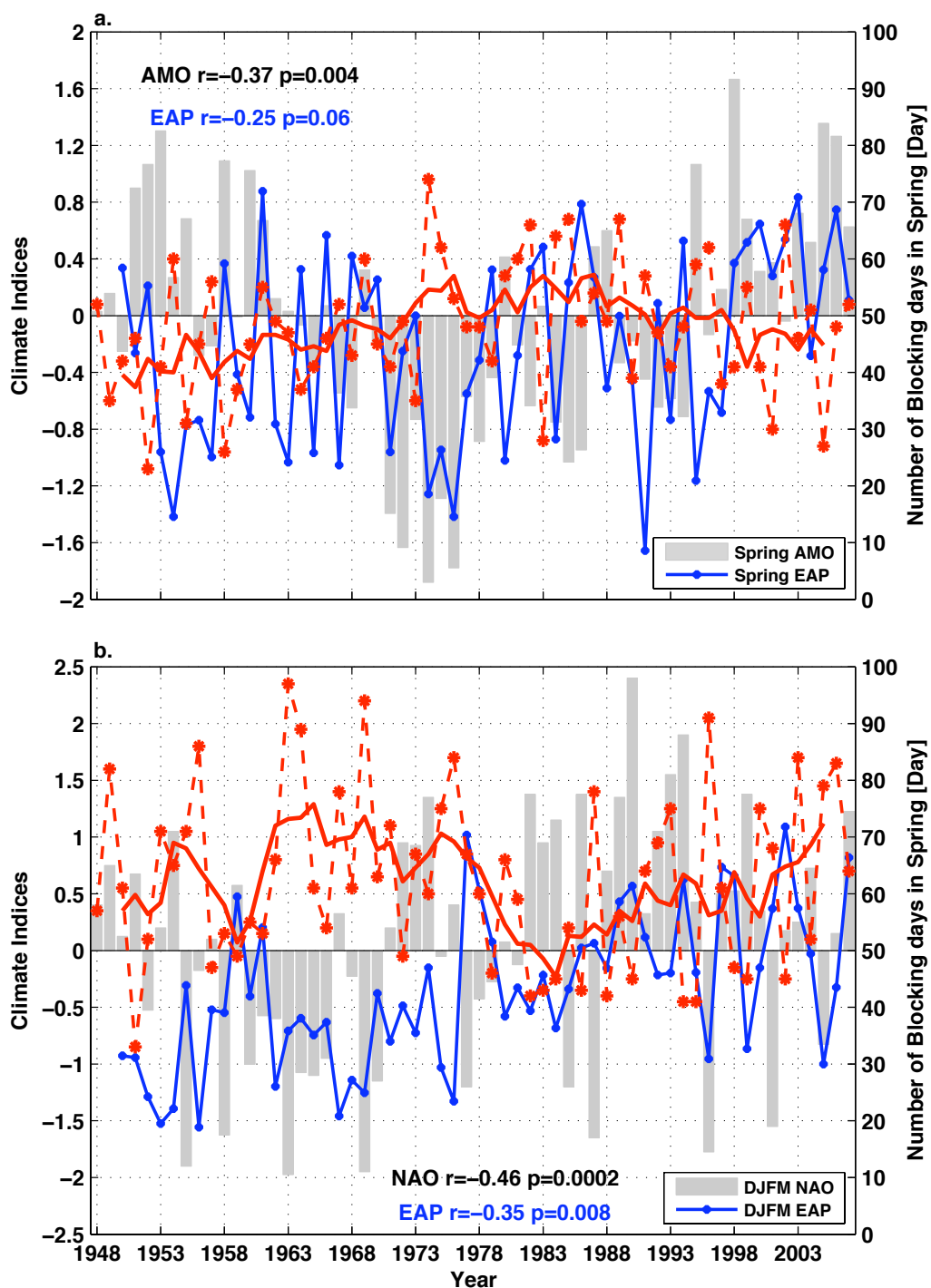
Figure 5.20 The number of blocking days in relation to climatic indices in the period 1948 – 2007: (a) the number of blocking days in spring (dashed red line) and 5-year running mean (solid red line), spring AMO index (grey bars) and spring EAP index (blue line); (b) the number of blocking days in the extended winter (dashed red line) and 5-year running mean (solid red line), winter NAO index (grey bars) and winter EAP index (blue line).

Chapter 6

Conclusion & Outlook

6.1   Introduction

This thesis contributes to the understanding of the decadal to multi-decadal variability of the SST annual cycle and phytoplankton abundance in the subpolar North Atlantic. The chapters of this thesis describe the observed variability of SST annual cycle using simple and more advanced statistical methods and the variation of phytoplankton abundance is analysed using a long-term *in situ* observation data source, the Continuous Plankton Recorder (CPR). The physical controls on phytoplankton variability on decadal and longer time scales are discussed using state-of-the-art coupled physical and biogeochemical models, with model performance assessed from a comparison analysis between model outputs and observations. The major questions answered to some extent by these chapters were:

- Does the physical annual cycle, in particular SST, change on decadal or longer time scales?
- What climatic processes possibly contribute to the observed variability?
- Does phytoplankton abundance present a clear variability pattern on decadal or longer time scales, especially under a changing climate?
- How well does the current generation of coupled physical and biogeochemical models simulate the variability of physical and biological parameters relevant for phytoplankton growth and its surrounding environment?
- What are the most important physical mechanisms determining the observed phytoplankton variability?

The observed variability of SST annual cycle is not substantially studied in the subpolar North Atlantic previously and distinct patterns are seen in different parts of the subpolar basin. The results of this study will be concluded in this chapter, concerning this variability and the responsible processes, with a view on the questions listed above.

6.2   Conclusions

6.2.1   Decadal to Multi-decadal Variability in SST Annual Cycle

Firstly, the variability of SST annual cycle on decadal and longer time scales is addressed. In the subpolar North Atlantic, decadal to multi-decadal variability of the SST annual cycle amplitude (ACA) is observed and these patterns are not consistent across the basin (Chapter 2). The SST ACA was at high levels during the 1890s, the 1940s and after the 1990s in the eastern shelf seas, presenting variability with a period of ~50 years whereas in the eastern oceanic regions the amplitudes were at low levels during the 1940s, but have remained above their long-term average since the 1990s. Multi-decadal variability with a period of ~50 years in SST ACA is observed in the western shelf seas: the amplitude was higher than the average level from the 1930s to the 1950s and after the early 1990s, while the amplitude was lower than average before the 1930s and between the two peaks. In the western oceanic regions, a low-frequency variability was seen over the whole time series. From the early 1920s to the late 1970s, a decadal variation overrode the low-frequency fluctuation with peaks in the early 1930s and the 1950s and low amplitude in the 1940s. The winter SSTs were strongly affected by a cold event in the 1990s, which was possibly related to the cooling events in the Labrador Sea in the 1970s, 1980s and 1990s [De-Jong, 2010].

Before 1995, the peaks observed in the SST annual cycle amplitude coincide with higher than average summer SSTs and lower than average winter SSTs in all groups of locations. After 1995, however, both winter and summer SSTs are higher than their respective long-term average, suggesting the controlling mechanisms of the seasonal SSTs might have changed in the later period. The anomalies of seasonal SSTs between the earlier period, 1870—1994, and the later period, 1995—2009, indicate that the warming signals in the later period are statistically significant in summer, especially in the shelf seas. However, in the interior subpolar basin the warming signals are less significant and in a small region in the southern Labrador Sea weak statistically significant cooling signal is seen in winter (Figure 2.9a).

6.2.2   Climate Processes Impact on SST Annual Cycle

Various factors can be responsible for this multi-decadal variability. The subpolar North Atlantic is one of the few places where significant surface heat losses and strong winds are observed. The regions at 50-55 °N are subject to wind stress comparable to that in the Southern Ocean during winter months. Both the atmospheric heat flux and wind stress curl show a multi-decadal signal and both factors are closely correlated to the North Atlantic Oscillation (NAO) index [De-Jong, 2010]. The influence of NAO on the changes in temperature and salinity in the North Atlantic Ocean has been investigated by a few studies [Flatau *et al.*, 2003; Häkkinen and Rhines, 2004; Hátún *et al.*, 2005]. Positive NAO index leads to strong westerlies near its action centers, which affects the strength and shape of the subpolar gyre and shifts the position of the North Atlantic Current (NAC). NAC brings warm and saline water into the subpolar gyre and therefore affects the temperature directly. The transport volume is strongest in autumn, which compensates for the increasing heat losses together with the Shelf Edge Current (SEC, also known as European Shelf Current, ESC) [Yaremchuk *et al.*, 2001]. This following subsection addresses the climatic impact on the observed variability in SST annual cycle.

6.2.2.1   Evidence

The potential basin-scale climatic signals contribute to the differences in the variation of the seasonal SSTs, and hence the SST annual cycle is analysed by applying Empirical Orthogonal Function (EOF) analysis on winter and summer SSTs. In both seasons, the dominant signal is the Atlantic Multi-decadal Oscillation (AMO), which is a climate index defined using SST anomalies in the North Atlantic. The mechanisms driving AMO are unclear, with some studies claiming that AMO reflects modulation within the oceanic processes and is related to the Atlantic Meridional Overturning Circulation (AMOC) [Dijkstra *et al.*, 2005] while others suggest that AMO reflects the variation in atmospheric aerosols [Booth *et al.*, 2012]. The second EOF modes in both seasons are correlated with NAO, which has been listed as one the most effective climatic signals in the North Atlantic (e.g. [Herbaut and Houssais, 2009; Hurrell and Deser, 2010]). As discussed above, NAO modulates SST mainly through influencing the strength of heat fluxes and wind stress. Summer SSTs present stronger AMO characteristics and NAO plays a more important role in adjusting winter SSTs. This can partially explain the differences in the evolution of winter and summer SSTs.

The third EOF mode is weakly associated with Arctic Oscillation (AO) in summer. AO is a known climate index that also modulates the wind stress in the North Atlantic, though the impact is weaker compared to NAO. Winter EOF4 presents a clear Eastern Atlantic Pattern (EAP) in winter whilst this pattern is less developed in summer EOF4. EAP is currently seen as a southeast shift of NAO, which also indicates an atmosphere-ocean teleconnection. The seasonal changes in the strength of the climate indices and the importance of each index in the two seasons contribute to the observed seasonal discrepancies in SST. However, the results presented in this chapter and in Chapter 2 could not estimate whether the climatic influence is generated locally or responds to variability in other ocean basins through teleconnection. In the regions where large amplitudes of the annual cycle and high biodiversity are seen, changes to physical annual cycles could lead to noticeable variations in marine organisms.

6.2.2.2   Remaining problem

The study showed that the amplitude of SST annual cycle presented a multi-decadal variability in the subpolar basin and the variability is not consistent across the basin. Attempts to explain the observed variability were made by separating the dominant signals controlling seasonal SSTs and establishing links to climatic indices at the basin scale. About 70% of the total variability in winter and summer and the differences between the evolutions of seasonal SSTs can be explained by a combination of the AMO, NAO, AO and EAP indices. However, the variation of the phase of SST annual cycle has not been the focus of this study, which could provide information on the changes to SST annual cycle from another aspect.

In addition to the attempts to explain the observed variability using climatic indices, preliminary analysis that explicates the inter-annual variability in SST through the variation of net heat fluxes was carried out using heat flux data developed at the National Oceanography Centre, Southampton (see Appendix 2). Inter-annual variability of the net heat flux explains changes in winter SST in the northern subpolar basin, especially in the Labrador and Irminger Seas. In summer, however, net heat flux can only explain the SST variation in a few locations in the eastern subpolar basin. Negative correlations between net heat flux and SST were observed in nearly all months in the Gulf Stream area, possibly related to the dominant roles of the turbulent heat flux (combination of sensible and latent heat fluxes) in the net heat flux due to the active

turbulence in this region. This analysis partially shows the importance of local atmospheric forcing on SST annual cycle in parts of the subpolar basin; however, the net heat flux could not explain the observed variability at basin scale. The seasonal variation of the main advection could provide additional information about the SST annual cycle, but is difficult to measure. Improvement in this estimate in the future could provide an opportunity to address the mechanism more conclusively.

6.2.3   Decadal Variability in Phytoplankton Abundance

6.2.3.1   Observed variability

The decadal to multi-decadal variability of phytoplankton abundance in the subpolar North Atlantic is addressed in the following subsection. CPR observations were used to examine the long-term variability of phytoplankton in the subpolar basin (Chapter 3). In the majority of the standard areas chosen for this study, significant increases in phytoplankton abundance were observed since the late 1980s. In some locations, this increase was part of a multi-decadal variation (e.g. Rockall Plateau) and in other locations, a consistent increase in phytoplankton abundance was observed from 1946 (e.g. North Sea). In regions where distinct spring and autumn blooms occur regularly in the early decades, the two blooms merged and the overall bloom intensity enhanced from the 1980s onwards. Though the rapid increase in phytoplankton abundance has coincided with the warm phase of SST since the 1980s, only a few locations in the eastern subpolar basin showed statistically significant correlation between SST and phytoplankton colour index (PCI) on the decadal scale. A major problem faced when analysing the time series collected from the western subpolar basin was the gaps in data coverage, which could be decades long at some locations.

The average annual cycles of PCI in the chosen locations between the earlier period, 1946—1994, and the later period, 1995—2007, were compared. In the eastern shelf seas, statistically significant increase in phytoplankton abundance was observed mainly in late spring to summer, possibly related to an increase in the metabolic rate or stronger increase in dinoflagellate abundance than for diatoms, while in the western shelf seas, statistically significant increase was seen in late winter to early spring, when the nutrients are relatively abundant. In the oceanic regions, statistically significant increases were observed only in the northernmost locations and in the other oceanic

locations both the amplitude and timing of spring blooms remained stable in the second period.

The calculation of the timing of phytoplankton spring bloom and SST increase (as the month coordinate of the centre of gravity of the area below x-axis when graphing monthly mean SST or PCI for January to June on an x-y coordinate), the duration of spring bloom seasons or SST warming season and PCA analysis on PCI and SST datasets confirmed that the simple methods captured the major variation in PCI time series. The differences of phytoplankton variability in shelf seas and oceanic regions were consistent with the findings presented in Colebrook (1979), though the shelf-oceanic contrast seemed to have strengthened, possibly due to the increased phytoplankton abundance in the shelf seas in recent decades. Water column stability (the standard deviation of SST from January to June, higher standard deviation suggests stronger stratification in late spring/early summer) appeared to be a more direct factor determining the timing of phytoplankton spring bloom than the timing of SST increase.

6.2.3.2   Implication & remaining problems

Biological responses to SST variation are complex as phytoplankton is modulated by SST directly (e.g. metabolic rate) and by processes related to SST (e.g. stratification). On the decadal scale, phytoplankton variation coincided with the variation of SST in some locations, though such correlation was in the western interior subpolar basin. This suggests that SST impacts the changes in phytoplankton abundance to some extent, whilst there are other parameters and processes that play a more direct role in determining the phytoplankton variability, e.g. vertical mixing and nutrients cycle.

The direct links between SST and phytoplankton abundance were conducted using correlation analysis, which was affected by the sparse data coverage and low temporal resolution of the observation in the western subpolar basin. Other physical processes linked to SST could also influence the phytoplankton growth, such as the rate of SST increase at critical stages of the phytoplankton life cycle and its impact on the development of zooplankton population. With the current observation datasets at hand, it was difficult to statistically evaluate the responses of different phytoplankton functional groups to SST variation, its longer-term changes, its interaction with zooplankton and potential changes to the structure of local ecosystems.

6.2.4   Model Validation

The performance of physical and biogeochemical models (point 4 in Section 6.1) is summarised in the following subsection. A physical model Nucleus for European Modelling of the Ocean (NEMO) and the biogeochemical model MEDUSA (Model of Ecosystem Dynamics, nutrient Utilisation, Sequestration and Acidification) were used to further analyse the physical mechanisms controlling phytoplankton growth. The model outputs were first compared to observations to evaluate the accuracy of the simulation. Seasonal SSTs simulated in NEMO agreed very well with observed SSTs (HadISST1) over the overlapping time period, 1990—2007. Seasonal SST anomalies between the period of 1990—1994 and the period of 1995—2007 were constructed for both observed and simulated SSTs. The overall patterns of these seasonal SST anomalies were generally reproduced in the simulated SST, though regional boundaries in the Irminger basin and the Iceland basin were more pronounced in the simulation than in observations.

The long-term average simulated seasonal MLDs over the period 1990—2007 reproduced the patterns of deep convection observed by the Levitus climatology using three different criteria, especially in summer. In winter, the three MLD climatology observations showed differences in the maximum MLD at the magnitude of ~ 1000m, which led to difficulties to quantitatively evaluate simulated MLD. Simulated deep mixing was observed mainly in the Labrador Sea, Irminger basin, northern Iceland basin and the Rockall Trough, which agreed very well with the observations and enhanced the confidence in using modeled MLD in further analysis.

EOF analysis was used to compare the simulated winter MLD and SST with observations statistically. The spatial patterns of the first leading modes of the two SST datasets agreed very well and values of opposite signs were seen in the MLD spatial pattern. All three associated principal components agreed very well and presented a gradual increasing signal. These linear trends were then removed and EOF analysis was applied to these de-trended datasets. The EOF1 of the two de-trended SST data showed positive values in the open ocean and negative values in the shelf seas and values of opposite signs were seen for the de-trended EOF1 of MLD. The three principal components corresponding to these new EOF1 were linked to the NAO index. Lower SSTs and deeper MLD was associated with positive NAO, especially during the first 10

years. The EOF2 of de-trended data showed similar spatial patterns for SST and MLD and the EAP index was correlated to SST principal components, but not to MLD. Both leading modes of the de-trended datasets addressed the atmospheric modulation of SST and NAO also played a role in adjusting deep convection in the subpolar North Atlantic.

Simulated surface chlorophyll-a (Chl-a) was compared to the observed Chl-a from the Sea-viewing Wide Field-of-view Sensor (SeaWiFS). The seasonal distribution of simulated surface Chl-a agreed well with the observation, though discrepancies were seen in the shelf seas in summer and the southern subpolar basin in winter. In the shelf seas, the model applied physical processes similar to that in the open ocean, which might differ from the real shelf processes and hence lead to differences between the simulation and the observation. In addition, the Chl-a concentration observed using satellite also contains error in the shelf region, which may affect the validation. The zonally averaged annual cycle in the subpolar basin indicated that the simulated surface Chl-a was higher than observations in winter and spring, but lower than observation in summer. In the southern subpolar basin, the nutrient depletion occurred (very low Chl-a in summer) in larger areas in the model than in the observation. Yool *et al.* (2011) amplified nutrient depletion was due to the stronger impact of nutrient kinetics on phytoplankton growth assumed in the model than in reality. The following analysis only focuses on the potential processes controlling phytoplankton growth in the open ocean, as there might be a larger mismatch between model and observations in the shelf seas.

6.2.5   Physical Mechanism Controlling Phytoplankton Bloom Dynamics

6.2.5.1   Key physical processes

The physical mechanism controlling phytoplankton bloom dynamics (point 5 in Section 6.1) is addressed in this subsection. The links between SST and MLD are first established as both parameters are important for determining the physical environment within which phytoplankton grow. In the subpolar region, the dominant phytoplankton functional group diatom is more sensitive to stratification than directly to temperature variation [Richardson and Schoeman, 2004]. In the parts of the subpolar basin where deep mixing is driven by large surface heat loss, shallower than average MLD corresponds to warmer than average winter SST, such as in the Labrador Sea-south Greenland area, Rockall Trough and PAP region. In summer, such connection between

MLD and SST is only seen in the eastern subpolar basin. This connection suggests that in addition to the impact on metabolic rate, SST also impacts phytoplankton distribution by affecting the stratification in the water column.

The MLD impacts phytoplankton growth through its modulation of the distribution of light and nutrients within the water column. Deep mixing during winter is the main process that brings nutrients to the surface from deeper layers in the subpolar basin, thus the maximum MLD indicates the amount of nutrients available for the following spring phytoplankton bloom. The deepening of MLD also decreases the average light intensity within the mixed layer where phytoplankton cells are assumed to distribute evenly. In the subpolar North Atlantic, stronger phytoplankton blooms and a larger amount of PP are associated with deeper than average winter MLD in regions south of 45 °N, while in regions north of 45 °N, connections between maximum MLD and phytoplankton bloom are observed patchily south of Greenland, in the southern Iceland basin and east of Iceland.

6.2.5.2   Ecological provinces

A glimpse at the discontinuity in direct biological responses to the maximum MLD was presented in the previous analysis, which leads to the need to divide the subpolar basin into ecological provinces. The differences in biological response are determined by the discontinuity in physical processes that form the environment in which marine organisms live. Seven ecological provinces are divided based on the distribution of major fronts, the variation of MLD, dominant movement of water masses in the water column and the occurrence of nutrient depletion during the period of 1990—2007. Five of the resulting provinces (excluding shelf seas and the very narrow Labrador Shelf) are the focus of further analysis: 1) mixed Atlantic Arctic Province (mAAP) where SST is colder than 7 °C and is located to the west of the SST gradient, the maximum MLD is deeper than 1000m, vertical upwelling dominates the annual movement of water masses and nutrient depletion seldom occurs in summer; 2) mixed Atlantic Subarctic Province (mASP) where SST is warmer than 7 °C and is located to the east of the SST gradient, the maximum MLD is about 800m, vertical upwelling dominates water movement and nutrient depletion occurs frequently and lasts about 20 days; 3) mixed North Atlantic Drift Province (NADP) that is located to the east of the SST gradient, the maximum MLD is deeper than 150m, upwelling and downwelling distribute patchily and nutrient

depletion occurs very frequently, its duration varying from three months in the north to five months in the south; 4) Gulf Stream Province (GFSP) where SST is warm, the maximum MLD is shallower than 150m, upwelling and downwelling distribute patchily and nutrient depletion occurs very frequently and lasts about five months; 5) North Atlantic Subtropical Province (NASP) where SST is warm, the maximum MLD is shallower than 150m, downwelling dominates vertical water movement and nutrient depletion occurs every year and lasts about eight months.

In mAAP, the first hint of phytoplankton accumulation is seen in the northeast Labrador Sea and east of Iceland in late March to April where Arctic-origin fresh water stabilizes the water column earlier than the rest of the provinces. For the majority of the provinces, shallow stratification is established in late May to early June when Chl-a increases rapidly. Chl-a remains relatively high through the summer, as nutrients are relatively abundant. The decrease of phytoplankton accumulation follows MLD deepening when light limitation curtails further bloom. In mASP, the major spring phytoplankton bloom commences in late April to mid-May following the establishment of shallow stratification, though large inter-annual variability is seen in this province. Frequent nutrient depletion occurs, especially on the western side of the province, thus Chl-a decreases in summer, followed by a small autumn bloom in September—October as MLD deepens. NADP includes regions with strong wind stress comparable to that in the Southern Ocean, especially in winter. Phytoplankton starts to accumulate from early winter along the NAC pathway, which is possibly related to the wind-driven mixing and eddies that bring phytoplankton cells to the surface and increases the light exposure for these cells. With abundant nutrients during winter, Chl-a concentration increases gradually. The major phytoplankton bloom is observed in April when MLD is shallower than 100m and summertime nutrient depletion occurs very frequently and the spring bloom is curtailed due to nutrient limitation.

In GFSP, phytoplankton accumulates through winter and peaks in March, when MLD is relatively deep. The maximum MLD is about 100m, thus surface nutrients are consumed quickly and Chl-a concentration remains low through summer. In NASP, phytoplankton bloom peaks when MLD is deepest in the year, in February – March and from late spring to late autumn, and Chl-a concentration remains low before it increases again as MLD deepens. Though the MLD is comparable in GFSP and NASP, the

overall strength of Chl-a and PP is higher in GFSP than in NASP, which is possibly related to the active mixing along the pathway of the Gulf Stream and hence more nutrients are available for phytoplankton consumption.

6.2.5.3   Key phytoplankton and zooplankton stages in mASP

Simulated Chl-a concentration at locations in mAAP, mASP and NADP are compared to the phytoplankton colour index (PCI) in the standard areas that correspond to these locations. On both annual and inter-annual scales, PCI agrees best with modeled Chl-a and depth-integrated PP in mASP. This province is hence selected to focus on the physical mechanisms controlling phytoplankton variability.

The timing of phytoplankton bloom initiation, bloom peak and spring bloom termination is determined using the 5-Day Chl-a concentration in mASP. The time series of MLD and DIN at these three stages are also determined. At the bloom initiation stage, the variation of MLD determined the strength of bloom initiation, with deeper than average MLD corresponding to lower than average bloom strength, suggesting light limitation. At bloom peak and termination stages, MLD and DIN are both weakly correlated to the Chl-a concentration, suggesting other factors (e.g. zooplankton grazing) perhaps play more direct roles in determining phytoplankton accumulation at these stages. However, variations of MLD and DIN at these three stages could not provide information of the timing of the biological terms.

The time series in mASP also indicate seasonal variations of the constitution of the phytoplankton functional groups through the strength of different types of grazing. At the end of winter, small non-diatoms start to accumulate first and PP starts to increase steadily when MLD is still deeper than 100m. Micro-zooplankton grazing on non-diatom thus peak first. This suggests that small non-diatom can survive low-light conditions better than the other functional groups. Once stable spring stratification is established, diatom growth increases rapidly and becomes the dominant functional group. Meso-zooplankton grazing on diatom peaks closely after the phytoplankton spring peak and micro-zooplankton grazing on non-diatom is subdued. This indicates that diatoms are very sensitive to stratification and the associated changes in light intensity and are more competitive under turbulent conditions. From late summer, phytoplankton growth is largely reduced as nutrients are significantly consumed and

non-diatoms seem to be the dominant functional group again as both micro- and meso-zooplankton grazing on non-diatoms increases, especially the grazing rate on larger non-diatom cells. When MLD starts to deepen again in autumn, phytoplankton presents a slight increase as nutrients are replenished. From late autumn, phytoplankton accumulation decreases due to light limitation and zooplankton migrate to deeper depth, so the grazing rate is largely reduced.

6.2.5.4   Physical mechanism in mASP

The 5-Day MLD data reveals that in some years, MLD shoals to stable stratification quickly, while in other years, episodes of temporary MLD-shoaling occur prior to the establishment of stable spring stratification. The relationship between the length of the MLD-shoaling period (T_{MLDS}) and the timing, duration, strength of the spring phytoplankton bloom, surface and depth-integrated PP and three types of grazing rate is examined and discussed.

In years when the T_{MLDS} is short, the shoaling process starts from early April and stable spring stratification is established rapidly within 10—30 days. Short and intense phytoplankton bloom follows the stratification closely, which peaks in mid-April to mid-May. After this peak, Chl-a concentration remains at a moderate level and the depth-integrated PP agrees with surface Chl-a concentration very well. Under this condition, rapid zooplankton growth follows the main spring peak, which allows an intense phytoplankton spring bloom. Nutrients in the upper layer are consumed quickly and phytoplankton abundance decreases rapidly as a result of the combination of low nutrient concentration, increased grazing rate and/or self-shading. The autumn bloom that follows the MLD deepening is much weaker than the spring bloom and the overall PP produced and passed to higher trophic levels during both blooms is relatively low.

In years when the T_{MLDS} is long, episodes of short-term stratification occur before stable spring stratification from the mid- to late March and the shoaling process can last up to three months. Pulses of phytoplankton accumulation follow each episode of MLD-shoaling closely and lead to early growth of zooplankton. Short-term MLD-shoaling is then disturbed by resumed vertical mixing and hence restricts further phytoplankton growth, but replenishes nutrients in the upper layer. Once stable spring stratification is

established, the following bloom peak is lower than in previous case of the phytoplankton bloom, as the zooplankton population has accumulated and is ready to consume the phytoplankton cells during the development of the main spring bloom. Though the main bloom is weaker, the bloom season is longer as a result of the episodes of nutrient replenishment and the following autumn bloom is less separable from the spring bloom. Thus over the two bloom seasons, more PP is produced and passed to higher trophic levels.

The variation of the T_{MLDS} is not associated with either maximum winter MLD or seasonal SSTs. Instead, it is correlated to the amplitude of the SST annual cycle, suggesting the two processes may share a similar driving force, especially in the late winter to early spring. One possible influential factor is the atmospheric forcing that modulates westerly wind, surface circulation and potential heat fluxes, which can impact both SST and MLD. A time series of the number of atmospheric blocking days is generated over the northeastern subpolar basin (45 – 75 °N, 30 °W – 10 °E) for spring (April – June) and the extended winter (December – March). Atmospheric blocking occurs when consistent high-pressure system develops, which affects the track, frequency and intensity of storms and is related to negative NAO phase and a warm ocean surface. The T_{MLDS} is positively correlated to the number of atmospheric blocking days in the extended winter, which is also negatively correlated to the amplitude of the SST annual cycle.

One potential mechanism is that atmospheric blocking is more likely to occur when the ocean surface is warm, the NAO index is negative and the westerly wind and surface circulation are both weakened. Meanwhile, this high pressure system may also lead to southeastern wind around the high pressure centre, which drives warm southern air northward and reduces the surface heat flux loss. These processes all contribute to stabilising the water column, which may lead to temporary MLD-shoaling during blocking events. Atmospheric blocking events typically last four to eight days and the local wind stress and surface heat loss may increase after these events, which then disturbs the MLD-shoaling. Warmer winter ocean surface also contributes to a smaller amplitude for the SST annual cycle if summer SST does not show a dramatic increase. The atmospheric blocking activity in spring has an indirect modulation on the

phytoplankton abundance on the decadal scale, with more blocking events coinciding with lower PCI.

In summary, the characteristics of the MLD-shoaling period in the late winter to early spring determines the timing, strength and duration of phytoplankton spring blooms, in addition to modulating the distribution of nutrient and light intensity. The T_{MLDS} also alters the development of zooplankton grazing with late and rapid MLD-shoaling leading to three well-defined distinct grazing peaks (micro-zooplankton grazing on non-diatom, meso-zooplankton grazing on diatom and meso-zooplankton grazing on non-diatom, respectively), while early but lengthy MLD-shoaling leads to the coexistence of three types of grazing without significant peaks. When T_{MLDS} is short, due to the lag of zooplankton growth, the amount of phytoplankton consumed by its predator is limited; when T_{MLDS} is long, early episodes of phytoplankton growth provide a longer growing season for zooplankton and the total phytoplankton consumed by zooplankton is much larger. Thus, the energy passed to organisms of higher trophic levels through the food web is perhaps higher in the second scenario compared to the first. The T_{MLDS} may be linked to other physical parameters, such as the amplitude of the SST annual cycle. The variation of both parameters is associated with the atmospheric blocking activity in the northeastern subpolar basin in the extended winter, especially towards the end of the winter. The proposed physical mechanism provides an alternative hypothesis on the physical control of the phytoplankton bloom dynamics and local ecosystem to the classical Sverdrup's hypothesis.

6.2.5.5   Remaining problems

The physical mechanism controlling the timing and strength of spring bloom in one ecological province is discussed using model outputs. The exact underlying mechanisms that drive the observed MLD variability, and hence phytoplankton bloom dynamics, is suggested but not proved. The major factors that might modulate MLD intra-annually and inter-annually include wind stress, net heat fluxes, advection, North Atlantic Oscillation and possibly more. All of these factors also impact the variation of the amplitude of SST annual cycle, which is consistent with the observed link between MLD-shoaling and SST annual cycle. Thus, satisfactory explanation of the observed MLD variability is necessary to fully understand the phytoplankton bloom dynamics

and its interaction with the physical environment in this ecological province. In other provinces, the phytoplankton abundance might be controlled by other physical process but has not been proved in this study. It would be useful to test the extension of the area where this mechanism apply, which can further improve the understanding of phytoplankton bloom dynamics in the North Atlantic subpolar basin.

6.3   Future Challenges

The remaining problems described in previous sections are some of the future challenges and in this section some more practical challenges will be discussed. One of these is to maintain the present Continuous Plankton Recorder (CPR) observations in the North Atlantic, especially in the northwestern North Atlantic. The lack of continuous measurement of phytoplankton and zooplankton is one of the major obstacles for more detailed analysis of phytoplankton bloom dynamics in this region on decadal and longer scales. In these regions, satellite observations are not available in winter due to cloud coverage and low Sun angle. Local observations are limited as a result of frequent storms and rough conditions at sea. The CPR data coverage has improved in more recent years, which has provided a glimpse of phytoplankton activity. As CPR observations in the northwestern North Atlantic continue and accumulate, better understanding of the phytoplankton abundance variation could be achieved.

In addition to SST and MLD, physical parameters also play roles in constructing the physical environment for marine organisms, such as the sea surface salinity (SSS), advection, light and meso-scale eddies. Observations of some of the parameters are difficult, but can help illustrate a full picture of the physical processes in the North Atlantic subpolar region. Any improvement of the observation could lead to more thorough understanding of the involved processes. Even though observations of MLD related parameters are available on regional, and more recently, basin scales, the calculated results still vary significantly using different criteria. The criteria suitable for different parts of a basin are not consistent and better understanding of the determining processes and regular deployment of Argo floats are needed to improve the observation of MLD in the subpolar North Atlantic.

The ocean models and biogeochemical models need to be improved to understand (and ideally predict) future changes of physical and biological parameters in the subpolar

North Atlantic. SST is the best-simulated physical parameter, with relatively small discrepancies between observation and model. The simulation of MLD, however, is more difficult to evaluate as the observation of MLD shows significant variations using different criteria. For Chl-a, a larger mismatch between observation and model simulation is seen, but with longer observational records the skill of models in simulating both the mean state and the variability up to decadal time scales can be assessed using these records. The newer generations of models have a much-improved spatial and temporal resolution, which would allow more detailed study of the ocean. Thus, more interaction and collaboration between observation-based and model-based studies can lead to significant improvements in understanding the physical and biogeochemical processes in the ocean.

Appendices

Appendix 1 Time Series at the Cooling Centre

The winter SST anomalies between the period 1870 – 1994 and the period 1995 – 2009 shows a cooling signal in the latter period in the interior subpolar basin south of Greenland. The SST averaged over the area around the main cooling centre, 44.5 °– 39.5 °W, 53.5 °– 57.5 °N, is shown in Figure S1. An anomalous cold period is seen from the early 1970s to the late 1990s, during which SST started to increase from the mid-1990s but remain at low levels until the mid-2000s.
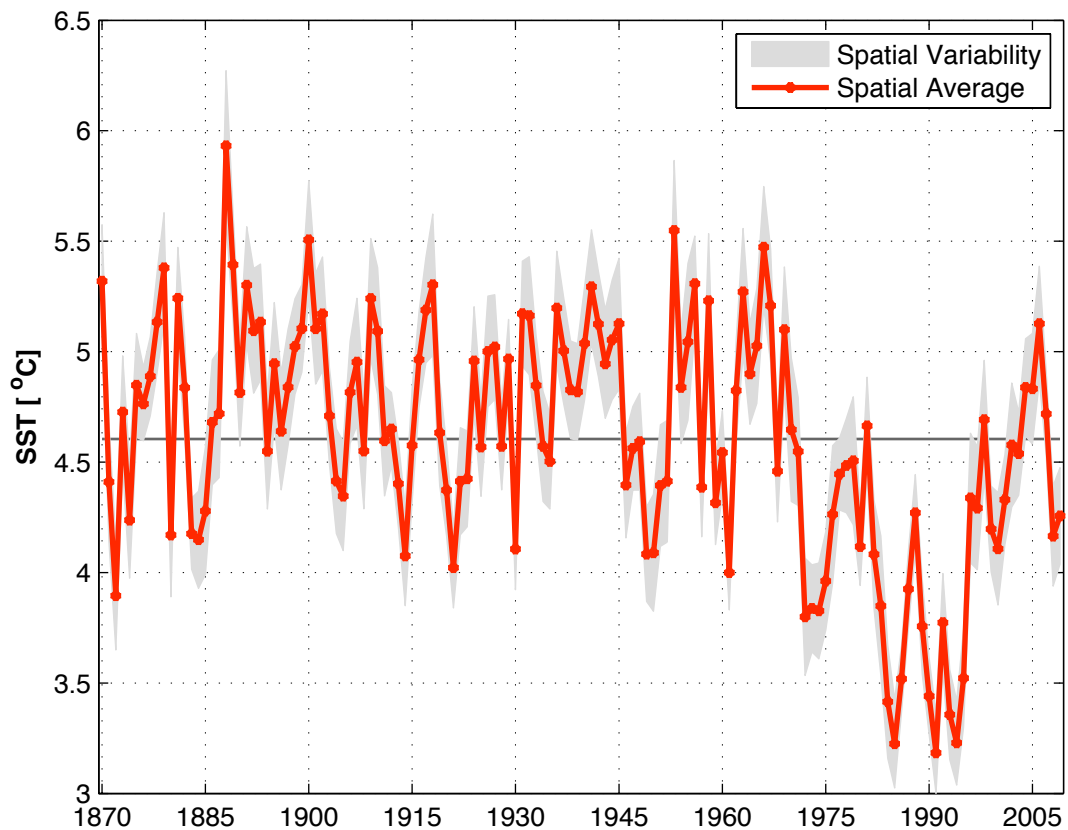
Figure S 1. The long-term winter SST in the interior subpolar basin (44.5 °– 39.5 °W, 53.5 °– 57.5 °N), where statistically significant cooling anomalies is seen between the period 1995 – 2009 and the period 1870 – 1994. The grey shade indicates the spatial variability within the area.

Appendix 2 EOF Analysis

In this study, the EOF analysis was carried out as follows:

(1) The long-term linear trend was removed from the dataset.

(2) The detrended dataset was arranged in a $N \times M$ matrix:

$$X = \begin{bmatrix} x_{11} & x_{12} & . & . & . & x_{1m} \\ x_{21} & . & & & & . \\ . & & . & & & . \\ . & & & . & & . \\ . & & & & . & . \\ x_{n1} & . & . & . & . & x_{nm} \end{bmatrix},$$

where each row was one map of all grid points and each column was a time series at one grid point.

(3) Remove the mean of each column, resulting in an anomaly matrix X_a.

(4) Calculate the covariance matrix as $C = X_a X_a^T$ because $M >> N$. The resulting C is a $N \times N$ matrix and is quicker to solve than solving the covariance matrix $R = X_a^T X_a$.

(5) Solve the equation $CB = B\Lambda$, Λ is the diagonal matrix of eigenvalues and B is the matrix with the eigenvectors as its columns.

(6) Calculate $L = X_a^T B$, this step converts the B to matrix L that contains eigenvectors proportional to the eigenvectors for R with $1/\sqrt{\lambda_i}$ as the proportionality factor.

(7) The eigenvectors for R is hence obtained using the eigenvalues contained in matrix Λ and the corresponding l_i contained in the resulting matrix from last step $l_i' = l_i/\sqrt{\lambda_i}$.

(8) Principal components, the time series corresponding to the eigenvectors that explain the amplitude of the eigenvectors, are obtained by calculating $PC_i = X_a * l_i'$

Appendix 3 Heat Flux

The influence of net heat flux on the SST annual cycle was examined using correlation analysis. The NOCS v2.0 was used in this study, which is a gridded monthly dataset on a 1 ° spatial resolution and available since January 1973. The surface meteorology and fluxes were constructed using optimal interpolation technique on ship data from ICOADS v2.4 [Berry and Kent, 2009]. The net heat flux was calculated as the sum of shortwave radiation, long wave radiation, latent heat flux and sensible heat flux as shown in Equation 1.1.

In the subpolar North Atlantic (see Figure S1), the impact of net heat flux on SST varies spatially and on the intra-seasonal scale. From December to the following April, the net heat flux has a positive influence on SST, which is likely related to the thermal driven deep convection and restratification. Hence larger heat loss on the surface is accompanied by lower SST. The net heat flux in the eastern subpolar basin plays a more important role in determining SST in April – May compared to in colder months. In the southern interior subpolar, the net heat flux shows no seasonally consistent impact on SST. The positive correlation between net heat flux and SST is strengthened in the southern and eastern subpolar basin when including a one-month lag (Figure S2), though the link still lacks a basin scale or seasonal consistence. This simple analysis suggests that the net heat flux is not the most direct forcing that drives the SST on the basin scale over the period 1973 – 2009.
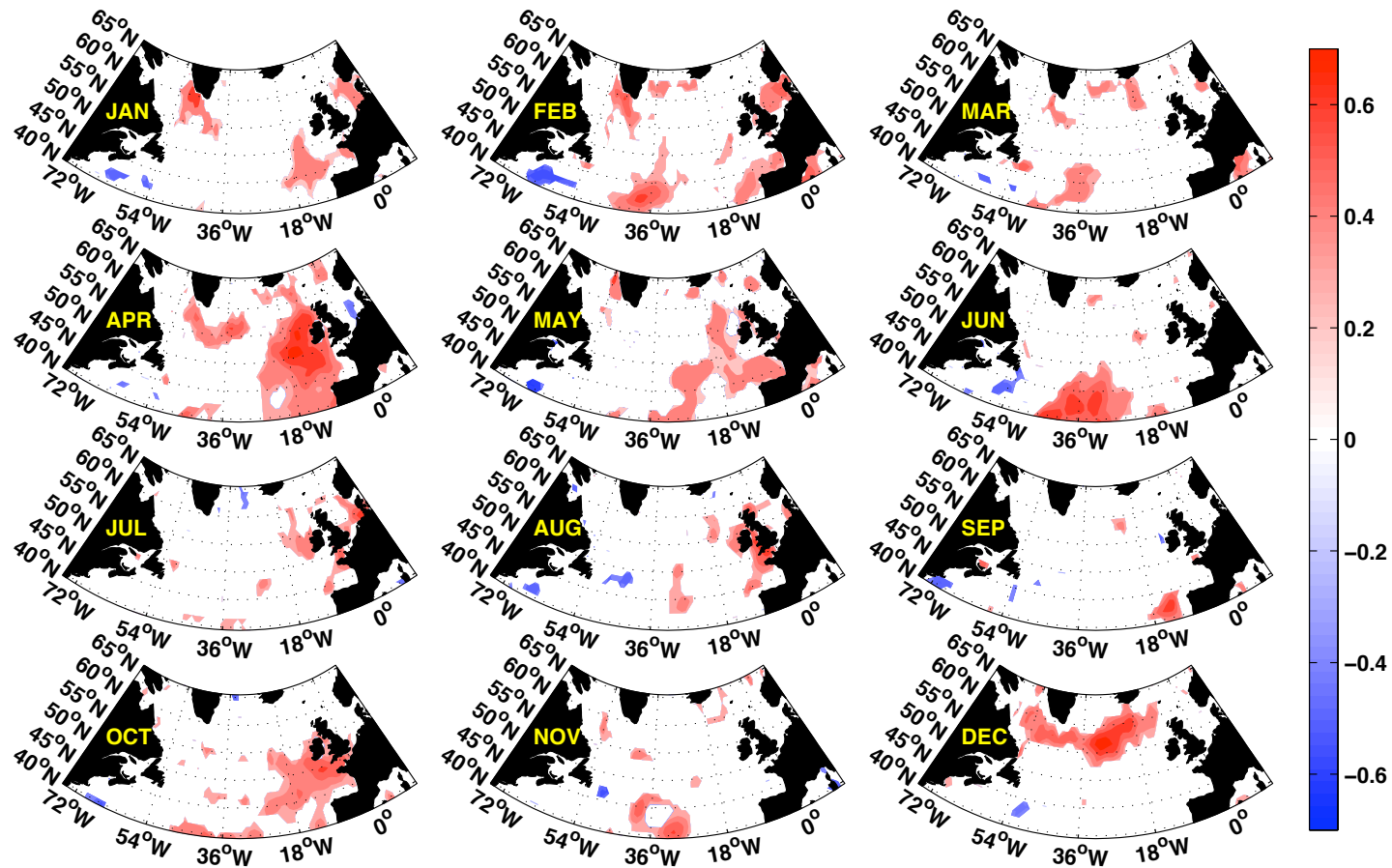
Figure S 2. The zero-lag correlation coefficients between monthly SST and net heat flux (NOCS v.2) over the period 1973 – 2009 with the linear trend removed. Coefficients presented here are over the 95% significance level.
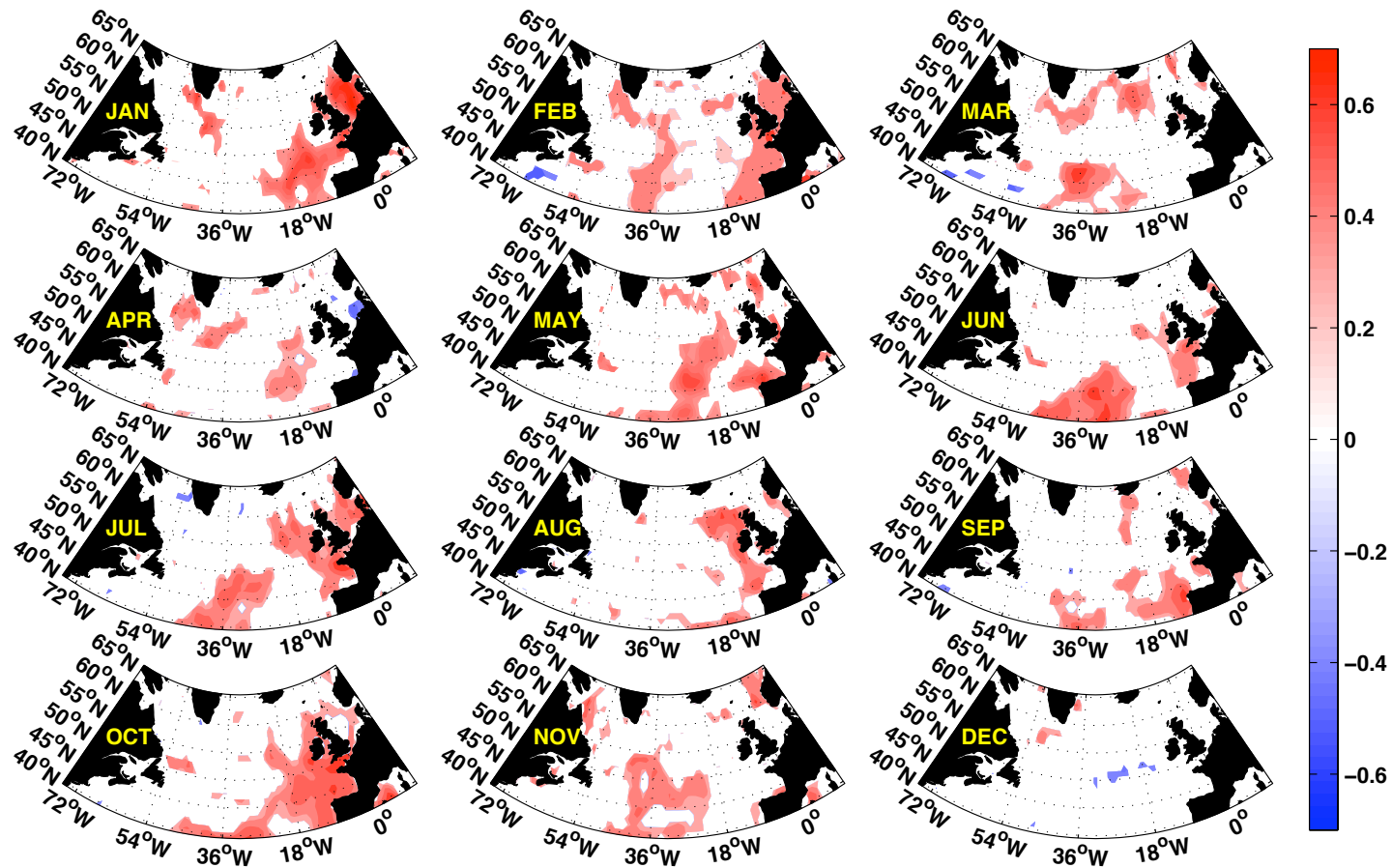
Figure S 3. The one-month-lag correlation coefficients between monthly SST and net heat flux (NOCS v.2) over the period 1973 – 2009 with the linear trend removed. Coefficients presented here are over the 95% significance level.

Appendix 4 Diatom and Dinoflagellate Ratio

The CPR observation does not quantitatively record the abundance of phytoplankton to species level, however, the occurrence of phytoplankton species is counted and its abundance is estimated based on the number of occurrence on the samples. Hence the total estimate (simply the sum of all species regarded as diatoms or dinoflagellates that occurred on samples corresponding to a certain standard area, SA, box) of diatoms and dinoflagellates are available for each SA box. The ratio of diatoms to dinoflagellates is shown below to indicate the phytoplankton community structure at each selected SAs in this study. From 1997 to 2007, shifts of the dominant phytoplankton group is seen in most locations from diatoms dominance before 2001 to diatom-dinoflagellate co-existence between 2001 and 2005/2006, before diatoms dominant again after 2006. The abundance of diatoms is extremely low around 2003 in the northeast continental North Sea (B1), Scotian Shelf shelf (E10) and Newfoundland shelf (E9) when the ratio is close to zero. The shifts of community structure has been linked to the NAO index [e.g. Henson *et al.*, 2012] and may response to changes in the source water feeding in the regions of interest (P. C. Reid, pers. comm., 2012).
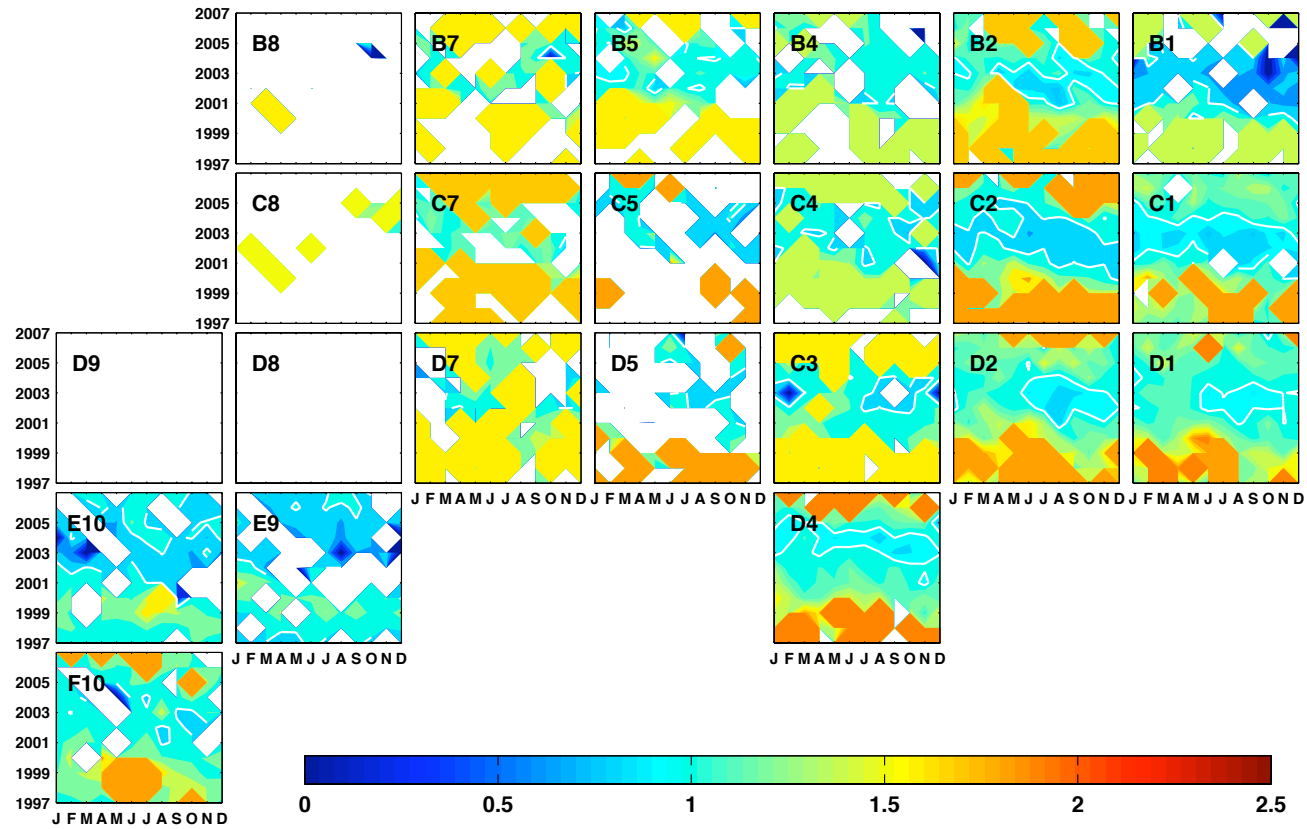
Figure S 4. The variation of diatom to dinoflagellate ratio in the chosen CPR standard areas from 1997 to 2007. Values larger than 1 suggest diatom dominance in one region whilst values smaller than 1 suggest dinoflagellate dominance in one region. The white lines indicate the contours where the ratio equals to 1 and the white area suggests no data coverage allowing the calculation of the ratio.

Reference

Alexander, M. A. and Deser, C. 1995. A Mechanism for the Recurrence of Wintertime Midlatitude Sst Anomalies. *Journal of Physical Oceanography,* 25**,** 16.

Ambaum, M. H. P., Hoskins, B. J. and Stephenson, D. B. 2001. Arctic Oscillation or North Atlantic Oscillation? *Journal of Climate,* 14**,** 13.

Armstrong, R. A., Lee, C., Hedges, J. I., Honjo, S. and Wakeham, S. G. 2002. A New, Mechanistic Model for Organic Carbon Fluxes in the Ocean: Based on the Quantitative Association of Poc with Ballast Minerals. *Deep-Sea Research II,* 49**,** 18.

Baines, S. B. and Pace, M. L. 1991. The Production of Dissolved Organic Matter by Phytoplankton and Its Imprtance to Bacteria: Patterns across Marine and Freshwater Systems. *Limnology and Oceanography,* 36**,** 13.

Barnston, A. G. and Livezey, R. E. 1987. Classification, Seasonality and Persistence of Low-Frequency Atmospheric Circulation Patterns. *Monthly Weather Review,* 115**,** 44.

Barton, A. D., Greene, C. H., Monger, B. C. and Pershing, A. J. 2003. The Continuous Plankton Recorder Survey and the North Atlantic Oscillation: Interannual- to Multi-Decadal Scale Patterns of Phytoplankton Variability in the North Atlantic Ocean. *Progress in Oceanography,* 58**,** 22.

Beaugrand, G. 2004. The North Sea Regime Shift: Evidence, Cause, Mechanism and Consequences. *Progress in Oceanography***,** 18.

Beaugrand, G. 2009. Decadal Changes in Climate and Ecosystems in the North Atlantic Ocean and Adjacent Seas. *Deep-Sea Research,* II**,** 18.

Beaugrand, G., Edwards, M., Brander, K., Luczak, C. and Ibanez, F. 2008. Causes and Projections of Abrupt Climate-Driven Ecosystem Shifts in the North Atlantic. *Ecology Letters,* 11**,** 12.

Beaugrand, G., Ibaiiez, F. and Reid, P. C. 2000. Spatial, Seasonal and Long-Term Fluctuations of Plankton in Relation to Hydroclimatic Features in the English Channel, Celtic Sea and Bay of Biscay *Marine Ecology Progress Seies,* 200**,** 10.

Beaugrand, G., Ibanez, F. and Lindley, J. A. 2001. Geographical Distribution and Seasonal and Diel Changes in the Diversity of Calanoid Copepods in the North Atlantic and North Sea. *Marine Ecology Progress Seies,* 219**,** 15.

Becker, G. A. and Pauly, M. 1996. Sea Surface Temperature Changes in the North Sea and Their Causes *ICES Journal of Marine Science,* 53**,** 12.

Behrenfeld, M. J. 2010. Abandoning Sverdrup's Critical Depth Hypothesis on Phytoplankton Blooms. *Ecology,* 91**,** 13.

Belchansky, G. I., Douglas, D. C. and Platonov, N. G. 2004. Duration of the Arctic Sea Ice Melt Season: Regional and Interannual Variability, 1979–2001. *Journal of Climate,* 17**,** 14.

Berry, D. I. and Kent, E. C. 2009. A New Air–Sea Interaction Gridded Dataset from Icoads with Uncertainty Estimates. *Bulletin of the American Meteorological Society,* 90**,** 12.

Biddanda, B. and Benner, R. 1997. Carbon, Nitrogen, and Carbohydrate Fluxes During the Production of Particulate and Dissolved Organic Matter by Marine Phytoplankton. *Limnology and Oceanography,* 42**,** 13.

Björnsson, H. and Venegas, S. A. 1997. A Manual for Eof and Svd Analyses of Climatic Data. McGill University.

Bonjean, F. 2001. Influence of Surface Currents on the Sea Surface Temperature in the Tropical Pacific Ocean. *Journal of Physical Oceanography,* 31**,** 19.

Booth, B. B. B., Dunstone, N. J., Halloran, P. R., Andrews, T. and Bellouin, N. 2012. Aerosols Implicated as a Prime Driver of Twentieth-Century North Atlantic Climate Variability. *Nature,* 484**,** 7.

Boss, E. and Behrenfeld, M. 2010. In Situ Evaluation of the Initiation of the North Atlantic Phytoplankton Bloom. *Geophysical Research Letters,* 37**,** 5.

Bryan, K. and Cox, M. D. 1967. A Numerical Investigation of the Oceanic General Circulation. *Tellus,* 19**,** 29.

Cannaby, H. and Husrevoglu, Y. S. 2009. The Influence of Low-Frequency Variability and Long-Term Trends in North Atlantic Sea Surface Temperature on Irish Waters. *ICES Journal of Marine Science*, 10.

Carcia-Soto, C. and Pingree, R. D. 2009. Spring and Summer Blooms of Phytoplankton (Seawifs/Modis) Along a Ferry Line in the Bay of Biscay and Western English Channel. *Continental Shelf Research,* 29, 12.

Carton, J. A. and Giese, B. S. 2005. Soda: A Reanalysis of Ocean Climate. *Journal of Geophysical Research*.

Carton, J. A., Grodsky, S. A. and Liu, H. 2008. Variability of the Oceanic Mixed Layer, 1960–2004. *Journal of Climate,* 21, 19.

Cattiaux, J., Vautard, R. and Yiou, P. 2011. North Atlantic Sst Amplified Recent Wintertime European Land Temperature Extremes and Trends. *Climate Dynamic,* 36, 16.

Cessi, P. and Otheguy, P. 2003. Oceanic Teleconnections: Remote Response to Decadal Wind Forcing. *Journal of Physical Oceanography,* 33, 14.

Chen, D., Busalacchi, A. J. and Rothstein, L. M. 1994. The Roles of Vertical Mixing, Solar Radiation, and Wind Stress in a Model Simulation of the Sea Surface Temperature Seasonal Cycle in the Tropical Pacific Ocean. *Journal of Geophysical Research,* 99, 15.

Colebrook, J. M. 1979. Continuous Plankton Records: Seasonal Cycles of Phytoplankton and Copepods in the North Atlantic Ocean. *Marine Biology,* 51, 10.

Curry, R. and Mauritzen, C. 2005. Dilution of the Norhthern North Atlantic Ocean in Recent Decades. *Science,* 308, 3.

Cushing, D. H. 1990. Plankton Production and Year-Class Strength in Fish Population: An Update of the Match/Mismatch Hypothesis. *Advances in marine biology,* 26, 45.

de-Blij, H. J. and Miller, P. O. 1996. *Physicsl Geography of the Global Environment,* New York, John Wiley.

De-Jong, M. F. 2010. *Hydrographic Variability in the Irminger Sea.* PhD, University of Utrecht, the Netherlands.

De-Mey, P. 1992. Synoptic Estimates of an Eddy Field in the North Atlantic Current. *oceanological Acta,* 15, 7.

Deser, C. 2000. On the Teleconnectivity of the "Arctic Oscillation". *Geophysical Research Letters,* 27, 4.

Deser, C., Alexander, M. A., Xie, S.-P. and Phillips, A. S. 2009. Sea Surface Temperature Variability: Patterns and Mechanisms. *The Annual Review of Marine Science,* 2, 31.

Dijkstra, H. A., Raa, L. t., Schmeits, M. and Gerrits, J. 2005. On the Physics of the Atlantic Multidecadal Oscillation. *Ocean Dynamics*, 15.

Dima, M. and Lohmann, G. 2007. A Hemispheric Mechanism for the Atlantic Multidecadal Oscillation. *Journal of Climate,* 20, 14.

Ding, H., Keenlyside, N. S. and Latif, M. 2009. Seasonal Cycle in the Upper Equatorial Atlantic Ocean. *Journal of Geophysical Research,* 114, 16.

DRAKKAR-Group 2007. Eddy-Permitting Ocean Circulation Hindcasts of Past Decades. *CLIVAR Exchanges,* 12, 4.

Dutkiewicz, S., Follows, M., Marshall, J. and Gregg, W. W. 2001. Interannual Variability of Phytoplankton Abundances in the North Atlantic *Deep-Sea Research II,* 48, 22.

Edwards, M., Beaugrand, G., Reid, P. C., Rowden, A. A. and Jones, M. B. 2002. Ocean Climate Anomalies and the Ecology of the North Sea. *Marine Ecology Progress Series, Mar Ecol Prog Ser,* 239, 10.

Edwards, M., Reid, P. C. and Planque, B. 2001. Long-Term and Regional Variability of Phytoplankton Biomass in the Northeast Atlantic (1960–1995) *ICES Journal of Marine Science,* 58, 11.

Edwards, M. and Richardson, A. J. 2004. Impact of Climate Change on Marine Pelagic Phenology and Trophic Mismatch. *Nature,* 430, 4.

Edwards, M., Stevens, D., Flavell, M., Hosie, G., Melrose, C., Batten, S., Walne, A., Stern, R., McQuatters-Gollop, A., Helaouet, P., Decelle, J., Moore, S., Trainer, V., Downes-Tettmar, N., Wotton, M., Castellani, C., Licandro, P. and Buckland, C., 2012: Sir Alister Hardy Foundation for Ocean Science: 2011 Annual Report. Plymouth, England.

Ellett, D. J. 1993. The North-East Atlantic: A Fan-Assisted Storage Heater? *Weather.* John Wiley & Sons Ltd.

Eppley, R. W. and Peterson, B. J. 1979. Particulate Organic Matter Flux and Planktonic New Production. *Nature,* 282**,** 4.

Fan, X., Send, U., Testor, P., Karstensen, J. and Lherminier, P. 2013. Observations of Irminger Sea Anticyclonic Eddies. *Journal of Physical Oceanography,* 43**,** 19.

Flatau, M. K., Talley, L. and Niiler, P. P. 2003. The North Atlantic Oscillation, Surface Current Velocities, and Sst Changes in the Subpolar North Atlantic. *Journal of Climate,* 15**,** 15.

Frajka-Williams, E. and Rhines, P. B. 2010. Physical Controls and Interannual Variability of the Labrador Sea Spring Phytoplankton Bloom in Distinct Regions *Deep-Sea Research I***,** 12.

Gaspar, P., Gr´egoris, Y. and Lefevre, J.-M. 1990. A Simple Eddy Kinetic Energy Model for Simulations of the Oceanic Vertical Mixing Tests at Station Papa and Long-Term Upper Ocean Study Site *Journal of Geophysical Research,* 95.

Gieskes, W. W. C., Leterme, S. C., Peletier, H., Edwards, M. and Reid, P. C. 2007. Phaeocystis Colony Distribution in the North Atlantic Ocean since 1948, and Interpretation of Long-Term Changes in the Phaeocystis Hotspot in the North Sea. *Biogeochemistry,* 83**,** 12.

Gloersen, P., Parkinson, C. L., Cavalieri, D. J., Comiso, J. C. and Zwally, H. J. 1999. Spatial Distribution of Trends and Seasonality in the Hemispheric Sea Ice Covers: 1978 - 1996 *Journal of Geophysical Research,* 104**,** 9.

Gregg, W. W. and Casey, N. W. 2004. Global and Regional Evaluation of the Seawifs Chlorophyll Dataset. *Remote Sensing of Environment,* 93**,** 17.

Gregg, W. W. and Casey, N. W. 2007. Sampling Biases in Modis and Seawifs Ocean Chlorophyll Data. *Remote Sensing of Environment,* 111**,** 11.

Gupta, S. K., Ritchey, N. A. and Wilber, A. C. 1992. Seasonal Variation of Surface Radiation Budget Derived from International Satellite Cloud Climatology Project C1 Data. *Journal of Geophysical Research,* 97**,** 20.

Häkkinen, S. 2002. Surface Salinity Variability in the Northern North Atlantic During Recent Decades. *Journal of Geophysical Research,* 107**,** 12.

Häkkinen, S. and Rhines, P. B. 2004. Decline of Subpolar North Atlantic Circulation During the 1990s *Science,* 304**,** 5.

Häkkinen, S., Rhines, P. B. and Worthen, D. L. 2011. Atmospheric Blocking and Atlantic Multidecadal Ocean Variability. *Science,* 334**,** 5.

Häkkinen, S., Rhines, P. B. and Worthen, D. L. 2013. Northern North Atlantic Sea Surface Height and Ocean Heat Content Variability. *Journal of Geophysical Research: Oceans,* 118**,** 9.

Han, G., Lu, Z., Wang, Z., Helbig, J., Chen, N. and Young, B. d. 2008. Seasonal Variability of the Labrador Current and Shelf Circulation Off Newfoundland. *Journal of Geophysical Research,* 113**,** 23.

Hanawa, K. and Sugimoto, S. 2004. 'Reemergence' Areas of Winter Sea Surface Temperature Anomalies in the World's Oceans. *Geophysical Research Letters,* 31**,** 4.

Hansell, D. A. and Carlson, C. A. 2001. Marine Dissolved Organic Matter and the Carbon Cycle. *Oceanography,* 14**,** 9.

Hansen, B. and Østerhus, S. 2000. North Atlantic–Nordic Seas Exchanges *Progress in Oceanography,* 45**,** 100.

Hátún, H., Payne, M. R., Beaugrand, G., Reid, P. C., Sandø, A. B., Drange, H., Hansen, B., Jacobsen, J. A. and Bloch, D. 2009. Large Bio-Geographical Shifts in the North-Eastern Atlantic Ocean: From the Subpolar Gyre, Via Plankton, to Blue Whiting and Pilot Whales. *Progress in Oceanography,* 80**,** 14.

Hátún, H., Sandø, A. B., Drange, H., Hansen, B. and Valdimarsson, H. 2005. Influence of the Atlantic Subpolar Gyre on the Thermohaline Circulation. *Science,* 309**,** 3.

Hegerl, G., Luterbacher, J., Gonzalez-Rouco, F., Tett, S. F. B., Crowley, T. and Xoplaki, E. 2011. Influence of Human and Natural Forcing on European Seasonal Temperatures. *Nature Geoscience,* 4**,** 5.

Henson, S., Lampitt, R. and Johns, D. 2012. Variability in Phytoplankton Community Structure in Response to the North Atlantic Oscillation and Implications for Organic Carbon Flux. *Limnology and Oceanography,* 57**,** 11.

Henson, S. A., Dunne, J. P. and Sarmiento, J. L. 2009a. Decadal Variability in Noth Atlantic Phytoplankton Blooms. *Journal of Geophysical Research,* 114**,** 11.

Henson, S. A., Raitsos, D., Dunne, J. P. and McQuatters-Gollop, A. 2009b. Decadal Variability in Biogeochemical Models: Comparison with a 50-Year Ocean Colour Dataset. *Geophysical Research Letters,* 36**,** 4.

Herbaut, C. and Houssais, M.-N. 2009. Response of the Eastern North Atlantic Subpolar Gyre to the North Atlantic Oscillation. *Geophysical Research Letters,* 36**,** 5.

Herring, H. J. and Mellor, G. L., 1970: A Study of Turbulend Boundary Layer Models. *Princeton University AMS Report.*

Hoegh-Guldberg, O. and Bruno, J. F. 2010. The Impact of Climate Change on the World's Marine Ecosystems. *Science,* 328**,** 6.

Holliday, N. P. 2002. *The Interannual Variability of the Circulation and Variation of the North Atlantic Subpolar Gyre.* PhD, University of Liverpool.

Holliday, N. P. and Reid, P. C. 2001. Is There a Connection between High Transport of Water through the Rockall Trough and Ecological Changes in the North Sea? *ICES Journal of Marine Science,* 58**,** 5.

Hopkinson, C. S. and Vallino, J. J. 2005. Efficient Export of Carbon to the Deep Ocean through Dissolved Organic Matter. *Nature,* 433**,** 4.

Hosoda, S., Ohira, T. and Nakamura, T. 2008. A Monthly Mean Dataset of Global Oceanic Temperature and Salinity Derived from Argo Float Observations. *JAMSTEC Report of Research and Development* 8**,** 13.

Hughes, S. L., Holliday, N. P., Colbourne, E., Ozhigin, V., Valdimarsson, H., Østerhus, S. and Wiltshire, K. 2009. Comparison of in Situ Time-Series of Temperature with Gridded Sea Surface Temperature Datasets in the North Atlantic. *International Council for the Exploration of the Sea***,** 13.

Hurrell, J. W. 1995. Decadal Trends in the North Atlantic Oscillation: Regional Temperatures and Precipitation. *Science,* 269**,** 4.

Hurrell, J. W. and Deser, C. 2010. North Atlantic Climate Variability: The Role of the North Atlantic Oscillation. *Journal of Marine Systems,* 79**,** 14.

Kallberg, P., Berrisford, P., Hoskins, B., Simmons, A., Uppala, S., Lamy-Thepaut, S. and Hine, R., 2005: Era-40 Atlas. *ECMWF ERA-40 Project Report Series.* Reading.

Kaplan, A., Kushnir, Y. and Cane, M. A. 2000. Reduced Space Optimal Interpolation of Historical Marine Sea Level Pressure: 1854-1992. *Journal of Climate,* 13**,** 16.

Kaplan, A., Kushnir, Y., Cane, M. A. and Blumenthal, M. B. 1997. Reduced Space Optimal Analysis for Historical Data Sets: 136 Years of Atlantic Sea Surface Temperatures. *Journal of Geophysical Research,* 102**,** 26.

Kara, A. B., Rochford, P. A. and Hurlburt, H. E. 2003. Mixed Layer Depth Variability over the Global Ocean. *Journal of Geophysical Research,* 108**,** 15.

Kara, A. B., Rochford, P. A. and Hurlbutt, H. E. 2000. An Optimal Definition for Ocean Mixed Layer Depth *Journal of Geophysical Research,* 105**,** 19.

Killworth, P. D. 1983. Deep Convection in the World Ocean. *Reviews of Geophysics and Space Physics,* 21**,** 26.

Kim, K.-Y. and Wu, Q. 1999. A Comparison Study of Eof Techniques: Analysis of Nonstationary Data with Periodic Statistics. *Journal of Climate,* 12**,** 15.

Knight, J. R., Folland, C. K. and Scaife, A. A. 2006. Climate Impacts of the Atlantic Multidecadal Oscillation. *Geophysical Research Letters,* 33**,** 4.

Kump, L. R., Kasting, J. F. and Crane, R. G. 2011. *The Earth System,* New Jersey, Pearson Education, Inc.

Kwon, Y.-O. and Frankignoul, C. 2012. Stochastically-Driven Multidecadal Variability of the Atlantic Meridional Overturning Circulation in Ccsm3. *Climate Dynamic,* 38**,** 18.

Lagerloef, G., Schmitt, R., Schanze, J. and Kao, H.-Y. 2010. The Ocean and the Global Water Cycle. *Oceanography,* 23**,** 12.

Lalli, C. M. and Parsons, T. R. 1997. *Biological Oceanography an Introduction*, Butterworth-Heinemann.

Large, W. G. and Yeager, S., 2004: Diurnal to Decadal Global Forcing for Ocean and Sea-Icd Models: The Data Sets and Flux Climatologies. *NCAR Technical Note, NCAR/TN-460+STR.*

Lavigne, H., D'Ortenzio, F., Claustre, H. and Poteau, A. 2011. Towards a Merged Satellite and in Situ Fluorescence Ocean Chlorophyll Product. *Biogeosciences Discussions,* 8**,** 41.

Levitus, S., Antonov, J. I., Boyer, T. P. and Stephens, C. 2000. Warming of the World Ocean. *Science,* 287**,** 5.

Lévy, M., Lehahn, Y., Andre´, J.-M., Me´mery, L., Loisel, H. and Heifetz, E. 2005. Production Regimes in the Northeast Atlantic: A Study Based on Sea-Viewing Wide Field-of-View Sensor (Seawifs) Chlorophyll and Ocean General Circulation Model Mixed Layer Depth. *Journal of Geophysical Research,* 110**,** 19.

Lillya, J. M., Rhinesa, P. B., Schottb, F., Lavenderc, K., Lazierd, J., Sendb, U. and D'Asaro, E. 2003. Observations of the Labrador Sea Eddy Field. *Progress in Oceanography,* 59**,** 102.

Longhurst, A. 2007. *Ecological Geography of the Sea,* London, UK, Elsevier.

Lutgens, F. K. and Tarbuck, E. J. 2000. *The Atmosphere,* Upper Saddle River, NJ, Prentice Hall.

Madec, G., 2012: Nemo Reference Mannual, Ocean Dynamic Component: Nemo-Opa. *Technique Report.* Paris.

Madec, G., Delecluse, P., Imbard, M. and Levy, C., 1998: Opa 8 Ocean General Circulation Model-Reference Manual. *Technique Report.*

Mahadevan, A., D'Asaro, E., Lee, C. and Perry, M. J. 2012. Eddy-Driven Stratification Initiates North Atlantic Spring Phytoplankton Blooms. *Nature,* 337**,** 5.

Manabe, S. and Bryan, K. 1969. Climate Calculations with a Combined Ocean-Atmosphere Model. *Journal of the Atmospheric Sciences,* 26**,** 4.

Manabe, S., Smagorinsky, J. and Strickler, R. F. 1965. Simulated Climatology of a General Circulation Model with a Hydrologic Cycle. *Monthly Weather Review,* 93**,** 30.

Margalef, R. 1978. Life-Forms of Phytoplankton as Survival Alternatives in an Unstable Environment. *oceanological Acta,* 1**,** 17.

Martin, A. P. 2003. Phytoplankton Patchiness: The Role of Lateral Stirring and Mixing. *Progress in Oceanography,* 57**,** 50.

Martin, J. H., Knauer, G. A., Karl, D. M. and Broenkow, W. W. 1987. Vertex: Carbon Cycling in the Northeastern Pacific. *Deep-Sea Research I,* 34**,** 19.

Martin, S. 2004. *An Introduction to Ocean Remote Sensing,* New York, USA, Cambridge University Press.

Martinez, E., Antoine, D., D'Ortenzio, F. and Gentili, B. 2009. Climate-Driven Basin-Scale Decadal Oscillations of Oceanic Phytoplankton. *Science,* 326**,** 4.

Mauritzen, C. and Häkkinen, S. 1997. Influence of Sea Ice on the Thermohaline Circulation in the Arctic- North Atlantic Ocean. *Geophysical Research Letters,* 24**,** 4.

McAllister, C. D., Parsons, T. T., Stephen, K. and Strickland, J. D. H. 1961. Measurements of Primary Production in Coastal Seawater Using a Large-Volumn Plastic Sphere. *Limnology and Oceanography,* 6**,** 22.

McClain, C. R. 2009. A Decade of Satellite Ocean Color Observation. *Annual Review of Marine Science,* 1.

McKnight, T. L. and Hess, D. 2005. *Physical Geography: A Landscape Appreciation*, Pearson Education Inc.

Montegut, C. d. B., Madec, G., Fischer, A. S., Lazar, A. and Iudicone, D. 2004. Mixed Layer Depth over the Global Ocean: An Examination of Profile Data and a Profile-Based Climatology. *Journal of Geophysical Research,* 109**,** 20.

Moore, G. W. K., Renfrew, I. A. and Pickart, R. S. 2012. Spatial Distribution of Air-Sea Heat Fluxes over the Sub-Polar North Atlantic Ocean. *Geophysical Research Letters,* 39**,** 5.

North, G. R., Bell, T. L., Cahalan, R. F. and Moeng, F. J. 1982. Sampling Errors in the Estimation of Empirical Orthogonal Functions. *Monthly Weather Review,* 110**,** 8.

Núñez-Riboni, I., Bersch, M., Haak, H., Jungclaus, J. H. and Lohmann, K. 2012. A Multi-Decadal Meridional Displacement of the Subpolar Front in the Newfoundland Basin. *Ocean Science,* 8**,** 12.

Orvik, K. A. and Skagseth, Ø. 2003. The Impact of the Wind Stress Curl in the North Atlantic on the Atlantic Inflow to the Norwegian Sea toward the Arctic. *Geophysical Research Letters,* 30**,** 4.

Parkinson, C. L. 1992. Spatial Patterns of Increases and Decreases in the Length of the Sea Ice Season in the North Polar Region, 1979-1986. *Journal of Geophysical Research,* 97**,** 12.

Pickard, G. L. and Emery, W. J. 1990. *Descriptive Physical Oceanography: An Introduction,* Oxford, Pergamon Press Ltd.

Popova, E. E., Yool, A., Coward, A. C., Aksenov, Y. K., Alderson, S. G., B. A. de Cuevas and Anderson, T. R. 2010. Control of Primary Production in the Arctic by Nutrients and Light: Insights from a High Resolution Ocean General Circulation Model. *Biogeosciences,* 7**,** 23.

Popova, E. E., Yool, A., Coward, A. C., Dupont, F., Deal, C., Elliott, S., Hunke, E., Jin, M., Steele, M. and Zhang, J. 2012. What Controls Primary Production in the Arctic Ocean? Results from an Intercomparison of Five General Circulation Models with Biogeochemistry. *Journal of Geophysical Research,* 117**,** 16.

Portis, D. H., Walsh, J. E., Hamly, M. E. and Lamb, P. J. 2001. Seasonality of the North Atlantic Oscillation. *Journal of Climate,* 14**,** 10.

Pörtner, H. O. and Farrell, A. P. 2008. Physiology and Climate Change. *Science,* 322**,** 3.

Quadrelli, R., Bretherton, C. S. and Wallace, J. M. 2005. On Sampling Errors in Empirical Orthogonal Functions. *Journal of Climate,* 18**,** 7.

Rasmusson, E. M. and Mo, K. C. 1996. Large-Scale Atmospheric Moisture Cycling as Evaluated from Nmc Global Analysis and Forecast Products. *Journal of Climate,* 9**,** 22.

Rayner, N. A., Parker, D. E., Horton, E. B., Folland, C. K., Alexander, L. V., Rowell, D. P., Kent, E. C. and Kaplan, A. 2003. Global Analyses of Sea Surface Temperature, Sea Ice, and Night Marine Air Temperature since the Late Nineteenth Century *Journal of Geophysical Research,* 108**,** 37.

Reid, C. 2005. Atlantic Wide Regime Shift? *GLOBEC INTERNATIONAL NEWSLETTER.*

Reid, P. C., Colebrook, J. M., Matthews, J. B. L., Aiken, J. and Team, C. P. R. 2003. The Continuous Plankton Recorder: Concepts and History, from Plankton Indicator to Undulating Recorders. *Progress in Oceanography,* 58**,** 57.

Reid, P. C., Edwards, M., Hunt, H. G. and Warner, A. J. 1998. Phytoplankton Change in the North Atlantic. *Nature,* 391**,** 1.

Reid, P. C. and Valdés, L., 2011: Ices Status Report on Climate Change in the North Atlantic. *ICES Cooperative Research Report.*

Reynolds, R. W., Rayner, N. A., Smith, T. M., Stokes, D. C. and Wang, W. 2002. An Improved in Situ and Satellite Sst Analysis for Climate. *Journal of Climate,* 15**,** 17.

Richardson, A. J. and Schoeman, D. S. 2004. Climate Impact on Plankton Ecosystems in the Northeast Atlantic. *Science,* 305**,** 4.

Richardson, A. J., Walne, A. W., John, A. W. G., Jonas, T. D., Lindley, J. A., Sims, D. W., Stevens, D. and Witte, M. 2006. Using Continuous Plankton Recorder Data. *Progress in Oceanography,* 68**,** 48.

Richardson, P. L. 1993. A Census of Eddies Observed in North Atlantic Sofar Float Data. *Progress in Oceanography,* 31**,** 50.

Rykova, T., Straneo, F., Lilly, J. M. and Yashayaev, I. 2009. Irminger Current Anticyclones in the Labrador Sea Observed in the Hydrographic Record, 1990–2004. *Journal of Marine Research,* 67**,** 24.

Sarmiento, J. L., Slater, R., Barber, R., Bopp, L., Doney, S. C., Hirst, A. C., Kleypas, J., Matear, R., Mikolajewicz, U., Monfray, P., Soldatov, V., Spall, S. A. and Stouffer, R. 2004. Response of Ocean Ecosystems to Climate Warming. *Global Biogeochemical Cycles,* 18**,** 23.

Scherrer, S. C., Croci-Maspoli, M., Schwierz, C. and Appenzeller, C. 2006. Two-Dimensional Indices of Atmospheric Blocking and Their Statistical Relationship with Winter Climate Patterns in the Euro-Atlantic Region. *International Journal of Climatology,* 26**,** 17.

Schiemann, R., Liniger, M. A. and Frei, C. 2010. Reduced Space Optimal Interpolation of Daily Rain Gauge Precipitation in Switzerland. *Journal of Geophysical Research,* 115**,** 18.

Serreze, M. C., Carse, F., Barry, R. G. and Rogers, J. C. 1997. Icelandic Low Cyclone Activity: Climatological Features, Linkages with the Nao, and Relationships with Recent Changes in the Northern Hemisphere Circulation. *Journal of Climate,* 10**,** 12.

Siegel, D. A., Doney, S. C. and Yoder, J. A. 2002. The North Atlantic Spring Phytoplankton Bloom and Sverdrup's Critical Depth Hypothesis. *Science,* 296**,** 4.

Steele, M., Morley, R. and Ermold, W. 2001. Phc: A Global Ocean Hydrography with a High-Quality Arctic Ocean. *Journal of Climate,* 14**,** 9.

Stewart, R. H. 1997. *Introduction to Physical Oceanography*.

Stine, A. R., Huybers, P. and Fung, I. Y. 2009. Changes in the Phase of the Annual Cycle of Surface Temperature. *Nature,* 457**,** 7.

Stramska, M. 2005. Interannual Variability of Seasonal Phytoplankton Blooms in the North Polar Atlantic in Response to Atmospheric Forcing. *Journal of Geophysical Research,* 110**,** 20.

Sugimoto, S. and Hanawa, K. 2005. Why Does Reemergence of Winter Sea Surface Temperature Anomalies Not Occur in Eastern Mode Water Areas? *Geophysical Research Letters,* 32**,** 5.

Sverdrup, H. U. 1953. On Conditions for the Vernal Blooming of Phytoplankton. *Journal du Conseil,* 18**,** 9.

Swift, J. H. 1986. The Arctic Waters. *The Nordic Seas***,** 26.

Taylor, A. H. and Stephens, J. A. 1998. The North Atlantic Oscillation and the Latitude of the Gulf Stream. *Tellus,* 50**,** 9.

Taylor, J. R. and Ferrari, R. 2011a. Ocean Fronts Trigger High Latitude Phytoplankton Blooms. *Geophysical Research Letters,* 38**,** 5.

Taylor, J. R. and Ferrari, R. 2011b. Shutdown of Turbulent Convection as a New Criterion for the Onset of Spring Phytoplankton Blooms. *Limnology and Oceanography,* 56**,** 15.

Thompson, D. W. J. and Wallace, J. M. 1998. The Arctic Oscillation Signature in the Wintertime Geopotential Height and Temperature Fields. *Geophysical Research Letters,* 25**,** 4.

Thomson, R. E. and Fine, I. V. 2003. Estimating Mixed Layer Depth from Oceanic Profile Data. *Journal of Atmospheric and Oceanic Technology,* 20**,** 11.

Tomczak, M. and Godfrey, J. S. 1994. *Regional Oceanography: An Introduction,* Oxford, Elsevier Science Ltd.

Townsend, D. W., Cammen, L. M., Holligan, P. M., Campbell, D. E. and Pettigrew, N. R. 1994. Causes and Consequences of Variability in the Timing of Spring Phytoplankton Blooms. *Deep-Sea Research,* 41**,** 19.

Treguier, A. M., Theetien, S., Chassignet, E. P., Penduff, T., Smith, R., Talley, L., Beismann, J. O. and Boning, C. 2005. The North Atlantic Subpolar Gyre in Four High-Resolution Models *Journal of Physical Oceanography,* 35**,** 18.

Trenberth, K. E. 1983. What Are the Seasons? *Bulletin of the American Meteorological Society,* 64**,** 7.

Trenberth, K. E., Large, W. G. and Olson, J. G. 1990. The Mean Annual Cycle in Global Ocean Wind Stress. *Journal of Physical Oceanography,* 20**,** 19.

Vage, K., Pickart, R. S., Sarafanov, A., Knutsen, Ø., Mercier, H., Lherminier, P., Aken, H. M. v., Meincke, J., Quadfasel, D. and Bacon, S. 2011. The Irminger Gyre: Circulation, Convection, and Interannual Variability. *Deep-Sea Research I,* 58**,** 25.

Våge, K., Pickart, R. S., Thierry, V., Reverdin, G., Lee, C. M., Petrie, B., Agnew, T. A., AmyWong and Ribergaard, M. H. 2009. Surprising Return of Deep Convection to the Subpolar North Atlantic Ocean in Winter 2007–2008. *Nature Geoscience,* 2**,** 6.

Vancoppenolle, M., Bouillon, S., Fichefet, T., Goosse, H., Lecomte, O., Maqueda, M. A. M. and Madec, G., 2012: Lim the Louvain-La-Neuve Sea Ice Model.

Wallace, C. 2003. *Variability in the Annual Cycle of Temperature and the Atmoshperic Circulation.* PhD, University of East Anglia.

Wallace, J. M. 2000. North Atlantic Oscillatiodannular Mode: Two Paradigms-One Phenomenon. *Quarterly Jornal of the Royal Meteorological Society,* 126**,** 15.

Walsh, J. E. and Portis, D. H. 1999. Variations of Precipitation and Evaporation over the North Atlantic Ocean, 1958-1997. *Journal of Geophysical Research,* 104**,** 19.

Waniek, J. J. 2003. The Role of Physical Forcing in Initiation of Spring Blooms in the Northeast Atlantic. *Journal of Marine Systems,* 39**,** 26.

White, M. and Bowyer, P. 1997. The Shelf-Edge Current North-West of Ireland. *Annales Geophysicae,* 15**,** 8.

Wild, M. 2009. Global Dimming and Brightening: A Review. *Journal of Geophysical Research: Atmospheres,* 114**,** 31.

Woodgate, R. A., Fahrbach, E. and Rohardt, G. 1999. Structure and Transports of the East Greenland Current at 75øn from Moored Current Meters. *Journal of Geophysical Research,* 104**,** 14.

Yang, J. and Huang, R. X. 1996. Decadal Oscillations Driven by the Annual Cycle in a Zonally-Averaged Coupled Ocean-Ice Model. *Geophysical Research Letters,* 23**,** 4.

Yaremchuk, M. I., Nechaev, D. A. and Thompson, K. R. 2001. Seasonal Variation of the North Atlantic Current. *Journal of Geophysical Research,* 106**,** 17.

Yashayaev, I. M. and Zveryaev, I. I. 2001. Climate of the Seasonal Cycle in the North Pacific and the North Atlantic Oceans. *International Journal of Climatology,* 21**,** 17.

Yool, A., Popova, E. E. and Anderson, T. R. 2011. Medusa-1.0: A New Intermediate Complexity Plankton Ecosystem Model for the Global Domain. *Geoscientific Model Development,* 4**,** 37.

Yool, A., Popova, E. E. and Anderson, T. R. 2013. Medusa-2.0: An Intermediate Complexity Biogeochemical Model of the Marine Carbon Cycle for Climate Change and Ocean Acidification Studies. *Geoscience Model Development,* 6**,** 45.

Yu, L., Jin, X. and Weller, R. A. 2006. Role of Net Surface Heat Flux in Seasonal Variations of Sea Surface Temperature in the Tropical Atlantic Ocean. *Journal of Climate,* 19**,** 17.

Zhai, L., Platt, T., Tang, C., Sathyendranath, S. and Walne, A. 2013. The Response of Phytoplankton to Climate Variability Associated with the North Atlantic Oscillation. *Deep-Sea Research II,* 93**,** 10.

Zhang, H. and Wu, L. 2010. Predicting North Atlantic Sea Surface Temperature Variability on the Basis of the First-Mode Baroclinic Rossby Wave Model. *Journal of Geophysical Research,* 115**,** 15.

Zveryaev, I. I. and Gulev, S. K. 2009. Seasonality in Secular Changes and Interannual Variability of European Air Temperature During the Twentieth Century. *Journal of Geophysical Research,* 114**,** 14.